INAUGURAL - DISSERTATION

submitted to the
Combined Faculties for the Natural Sciences and for Mathematics
of the Ruperto-Carola University of Heidelberg, Germany
for the degree of
Doctor of Natural Sciences

presented by

MSc. in Science Sònia Nielles-Vallespin
born in Barcelona (Catalunya - Spain)

Oral Examination: 22. December 2004

Development and Optimisation of Radial Techniques for Sodium Magnetic Resonance Imaging

Referees: **Prof. Dr. Josef Bille**

Prof. Dr. Lothar Rudi Schad

Entwicklung und Optimierung von RadialTechniken für die Natrium-Magnetresonanzbildgebung

Das Ziel dieser Arbeit war die Bereitstellung von Techniken und Hardware für die ^{23}Na-MRT des menschlichen Gehirns, Herzens und Muskels an einem klinischen Tomographen bei 1.5T. Zu diesem Zweck wurden Hochfrequenz-(HF)-spulen entwickelt und Sende-Empfangsweichen auf 16.84 MHz angepasst. Eine radiale 3D Gradientenecho-(GRE)-sequenz wurde mit einer minimalen Echozeit von $TE_{min} = 70\,\mu$s für ^{1}H und 200 μs für ^{23}Na implementiert, um sowohl die kurze ($T_2^* = 0.5$ ms) als auch die lange ($T_2^* = 12 - 25$ ms) Komponente des ^{23}Na NMR Signals bei der Messung des gesamten Natriumgehalts zu detektieren. Ein Gridding Rekonstruktionsalgorithmus mit einem rho-Filter und einem Kaiser-Bessel-Fenster wurde implementiert und sowohl fr ^{23}Na als auch für ^{1}H MRT optimiert. Bei einer Gesamtmesszeit von $T_{acq} = 10$ min und einer nominellen Auflösung von $\Delta x = 4$ mm wurde ein zweifach höheres Signal-zu-Rausch Verhältnis SNR *in in-vivo* ^{23}Na Radialbildern beobachtet als in konventionellen cartesischen 3D GRE Daten. In den Radialbildern wurden aufgrund des T_2-Signalzerfalls während der Datenaufnahme Unschärfen beobachtet, die die Auflösung um einen Faktor von ungefähr zwei reduzierten. Sowohl cartesische als auch radiale GRE-Methoden wurden bei 1.5 T und 4 T miteinander verglichen. Eine Zunahme des SNR von $SNR_{4T}/SNR_{1.5T} \sim 4$ wurde *in-vivo* gemessen. In Hirntumorpatienten wurde eine 20%ige Zunahme des 23Na MR Signals in der Tumorregion detektiert. Das Kontrast-zu-Rausch Verhältnis $CNR = 23\%$ zwischen gesundem Gewebe und Tumor gemessen mit der 3D Radialtechnik war 20% gröer als das CNR der cartesischen Sequenz. In Patienten mit einer Disfunktion der Natriumkanle der Zelle wurde eine ^{23}Na Signalerhöhung von 10% gemessen. Diese Methode erlaubt es, Änderungen der intrazellulären ^{23}Na Konzentration zu detektieren und könnte ein neues Werkzeug zur nichtinvasiven Evaluation der Gewebevitalität darstellen.

Development and Optimisation of Radial Techniques for Sodium Magnetic Resonance Imaging

The goal of this work was to provide techniques and hardware for ^{23}Na MRI of the human brain, heart and muscle in a clinical scanner at 1.5 T. For this purpose, radiofrequency (RF) coils were developed and a transmit/receive switch was adapted to 16.84 MHz. A 3D radial gradient echo (GRE) sequence was implemented, with a minimum echo time $TE_{min} = 70\,\mu$s for ^{1}H and 200 μs for ^{23}Na, allowing to detect both the short ($T_2^* = 0.5$ ms) and the long ($T_2^* = 12-25$ ms) components of the ^{23}Na NMR signal for total ^{23}Na content evaluation. A gridding reconstruction algorithm with a Kaiser-Bessel window and a rho filter was implemented and optimised for both ^{23}Na and ^{1}H MRI. At an acquisition time $T_{acq} = 10$ min and a nominal resolution $\Delta x = 4$ mm, the signal-to-noise ratio SNR of the *in-vivo* ^{23}Na 3D radial images was twofold higher than in standard cartesian GRE MRI ($TE_{min} = 2$ ms). In the radial images blurring due to T_2 signal decay during data acquisition was observed, reducing the resolution by approximately a factor of two. Both cartesian and radial GRE methods were compared at 1.5 T and 4 T. An SNR increase of $SNR_{4T}/SNR_{1.5T} \sim 4$ was measured *in-vivo*. In brain tumour patients, a 20% ^{23}Na MRI signal increase in the tumour region was detected. A contrast-to-noise ratio $CNR = 23\%$ between healthy tissue and tumour achieved with the 3D radial was 20% higher than the CNR of the cartesian sequence. In patients with a ^{23}Na channel disfunction, a ^{23}Na MRI signal increase of $\sim 10\%$ was measured. This method allows for the detection of changes in the intracellular ^{23}Na concentration and may provide a new tool to non-invasively evaluate tissue vitality.

Desarrollo y Optimización de Técnicas Radiales para la Resonancia Magnética de Sodio

El objetivo de este trabajo era proporcionar técnicas y hardware para IRM de ^{23}Na del cerebro, corazón y músculo humanos en un escáner clínico a 1.5 T. Con este propósito, antenas de radiofrecuencia (RF) fueron desarrolladas y un conmutador de transmisión/recepción se adaptó a 16.84 MHz. Para la evaluación del contenido total de ^{23}Na, una secuencia de gradiente-eco (GRE) en 3D se implementó, con un tiempo de eco mínimo $TE_{min} = 70\,\mu$s para ^{1}H y $200\,\mu$s para ^{23}Na, permitiendo la detección tanto de la componente corta ($T_2^* = 0.5$ ms) como de la larga ($T_2^* = 12 - 25$ ms) del señal de RMN de ^{23}Na. Un algoritmo de reconstrucción *gridding* con una ventana Kaiser-Bessel y un filtro rho fue implementado y optimizado tanto para IRM de ^{23}Na como de ^{1}H. Con un tiempo de adquisición $T_{acq} = 10$ min y una resolución nominal $\Delta x = 4$ mm, la proporción de señal a ruido SNR de las imágenes 3D radiales *in-vivo* era el doble comparada con la de las técnicas cartesianas GRE estándar ($TE_{min} = 2$ ms). En las imágenes radiales se observó enturbiamiento debido a la relajación de la señal durante la adquisición de datos, reduciendo la resolución a la mitad. Tanto el método GRE cartesiano como el radial fueron comparados a 1.5 T y 4 T. Un incremento en SNR de $SNR_{4T}/SNR_{1.5T} \sim 4$ fue medido *in-vivo*. En pacientes con tumor cerebral, un 20% de aumento en el señal de RMN de ^{23}Na fue detectado. La proporción de contraste a ruido $CNR = 23\%$ entre tejido saludable y tumor conseguida con la secuencia radial era un 20% más elevada que la CNR de la secuencia cartesiana. En pacientes con una disfunción del canal de ^{23}Na, se midió un incremento de $\sim 10\%$ en la señal de ^{23}Na. Este método permite la detección de variaciones en la concentración de ^{23}Na intracelular y podría proporcionar un nuevo instrumento no invasivo para la evaluación de la vitalidad del tejido.

Desenvolupament i Optimització de Tècniques Radials per a la Resonància Magnètica de Sodi

L'objectiu d'aquest treball era proveïr tècniques i hardware per IRM de ^{23}Na del cervell, cor i muscle humans en un escàner clínic a 1.5 T. Per aquesta raó, antenes de radiofreqüència (RF) foren desenvolupades i un commutador de transmissió/recepció fou adaptat a 16.84 MHz. Per l'evaluació del contingut total de ^{23}Na, una seqüència 3D radial de gradient-eco (GRE) va ser implementada amb un temps d'eco mínim $TE_{min} = 70\,\mu$s per ^{1}H i $200\,\mu$s per ^{23}Na, permetent la detecció tant de la component curta ($T_2^* = 0.5$ ms) com de la llarga ($T_2^* = 12 - 25$ ms) del senyal de RMN de ^{23}Na. Un algoritme de reconstrucció *gridding* amb una finestra Kaiser-Bessel i un filtre rho foren implementats i optimitzats tant per IRM de ^{23}Na com de ^{1}H. Amb un temps d'adquisició $T_{acq} = 10$ min i una resolució nominal $\Delta x = 4$ mm, la proporción de senyal a soroll SNR de les imatges 3D radials *in-vivo* era el doble comparada amb la de les tècniques cartesianes GRE estàndard ($TE_{min} = 2$ ms). En les imatges radials es va observar enterboliment degut a la relaxació del senyal durant l'adquisició de dades, reduint la resolució a la meitat. Tant el mètode GRE cartesià com el radial foren comparats a 1.5 T i 4 T. Un increment en SNR de $SNR_{4T}/SNR_{1.5T} \sim 4$ fou mesurat *in-vivo*. En pacients amb tumor cerebral, un 20% d'augment en el senyal de RMN de ^{23}Na fou detectat. La proporció de contrast a soroll $CNR = 23\%$ entre teixit saludable i tumor assolida amb la seqüència radial era un 20% més elevada que la CNR de la seqüència cartesiana. En pacients amb una disfunció del canal de ^{23}Na, es va mesurar un increment de $\sim 10\%$ en el senyal de ^{23}Na. Aquest mètode permet la detecció de variacions en la concentració intracel·lular del ^{23}Na i podria proporcionar una nova eina no invasiva per l'evaluació de la vitalitat del teixit.

A la meva família, amb tot el meu amor.
To my family, with all my love.

Contents

Introduction

In the human body sodium (^{23}Na) ions are ubiquitous and they are known to play a vital role in maintaining cellular homeostasis by establishing an electrochemical concentration gradient across the plasma membrane. This gradient regulates osmosis, balances pH, and conducts the action potential along axons in the brain parenchyma. Sodium ions are found predominantly outside the cell in a concentration of approximately 140 mM; inside the cell, they occur in a concentration of approximately 10 mM.

^{23}Na possesses a nuclear spin of 3/2, which results in four distinct energy states in the presence of an external magnetic field. This allows three possible single-quantum energy-degenerate transitions that are observed at magnetic resonance (MR) spectroscopy as a single spectral line. However, these transitions lose their degeneracy in the presence of local electric field gradients due to quadrupolar interactions and three distinct resonance lines are observable: Two satellite spectral lines (each having 30% of the total signal intensity) appear on either side of the unperturbed resonance (40% of the total signal). In tissue, however, this line splitting is averaged out by various processes (e.g. molecular motion and chemical exchange), and another property resulting from quadrupolar mechanisms is observed: a bi-exponential T_2 relaxation, consisting of the superposition of fast- and slow-decaying components. In vivo studies have measured the fast-decaying T_2 component to be approximately $0.5 - 3.0$ msec, the slow-decaying T_2 component to be approximately $15 - 30$ msec.

Despite its relatively low gyromagnetic ratio γ (approximately one-fourth that of protons ^{1}H, $\gamma_{^1H}/\gamma_{^{23}Na} \sim 4$), low tissue equivalent concentration (approximately $2 \cdot 10^{-4}$ times that of ^{1}H), and short T_2 ($T_2^{^1H}/T_2^{^{23}Na} \sim 1000$), ^{23}Na is the second nucleus with the highest NMR sensitivity *in vivo*.

Investigations of sodium with MR can be grouped into three main categories: paramagnetic shift reagents [Van Emous 2001], multiple-quantum filtering [Borthakur 99], and ^{23}Na MRI of the total tissue concentration [Boada 1997c]. While MR studies using shift reagents offer a direct way of discriminating between extracellular and intracellular sodium, the toxicity of effective reagents prohibits their use in humans. MR studies with multiple-quantum filtering offer a way of differentiating between fractions of sodium on the basis of fast-decaying and slow-decaying T_2 components. The results, however, are limited by the considerably lower signal-to-noise ratio (SNR) and lower resolution of multiple-quantum

filtering. Therefore, this work focuses on the imaging of total tissue sodium concentration *in vivo* by single-quantum methods, since these may currently hold the greatest potential for future clinical application.

To date, various articles have been published about sodium imaging of pathologic conditions in the human brain such as stroke Hilal85,Thulborn99b, edema Hilal85, vascular malformation Hilal85, and tumours Hilal85,Thulborn99. A primary concern when using single-quantum methods is the need to limit signal loss from fast T_2 by keeping the echo time TE as short as possible. Spin-echo sequences were employed in early studies [Hilal 83]. However, because of the low γ and because relaxation is dominated by the interaction between the nuclear quadrupole moment and local electric field gradients, T_2 is approximately equal to T_2^*. Therefore, the use of refocusing radiofrequency (RF) pulses does not provide any substantial advantage over gradient-echo (GRE) methods [Joseph 87].

More recently, there have been several reports of sodium studies with three-dimensional (3D) MR projection imaging [Boada 1997a] and twisted projection imaging TPI [Boada 1997c]. Because of the absence of section-select and phase-encoding gradient pulses, these methods allow for very short $TE \leq 400\mu s$. However, they may cause blurring and TPI is hindered by lengthy repetition time TR and readout time which prevents the exploitation of the short T_1 (approximately $5060msec$) of sodium in vivo. Furthermore, the implementation of such sequences requires the use of complicated reconstruction methods and places high demands on gradient hardware.

In the first chapter of this thesis, the physiological relevance of ^{23}Na to study cell vitality is outlined. The Nuclear Magnetic Resonance (NMR) and Magnetic Resonance Imaging (MRI) basics are introduced in chapters 2 and 3, and the particularities of ^{23}Na NMR and MRI are discussed. The development of the radiofrequency RF coils and the measurement techniques developed during this thesis are described in chapters 4, 5 and 6. Chapters 7, 8 and 9 include a compilation of the measurements and results achieved with the methods and the hardware developed in this thesis. The clinical applications are described in chapter 10. Chapters 11 and 12 conclude with a discussion of the results and a summary.

Part I

Background

Chapter 1

Physiological Background of Sodium

In this chapter, the physiological relevance of sodium to study cell vitality is described.

1.1 General concepts

Sodium (^{23}Na) plays an important role in many key biological processes in the human body. Together with potassium (K), ^{23}Na has the highest ion concentration in the body and it is distributed all over the body. At the same time, the extracellular ^{23}Na concentration is $\left[^{23}\mathrm{Na}\right]_{ext} \simeq 145\,\mathrm{mM}$ and the intracellular $\left[^{23}\mathrm{Na}\right]_{int} \simeq 5 - 10\,\mathrm{mM}$, in contrast with potassium, whose concentrations are $\left[K\right]_{ext} \simeq 4\,\mathrm{mM}$ and $\left[K\right]_{int} \simeq 144mM$. Both ions generate through their concentration gradient the equilibrium potential of the cell of approximately 90 mV, depending on cell type. This big concentration gradient is normally maintained by the Na-K pump, which actively transports the ions through the cell membrane (Figure 1.1). Potential variations can induce amongst other things the transport of other substances in and out of the cell, which at the same time can trigger other reactions. This is why the cell vitality is directly related to the Na-K pump. There are also many other channels in the cell in which ^{23}Na is involved, including the ^{23}Na-K pump, the ^{23}Na-^{1}H pump, etc. Synaptic transmission, osmotic balance, solute transport and calcium exchange in muscular contraction are some of the cellular processes in which ^{23}Na plays an important role.

The intracellular space corresponds to $30 - 40\,\%$ of the body weight. The extracellular space, on the other hand, corresponds only to $25 - 35\,\%$. This results in an average ^{23}Na concentration of around 55 mM. In comparison, hydrogen has a body concentration of 111 M. This approximately 2000 times lower ^{23}Na concentration diminishes the anyway low MR sensitivity of sodium ($S = 9,27\,10^{-2}$) to 20000 times lower compared to the MR sensitivity of hydrogen [Parrish 97].

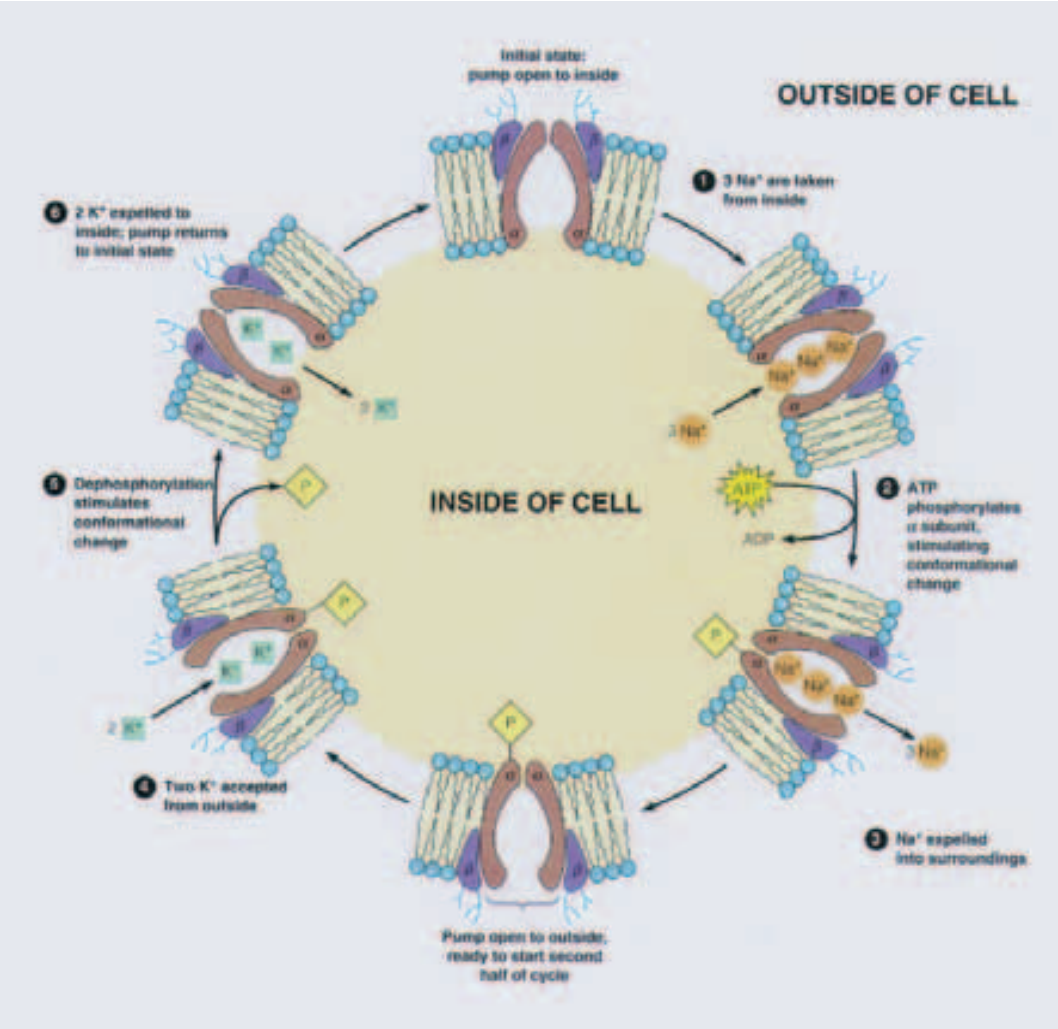

Figure 1.1: Schematic model of the sodium potassium (Na^+/K^+) pump in operation. Courtesy of (http://www.nd.edu/ aseriann/nak.html)

1.2 Head

Sodium concentration is sensitive to disease as an indicator of cellular and metabolic integrity and ion homeostasis [Goldsmith 75]. Angiogenesis and cellular proliferation are important indicators of tumour malignancy. Changes in sodium/hydrogen (Na^+/H^+) exchange kinetics are part of the signaling mechanism that initiates cell division [Rotin 89]. Cell division and the acidic extracellular microenvironment of tumour cells are both associated with an increase in intracellular Na concentration ($[Na^+]_{in}$). Increased $[Na^+]_{in}$, increased Na/H transporter activity, and altered (Na^+/K^+)-adenosine triphosphatase activity have all been linked to tumour malignancy. In a recent study Winter01, investigators subcutaneously implanted a 9L glioma model in rats and indicated that successful chemotherapy can lead to normalisation of the initially elevated sodium concentration as seen with conventional (single-quantum) and multiple-quantum ^{23}Na magnetic resonance (MR) spectroscopy [Ouwerkerk 03].

The observed tissue sodium concentration is composed of the weighted average of extracellular sodium content $[Na^+]_{ex}$ and intracellular sodium content $[Na^+]_{in}$ in the tissue being examined. $[Na^+]_{ex}$ at 140 mmol/L is typically much higher than is $[Na^+]_{in}$, which is about $10 - 15$ mmol/L. Arguably, the more physiologically relevant information is in the intracellular component, reflecting the ability of the cell to pump out sodium ions, whereas $[Na^+]_{ex}$ will remain virtually constant as long as there is adequate perfusion to the tissue. When the relative contribution of the $[Na^+]_{in}$ to the tissue sodium concentration is large, as it is in brain tumours, the sodium concentration provides a measure of metabolic changes affecting $[Na^+]_{in}$. Estimates for the extracellular volume fraction in the brain vary from 6% to 20%. When one considers that tissue perfusion fixes the extracellular concentration at about 140 mmol/L, assuming a normal intracellular concentration of 12 mmol/L, it can be calculated that the contribution of $[Na^+]_{in}$ in normal tissue is between 26% and 57%. More than half of the combined ^{23}Na signal is due to intracellular ^{23}Na when the partial volume of the extracellular compartment is less than 7%. Thus, despite the inability to resolve intra- and extracellular components of the ^{23}Na signal, the measurement of sodium concentration is a sensitivity measure of $[Na^+]_{in}$ [Ouwerkerk 03].

^{23}Na MR imaging can help identify malignant tumours with regard to the intrinsic changes that occur in tumour Na^+/K^+ pump function. Therapies that alter tumour ion homeostasis or affect or destroy tumour cell membrane integrity are likely to generate changes that are observable with ^{23}Na MR imaging and sodium concentration measurements. With these measurements, changes can be observed much earlier than the effects of anatomic remodeling. Therefore, these techniques may prove useful in providing early noninvasive metabolic markers of tumour response to therapy without requiring exogenous contrast-enhanced or radionuclide imaging agents. When used in conjunction with ^{1}H MR imaging protocols such as the FLAIR sequence, MR imaging contrast agents, and T2-weighted imaging methods, ^{23}Na MR imaging may provide additional functional information on the morphology of tumours that may enhance visualisation of a necrotic core or proliferating periphery and most important, improve diagnostic specificity with multiparametric

analysis methods [Ouwerkerk 03].

1.3 Heart

Assessment of the extent and location of nonviable myocardium is important clinically in both acute and chronic syndromes of ischemic heart disease. For example, it is known that the quantity of necrotic myocardium is one of the most important prognostic indicators of both short- and long-term outcome after acute myocardial infarction (AMI). In addition, it is recognised that coronary revascularisation in patients with chronic coronary artery disease and left ventricular (LV) dysfunction best improves symptoms and prognosis if the dysfunctional myocardium is viable. In this situation, a noninvasive imaging examination that verifies the absence of infarcted myocardium in regions with impaired contractility could be vital in the decision to undergo a revascularisation procedure, with its attendant morbidity and mortality. Although the presence of nonviable myocardium can be inferred by use of a variety of techniques, it has been suggested that the loss of cell membrane integrity as evidenced by the loss of intracellular to extracellular ionic gradients is perhaps the best criterion to identify myocyte death [Kim 97], [Kim 97b].

Normal myocardial function depends on active cellular maintenance of electrochemical gradients. Disruption of these gradients indicates cellular injury or dysfunction. In viable myocytes, $[Na^+]_{in}$ is much lower than $[Na^+]_{ex}$ due to active outward transport of sodium by Na+/K+-ATPase. During ischemia, $[Na^+]_{in}$ rises steadily in a nearly linear fashion, reaching two- to fivefold increases over 20 to 30 minutes. Upon reperfusion, $[Na^+]_{in}$ returns to near baseline levels within minutes, unless the ischemic insult was prolonged and caused irreversible injury, in which case sodium concentrations remain elevated. This sequence of events suggests that measurement of tissue sodium content can be used to distinguish viable from nonviable myocardium after ischemic injury [Kim 97], [Kim 97b].

Cannon et al [Cannnon 86] have shown that ^{23}Na image intensity is elevated in myocardial regions subject to ischemia and reperfusion. Their data suggest that regional determination of myocardial viability may not require differentiation of intra- and extracellular sodium signals. Since myocardial tissue volume is primarily intracellular (75% of the water space), a weighted average of intra- and extracellular sodium is much lower than the extracellular level under normal conditions. For example, assuming that $[Na^+]_{in} = 15\,\text{mmol/L}$, $[Na^+]_{ex} = 145\,\text{mmol/L}$, and 77% of myocardial tissue is water space, then the composite concentration would equal 37 mmol/L, (i.e. $0.77 \times ([0.75 \times 15] + [0.25 \times 145]) = 37$). In the extreme case in which all myocytes within a nonviable region failed to maintain a sodium concentration gradient, the tissue sodium concentration would reach the extracellular level, an increase of $> 200\%$, ie, $[(0.77 \times 145) - 37]/37 = 202\%$, above viable myocardium. This difference is likely large enough to be detected on ^{23}Na images [Kim 97], [Kim 97b].

1.4 Muscle

Alterations in total ^{23}Na content and in transmembrane ^{23}Na flux rates occur in numerous normal and disease conditions in the muscle, such as exercise muscle or skeletal myopathies. ^{23}Na MRI in muscle is more challenging than brain studies because the total ^{23}Na concantration is about 32% lower than the brain value of $43 - 45\,\mathrm{mmol/kg}$ of wet weight. This translates directly into a reduced signal-to-noise ratio that leads to decreased spatial resolution, prolonged image acquisition times, or both. It would provide, however, a non-invasive tool to examine ^{23}Na concentration in the muscle, as an alternative to the needle biopsy, which is nowadays the standard method of providing tissue ^{23}Na levels in the muscle [Constantinides 2000].

Chapter 2

Nuclear Magnetic Resonance

In this chapter, the Nuclear Magnetic Resonance (NMR) basics are introduced and the particularities of Sodium (^{23}Na) NMR are discussed.

The equations of motion for the magnetic moment in the presence of an external magnetic field are presented. The combined effect of a static magnetic field and a perpendicular radiofrequency RF field is considered, and the motion of a magnetic moment immersed in these fields is analysed. The interactions of spins amongst themselves and with their surroundings under the presence of external fields are modeled by the phenomenological Bloch equations and the relaxation times T_1, T_2 and T_2^* are introduced.

The particularities of sodium ^{23}Na NMR in comparison to proton ^{1}H NMR are described. The ^{23}Na NMR sensitivity and relaxation times are compared to those of protons (^{1}H). ^{23}Na is characterised as a spin 3/2 nucleus with magnetic dipole moment and electric quadrupole moment. The quadrupolar interaction of spin 3/2 nuclei in the presence of external magnetic and electric fields is described and the different types of ^{23}Na NMR spectra, related to the nature of the molecular environment, are presented. The relaxation process of quadrupolar nuclei is described.

2.1 Nuclear Spin and Magnetic Moment

The interaction between a spin and a magnetic field is a quantum mechanical phenomenon. The spin quantum number I can only take integer or half integer values. If $I = 0$, no interactions will occur with a magnetic field. The term spin implies that the particle possesses an angular momentum, $\vec{p}$, related to the spin $\vec{I}$ by:

$$\vec{p} = \hbar \vec{I} \tag{2.1}$$

where $\hbar = h/2\pi$ and h is Planck's constant.

The rotating electric charge of the spin gives rise to an associated magnetic dipole moment, $\vec{\mu}$ defined as:

$$\vec{\mu} = \gamma \vec{p} = \gamma \hbar \vec{I} \tag{2.2}$$

where γ is the gyromagnetic ratio, which is a constant characteristic of every nucleus. It can be expressed as:

$$\gamma = \frac{-g\mu_B}{\hbar} \tag{2.3}$$

g is the particle's g factor ($g = 5.58$ for the proton) and μ_B is the Bohr magneton, defined as $e\,\hbar/2\,m\,c$, where e is the charge of the particle, c is the speed of light and m is its rest mass.

The hydrogen nucleus ^{1}H has a single proton and $\gamma_H/2\pi = 42.58\,\mathrm{MHzT}^{-1}$. ^{1}H is the most commonly observed nucleus in MRI because it has the greatest NMR sensitivity and is the most abundant in living tissue. The sodium nucleus ^{23}Na, on the other hand, has 11 protons and 12 neutrons and $\gamma_H/2\pi = 11.26\,\mathrm{MHzT}^{-1}$. ^{23}Na has the second highest NMR sensitivity after ^{1}H.

In the quantum mechanical description $\vec{I}$ and $\vec{\mu}$ are operators. For the angular momentum operator the following equations hold true:

$$\hat{I}^2\,|\,I,\,m\rangle = \hbar^2 I(I+1)\,|\,I,\,m\rangle \tag{2.4}$$
$$\hat{I}_z\,|\,I,\,m\rangle = m\hbar\,|\,I,\,m\rangle \tag{2.5}$$

where $|\,I,\,m\rangle$ are the eigenstates of the angular momentum operator, I is the angular quantum number, and m is the magnetic quantum number. m takes values between $m = -I, -I+1, \ldots, I-1, I$. This implies that there are $2I+1$ possible states for the nucleus spin, corresponding to the $2I+1$ orientations of the magnetic dipole moment.

2.2 Interaction with a static Magnetic Field

2.2.1 Quantum mechanical description

In the presence of an external magnetic field $\vec{B}$, the magnetic moments of the sample orient themselves along $\vec{B}$. The Hamilton operator describes the interaction of the magnetic moment with the external magnetic field as follows:

$$\hat{H} = -\hat{\mu}\vec{B} = -\gamma\hbar\hat{I}\vec{B} \tag{2.6}$$

Assuming a homogeneous, time-independent external magnetic field oriented in the z direction $\vec{B}_0 = (0,\, 0,\, B_0)$, the Hamilton operator can be simplified to:

$$\hat{H}_Z = -\gamma\hbar\hat{I}_Z B_0 \tag{2.7}$$

The Hamilton operator $\hat{H}_Z$ commutes with the absolute value $\hat{I}^2$ and the z component $\hat{I}_Z$ of the angular momentum operator, so that both the Hamilton operator and the angular momentum operator have the same eigenstates $|\, I,\, m\rangle$.

The energy eigenvalues $E_{m,Z}$ of a magnetic moment in a homogeneous magnetic field are derived from the Schrödinger equation:

$$\hat{H}_Z\,|\, I,\, m\rangle = E_{m,Z}\,|\, I,\, m\rangle \tag{2.8}$$

$$E_{m,Z} = -m\gamma\, B_0\hbar \tag{2.9}$$

The splitting of the energy states caused by the presence of an external magnetic field is called the Zeeman effect.As mentioned before, for a spin nucleus with spin quantum number I there are $2I + 1$ possible energy levels. The energy difference between neighbouring energy levels corresponds to:

$$\Delta E_{m,Z} = E_m - E_{m-1} = \gamma\,\hbar\, B_0 = \hbar\,\omega_0 \tag{2.10}$$

For protons $I = 1/2$, thus two energy levels are present. Sodium, on the other hand, with $I = 3/2$ will have four possible energy levels with a constant energy difference ΔE. The energy difference is proportional to the magnetic field strength and the gyromagnetic ratio. Consequently, at the same field strength B_0, ΔE for sodium will be four times smaller than for protons.

Apart from the splitting of the energy levels, the external magnetic field $\vec{B}_0$ introduces a precession of the spin about the quantisation axis z. The time evolution of the system is described by the Schrödinger equation:

$$i\hbar\frac{\partial|\Psi(t)\rangle}{\partial t} = \hat{H}|\Psi(t)\rangle \tag{2.11}$$

where $\hat{H}$ is the Hamilton or energy operator and $|\Psi(t)\rangle$ is an arbitrary state. If $\hat{H}$ is constant with time, the Schrödinger equation yields the result:

$$|\Psi(t)\rangle = \hat{U}(t)|\Psi(0)\rangle \tag{2.12}$$

with the evolution operator $\hat{U}(t)$ defined as:

$$\hat{U}(t) = e^{-i\hat{H}_Z t/\hbar} = e^{i\gamma B_0 t\hat{I}_z} = e^{-i\alpha\hat{I}_z} \tag{2.13}$$

The quantity $\alpha = -\gamma B_0 t$ is the expectation value of the rotation angle about the z axis. The existence of the magnetic field $\vec{B}_0$ causes all states to precess about the quantisation axis z at the Larmor frequency $\omega_0 = \gamma B_0$. At $1.5\,T$, the ^{1}H Larmor frequency is $\omega_0^{^1\mathrm{H}} = 63.6\,MHz$, while for ^{23}Na it is $\omega_0^{^{23}\mathrm{Na}} = 16.8\,MHz$.

2.2.2 Bulk magnetisation in a magnetic field

In the following we will consider not only one, but a population of N spins in a homogeneous magnetic field. In thermal equilibrium at temperature T, a population difference of the energy states arises according to the Boltzmann probability factor:

$$p_m = \frac{1}{Z} e^{-\frac{E_m}{kT}} = \frac{1}{Z} e^{-\frac{\gamma\hbar m B_0}{kT}} \tag{2.14}$$

where k is the Boltzmann constant ($k = 1.38 \times 10^{-23} J/K$). The sum of probabilities:

$$Z = \sum_{m=-I}^{I} e^{-\frac{E_m}{kT}} \tag{2.15}$$

is introduced to normalise the values of the p_m to values between 0 and 1. The individual energy levels have different populations. From these, the absolute value of the macroscopic magnetisation in thermal equilibrium can be calculated as follows:

$$M_0 = \frac{N}{V}\gamma\hbar \frac{\sum_{m=-I}^{I} m e^{-\frac{E_m}{kT}}}{\sum_{m=-I}^{I} e^{-\frac{E_m}{kT}}} \tag{2.16}$$

At room temperature $E_m \ll kT$, so that $e^x \approx 1 + x$. Equation 2.16 then simplifies to the Curie Law:

$$M_0 \approx \frac{N}{V}\,\gamma\hbar\,\frac{\Delta E_m}{kT}\frac{\sum_{m=-I}^{I} m^2}{2I+1} = \frac{N}{V}\frac{\hbar^2\gamma^2 I(I+1)B_0}{3kT} \tag{2.17}$$

For the transition between the states $|\frac{1}{2}\rangle$ and $-|\frac{1}{2}\rangle$, the population difference can be calculated as follows:

$$\frac{N_{-\frac{1}{2}}}{N_{+\frac{1}{2}}} = e^{-\frac{\gamma\hbar B_0}{kT}} = 1 - \frac{\gamma\hbar B_0}{kT} \tag{2.18}$$

2.2.3 Semi-classical description: Equation of Motion

At room temperature $E_m \ll kT$ and the predictions of the classical model agree with those of the quantum theory for the macroscopic magnetisation $\vec{M}$, which is defined as the sum of the expectation values of N individual magnetic moments $\vec{\mu}$ per unit volume V:

$$\vec{M} = \sum_{i=1}^{N} \frac{\langle \vec{\mu}_i \rangle}{V} \tag{2.19}$$

In the quantum mechanical description, the time evolution of the expectation value of the macroscopic magnetisation reads:

$$\frac{d\vec{M}}{dt} = -\frac{i}{\hbar}[\vec{M}, \hat{H}] \tag{2.20}$$

By equating the torque to the rate of change of angular momentum:

$$\frac{d\vec{M}}{dt} = \vec{M}(t) \times \gamma \vec{B}(t) \tag{2.21}$$

The magnetisation precesses about the direction of the applied field at an angular frequency $\omega = -\gamma B_0$.

2.3 Effects of a Radiofrequency Pulse

According to equation 2.21, the magnetisation angle between $\vec{M}$ and $\vec{B}$ cannot change. In order to tip the magnetisation $\vec{M}$ from its equilibrium, a radiofrequency (RF) pulse needs to be applied. The precession of the resulting transverse component of magnetisation produces its own rotating field, which can be detected with a nearby antenna. The RF field $\vec{B}_1$, with angular moment ω, is applied orthogonal to $\vec{B}_0$, and can be described as:

$$\vec{B}_1 = B_1(\hat{x}\, cos\omega t + \hat{y}\, sin\omega t) \tag{2.22}$$

The expanded Hamilton operator then reads:

$$\hat{H} = -\gamma \hbar \hat{I}(\vec{B}_0 + \vec{B}_1) \tag{2.23}$$

From eq 2.21 the following equation of motion of the macroscopic magnetisation in the laboratory frame of reference can be derived:

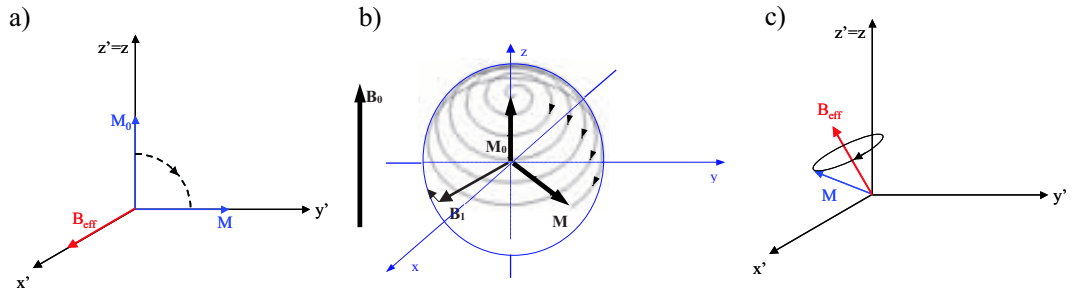

Figure 2.1: (a) Precession of the magnetisation $\vec{M}$ in the rotating frame of reference about the effective magnetic field $\vec{B}_{eff}$. (b) Precession of the magnetisation $\vec{M}$ in the laboratory frame of reference. (c) Precession of a magnetic moment about the effective magnetic field $\vec{B}_{eff}$ in the rotating frame of reference.

$$\frac{d\vec{M}}{dt} = \vec{M}(t) \times \gamma[\hat{x}\, B_1 cos\omega t + \hat{y}\, B_1 sin\omega t + \hat{z}\, B_0] \tag{2.24}$$

This somewhat complicated expression can be simplified using a rotating frame of reference that rotates about the z axis at a frequency ω. Equation 2.24 then becomes time-independent:

$$\frac{d\vec{M}}{dt} = \vec{M} \times \gamma\vec{B}_{eff} \tag{2.25}$$

In the rotating frame, the magnetisation rotates about an effective magnetic field $\vec{B}_{eff} = (B_1, 0, B_0 - \frac{\omega}{\gamma})$ at a frequency $\omega_{eff} = \gamma|\vec{B}_{eff}|$ (figure 2.1).

At resonance ($\omega = \gamma B_0$), the z component of the effective magnetic field is cancelled and the magnetisation precesses about the x axis. The application of an RF pulse B_1 for a time t_p flips the magnetisation about x axis by an angle α:

$$\alpha = \gamma \int_0^{tp} B_1(t')dt' \tag{2.26}$$

which, for a constant $B_1(t) = B_1$ reads:

$$\alpha = \gamma B_1 t_p \tag{2.27}$$

2.4 Phenomenological Relaxation - The Bloch Equations

2.4.1 Physical Origins of Relaxation

Taking only into account the interaction of the magnetic moment of a nucleus with external magnetic fields and oscillating RF fields, after an RF excitation, $\vec{M}$ should precess about B_0 at a constant angle α (eq 2.27). In order to obtain a realistic model, also the interactions of spins amongst themselves and with their environment need to be taken into account. Due to these interactions, the precessing magnetic moment gradually realigns with B_0 and returns to its equilibrium state M_0. There are two main types of spin relaxations:

- Due to the exchange of energy of the spins with their surroundings, the longitudinal (i.e. parallel to B_0) component of $\vec{M}$, M_z, decays towards its equilibrium value M_0 with a time constant T_1 called **spin-lattice** or **longitudinal relaxation** time.

- The instantaneous magnetic field experienced by any given nucleus is dominated by the externally applied magnetic field B_0. However, there is also a contribution to the local field from any other nucleus which happens to be close. This dipole-dipole interaction causes the precession rate of individual nuclei to vary slightly. The consequence is the loss of phase coherence, which leads to the reduction of the transverse (perpendicular to B_0) component of $\vec{M}$, M_{xy}, to zero. The time constant of the decay of M_{xy} is called the **spin-spin** or **transverse relaxation** time T_2.

T_2 is always less than or equal to T_1.

Hydrogen (^{1}H) is the nucleus most commonly observed in MRI due to the fact that it has the greatest NMR sensitivity, a natural abundance of $99,98\%$ and 10% of the lean body weight is ^{1}H. It appears in the form of water and hydrocarbons, which have different resonance frequency and relaxation times depending on their chemical binding. The large range of values of relaxation times in biological tissue generates the contrast in the NMR image. Moreover, pathologies can be localised due to changes in the relaxation characteristics of affected tissues. Table 2.1 shows typical relaxation times for ^{1}H at $1.5T$.

Tissue	$T_1(ms)$	$T_2(ms)$
gray matter (GM)	950	100
white matter (WM)	600	80
muscle	900	50
cerebrospinal fluid (CSF)	4500	2200
fat	250	60
blood	1200	100-200

Table 2.1: Representative values of the relaxation times T_1 and T_2 in milliseconds, for ^{1}H components of different human body tissues at $B_0 = 1.5T$ and $37°C$ (human body temperature) [Haacke 99].

2.4.2 Bloch equations

In order to describe the relaxation processes, the two decay time constants T_1 and T_2 can be incorporated into the equation of motion of the magnetisation (equation 2.21), resulting in the Bloch equations (Bloch 1946):

$$\frac{dM_x}{dt} = \gamma\,(\vec{M} \times \vec{B})_x - \frac{M_x}{T_2} \tag{2.28}$$

$$\frac{dM_y}{dt} = \gamma\,(\vec{M} \times \vec{B})_y - \frac{M_y}{T_2} \tag{2.29}$$

$$\frac{dM_z}{dt} = \gamma\,(\vec{M} \times \vec{B})_z + \frac{M_0 - M_z}{T_1} \tag{2.30}$$

These equations adequately describe the interactions for liquids and biological tissue, but not for solids, because in solids the crystal structure determines a preferred direction and the relaxation process needs to be expressed by tensors. For a constant, homogeneous magnetic field $\vec{B}_0 = (0, 0, B_0)$, the solutions for the longitudinal magnetization $M_z(t)$ and the transversal magnetization $M_{xy}(t) = M_x + iM_y$ are:

$$M_z(t) = M_0 - (M_0 - M_z(t_0))\, e^{-\frac{t}{T_1}} \tag{2.31}$$

$$M_{xy}(t) = M_{xy}(t_0)\, e^{i\Delta\omega t - \frac{t}{T_2}} \tag{2.32}$$

where $M(t = t_0) = (M_x(t_0), M_y(t_0), M_z(t_0))$ and $\Delta\omega = \omega_0 - \omega_{rot}$, being ω_{rot} the frequency of the rotating frame of reference.

Figure 2.2.a shows the exponential decay of M_{xy} with the time constant T_2. In the laboratory frame an oscillating signal with frequency $\omega_0 = \gamma B_0$ is observed. This is the free induction decay or FID. The longitudinal magnetization, on the other hand, decays towards the equilibrium value M_0 with a time constant T_1 (Figure 2.2.b).

2.4.3 Magnetic field gradients

In order to produce NMR images, magnetic field gradients are necessary:

$$\vec{G} = \left(\frac{\partial Bz}{\partial x}, \frac{\partial Bz}{\partial y}, \frac{\partial Bz}{\partial z}\right) \tag{2.33}$$

The application of a field gradient in a specific direction causes the magnetic field strength to vary according to $\vec{B}(\vec{r}, t) = \vec{B}_0 + \vec{r}\vec{G}(t)$. The Larmor frequency becomes time dependent and varies in $\vec{G}$ direction:

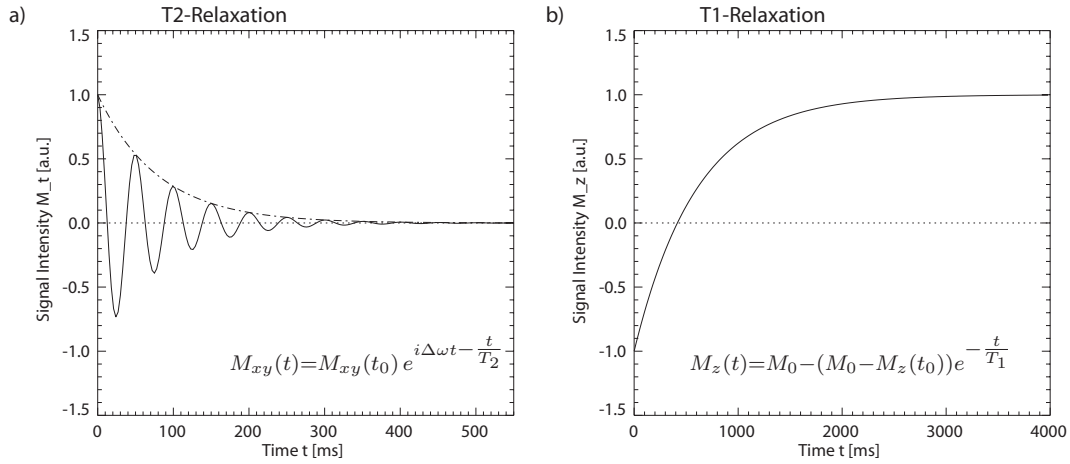

Figure 2.2: T_1 and T_2 relaxation:
a) Transverse magnetisation decay with the time constant T_2 $[M_{xy}(t_0) = M_0 = 1]$.
b) Longitudinal magnetisation recovery with the time constant T_1 $[M_z(t_0) = -M_0]$.

$$\omega(\vec{r}, t) = \gamma(\vec{B}_0 + \vec{r}\vec{G}(t)\,) \tag{2.34}$$

When a linear field gradient is switched on, additional fields with a non-linear spatial dependency arise, the so called concomitant or Maxwell fields. These additional fields are a consequence of the Maxwell equations, which in the case of MR imaging (MRI) imply that inside the imaging volume $\bigtriangledown \times \vec{B} = 0$ (due to the neglectful current density) and $\bigtriangledown \cdot \vec{B} = 0$ must be fulfilled. However, as the strength of the Maxwell fields in first approximation is proportional to G^2/B_0, for a maximum gradient strength of $G_{max} = 25mT/m$ and a filed strength $B_0 = 1,5T$ this effect can be neglected ([Bernstein 1998]).

Taking into account the effects of both the gradients and the radiofrequency field B_1, the Bloch equations read:

$$\frac{dM_{x'}}{dt} = \gamma\vec{G}(t)\vec{r}M_{y'} - \frac{M_{x'}}{T_2} \tag{2.35}$$

$$\frac{dM_{y'}}{dt} = -\gamma\vec{G}(t)\vec{r}M_{x'} - \frac{M_{y'}}{T_2} + \gamma B_1 M_z \tag{2.36}$$

$$\frac{dM_{z'}}{dt} = -\gamma B_1 M_{y'} + \frac{M_0 - M_{z'}}{T_1} \tag{2.37}$$

- **Solution for RF fields.** Setting $\vec{G} = 0$ in equations 2.35, 2.36 and 2.37, and neglecting the relaxation effects during the RF excitation, the solution reads:

$$M_{x'}(t) = M_{x'}(t_0) \quad (2.38)$$
$$M_{y'}(t) = M_{y'}(t_0)\cos(\omega_1 t) + M_{z'}(t_0)\sin(\omega_1 t) \quad (2.39)$$
$$M_{z'}(t) = -M_{y'}(t_0)\sin(\omega_1 t) + M_{z'}(t_0)\cos(\omega_1 t) \quad (2.40)$$

where $\omega_1 = \gamma B_1$. The previous equations define a rotation of the magnetisation about the x axis at an angle $\alpha = \omega_1 t$. This is the so-called free induction decay or FID.

- **Solution for Gradient fields.** For pure gradient fields in equations 2.35, 2.36 and 2.37, the solution reads:

$$M_{x'y'}(t) = M_{x'y'}(t_0)e^{i\Phi(\vec{r}(t),t)}e^{-\frac{t}{T_2}} \quad (2.41)$$
$$M_{z'}(t) = M_{z'}(t_0)e^{-\frac{t}{T_1}} + M_0(1 - e^{-\frac{t}{T_1}}) \quad (2.42)$$

with

$$\Phi(\vec{r}(t),t) = -\gamma \int_0^t \vec{r}(\tau)\vec{G}(\tau)d\tau + \Phi(0) \quad (2.43)$$

Equation 2.43 defines the rotation of the transversal magnetisation about the z axis with a spatially varying frequency $\omega(t) = -\gamma\vec{r}(t)\vec{G}(t)$. The gradient field causes a spatial encoding of the measured signal. In the case of static spins, where $\frac{d\vec{r}(t)}{dt} = 0$, the integral can be written as follows:

$$\Phi(\vec{r}(t),t) = \vec{k}(t)\vec{r} + \Phi(0) \quad (2.44)$$

with

$$\vec{k}(t) = -\gamma \int_0^t \vec{G}(\tau)d\tau \quad (2.45)$$

In the case of a time constant gradient field:

$$\vec{k}(t) = -\gamma\vec{G}t \quad (2.46)$$

and the phase reads:

$$\Phi(\vec{r}(t),t) = \vec{k}\vec{r} + \Phi(0) \quad (2.47)$$

- **Solution for simultaneous gradient and RF fields.** In contrast to both previous cases, no general analytical solution of the Bloch equations exists for this case. An approximation can be calculated for small flip angles. If an RF pulse is switched on for a period of time t_p simultaneously with a constant gradient pulse in the z direction, the following expression holds true for the transverse magnetisation:

$$M_{x'y'}(t) = i\gamma M_0 e^{-i\gamma G z \frac{t_p}{2}} \int_0^{t_p} B_1(\tau) e^{i\gamma G z \tau} d\tau \tag{2.48}$$

$B_1(t)$ is the envelope of the RF pulse. The integral represents the Fourier Transform (FT) of the envelope in the frequency domain. So as to achieve a rectangular slice profile, the envelope of the RF pulse needs to be the Fourier Transform of the of the boxcar function, which is the sinc function ($sinc(x) = \frac{sin\, x}{x}$).

2.4.4 T_2^* Relaxation

Although the NMR scanners are equipped with additional coils that allow to make the B_0 field in the imaging region more homogeneous (shim coils), some variation in $\vec{B}_0$ occurs across the sample. This leads to a line broadening of typically a few Hz in the NMR spectrum, which implies a decay of the FID more rapid than that caused by T_2 effects alone. The resultant time constant is labelled T_2^* and can be expressed:

$$\frac{1}{T_2^*} = \frac{1}{T_2} + \frac{\gamma}{2\pi}\Delta B \tag{2.49}$$

where ΔB is the magnetic field inhomogeneity in $\vec{B}_0$ direction. The effective relaxation time T_2^* is always smaller than the tissue specific relaxation time T_2.

While the coherence loss due to T_1 and T_2 relaxation is inherently random and irreversible, T_2^* effects caused by field imperfections are ordered and, given the appropriate measurement technique, can be undone. Therefore, one distinguishes between inhomogeneous and homogeneous broadening of the NMR spectral line.

2.5 Sodium Nuclear Magnetic Resonance

2.5.1 Sodium NMR Sensitivity

According to equation 2.18, the population difference of the $|\pm\frac{1}{2}\rangle$ at 1.5 T and room temperature for ^{1}H is $10.5 \cdot 10^{-6}$, while for ^{23}Na it is about four times smaller ($2.8 \cdot 10^{-6}$).

Table 2.2 compares the ^{23}Na signal with the ^{1}H signal in terms of their relative concentrations, natural abundance and NMR sensitivities. It can be seen that the MR sensitivity for

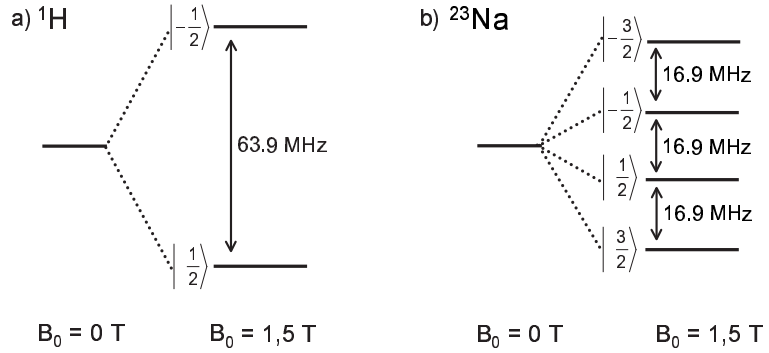

Figure 2.3: Zeeman energy levels of ^{1}H (a) and ^{23}Na (b).

^{23}Na is only 9.2% of the ^{1}H MR sensitivity and that the *in vivo* concentration is approximately 1000 times lower than the *in vivo* water proton concentration. The combination of these factors results in a ^{23}Na signal which is approximately 22000 times ($4.63 \cdot 10^{-5}$) smaller than the standard ^{1}H signal.

Nucleus	Natural Abundance (%)	Relative Sensitivity	*in vivo* concentration (mM)	*in vivo* signal
^{1}H	99.99	1.0000	100000	1
^{23}Na	100.00	0.0925	50	$4.63 \cdot 10^{-5}$

Table 2.2: *In-vivo* NMR Sensitivities of ^{1}H and ^{23}Na.

2.5.2 Quadrupolar Interaction

The proton nucleus has a spin quantum number $I = 1/2$ (section 2.2.1). In the presence of a magnetic field, two energy levels $m = -\frac{1}{2}, \frac{1}{2}$ will arise. ^{23}Na, on the other hand, has a spin $I = 3/2$, so that four Zeeman energy levels appear classified by the magnetic quantum numbers $m = -\frac{3}{2}, -\frac{1}{2}, \frac{1}{2}, \frac{3}{2}$ (figure 2.3). The energy difference is proportional to the magnetic field strength B_0 and the gyromagnetic ratio γ. Consequently, at the same field strength B_0, ΔE for sodium will be four times smaller than for protons due to the lower γ.

A consequence of the sodium nucleus having a spin quantum number $I = 3/2$ is that it exhibits, in addition to the magnetic dipole moment $\vec{\mu}$, an electric quadrupole moment Q. The electric quadrupole moment Q results from the non-spherical distribution of the electric charge in the nucleus. If a nucleus with quadrupolar moment is placed in an environment with a homogeneous electric field (for example the atomic environment in a human cell), quadrupolar interaction takes places and influences the energy spectrum depending on the orientation of the nucleus. This electrostatic energy can be described in

terms of the classical charge density ρ of a nucleus. The interaction energy W of a nucleus of charge distribution $\rho(\vec{r})$ with an electrical potential $V(\vec{r})$ is given by:

$$W = \int \rho(\vec{r}) V(\vec{r}) d^3\vec{r} \tag{2.50}$$

Using the Taylor series' expansion of the potential at the origin $\vec{r} = 0$:

$$V(\vec{r}) = V(\vec{r}=0) + \sum_{k=1}^{3} \frac{\partial V}{\partial x_k}\bigg|_{\vec{r}=0} x_k + \frac{1}{2!} \sum_{k,j=1}^{3} \frac{\partial^2 V}{\partial x_k \partial x_j}\bigg|_{\vec{r}=0} x_k x_j + \cdots \tag{2.51}$$

and inserting eq. 2.51 into eq. 2.50 yields (with $V_k = \frac{\partial V}{\partial x_k}\Big|_{\vec{r}=0}$ and $V_{kj} = \frac{\partial^2 V}{\partial x_k \partial x_j}\Big|_{\vec{r}=0}$):

$$W = V(0) \underbrace{\int \rho(\vec{r}) d^3\vec{r}}_{L=0\text{: charge } q} + \sum_{k=1}^{3} V_k \underbrace{\int x_k \rho(\vec{r}) d^3\vec{r}}_{L=1\text{: electric dipolar moment}} + \sum_{k,j=1}^{3} \frac{1}{2} V_{kj} \underbrace{\int x_k x_j \rho(\vec{r}) d^3\vec{r}}_{L=2\text{: electric quadrupolar moment}} \tag{2.52}$$

Choosing the origin of the coordinate system as the centre of mass of the nucleus, the first term is the electrostatic energy $V(0)$ of the charge q of the nucleus. The second term describes the energy of an electric dipole in a field $\vec{E} = -\vec{\nabla} V$. In quantum mechanics, the charge density of a nucleus with charge q is given by its wave function:

$$\rho(r) = q\Psi^*(r)\Psi(r) \tag{2.53}$$

Ψ has a well defined parity, $\rho(-r) = \rho(r)$, as a consequence, the dipole moment is the integral over a product of an even and an odd function, and therefore cancels, so that nuclei posses no static electrical dipole moment. A similar argument for the higher order terms leads to the result that all odd electrical ($L = 2n+1$) and all even magnetic ($L = 2n$) terms vanish.

The third term in eq. 2.52 is the quadrupolar term. The quadrupolar tensor Q_{kj} describes the deviation of the charge distribution from the spherical symmetry and is defined as follows:

$$Q_{kj} = \int (3x_k x_j - \delta_{kj} r^2) \rho(\vec{r}) d^3\vec{r} \tag{2.54}$$

therefore

$$\int x_k x_j \rho(\vec{r}) d^3\vec{r} = \frac{1}{3} Q_{kj} + \frac{1}{3} \delta_{kj} \int r^2 \rho(\vec{r}) d^3\vec{r} \tag{2.55}$$

The contribution to the energy of the quadrupolar term in equation 2.52 is:

$$E_Q = \frac{1}{6}\sum_{k,j}\left[V_{kj}Q_{kj} + V_{kj}\delta_{kj}\int r^2\rho(\vec{r})d^3\vec{r}\right] \tag{2.56}$$

This term contains components of the electric field gradient (EFG) tensor V_{kj}. As for each symmetric tensor, there is a principal axis system where the V_{kj} is diagonal. Due to the fact that the field is created from sources outside this reference system, Gauss' law for the electric field $\vec{E}$ reads $\vec{\nabla}\cdot\vec{E} = 0$, hence the potential energy V has to fulfil the Laplace equation $\nabla^2 V = \sum_k V_{kk} = \sum_{kj} V_{kj}\delta_{kj} = 0$. Therefore, the second term in equation 2.56 does not contribute and the equation reduces to:

$$E_Q = \frac{1}{6}\sum_{k,j} V_{kj}Q_{kj} \tag{2.57}$$

To obtain a quantum mechanical expression for this energy term (i.e. the corresponding Hamiltonian), the classical charge density of the nucleus ρ is replaced by the operator $\hat{\rho}(\vec{r})$:

$$\hat{\rho}(\vec{r}) = \sum_Z q_k\delta(\vec{r}-\vec{r}_k) \;\Rightarrow\; \hat{Q}_{kj} = e\sum_Z(3x_kx_j - \delta_{kj}r_k^2) \tag{2.58}$$

where the sum extends over the Z nuclear particles of charge q (e.g. the protons in the nucleus). The Hamilton operator of the quadrupolar interaction is then given by:

$$\hat{H}_Q = \frac{1}{6}\sum_{k,j} V_{kj}\hat{Q}_{kj} \tag{2.59}$$

By recalling that $\hat{I}_x$, $\hat{I}_y$ and $\hat{I}_z$ are the operators of the total angular momentum of the nucleus:

$$\hat{I}_x = \sum_k(\hat{l}_{xk} + \hat{s}_{xk}) \tag{2.60}$$

where $\hat{l}_{xk}$ and $\hat{s}_{xk}$ are the x components of the orbital and spin angular momenta of the k^{th} nucleon, and considering that:

$$[\hat{l}_{xk},\hat{y}_k] = i\hat{z}_k, [\hat{s}_{xk},\hat{y}_k] = 0, [\hat{l}_{xk},\hat{s}_{yk}] = 0, [\hat{I}_{zk},\hat{x}_k] = i\hat{y}_k \tag{2.61}$$

from equations 2.58 and 2.59 results:

$$\hat{H}_Q = \frac{eQ}{6I(2I+1)} \sum_{k,j} \left[\frac{3}{2}(\hat{I}_k\hat{I}_j + \hat{I}_j\hat{I}_k - \delta_{kj}\hat{I}^2) \right] \tag{2.62}$$

Due to the fact that this tensor is diagonal in the principal axis system, and the Laplace equation is fulfilled, two parameters suffice to characterise the system: the largest component of the electric field gradient tensor $V_{zz} = eq$, and the asymmetry parameter $\eta = \frac{V_{xx}-V_{yy}}{V_{zz}}$. Using the raising and lowering operators $\hat{I}_+ = \hat{I}_x + i\hat{I}_y$ and $\hat{I}_- = \hat{I}_x - i\hat{I}_y$, the Hamilton operator reads [Schlichter 89]:

$$\hat{H}_Q = \frac{e^2qQ}{4I(2I+1)} \left[3\hat{I}_z^2 - I(I+1) + \frac{1}{2}\eta(\hat{I}_+^2 + \hat{I}_-^2) \right] \tag{2.63}$$

The quadrupolar coupling strength depends on the nucleus-specific parameter eQ and the magnitude of the field gradient eq generated by the environment. Therefore, the quadrupolar interaction of a nucleus is a constant characteristic of any molecular environment. The coupling strength is often given in frequency units through the quadrupolar coupling constant $C_Q = \frac{e^2qQ}{h}$; for ^{23}Na it is approximately 2 MHz [Schlichter 89]. This value varies depending on the environment of the nucleus. In general, though, $C_{Q,^{23}Na}$ does not diverge more than a factor of 3 from that value, unless the nucleus is located in a cubic symmetrical environment ($V_{xx} = V_{yy} = V_{zz}$) ([Schlichter 89]). In this case there is no quadrupolar interaction because eq is zero due to the symmetry.

The Wigner-Eckart theorem ([Schlichter 89],[Werbelow 96]) shows that, independent of the electric environment, for a state with angular momentum I, the expectation values of all multipolar terms with $L > 2I$ disappear, so that nuclei with $I = 0$ or $1/2$ have no quadrupolar moment.

2.5.2.1 Quadrupolar interaction as perturbation of the Zeeman coupling

When a spin with angular momentum I is introduced into a static magnetic field, the Zeeman interaction of the magnetic moment with the external field creates $2I + 1$ energy levels $|m\rangle$ (section 2.2.1), whose energy is defined by

$$\langle m|\hat{H}_Z|m\rangle = -m\omega_0 \tag{2.64}$$

and the difference between two consecutive energy levels $(m-1, m)$, expressed in frequency units, is

$$\omega^Z_{(m-1,m)} = \langle m-1|\hat{H}_Z|m-1\rangle - \langle m|\hat{H}_Z|m\rangle = \omega_0 \tag{2.65}$$

Equation 2.65 implies that the energy levels $|m\rangle$ of a free spin in a magnetic field $\vec{B}_0$ are equally spaced. The separation between two adjacent levels is ω_0. In the spectrum, the central line $(-\frac{1}{2}, \frac{1}{2})$ is located at $\omega_0 = \gamma B_0$. The quadrupolar interaction, described by the hamiltonian $\hat{H}_Q$, can be treated as a weak perturbation of the Zeeman interaction. The Hamilton operator for ^{23}Na reads:

$$\hat{H} = \hat{H}_0 + \hat{H}_Z + \hat{H}_Q \tag{2.66}$$

with eigenvalues

$$E_m = E_0 - \gamma\hbar m B_0 + E_Q \tag{2.67}$$

When the interaction is calculated in a frame of reference that rotates relative to the main frame of reference with Larmor frequency ω_0, $\hat{H}_Q$ becomes time-dependent. Averaging $\hat{H}_Q(t)$ over one Larmor period $2\pi/\omega_0$ the quadrupolar interaction becomes time-independent. The first-order perturbation terms read:

$$\hat{H}_Q = \frac{eQ}{4I(2I-1)}\frac{\sqrt{6}}{3}\left[3\hat{I}_z^2 - I(I+1)\right]V_0 \tag{2.68}$$

with the corresponding energy eigenvalues

$$E_Q = \frac{eQ}{4I(2I-1)}\frac{\sqrt{6}}{3}\left[3m^2 - I(I+1)\right]V_0 \qquad \text{where} \tag{2.69}$$

$$V_0 = \sqrt{\frac{3}{2}}\,eq\left[\frac{1}{2}(3\cos^2\beta - 1) + \frac{1}{2}\eta\sin^2\beta\cos 2\alpha\right] \tag{2.70}$$

where the Euler angles α and β describe the direction of $\vec{B}_0$ in the principal axis system of the EFG tensor during a static experiment. Note that the energies depend on the square of the magnetic quantum number (m^2).

The energy levels are shifted by an amount E_Q (equation 2.69) and, in the spectrum, the first-order quadrupolar frequency shift of the resonance associated with the transition $(m-1, m)$ is ([Man 96]):

$$\omega^Q_{(m-1,m)} = \frac{eQ}{4I(2I-1)}\frac{\sqrt{6}}{3}(1-2m)V_0 \tag{2.71}$$

The spectrum consists of $2I$ lines, the central one of which, associated with the transition $(|\frac{1}{2}\rangle \rightarrow |-\frac{1}{2}\rangle)$, is still located at ω_0. The $2I-1$ satellite lines, whose position is determined

by the strength of the interaction, are positioned symmetrically with respect to the inner line.

Equations 2.69 and 2.70 show that the energy differences, and consequently the position of the satellite lines, depend on the orientation of the symmetry axis relative to the external magnetic field $\vec{B}_0$. Neglecting the asymmetry term, the frequency shift is modulated by the $(3\cos^2\beta - 1)$ term. At the *Magic Angle* $\beta = 55,3°$ this term vanishes and the lines collapse [Narayana 88]. In isotropic liquids, and for most tissue *in-vivo*, the orientation angle is homogeneously distributed and the quadrupolar interaction averages to zero. In this case again only one line is observed, but it corresponds to the superposition of two Lorenzian curves of different width.

For ^{23}Na, quantum-mechanical calculations show that the central line corresponding to the inner transition $(|+\frac{1}{2}\rangle \rightarrow |-\frac{1}{2}\rangle)$ represent 40% of the total signal intensity, while each of the satellite lines represents 30% of the total signal intensity.

2.5.3 Relaxation of quadrupolar nuclei

Figure 2.4 shows the rotating frame energy level diagrams for isolated $I = \frac{3}{2}$ systems. Four types of motionally narrowed single-quantum transitions are allowed (a, b, c and d). Representative ^{23}Na spectra are displayed below the corresponding energy level diagrams [Springer 96].

In the molecular environment of the spin 3/2 nucleus, the relative energies of the four nuclear spin states are modulated by electric field gradient (EFG) effects which fluctuate in time due to thermal motions. Figure 2.5 shows stylised fluctuations of the quadrupolar interaction frequency $\omega_Q\,(rad/s)$ sensed by a nucleus in different environments. Using equations 2.70 and 2.71, and assuming an axial EFG tensor ($\eta = 0$), the time-averaged quadrupolar interaction frequency $\tilde{\omega}_Q$ reads:

$$\tilde{\omega}_Q \propto e^2 Q \langle q(3\cos^2\beta - 1)\rangle \tag{2.72}$$

The fluctuations of the EFG tensor strength and/or orientation can be described with a single correlation time τ_C (Debye model). As a typical example, the Larmor period (reciprocal of the Larmor frequency) ω_0^{-1} for ^{23}Na is 2.00 ns [Rooney 96].

If the fluctuations are so rapid that the correlation time τ_C is small compared with ω_0^{-1}, which is typically of the order of nanoseconds, $\tilde{\omega}_Q = 0$ even if the fluctuations of the EFG tensor are large. The top time course in Figure 2.5 is an attempt to display this situation. This is the extreme narrowing condition $\omega_0\tau_C \ll 1$, where the three single-quantum coherences give rise to three isochronous spectral peaks which are equally narrow (with equal widths) (type d in figure 2.4). Both T_1 and T_2 decay mono-exponentially with $R_1 = R_2$. This type d spectrum can be found in aqueous NaCl solutions.

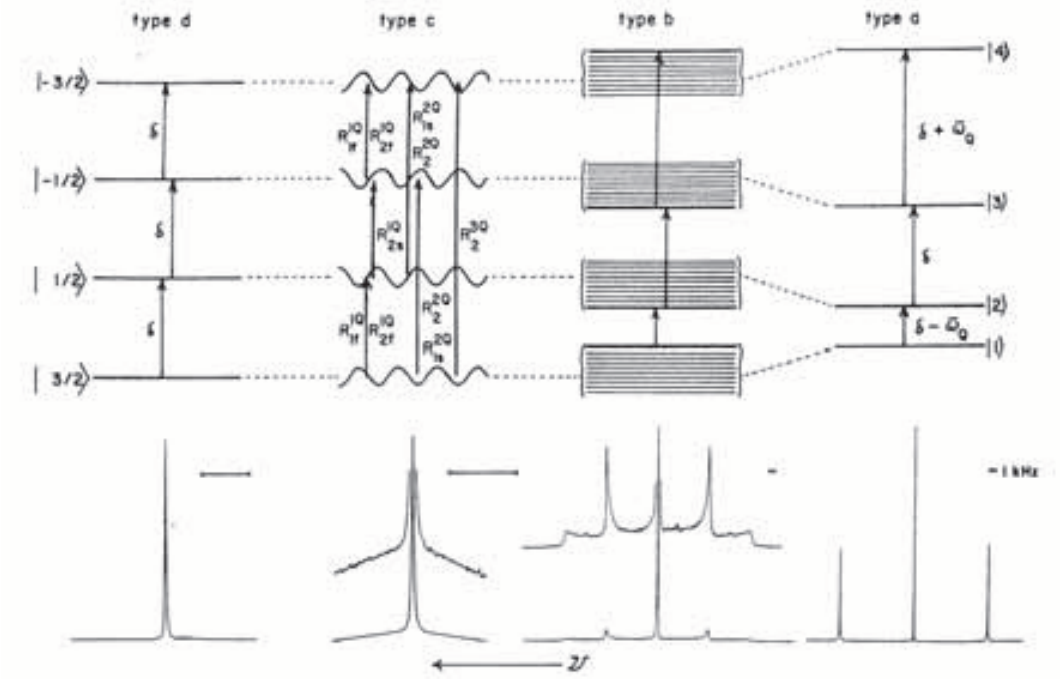

Figure 2.4: Rotating frame energy level diagrams for isolated $I = \frac{3}{2}$ systems. Four types of motionally narrowed single-quantum transitions are allowed (a, b, c and d). Representative ^{23}Na spectra are seen below each of the energy level diagrams. Courtesy of [Rooney 96].

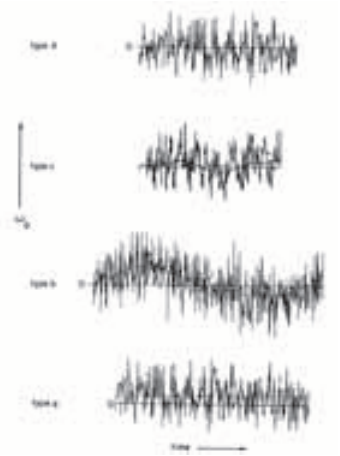

Figure 2.5: Depictions of the time dependence of the quadrupolar modulation in the laboratory frame of reference corresponding to the spectra in figure 2.4. ω_Q is modulated in time due to random thermal motions within the lattice. Four possible motionally narrowed spectral types (a, b, c and d) can result depending on the timescale and nature of the modulation. Courtesy of [Rooney 96].

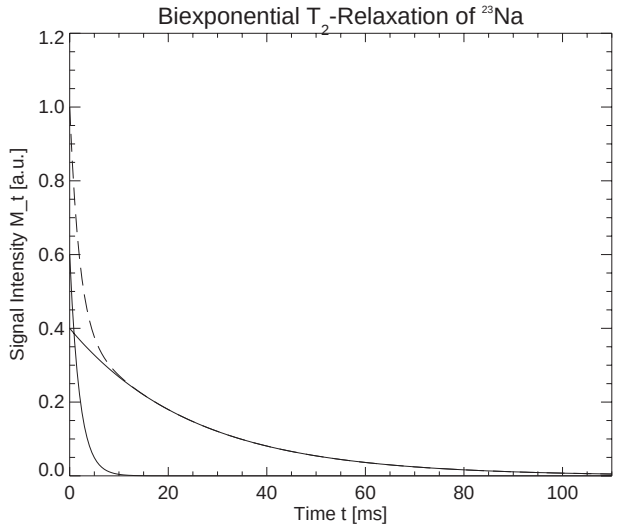

Figure 2.6: Simulation of the ^{23}Na biexponential T_2 relaxation.

Both in intra- and extracellular compartment, Na^+ cations encounter macromolecules, which produces a slower modulation of ω_Q, as shown in figure 2.5 type c. In this case $\omega_0\tau_C > 1$ but $\omega_Q\tau_C \ll 1$, so that $\tilde{\omega}_Q = 0$. The single-quantum spectrum arising in this situation comprises three isochronous homogeneous resonances . The narrow inner resonance ($|\frac{1}{2}\rangle \rightarrow |-\frac{1}{2}\rangle$) superimposing with the equally broader outer resonances ($|\frac{3}{2}\rangle \rightarrow |\frac{1}{2}\rangle$) and ($|-\frac{1}{2}\rangle \rightarrow |-\frac{3}{2}\rangle$) (type c in figure 2.4). T_1 and T_2 decay is bi-exponential. The outer transitions comprise 60% of the signal and produce the short relaxation component. The inner transition comprises 40% of the signal and produces the long relaxation component (figure 2.6).

If $\omega_0\tau_C \gg 1$ and $\omega_Q\tau_C \gg 1$, the time-averaged quadrupolar interaction frequency does not vanish $\tilde{\omega}_Q \neq 0$, and type b or type a spectra can arise depending on the macroscopic order of the sample (figure 2.4). If the sample is disordered, say a powder with random distribution of the orientations of the EFG tensor, a type b spectrum emerges. This single-quantum spectrum is the superposition of the homogeneous central resonance with two different inhomogeneous powder patterns of the satellite resonances. The simultaneous response from many nuclei experiencing a distribution of non-zero values of $\tilde{\omega}_Q \neq 0$ is detected. When the sample is anisotropic on the macroscopic scale (for example for single crystals or oriented liquid crystals), $\tilde{\omega}_Q$ can never be averaged to zero and a type a spectrum appears (figure 2.4).

2.5.3.1 Relaxation Process

The relaxation process can be described with the correlation function $K(t)$, which measures the influence in time of the interaction of a nucleus with other particles. The Bloembergen-

Purcell-Pound (BPP) theory [Vega 96] assumes that, for an average correlation time τ_C between two interactions, $K(t)$ decays exponentially as follows:

$$K(t) = K(0)e^{-\frac{|t|}{\tau_C}} \tag{2.73}$$

The Fourier transform of the correlation function is the spectral density function $J(\omega)$. It is a measure of the probability that the fluctuating field possesses the frequency ω at a certain instant in time. The spectral densities for isotropic motion read:

$$J(\omega)_n = \frac{2\tau}{1 + (n\omega_0\tau_C)^2} \tag{2.74}$$

Transverse Relaxation

For $S = 3/2$ spins in isotropic solution, where the quadrupolar interactions are averaged to zero, $\tilde{\omega}_Q = 0$, there are three degenerate single-quantum transitions. The density operator may be expressed in terms of single-quantum operators [Jaccard 86]:

$$\sigma(t) = \sum \sigma_{rs}(t)|r\rangle\langle s| \tag{2.75}$$

with the eigenstates numbered $|1\rangle = |m = \frac{3}{2}\rangle, |2\rangle = |m = \frac{1}{2}\rangle, |3\rangle = |m = -\frac{1}{2}\rangle$ and $|4\rangle = |m = -\frac{3}{2}\rangle$. The decay of the three degenerate single-quantum coherences is described by the Redfield equations:

$$\begin{pmatrix} \dot{\sigma}_{12}(t) \\ \dot{\sigma}_{23}(t) \\ \dot{\sigma}_{34}(t) \end{pmatrix} = \underbrace{C \begin{pmatrix} -(J_0 + J_1 + J_2) & 0 & J_2 \\ 0 & -(J_1 + J_2) & 0 \\ J_2 & 0 & -(J_0 + J_1 + J_2) \end{pmatrix}}_{\text{Redfield Matrix}} \begin{pmatrix} \sigma_{12}(t) \\ \sigma_{23}(t) \\ \sigma_{34}(t) \end{pmatrix} \tag{2.76}$$

where the constant C for $S = 3/2$ is:

$$C = \frac{1}{40}\left(\frac{e^2qQ}{\hbar}\right)^2\left(1 + \frac{\eta^2}{3}\right) \tag{2.77}$$

The Redfield matrix $R^{(1)}$ (relaxation among the $|p| = +1$ quantum coherences) can be diagonalised. The resulting single-quantum coherences decay exponentially ($R_i^{(1)} < 0$).

$$\sigma_i^{(1)}(t) = \sigma_i^{(1)}(0)e^{R_i^{(1)}t} \tag{2.78}$$

where the rate constants are:

$$R_1^{(1)} = -C(J_0 + J_1) \quad \Leftrightarrow \quad \sigma_1^{(1)} = \sqrt{\frac{1}{2}}(\sigma_{12} + \sigma_{34}) \tag{2.79}$$

$$R_2^{(1)} = -C(J_1 + J_2) \quad \Leftrightarrow \quad \sigma_2^{(1)} = \sigma_{23} \tag{2.80}$$

The sum of the outer components of the three degenerate single-quantum coherences of the spin $S = 3/2$ in isotropic phase decays with

$$e^{R_1^{(1)}t} = e^{-C(J_0+J_1)t} \tag{2.81}$$

while the inner component decays with

$$e^{R_1^{(1)}t} = e^{-C(J_1+J_2)t} \tag{2.82}$$

In the extreme narrowing limit ($\omega_0\tau_C \ll 1$) and in the case of isotropic motion, $J_0 = J_1 = J_2 = J = 2\tau_C$ and all components decay with the same rate constants $R_1^{(1)} = R_2^{(1)} = 4C\tau_C = \frac{1}{T_2}$.

The deviations from simple exponential behaviour tend to be more pronounced for transverse relaxation ([Bull 72], [Bull 79]).

Longitudinal Relaxation

Longitudinal relaxation processes involve exchange between the populations P_i of the four eigenstates of the $S = 3/2$ system which correspond to diagonal matrix elements σ_{ii}.

$$\sigma = \sum \sigma_{ii}|i\rangle\langle i| = \sum P_i|i\rangle\langle i| \tag{2.83}$$

The dynamics of the populations are described by the master equation or McLachlan equation ([Jaccard 86]) which for $S = 3/2$ reads:

$$\begin{pmatrix} \dot{P}_1(t) \\ \dot{P}_2(t) \\ \dot{P}_3(t) \\ \dot{P}_4(t) \end{pmatrix} = \underbrace{C \begin{pmatrix} -(J_1+J_2) & J_1 & J_2 & 0 \\ J_1 & -(J_1+J_2) & 0 & J_2 \\ J_2 & 0 & -(J_1+J_2) & J_1 \\ 0 & J_2 & J_1 & -(J_1+J_2) \end{pmatrix}}_{\mathrm{W}} \begin{pmatrix} \Delta P_1(t) \\ \Delta P_2(t) \\ \Delta P_3(t) \\ \Delta P_4(t) \end{pmatrix} \tag{2.84}$$

where $\Delta P_i = P_i - P_i^{eq}$ is the deviation of the population from thermal equilibrium values. The matrix W can be diagonalised which yields the rate constants

$$R_0^{(3)} = -2CJ_2 \quad \Leftrightarrow \quad \sigma_3^{(0)} = \frac{1}{2}(+\Delta P_1 + \Delta P_2 - \Delta P_3 - \Delta P_4) \tag{2.85}$$

$$R_0^{(4)} = -2CJ_1 \quad \Leftrightarrow \quad \sigma_4^{(0)} = \frac{1}{2}(+\Delta P_1 - \Delta P_2 + \Delta P_3 - \Delta P_4) \tag{2.86}$$

The eigenoperators can be expressed in terms of irreducible tensor operators, the resulting time evolution is:

$$\Delta\sigma(t) = -2\sqrt{5}T_{1,0}f_{11}^0(t) - 2\sqrt{5}T_{3,0}f_{31}^0(t) \tag{2.87}$$

where the transfer functions $f_{l'l}^0$ correspond to

$$f_{11}^0(t) = \frac{1}{5}(4e^{R_3^0 t} + e^{R_4^0 t}) \tag{2.88}$$

$$f_{31}^0(t) = \frac{2}{5}(-e^{R_3^0 t} + e^{R_4^0 t}) \tag{2.89}$$

The net effect of the longitudinal relaxation can be expressed with symbolic arrow notation as follows

$$T_{1,0} \longrightarrow^{R^0} T_{1,0}f_{11}^0(t) + T_{3,0}f_{31}^0(t) \tag{2.90}$$

In the fast motion limit ($\omega_Q\tau_C \ll 1$) $R_0^{(3)} = R_0^{(4)} = -2CJ = -4C\tau_C$, hence:

$$f_{11}^0(t) = e^{2CJt} = e^{-\frac{1}{T_1}} \tag{2.91}$$

$$f_{31}^0(t) = 0 \tag{2.92}$$

and monoexponential relaxation with $T_1 = T_2$ occurs.

2.5.4 Comparison of ^{1}H and ^{23}Na relaxation times

Figure 2.7 shows a simulation of the ^{1}H and ^{23}Na relaxation processes. As can be seen, both T_1 and T_2 relaxation of ^{23}Na is faster than that of ^{1}H.

Figure 2.3 shows the comparison between ^{1}H and ^{23}Na relaxation times of skeletal muscle at $B_0 = 1.5T$ and $37°C$. Because the T_1 and T_2 relaxation times of ^{23}Na are much shorter than those of ^{1}H (table 2.3) direct application of fast imaging concepts derived from experience with proton imaging would not result in optimal imaging parameters for ^{23}Na imaging.

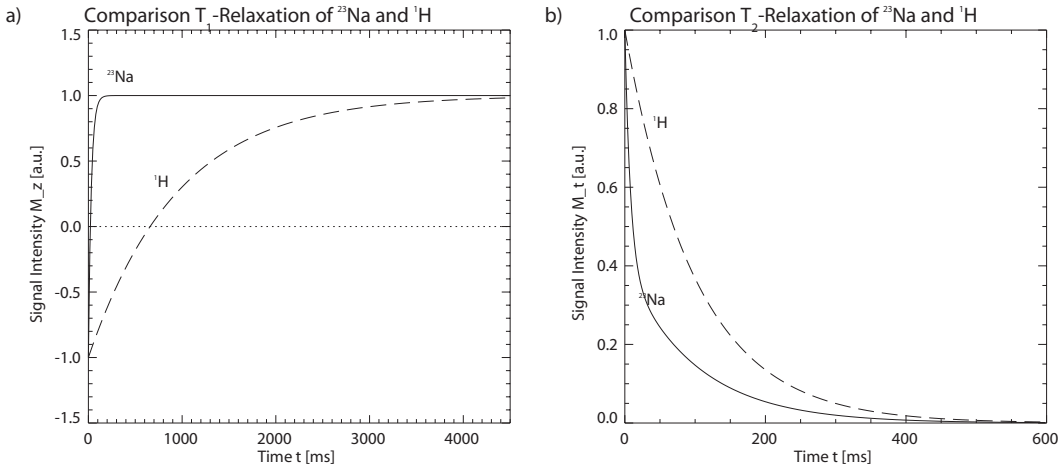

Figure 2.7: Comparison of ^{1}H and ^{23}Na relaxation. The relaxation times of ^{23}Na are very short compared to the ^{1}H relaxation times.

Nucleus	Gyromagnetic ratio γ (MHz/T)	T_1 (ms)	T_2 (ms)
^{1}H	42.5	900	50
^{23}Na	11.2	33	$0.5 - 13$

Table 2.3: Gyromagnetic ratios and relaxation times for ^{1}H and ^{23}Na of skeletal muscle at $B_0 = 1.5T$ and $37°C$. Data taken from references [Haacke 99] and [Constantinides 2000]. Two values are given for the T_2 of ^{23}Na due to its biexponential decay.

2.5.5 T_2^* Relaxation

Due to the short ^{23}Na relaxation times, gradient echo techniques are generally used for ^{23}Na MRI (section 5.1, page 57). These techniques, however, do not compensate for the spatial main magnetic field $\vec{B}_0$ inhomogeneities, which leads to a transversal decay of the magnetisation with time constant T_2^*. On the other side, the T_2 values of ^{23}Na are important parameters that need to be measured.

Nevertheless, it is possible to show that, for short relaxation times and small field inhomogeneities of few μT, T_2^* drifts very slightly from T_2. Due to the fact that ΔB is the same for ^{23}Na and ^{1}H, it is possible to guess the strength of the field inhomogeneity from the T_2^* values of ^{1}H at $1,5T$. Figure 2.8 shows the variation of ^{23}Na T_2^* for a typical range of ΔB between $0,2 - 10\mu T$. From equation 2.49

$$T_2^* = \frac{T_2}{1 + yT_2} \quad \text{with} \quad y = \frac{\gamma}{2\pi}\Delta B \tag{2.93}$$

As numerical example, an average field inhomogeneity of $\Delta B = 3,4\mu T \simeq 2ppm$ and typical

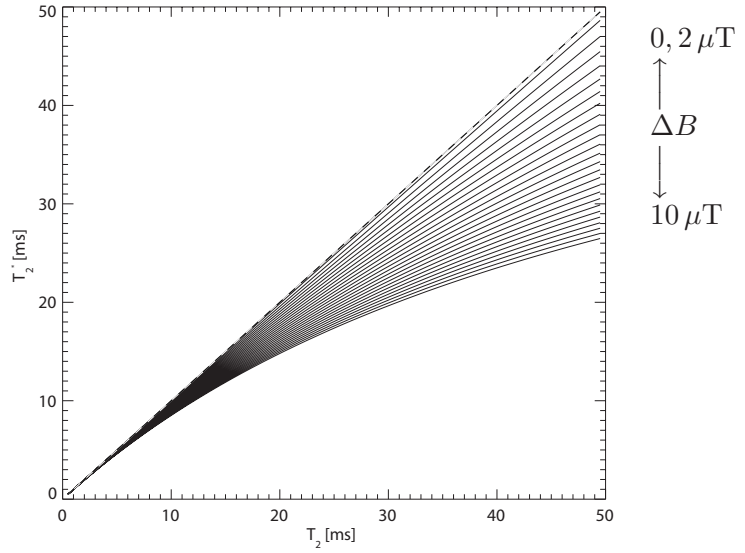

Figure 2.8: T_2^* Relaxation dependency on field inhomogeneity and T_2.

in-vivo ^{23}Na relaxation times at $1,5T$ of $T_2 = 30ms$ and $1ms$ have been assumed. In this case T_2^* amounts to $25,3ms$ and $0,99ms$ respectively. This demonstrates that the use of gradient echo techniques for the measurement of ^{23}Na T_2 values yields an acceptable accuracy ([Jerecic 2001].

Chapter 3

Magnetic Resonance Imaging

In this chapter the basics of magnetic resonance imaging (MRI) are introduced and the particularities of ^{23}Na MRI are discussed.

A field gradient is an additional magnetic field in the same direction as $\vec{B}_0 = (0, 0, B_0)$ whose amplitude varies linearly with position along a chosen axis. The application of a field gradient $\vec{G}(\vec{r})$ in a given direction $\vec{r}$ causes the magnetic field strength to vary according to:

$$B_z(\vec{r}) = B_0 + \vec{r}\vec{G}_{\vec{r}} \tag{3.1}$$

An imager has three gradient coils to generate gradients along any of the three orthogonal axes x, y or z. There are three main techniques of spatial discrimination based on the use of field gradients. These techniques are called Selective Excitation, Frequency Encoding and Phase Encoding.

3.1 Slice Selection

Selective excitation is the method by which the NMR excitation, and therefore the signal, is limited to a chosen slice within the sample or patient. It is achieved by applying the excitation pulse simultaneously with a gradient that is oriented perpendicular to the desired slice. Suppose that the desired slice lies in the xy plane, the slice selection gradient will be applied in the z direction. The gradient makes the resonance frequency a function of position along the z direction:

$$\omega(z) = \gamma B_z(z) = \gamma(B_0 + zG_z) \tag{3.2}$$

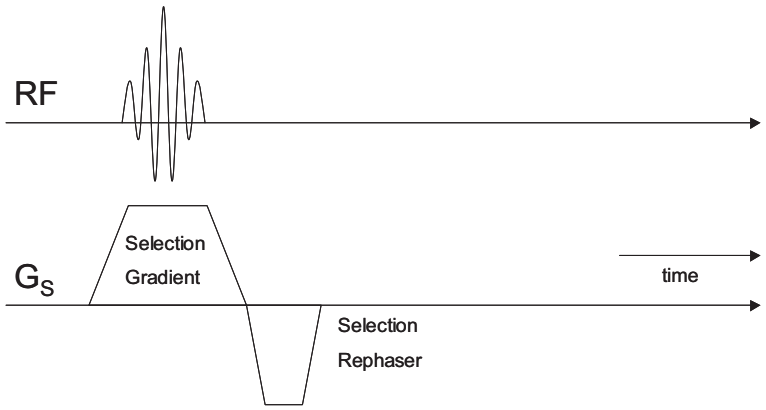

Figure 3.1: Selective excitation pulse sequence. By applying a shaped excitation pulse in the presence of a selection gradient, only a thin slice of the sample is affected by the NMR excitation. Only these spins will contribute to the signal and to the image.

When the selective excitation RF pulse is amplitude modulated so that it contains a narrow spread of frequencies $\Delta\omega$, only those spins will be excited whose resonance frequency lies within this range (Figure 3.2).

The slice width and slice profile are determined by the spectral contents of the RF pulse and, for small flip angles, are given by the Fourier Transform FT of the RF pulse envelope. The width of the slice is given by

$$\Delta z = \frac{\Delta\omega}{\gamma G_z} \tag{3.3}$$

where $\Delta\omega$ is the bandwidth BW of the RF pulse and is related to the shape and the duration of the pulse. To generate a rectangular slice profile, a sinc-pulse ($\mathrm{sinc}(x) = \frac{\sin(x)}{x}$) needs to be applied in the time domain.

$$B_1(t) = B_1 \mathrm{sinc}(\frac{\pi t}{\tau_{sinc}}) \tag{3.4}$$

$$\Delta\omega = \frac{1}{\tau_{sinc}} \tag{3.5}$$

where τ_{sinc} is the moment in time when the first zero crossing occurs.

If a Gaussian pulse shape is applied, a gaussian profile will be achieved. The BW of the gaussian pulse $\Delta\omega$ is

$$\Delta\omega = \frac{2\pi}{\Delta t} \tag{3.6}$$

where Δt is the FWHM of the pulse envelope (Figure 3.3). If no gradient is applied, a

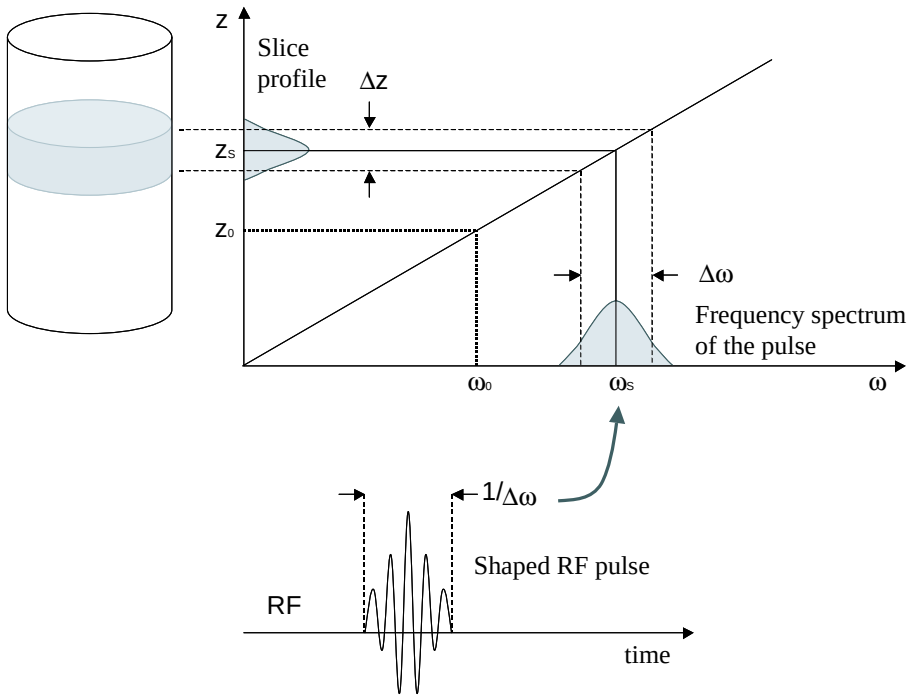

Figure 3.2: Slice selection principle. The bandwidth of the *RF* pulse ω determines the slice thickness Δz, while the central frequency ω_s determines the position position z_s.

non-selective or hard *RF* pulse (e.g. a boxcar function) is used and the whole imaging volume is excited.

The slice selection gradient is typically followed by a reversed gradient pulse (Figure 3.1). This so-called rephaser gradient brings the spin phases that are dephased under the slice selection gradient back into coherence.

By means of the slice selection, the MRI localisation problem is reduced from three to two dimensions. In 3D imaging, however, a thick slab is excited and additional encoding in slice selection direction is necessary to separate the individual signals from the different partitions that conform the excited volume.

3.2 Frequency Encoding

Frequency encoding is the technique used to encode the spatial information in one of the two in-plane axes of the excited slice. Simultaneously with the MR signal acquisition, a gradient is switched on (without loss of generality) in x direction, so that the spins precess at a frequency

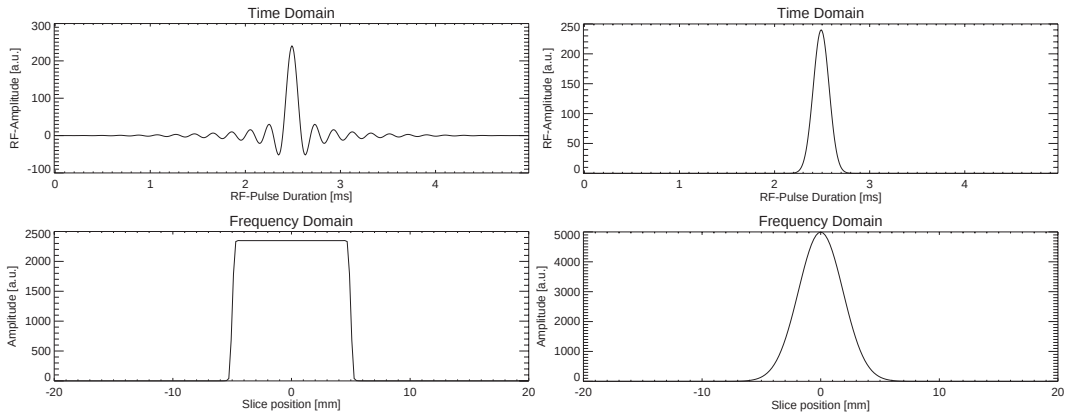

Figure 3.3: Slice Selection with a *Gauss* (a) and a *Sinc* (b) pulse, and respective slice profiles.

$$\omega(x) = \gamma B_z(x) = \gamma(B_0 + xG_x) \tag{3.7}$$

generating a position- and time-dependent phase shift of the magnetisation vector in the rotating frame of reference.

From equations 2.41, 2.46 and 2.47 the signal is

$$S(\vec{k}) = \int M_{xy}(x,y,t)dxdy = \int M_{xy}(x,y,t_0)e^{-i\gamma\vec{r}\vec{G}t+\Phi_0}dxdy \tag{3.8}$$

To simplify this equation, the initial phase Φ_0 is assumed to be zero. Considering that the magnetisation $M_{xy}(t_0)$ in the xy plane after the RF pulse excitation is proportional to the spin density ρ and using equation 2.47:

$$S(\vec{k}) \propto \int \rho(\vec{r})e^{-i\vec{k}\vec{r}}d\vec{r} \tag{3.9}$$

Equation 3.9 states that the signal and the spin density are mutually conjugates. Furthermore, the signal is given by the Fourier Transform of the magnetisation and vice versa. The one-dimensional projection of the sample is the Fourier transform of the FID as it evolves with time in the presence of a field gradient.

In order to get the gradient echo at the centre of the ADC acquisition, the frequency encoding gradient is preceded by a dephasing gradient whose momentum equals half the readout gradient momentum (figure **??**).

3.3 Phase Encoding

To encode the signal in the last remaining spatial direction (y), a constant gradient is applied perpendicular to both readout and slice selection direction before data sampling. This results in an additional phase $\Phi_y = G_y \cdot y$ in the MR signal that is constant over the readout period:

$$S(t) = \int M_{xy}(x, y, t_0) e^{-ik_y y} dx dy \tag{3.10}$$

To obtain a projection of the magnetisation on the y axis, it is necessary to repeat the experiment N times with variable gradient strength G_y.

3.4 Fourier Methods / Cartesian Methods

Spin Warp imaging is a two-dimensional Fourier transform technique (2DFT) that combines the three spatial encoding methods discussed above: selective excitation in z direction to define the imaging slice, frequency encoding in x direction and phase encoding in y direction (Figure 3.4).

The raw data are acquired in the so-called k-space, which is the Fourier transform of the image space. The vector $\vec{k} = (kx, ky, kz)$ represents a point in k-space, while in image space it corresponds to a sinewave pattern of wavelength $\lambda = 2\pi/k$, with the direction of the normal to the wavefronts being the direction of $\vec{k}$. By applying equation 2.45 to a 2D gradient echo (GRE) sequence (figure 3.4.a), a path in k-space can be traced (figure 3.4.b).

First, an RF pulse is applied in the presence of the slice selection gradient G_z to excite spins located in a slice perpendicular to z. The readout dephaser shifts $\vec{k}$ from $(0, 0, 0)$ to $(-k_{max}, 0, 0)$. Next, a constant time, variable amplitude gradient G_y performs the spatial encoding in y direction, which takes $\vec{k}$ to a new starting point $\vec{k} = (-k_{max}, k_y, 0)$, with $k_y \in [-k_{max}, +k_{max}]$. During signal reception the frequency encoding gradient G_x performs spatial encoding in x direction. $\vec{k}$ travels horizontally at a constant speed from $\vec{k} = (-k_{max}, k_y, 0)$ to $\vec{k} = (+k_{max}, k_y, 0)$. After the repetition time TR, the acquisition of a new line takes place due to the different G_y magnitude. The signal is sampled along lines parallel to the k_x axis, each line representing a digitally sampled gradient echo. The calculation of the imaging slice takes place through a two-dimensional Fourier transform along the encoding directions. This results in a matrix of $N \times M$ complex data points. Considering that $k_x = \gamma n G_x \Delta t$ and $k_y = \gamma m G_y t_p$ the discretised Fourier transform reads:

$$M_{xy}(x_l, y_l) = \frac{1}{MN} \sum_{m=0}^{M-1} \sum_{m=0}^{N-1} S(k_x^n, k_y^m) e^{-inx_l \Delta k_x} e^{-imy_k \Delta k_y} \tag{3.11}$$

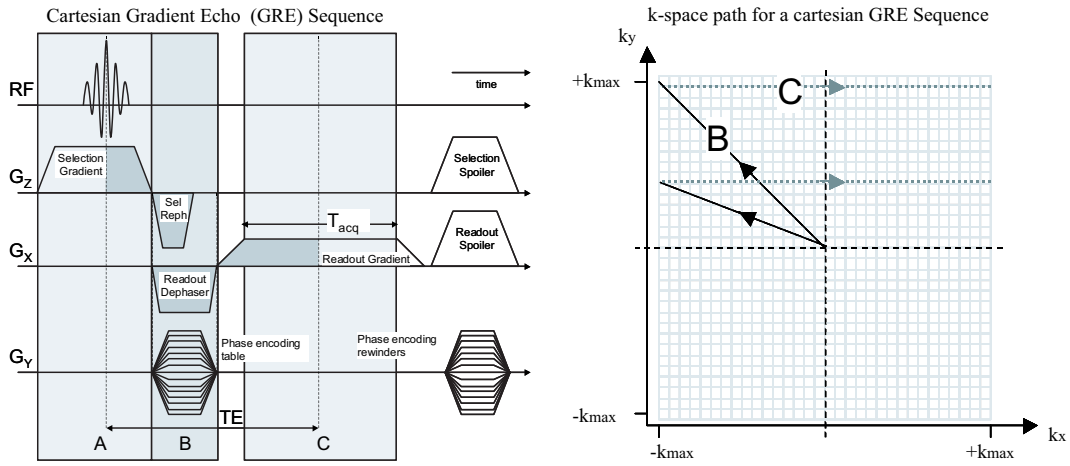

Figure 3.4: Spin Warp imaging pulse sequence. Selective excitation takes place in z direction to define the imaging slice (A), frequency encoding in x direction and phase (B) encoding in y direction. The phase encoding y gradient is pictured as a series of horizontal lines to denote that it is being stepped regularly through increasing values during different repetition times. k-space path for a Spin Warp sequence.

Note, that each point in k-space contributes to the entire image. The central data points contain information about the coarse structure of the object and contribute most to the contrast of the final image (figure 3.5). For more optimal use of the dynamic range of the gradient coils, the gradients are switched symmetrically between $-G_{max}$ and $+G_{max}$, so that these central k-space points are acquired during phase encoding steps with low amplitude (close to the zero crossing). At this point, the spins have maximum phase coherence, and hence high intensity. As can be seen from equation 3.11, $S(0,0)$ corresponds to the average signal intensity. The time between the centre of the RF excitation and the acquisition of the central k-space data points is called echo time TE. The choice of TE and TR determine the image contrast. Peripheral points in k-space will provide information of the fine detail (figure 3.5), as higher k-values yield higher spatial frequencies (i.e. resolution).

The acquisition speed of a given NMR imaging technique is determined by how quickly this spatial encoding may be performed and how fast the k-space data can be acquired. The time-consuming aspect of Fourier imaging is the large number of phase-encoded acquisitions needed to form an image. Although the processes of spatial encoding in read- and phase-encoding directions are mathematically similar, spatial frequencies in read-direction are encoded in only a few milliseconds , while the phase-direction encoding may take several seconds. For a standard gradient echo pulse sequence, the total magnetisation is excited once, one amplitude of the phase encoding gradient is applied, and a single line of k-space data is acquired. Scan time T_{acq} is given by

$$T_{acq} = N_{PE} \cdot TR \cdot N_{acq} \tag{3.12}$$

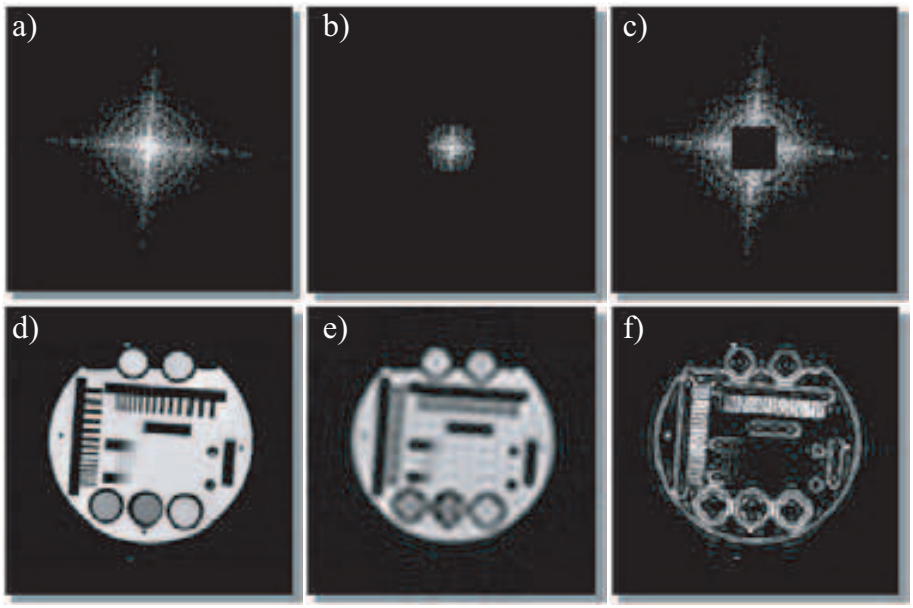

Figure 3.5: k-space and image space.(a) full k-space and corresponding image (d). The central data points contain information about the coarse structure of the object (e). The periferal points provide information about the fine detail and edges (f).

where N_{PE} is the number of phase encoding steps, TR the repetition time between successive RF excitations and N_{acq} the number of signal averages.

3.5 Image Resolution

In MRI the signal is digitised and, thus, represented in a finite space of data points. If, e.g., N time domain points are sampled at an interval Δt, the total acquisition time is $T_{acq} = N\Delta t$. When oscillatory data is digitised, there is a limit to the frequencies that can be represented, waveforms with periods less than $2\Delta t$ will appear to oscillate with a period longer than $2\Delta t$ (aliasing). The Nyquist or sampling theorem states that the maximum frequency that can be measured is $\nu_{max} = 1/2\Delta t$ [Callaghan 1991]. In the readout direction, the relationship between the frequency resolution $\Delta\nu$ and the image resolution Δx as a function of the readout gradient G_x are given by the inverse of T_{acq}:

$$\Delta\nu = \frac{1}{T_{acq}} = \frac{\gamma}{2\pi} G_x \Delta x \tag{3.13}$$

$$\Delta x = \frac{2\pi}{\gamma G_x T_{acq}} = \frac{1}{N\Delta k_x} = \frac{1}{2k_{max}} \tag{3.14}$$

where $\Delta k_x = \frac{\gamma}{2\pi} G_x \Delta t$ is the k-space step width in readout direction. The field-of-view in the read direction is $FOV = N\Delta x$, and spins between $-\frac{FOV}{2}$ and $+\frac{FOV}{2}$ are unambiguously visualised. The gradient strength in the readout gradient is

$$G_x = \frac{2\pi N}{\gamma FOV T_{acq}} \tag{3.15}$$

In phase encoding direction the gradient strength is chosen to vary between $-G_y$ and $+G_y$ so that M phase encoding steps with $\Delta G = \frac{G_y}{M/2}$ are necessary to cover the phase encoding $FOV = M\Delta y$. In the case of a square FOV (i.e. isotropic image resolution), the momentum of the maximum phase encoding step needs to be half the momentum of the readout gradient $G_y t_p = G_x T_{acq}$, where t_p is the duration of the phase encoding gradient G_y. Therefore, the maximum phase encoding gradient strength reads:

$$G_y = \frac{2\pi N}{\gamma FOV t_p 2} = M\Delta G_y \tag{3.16}$$

The k-space step width in phase encoding direction is then $\Delta k_y = \frac{\gamma}{2\pi} \Delta G_y t_p$ and the resolution Δy becomes:

$$\Delta y = \frac{1}{M\Delta k_y} = \frac{2\pi}{\gamma G_y t_p} \tag{3.17}$$

Until recently M and N where chosen to be integer power-of-two: $M = 2^m, N = 2^n$ $(m, n \in \mathbb{N})$. This enables the use of the Fast Fourier Transform algorithm (FFT) for MR image reconstruction [Cooley 1965], and consequently reduces post-processing time. However, recently new algorithms have been developed that allow for non-power-of-two FFT calculations that are as fast or even faster than the classic power-of-two FFT [Pauly 2004].

As mentioned in equation 3.3, the slice selection resolution in 2D imaging is given by $\Delta z = \frac{2\pi\Delta\nu}{\gamma G_z}$. In 3D imaging (explained in section 3.6), the partition encoding resolution is calculated in the same manner as the phase encoding resolution $\Delta z = \Delta y$.

Equations 3.15 and 3.16 state that the minimum achievable spatial resolution at a given T_{acq} depends on the gyromagnetic ratio γ and the maximum gradient strength, which is limited by the current limit in the gradient coil. For a given gradient strength, a smaller the γ allows only a reduced resolution. The minimum achievable spatial resolution for ^{23}Na is four times smaller than for ^{1}H, or, to achieve the same resolution four times stronger gradients are necessary. Due to the fact that the ^{23}Na concentration in the body is low, a reduced resolution is necessary to achieve an acceptable SNR in feasible measurement times.

3.6 3D Volume Acquisitions

In the previous section the imaging process for a single slice was presented. Volumetric 3D data sets can be acquired in two different ways: The 2D multi-slice method excites each separate slice and encodes k-space as explained above. The raw data of each slice can be acquired in succession or in alternating slices. On the other hand, the whole image volume can be excited at once. In this case, additional encoding in slice selection direction is performed through a second independent phase encoding gradient table in slice selection direction. The 3D data set is then reconstructed by a 3D Fourier transform. In MRI, the excited volume is termed slab and the reconstructed slices are called partitions.

The 3D volume excitation has advantages over the multi-slice method: Due to the repeated excitation of the whole volume, the signal-to-noise SNR of this method is higher than that of the multi-slice technique, because the SNR is proportional to the square root of the number of individual data acquisitions:

$$\frac{SNR}{voxel} = \Delta x \Delta y \Delta z \sqrt{N_{acq} \cdot N_y \cdot N_z \cdot T_{acq}} \tag{3.18}$$

there, $\Delta x \Delta y \Delta z$ is the volume of a single volume element (voxel), N_{acq} is the number of averages and T_{acq} is the readout time. Additionally, in the 2D multi-slice technique, imperfect RF pulses excite spins not only within the selected slice, but also in the neighbouring slices. If the whole sensitive volume of the RF coil is to be imaged, non-selective RF pulses of only a few microseconds duration can be used, leaving the encoding in the z-direction entirely to the slice selection gradient G_z. This also results in shorter echo times as with slice selection excitations. With 3D acquisitions isotropic resolution data sets in the three directions can be acquired, which allow the reconstruction in any of the three directions without any penalty in resolution.

A general disadvantage of 3D acquisitions is the long measurement time.

$$T_{acq} = N_y \cdot N_z \cdot TR \cdot N_{acq} \tag{3.19}$$

In some cases, due to long relaxation times T_1, it is necessary to impose internal waiting periods for the recovery of the longitudinal magnetisation, which prolongs the sequence repetition time TR and therefore the total scan time T_{acq}. In these cases, it is better to use the 2D multi-slice methods, as the time between two RF excitation in the same slice can be used to excite other slices.

3.7 MRI Contrast

The choice of measurement technique and measurement parameters (TE, TR, flip angle α, etc.) determines the influence of the relaxation times on the NMR signal. Depending on

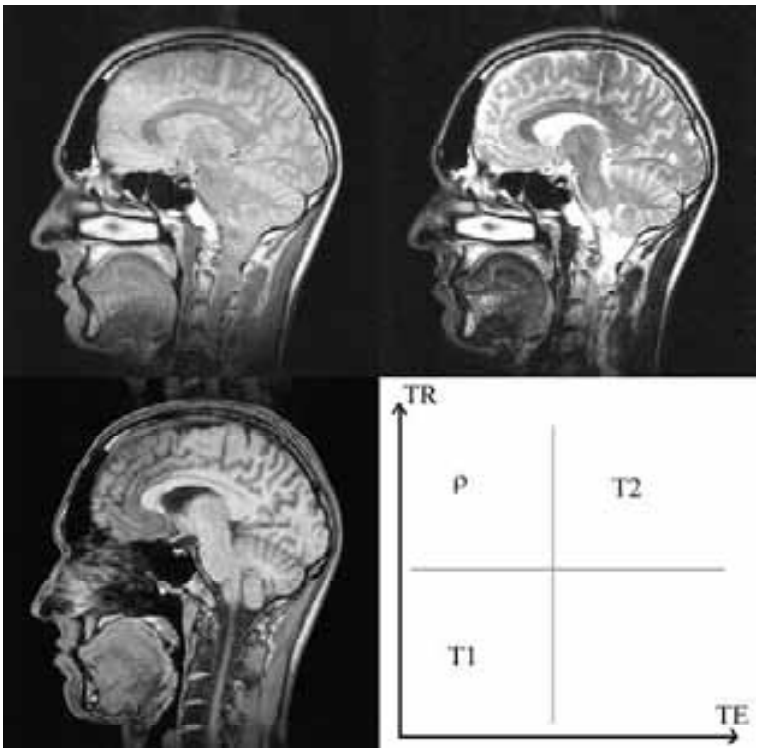

Figure 3.6: Image contrast. As can be seen in the diagram, short TE and TR will achieve T_1 weighting, long TE and long TR results in T_2 weighting and short TE and long TR results in density ρ weighting. Density (a), T_2 (b) and T_1 weighted sagittal images of a healthy volunteer. Courtesy of [Jerecic 2001].

the predominant relaxation process, the image contrast will vary and T_1-, T_2-, T_2^*- or spin density weighted images can be acquired. This is illustrated in figures 3.6.a, b and c, which show a density, T_2 and T_1 weighted image, respectively.

3.8 Sodium Magnetic Resonance Imaging

Sodium MRI differs from ^{1}H MRI in two aspects: Firstly, the ^{23}Na signal is 22000 times smaller than the ^{1}Hsignal. Secondly, ^{23}Na relaxation times are much shorter than ^{1}H relaxation times.

In this section, the optimisation of ^{23}Na measurement techniques is presented to maximise the SNR of the total sodium signal.

As shown in section 3.5, the minimum achievable spatial resolution Δx_{min} depends on the gyromagnetic ratio γ and the maximum gradient strength G_{max}. For a given G_{max}, the Δx_{min} for ^{23}Na is about four times larger than for ^{1}H. For this reason, the gradient strengths for all gradients in a ^{23}Na pulse sequence must be scaled by $\gamma_{^1\mathrm{H}}/\gamma_{^{23}\mathrm{Na}} \approx 4$ to

achieve a comparable spatial resolution as in ^{1}H MRI.

3.8.1 Short Echo Time K-Space Sampling

As was shown in section 2.5 , the ^{23}Na signal in tissue decays biexponentially. The long component of the transverse relaxation at $1.5T$ *in vivo* is about $T_{2s} = 30ms$, while the short component ranges between $T_{2f} = 0.5 - 3ms$, with a $T_1 = 50ms$. To acquire ^{23}Na signal from both long and short components, it is necessary to use pulse sequences with echo times $TE < T_{2\,short}$.

Several parameters can be optimised to minimise the echo time of standard gradient echo techniques:

- RF pulse duration and asymmetry [Haacke 99].
- Readout bandwidth BW: High BW implies short acquisition time and decreases TE. However, this limited by the gradient hardware and the $\gamma_{^{23}Na}$.
- Readout asymmetry [Haacke 99].
- 3D excitation: the slice selection rephaser is spared and the pulse duration reduced.

A detailed description of their optimisation can be found in section 5.1.2. For cartesian sequence parameter optimisation will only reduce the TE to around $2ms$. This is still too long to acquire the fast transverse relaxation component. Non-cartesian k-space sampling will therefore be necessary to achieve ultra-short TE. Its implementation will be described in section 5.2 (page 60).

3.8.2 Point Spread Function and Readout Bandwidth

During data acquisition, the NMR signal decays with T_2^*. This leads to an inhomogeneous weighting of the k-space data and to a decrease in image resolution due to the dampening of the outer k-space points (i.e. higher frequencies). In order to reduce this blurring effect, it is necessary to keep the readout time T_{read} smaller than the T_2^* decay time $T_{read} \ll T_2^*$. In other words, the readout bandwidth must be larger than the line width $1/T_2^*$ of the FID [Parrish 97]:

$$BW > \frac{1}{T_2^*} \tag{3.20}$$

Considering a $T_{2f}^* \simeq T_{2f} = 1ms$, the needed readout bandwidth should be $BW > 1000Hz$.

Part II

Materials and Methods

Chapter 4

Hardware

4.1 Transmit/Receive Switch, Preamplifiers, Plugs

To improve the SNR and avoid interferences that may corrupt the NMR signal, it is advantageous to construct the receiver chain as compact as possible. Therefore, the preamplifier and T/R switch should be as close as possible to the antenna. At the Symphony system coils are required to have their integrated preamplifier and T/R switch before being connected into the MRI scanner receiver.

To uniquely identify individual coils, the coil plug is coded by resistances connected to code pins. This coil code is recognised by the scanner when the coil is connected, and related to a coil file, which contains the characteristics of the coil (size, maximum voltage, etc.) needed by the scanner control its to performance (SAR calculation).

In order to connect different ^{23}Na coils to the Symphony system without the need for individual coil plugs that are difficult to acquire, a general chain consisting of preamplifier (figure B.7, page 168), T/R switch and plug was developed, that was terminated by a BNC connector. Therefore, a general-purpose preamplifier used in many Siemens *RF* coils and T/R Box were adapted to 16.84 MHz (Figure 4.1) and a plug was assembled, coded and attached to the rest of the system (Figure 4.1).

4.2 Coils

A large variety of different coil designs exist. According to their shapes, they can be categorised into two groups: volume coils and surface coils.

Volume coils include Helmholtz coils, saddle coils, highpass and lowpass birdcage coils and TEM coils. These coils can produce a very homogeneous B_1 field over a large volume within the coil [Hayes 1985] and they are often used both for transmission and reception.

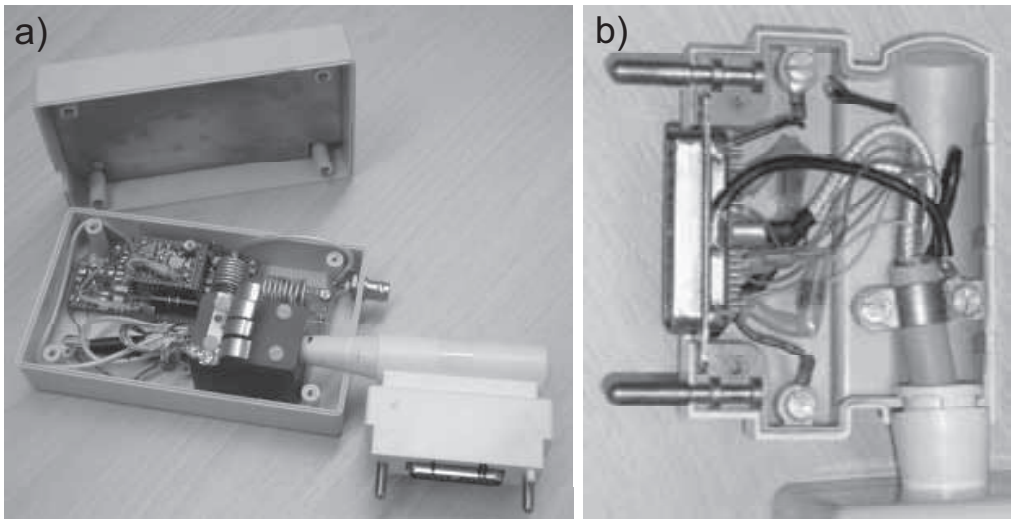

Figure 4.1: (a) T/R switch, preamplifier and coil plug (b) with coding resistances.

Surface coils include single-loop and multiple-loop coils of various shapes. These coils are usually much smaller than the volume coils and, hence, have a higher SNR because they receive noise from nearby regions only [Bedall 1988]. However, they have a relatively poor B_1 field homogeneity and, thus, are mainly used as receive coils.

Finally, so-called phased array coils exist that typically consist of arrays of surface coils. Each coil is connected to an independent preamplifier and receiver channel. The outputs from the receiver channels are combined in an optimum manner. Phased array coils provide, therefore, the large region of sensitivity typical of volume coils with the high SNR found in surface coils. Their major disadvantage is the need for additional receiver channels. To use only a single receiver channel, also *RF* time-multiplexing has been used. As clinical scanners typically only feature a single broadband receiver channel, phased array coils are not often the coil configuration of choice for non-proton MRI.

4.2.1 Volume coils

4.2.1.1 Saddle coil

The saddle coil is based on the Helmholtz pair principle, which consists of two coaxial loops located symmetrically about the origin. Using Taylor expansion of the field along the axis about $z = 0$, it is possible to show that the most homogeneous field is achieved when the radii of the coils equal the axial separation of their centres [Haacke 99]. The saddle coil consists of a pair of coils wrapped on a cylindrical surface. The loops are chosen so that their B_1 fields are mainly perpendicular to the cylinder axis and, consequently, to the axis of the magnet. The optimal field homogeneity is achieved when the opening angle

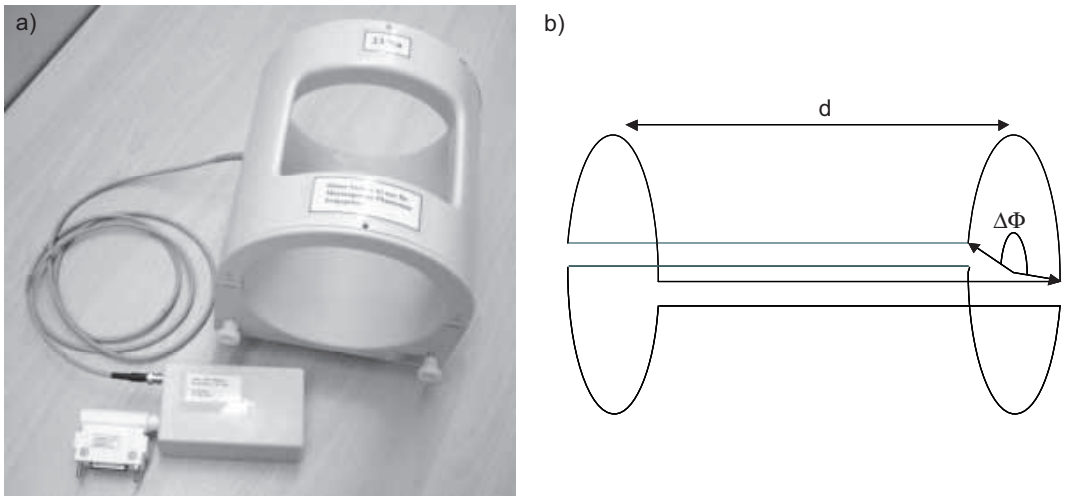

Figure 4.2: Saddle coil, T/R switch, Preamplifier and Plug (a). Diagram of a saddle coil (b).

$\Delta\phi = 2\pi/3 = 120°$ and the axial length $d = 4\rho$, where ρ is the coil's radius.

Figure 4.2 shows a 20 cm diameter and 26 cm long saddle coil made of silver plated copper foil. It was adapted to operate at 16.84 MHz by replacing the tuning and matching capacities. The corresponding tuning and matching circuit is depicted in figure B.5 (appendix B page 165).

4.2.1.2 Birdcage coil

The birdcage coil also generates an RF field perpendicular to the axis of a cylinder. It is comprised of a series of straight conductors equally spaced around the curved surface of a cylinder, which are joined by two end rings. Each segment comprising a straight conductor, capacitor and the arcs at its ends behaves like a lumped transmission line section. When the coil is correctly tuned the currents flowing along adjacent straight conductors produce an approximation to a sinusoidal current distribution around the surface of the cylinder, given by

$$I(t) = I_0 \sin(\omega t + \phi) \tag{4.1}$$

This generates a highly uniform transverse RF field. The flux lines are parallel over a greater volume than for the saddle coil, which implies more homogeneous B_1 over the sample volume. The B_1 homogeneity of the birdcage increases with the number of legs. The more legs, the better the B_1 homogeneity inside the sample volume. On the other hand, the quality factor Q can decrease if the number of legs is too high, because additional capacitors are required [Haase 2000]. A theoretical consideration for an infinitely

long birdcage shows that in this coil a continuous current distribution creates a perfectly uniform field. In a finite birdcage the uniformity decays axially. However, if the coil's length is approximately equal to its diameter, then an approximately spherical volume of the coil shows an excellent homogeneity.

Depending on the placement of the capacitors, there are two types of birdcage coils: high-pass and low-pass. The high-pass coil configuration consists of conductors whose ends are connected by several capacitors. In the low-pass configuration the capacitors are placed in the legs. The equivalent circuits of these two configurations are depicted in figures B.3 and B.2. The high-pass birdcage coil has advantages over the low pass design, in that there are no capacitors in the legs which produce electrical stray fields in the sample volume. Moreover, no eddy currents induced by switched gradient fields are possible in the end-rings, since low frequency eddy currents cannot pass through the capacitors. On the other hand, the low-pass birdcage is appropriate for the design of coils to be used at low frequencies because its frequency of the homogeneous mode is lower than all of the non-usable higher order modes, and lower than the homogeneous mode of a high-pass birdcage constructed with the same geometry and capacitance [Haase 2000]. The bandpass birdcage forming a hybrid between the two.

For phantom experiments, a linearly-polarised low-pass birdcage coil was developed, consisting of sixteen 2 cm-thick and 25 cm-long copper foil stripes glued onto a Perspex cylinder of 25 cm diameter (Figure 4.3). In the middle of each stripe a capacitors of 100 and $56pF$ were connected. The L-section tuning and matching network consists of two constant and two variable capacitors, as plotted in the circuit diagram (Figure B.4). On one side a variable end ring allows for a better adjustment of the frequency. Although in general an RF shield decreases the B_1 homogeneity [Jin 98]. A cylindrical copper foil RF shielding was placed around the coil to prevent interferences to affect the signal detection. The use of an end cup can eventually improve the homogeneity of the B_1 field [Hayes 1986], because the conducting sheet acts as a mirror for the coil and effectively doubles its electrical length. As a result, the homogeneity of the field produced inside the coil, particularly near the end capped with the mirror, can be improved. Such an end cap was developed and tested. In this particular case, no significant improvement was observed and so the end cup was rejected.

For volunteer and patient experiments a conventional, double-resonant quadrature high-pass birdcage coil (Rapid Biomed GmbH, Würzburg, Germany) was used (Figure 4.4), which resonates at both 63.64 MHz (^{1}H) and $\nu = 16.83$ MHz (^{23}Na).

4.2.2 Surface coil

Surface coils are used to improve the SNR when imaging superficial organs. The image intensity is highest near the coil windings and decreases with depth in the sample. The non-uniform B_1 field distribution results in an approximately hemispherical region of sensitivity which extends to a depth of about the radius a of the coil. When sample losses are

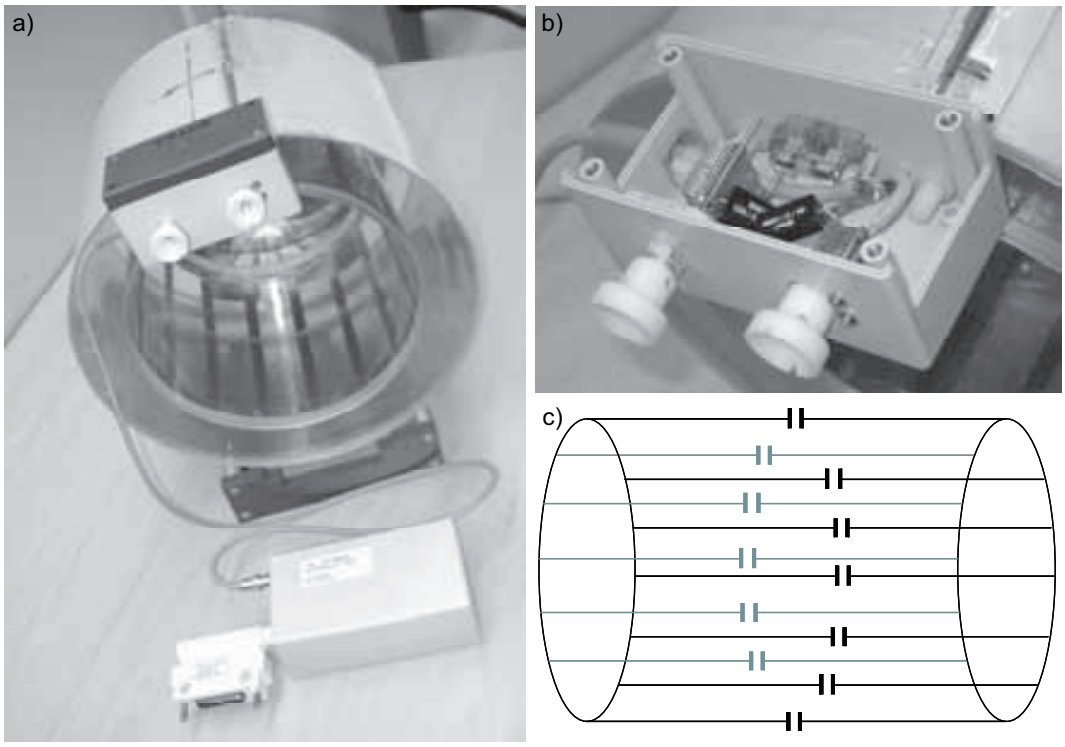

Figure 4.3: Low-pass birdcage coil (a), Preamplifier and Plug (a) and TR Box (b). Schematic diagram of a low-pass birdcage coil (c).

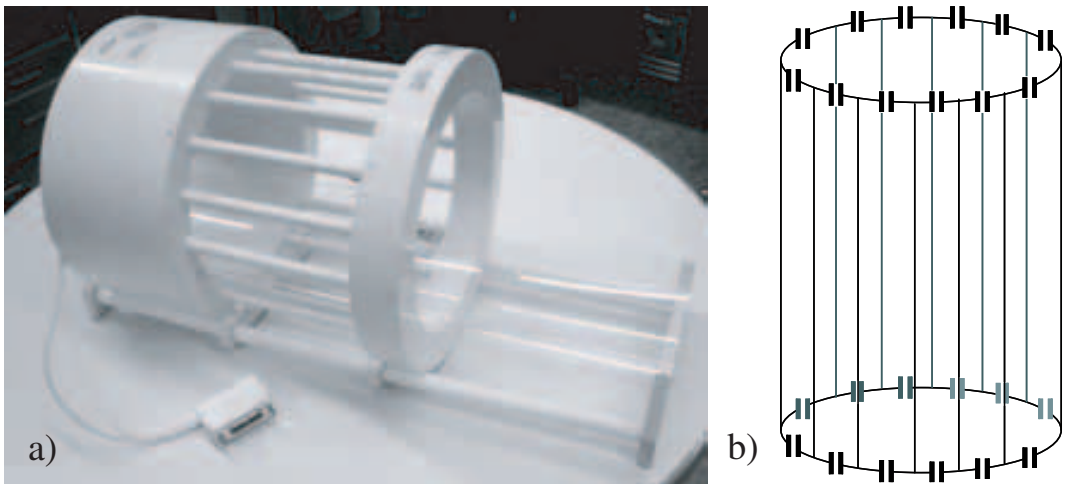

Figure 4.4: RAPID Birdcage coil. Schematic diagram of a high-pass birdcage coil (c).

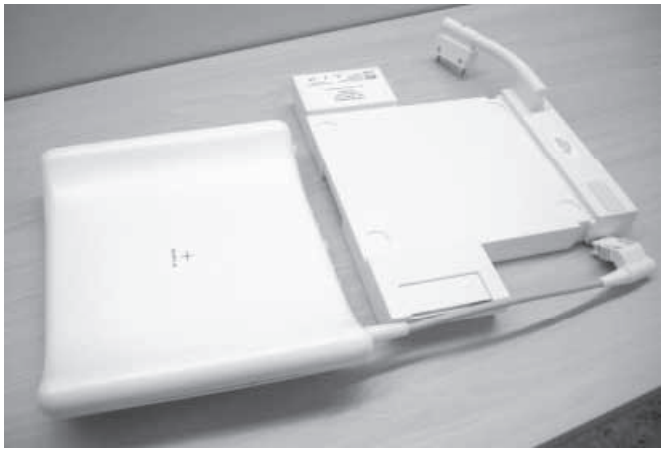

Figure 4.5: Surface coil, TR Box, preamplifier and plug.

negligible, the sensitivity scales with a^{-1}. A surface coil will experience noise from a conducting sample than the whole body coil, since the equivalent sample resistance, R_{Samp}, depends on the surface coil's radius, a, rather than the sample dimension [Harpen 87]:

$$R_{Samp} = 0.332\,\sigma\,\omega_0^2\mu_0^2 a^3 \tag{4.2}$$

where $\mu_0 = 4\pi \cdot 10^{-7}\,Hm^{-1}$ is the permeability of free space. As the surface coil has a higher B_1 field and less associated sample noise than a volume coil, images of superficial regions will have a better SNR.

For ^{23}Na MRI of the human heart experiments a quadrature surface coil tuned to 16.84 MHz (RAPID Biomed GmbH) was used (Figure 4.5).

4.2.3 Flip Angle Calibration

As shown in equation 2.27, the flip angle of an MR experiment depends not only on the duration of the RF pulse t_p, but also on the strength of the magnetic field B_1. This B_1 field strength in turn depends on the type of coil and the coil loading. When the equilibrium magnetisation M_0 is excited by an RF pulse, the resulting transversal magnetisation $M_\perp$ is proportional to the sine of the flip angle α:

$$M_\perp = M_0 \sin\alpha = M_0 \sin(\gamma B_1 t_p) \tag{4.3}$$

Due to the fact that the B_1 field depends on both the coil properties and the sample, a flip angle calibration is necessary before a measurement starts. In clinical MRI scanners the calibration process is automated for ^{1}H MRI. Thus, a reference voltage V_{ref} is determined,

which describes the voltage necessary to tip the magnetisation by 180° for a 1 ms long rectangular pulse. Later on, V_{ref} is used to calculate the necessary voltages for all other pulses of different length and/or pulse modulation. For non-proton coils, however, it is necessary to develop a method of estimating V_{ref}.

In order to calibrate the coils, phantoms were used that imitate the in-vivo load. For the volume coils, a 5 l cylindrical phantom with 50 mM saline solution was used. For the surface coil, a thorax phantom (1000g H_2O, 1.25g $NiSO_4 \times 6\,H_2O$, 5gNaCl) was used.

Gradient echo images ($TR = 200$ ms, $TE = 2.48$ ms, $FOV = 500$ mm, $matrixsize = 64 \times 64$ $N_{acq} = 10$, $BW = 200$Hz/Pixel) were acquired with varying voltage. Regions of interest (ROI) were defined and curves of the signal intensity as a function of transmitter voltage were plotted (figure 7.1). A curve fit to equation 4.3 then yielded the reference voltage V_{90}.

4.2.4 B_1 Homogeneity

To evaluate the field distribution of the coils, images of a homogeneous phantom were acquired in orthogonal scan planes. For the volume coils, a 5 l cylindrical phantom with a 50 mM saline solution was used, whereas for the surface coil, the thorax phantom was used.

A gradient echo sequence ($TR = 200$ ms, $TE = 2.48ms$, $FOV = 500$ mm, matrix size = 64×64, $N_{acq} = 10$, $BW = 200$ Hz/Pixel) was applied in the three orthogonal directions. Field inhomogeneity was assessed in the ^{23}Na images by plotting the intensity contours.

4.2.5 Quality Factor and Signal-to-Noise Ratio

In order to measure the Q value of a coil, the resonator was driven from the transmission port of the network analyser through its own matching network. The probe was matched to 50 Ω. An additional self-developed pick-up loop which coupled weakly to the resonator was connected to the other port of the network analyser. Care was taken that the presence of the pick-up loop did not dampen the resonator. Q was measured in transmission mode. In such a measurement, Q is defined as twice the centre frequency divided by the $-3\,dB$ bandwidth.

$$Q = \frac{2\nu_0}{\Delta\nu} \tag{4.4}$$

The reference level for this measurement is the maximum of the resonance curve observed. Figure 4.6 shows the tuning curve measured in reflexion attenuation mode in yellow, and the transmission curve in blue, both for the birdcage and the saddle coil.

The pick-up loop was designed as in [Watkins and Fukushima 1987]. It was constructed with semi-rigid coaxial cable. A gap was introduced in the outer shield to let the inner

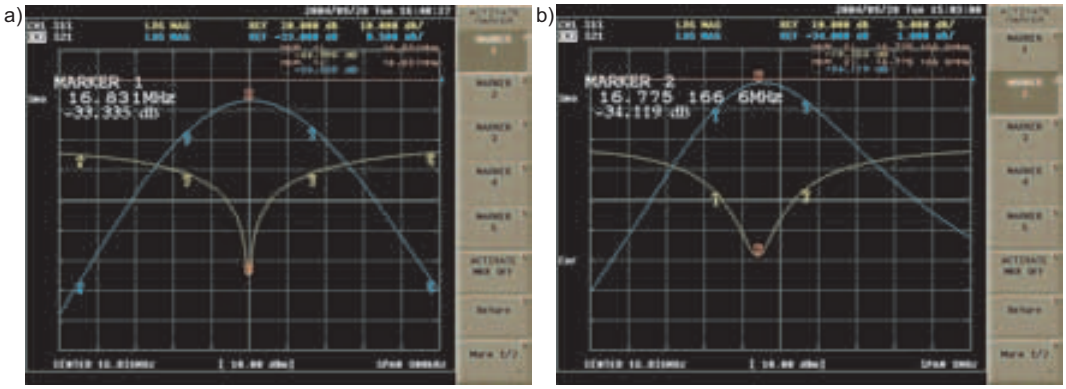

Figure 4.6: Network Analyser: tuning curve measured in reflexion attenuation mode in yellow, and the transmission curve in blue, both for the birdcage (a) and the saddle coil (b).

Figure 4.7: Schematic diagram of the pick-up loop. A gap introduced in the outer shield lets the inner conductor at this gap see the magnetic part of the *RF* field only and suppresses any interference with the electric field. A balun consisting of a cable wound around a small ferrite core removes any residual imbalance.

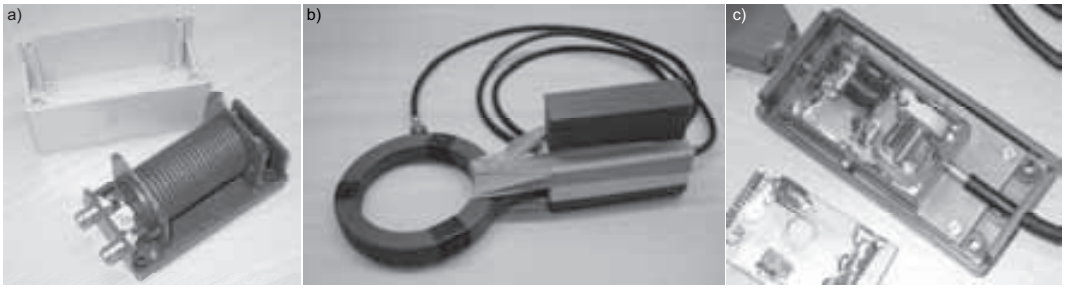

Figure 4.8: Developed hardware for RF interference detection and attenuation: (a) RF choke, (b) search loop and its tuning and matching box (c).

conductor at this gap see the magnetic part of the *RF* field only and to suppress any interference with the electric field. A balun was used to remove any residual imbalance, consisting of a cable wound around a small ferrite core (figure 4.7).

4.3 Spike Search and Elimination

In an MRI scanner, *RF* noise (spikes) can be produced through partial discharges in the gradient coils, discharges in other MR equipment or due to high frequency interferences. These interferences can originate from parts of the MR scanner that work at or close to the resonance frequency, or from external sources due to faulty or insufficient isolation of the scanner room. Spike signals can be picked up by the *RF* coil itself and get mixed with the signal received from the sample. They can also be picked up by some other part of the receiver chain, such as the coaxial cables that carry the signal from the coil to the preamplifiers.

Clinical scanners are generally optimised for the ^{1}H MRI applications. Non-proton NMR applications are still considered research, which might imply that MRI scanners will not be free of interference at other frequencies than the proton resonance (e.g. 64 MHz at 1.5 T).

In order to identify possible sources for the interferences a 15 cm diameter search loop was implemented consisting of 8 turns of thin coaxial cable. In the middle of the central turn a gap was introduced in the shielding to let the inner conductor receive the magnetic component of the *RF* signal only. The loop is connected to a tuning and matching system shielded from interference in a metal box (Fig 4.8). The L-section tuning and matching circuit consists of a series inductance L_1 and two capacitors in parallel, a constant C_1 and a variable C_2 (Circuit diagram in figure B.6).

The search coil was connected to a spectrum analyser standing outside the scanner room via a a long coaxial cable and through the scanner filter plate. The spectrum analyser could not be operated inside the scanner room because it was emitting *RF* noise close

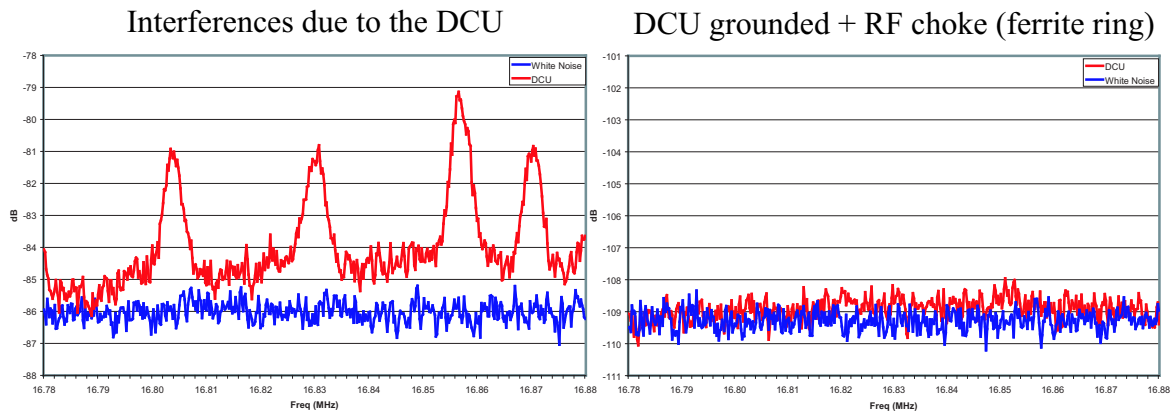

Figure 4.9: (a) Plots of the *RF* interference produced by the DCU. (b) Interference free spectrum after proper grounding of the DCU.

to the frequency of interest. By positioning the search loop at different points inside the scanner room and sweeping over the frequency range of interest it was possible to scan the room for interfering signals at the ^{23}Na frequency. Many sources of interference were found in this way.

The first noise source identified was the smoke detector wiring, which had been installed directly inside the room without going through the filter plate and without proper grounding. As a consequence, it was working as an antenna, even being able to receive signal from radio transmitters. Another interference arose from the so-called Digital Control Unit (DCU), which is the built-in computer controlling the movement of the patient couch, positioning, coil identification, etc. The DCU was not properly grounded and was emitting a $25KHz$ periodic signal with a peak at 16.83 MHz (Figure 4.9). Both of these problems could be solved by proper grounding of these elements. Finally, a strong interference was detected in the *RF* cable and liquifier cables. These cables could neither be isolated nor grounded, and their interferences became a limiting factor for the quality of the ^{23}Na NMR signals. At this point the decision was taken to continue the ^{23}Na measurements at the MAGNETOM Symphony, which has already been fabricated to be free of interference in a broader frequency range.

Chapter 5

Measurement Techniques

5.1 Optimisation of Cartesian Gradient Echo Sequences

Due to the fast T_2 decay of the ^{23}Na signal, the most appropriate technique for ^{23}Na MRI is the gradient echo sequence. As explained in section 3.4, a gradient echo is created after the RF excitation and a line in k-space is sampled. Due to the short T_1 of ^{23}Na, it is possible to use gradient echo pulse sequences with short repetition times TR. 3D techniques are preferred over 2D methods because the use sequences of shorter non-selective RF pulses allows for shorter echo times TE. Moreover, 3D methods have an intrinsically better SNR. However, the longer scan time of 3D sequences makes them inappropriate for applications such as time-resolved heart imaging. For this reason, both 2D and 3D gradient echo sequences were implemented and optimised for ^{23}Na MRI.

5.1.1 FLASH Principle

The FLASH (Fast Low Angle Shot) pulse sequence utilises a a cartesian k-space sampling in combination with a short TR and flip angles $\alpha < 50°$ [Haase 86]. Due to these low flip angles, only a fraction of the equilibrium magnetisation is rotated into the transverse plane. The remaining z magnetisation is available for the next pulse. The steady state signal of the FLASH sequence is given by:

$$S = S_0 \frac{\left(1 - e^{-\frac{TR}{T_1}}\right) e^{-\frac{TE}{T_2^*}} \sin\alpha}{1 - \cos\alpha \cdot e^{-\frac{TR}{T_1}}} \tag{5.1}$$

The maximum signal S_0 for a given TR, TE and T_1 is obtained at the Ernst Angle([Ernst66])

$$\alpha_E = \arccos(e^{-\frac{TR}{T_1}}) \tag{5.2}$$

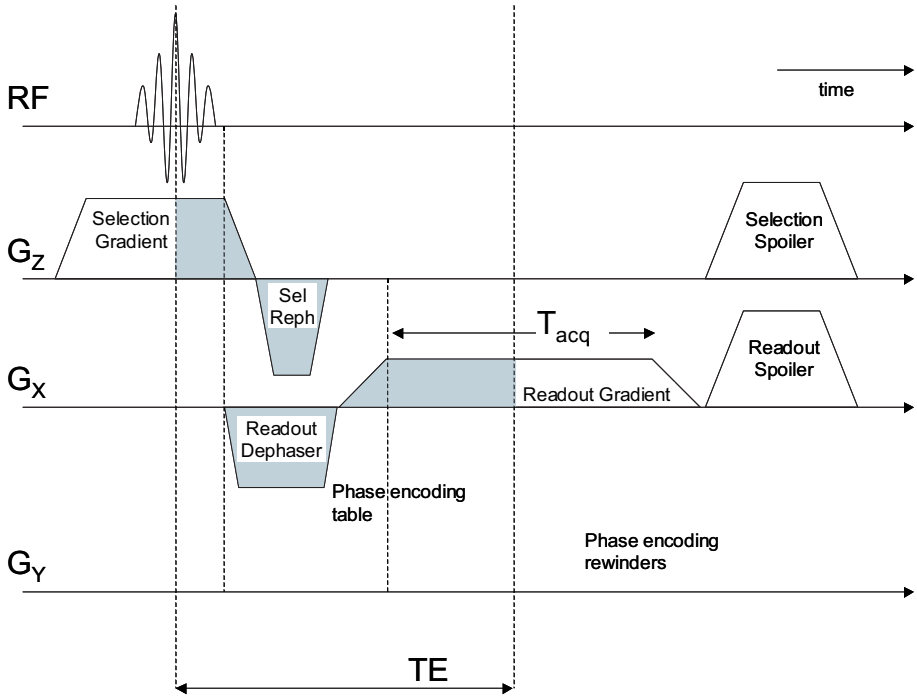

Figure 5.1: FLASH (Fast Low Angle Shot) pulse sequence optimised for short TE. It utilises cartesian k-space sampling in combination with a short TR and flip angles $\alpha < 50°$.

A key assumption in FLASH imaging is that the transverse magnetisation has completely decayed by the end of the TR interval, so that only z-magnetisation is present when the following RF pulse is applied. In case $T_2 \geq TR$, this assumption is not valid and remnant transverse magnetisation can cause severe imaging artefacts. One approach to prevent this problem is to spoil the remnant magnetisation by destroying phase coherence between successive TR intervals. Spoiling can be achieved either by inserting randomly varying gradient pulses after data acquisition (gradient spoiling) or by randomly jittering the phase of the RF pulses (RF spoiling). In RF spoiling, the phase of the receiver must be changed to follow the phase shift applied to the transmitter.

5.1.2 Optimisation of the echo time TE

The typical two-dimensional cartesian k-space sampling encodes the k_x and k_y directions as depicted in figure 5.2.a. The phase encoding gradient G_y varies in amplitude at each subsequent RF pulse so that the starting point in k_y direction varies from k_y^{max} to $-k_y^{max}$. During the data acquisition, the readout gradient G_x is switched on, so that a line is sampled from $-k_x^{max}$ to k_x^{max} (figure 5.1). The echo time TE is the interval between the beginning of the acquisition and the acquisition of $k_x = 0$. It is therefore limited by the duration of the RF pulse, the slice selection ramp-down time, the slice selection rewinder,

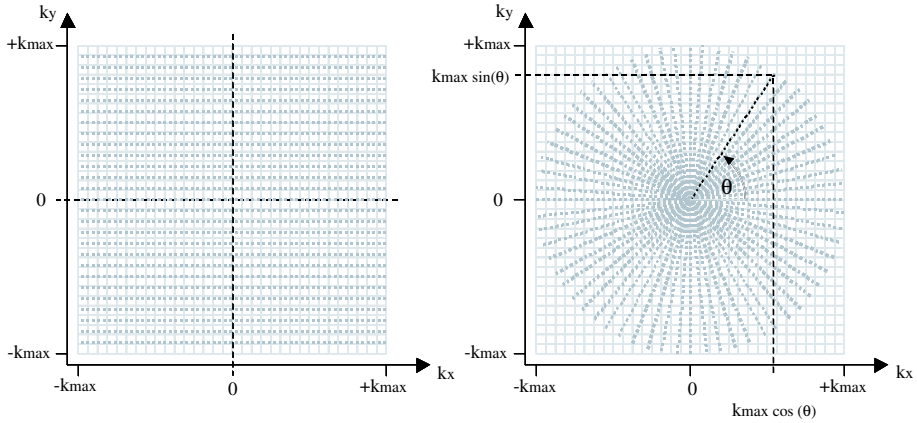

Figure 5.2: K-Space scanning of a cartesian (a) and a a radial (b) sequence.

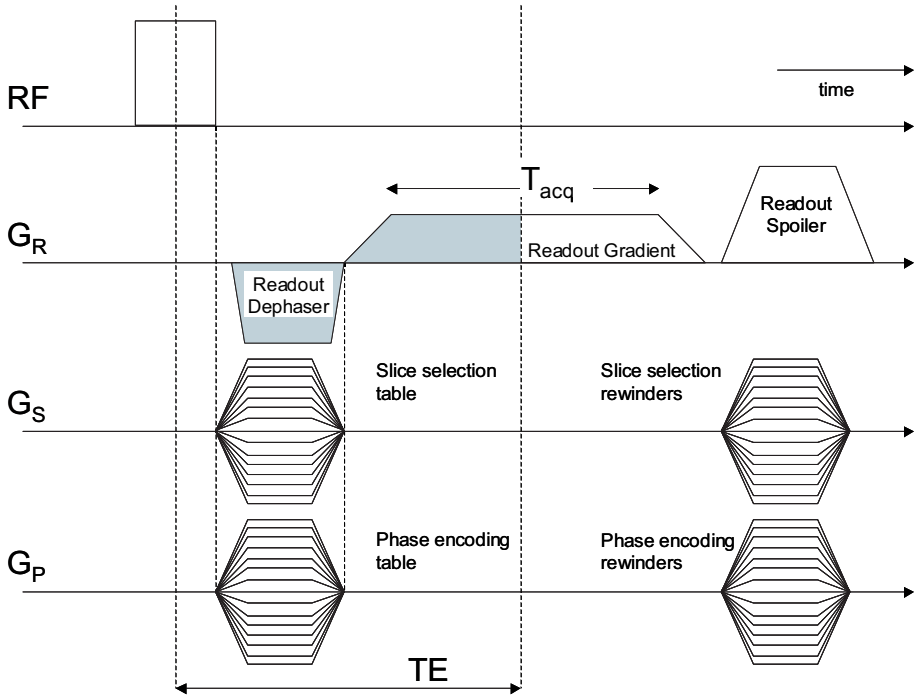

Figure 5.3: 3D FLASH Sequence. After a non-selective *RF* pulse, additional encoding in slice selection direction is performed through a second independent phase encoding gradient table in slice selection direction.

the phase encoding gradient and the readout dephaser. In three-dimensional cartesian sampling there is no slice selection gradient, but slice and phase encoding tables, as well as readout dephaser (figure 5.3).

The following parameters can be modified to shorten the echo time for ^{23}Na FLASH MRI:

- RF **pulse duration**: Shortening the RF pulse for a 2D method deteriorates the slice profile and is consequently limited. In a 3D method, non-selective RF pulses are used, which last no more than half a millisecond.
- The **duration of the Phase encoding and slice rephaser gradients** can be minimised by using the maximum available slew-rates, which are limited by the scanner's hardware to $30T/m/s$ to avoid peripheral nerve stimulation. If the image resolution is reduced, lower gradient strengths are needed to achieve space encoding. For ^{23}Na MRI, a minimum resolution of $6\,mm$ in-plane, for a slice thickness between $10 - 20mm$, is necessary to produce diagnostically useful information. The low resolution is additionally advantageous because it implies an improvement in SNR.
- As defined before, the echo time TE is the time between the centre of the RF pulse and the acquisition of $k_x = 0$. To reduce TE, it is possible to implement an **asymmetric readout**. If the integral of the readout dephasing gradient is reduced, the echo is not refocussed at the centre of the acquisition window, but before. In k-space this corresponds to an omission of data before the echo. Asymmetric data readout thus results in a truncation of k-space signal resulting in ringing artefacts (Gibbs ringing).
- The **readout time** $T_{acq} = BW^{-1}$ is an important parameter in the optimisation of techniques for ^{23}Na MRI, since a shorter T_{acq} implies shorter TE. Shortening T_{acq} also decreases SNR (eq. 3.18), which can be overcome by reducing TR and increasing the number of averages. The reduction of T_{acq} also minimises the blurring due to T_2 decay during readout, which is the case for ^{23}Na MRI. At fixed spatial resolution, the minimum T_{acq} is limited by the scanner's hardware and the maximum readout gradient strength.

5.2 Development of Radial Sequences

In cartesian k-space sampling the k-space is covered line after line in successive phase encoding steps. Rather than varying the phase encoding gradient, both gradients G_x and G_y can be turned on at the same time (see figure 5.4). The net gradient vector thus points along an arbitrary angle θ with respect to the x-axis (figure 5.2). The overall gradient strength G and angle θ are given by

$$G = \sqrt{G_x^2 + G_y^2} \quad \text{and} \quad \theta = \arctan\left(\frac{G_y}{G_x}\right) \tag{5.3}$$

such that

$$G_x = G\cos\theta \quad \text{and} \quad G_y = G\sin\theta \tag{5.4}$$

The k-space trajectory is defined by $\vec{k} = \gamma\vec{G}t$ where $\vec{G} = (G_x, G_y)$ and $\vec{k} = (k_x, k_y)$. Consequently

$$k = \sqrt{k_x^2 + k_y^2} \quad \text{and} \quad \theta = \arctan\left(\frac{k_y}{k_x}\right) \tag{5.5}$$

such that

$$k_x = k\cos\theta \quad \text{and} \quad k_y = k\sin\theta \tag{5.6}$$

Considering the polar coordinates $x = r\cos\phi$ and $y = r\sin\phi$, the signal becomes

$$s(k,\theta) = \int\int r dr d\phi \rho(r,\phi) e^{-i2\pi kr\cos(\phi-\theta)} \tag{5.7}$$

This so-called 2D radial k-space trajectory is depicted in figure 5.2.b and corresponds to the sequence in figure 5.4. The scanning of each radius begins at the centre of k-space $\vec{k}_0 = (0,0)$. In radial MRI, TE is only limited by the slice selection gradient timing and very short TE can be realised. The 3D radial sequence allows for an even shorter TE because it makes use of a non-selective RF excitation. There, the minimum TE is only limited by the duration of the RF pulse and the time needed to switch between the RF excitation and the data acquisition (T/R switch). This hardware dependent time is of the order of tenths of microseconds ($40\mu s$ for the MAGNETOM Symphony).

5.2.1 2D Radial Sequence

A 2D radial sequence was implemented as shown in figure 5.4. The sequence had the same number of projections as samples per projection. Given the number of projections N, the angular width steps $\Delta\theta_i$ was calculated as

$$\Delta\theta_i = \frac{2\pi}{N} \quad \text{with} \quad \theta_i = \frac{i}{N}2\pi \tag{5.8}$$

The RF pulse duration varied between 512 and $1024\mu s$. A readout bandwidth BW between $100 - 1000Hz$ could be chosen. Sampling could take place during readout gradient flat top time (in which case a readout gradient dephaser was needed to compensate for the readout gradient ramp-up time), or could start already during readout gradient ramp-up time to minimise TE (figure 5.4).

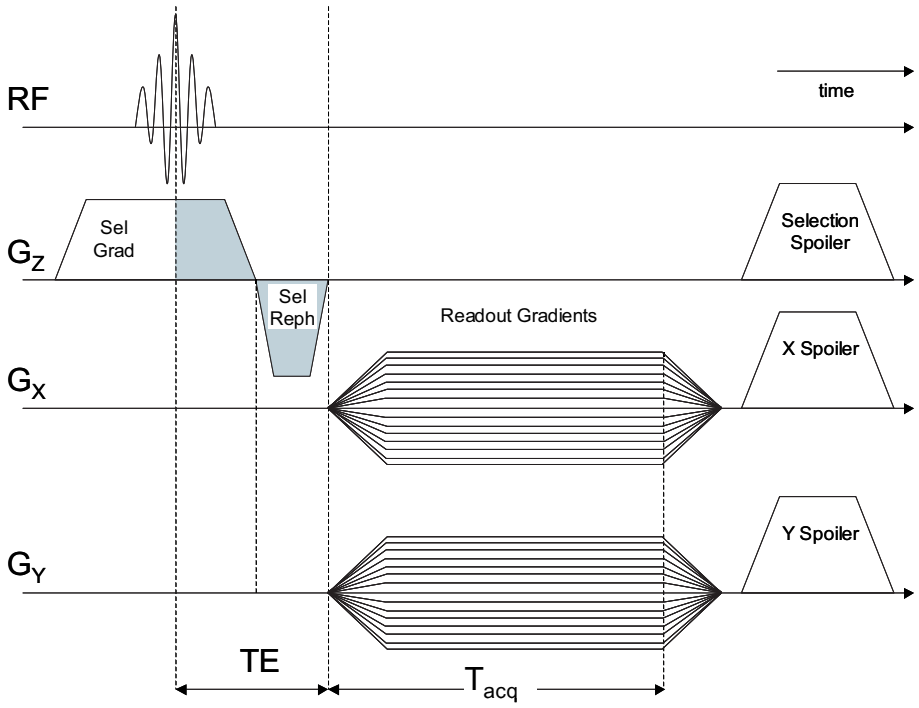

Figure 5.4: 2D radial sequence diagram. TE is only limited by the slice selection gradient train.

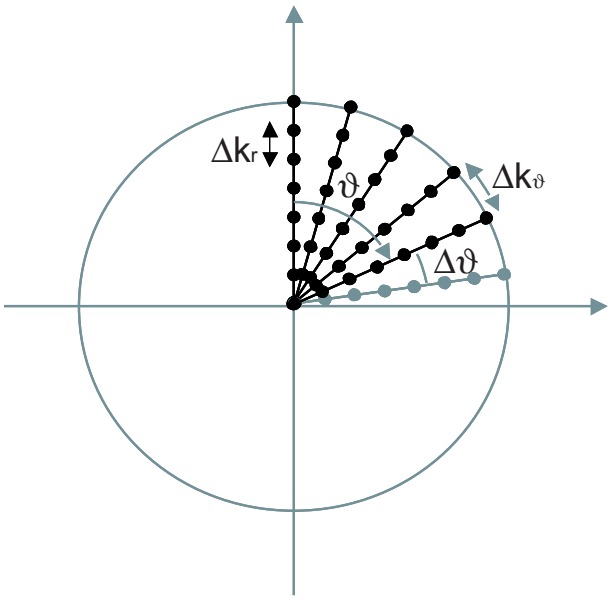

Figure 5.5: 2D radial k-space path. To achieve an isotropic k-space coverage, $\Delta k_r = \Delta k_\theta$.

To achieve an isotropical k-space coverage, the necessary number of projections can be calculated as follows. If every projection is associated with an area

$$\Delta S = \frac{1}{FOV} \tag{5.9}$$

the number of projections required to adequately sample a circular FOV with isotropic resolution (Nyquist criterion)

$$2k_{max}\Delta x = 1 \tag{5.10}$$

can be obtained as the ratio of the perimeter of a circle enclosing the area to be sampled in k-space

$$S = 2\pi R = 2\pi k_{max} \tag{5.11}$$

to the elementary area in equation 5.9. This yields

$$N_{Proj} = \frac{S}{\Delta S} = 2\pi k_{max} L = 2\pi N \tag{5.12}$$

where N is the number of sampling points in a projection.

5.2.2 3D Radial Sequence

For whole volume coverage, a 3D radial sequence was implemented that samples k-space from the centre to the surface of a sphere. Therefore, the three gradients G_x, G_y and G_z are applied simultaneously (figure 5.6), producing a gradient vector $\vec{G}$ which encodes the signal under the spherical angle (θ, ϕ). The components of $\vec{G}$ in spherical coordinates read:

$$G_x = G\sin\theta\cos\phi \tag{5.13}$$
$$G_y = G\sin\theta\sin\phi \tag{5.14}$$
$$G_z = G\cos\theta \tag{5.15}$$

Sampling efficiency in projection imaging is optimal when the sampling density is uniform in solid angle. The Nyquist condition requires that the distance between adjacent samples in k-space should be less than the FOV^{-1}. If every projection is associated with an area

$$\Delta S = \left(\frac{1}{FOV}\right)^2 \tag{5.16}$$

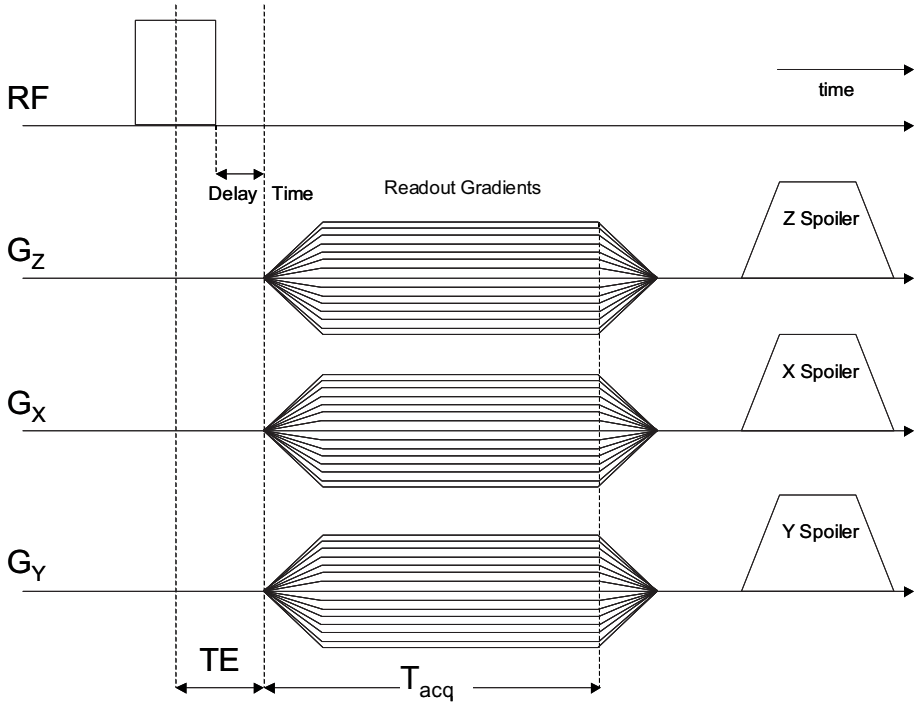

Figure 5.6: 3D radial sequence diagram. TE is only limited by the RF pulse duration and the delay time between RF pulse and data acquisition.

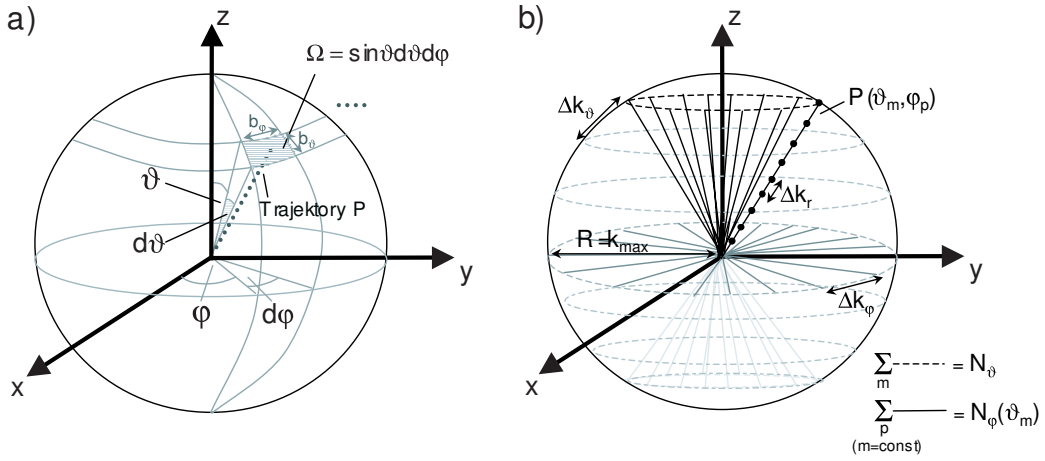

Figure 5.7: 3D radial k-space path. To achieve an isotropic k-space coverage, $\Delta k_r = \Delta k_\theta = \Delta k_\phi$.

the number of projections can be obtained as the ratio of the surface area of a sphere enclosing the volume to be sampled in k-space

$$S = 4\pi R^2 = 4\pi k_{max}^2 \tag{5.17}$$

to ΔS [Boada 1997a]:

$$N_{Proj} = \frac{S}{\Delta S} = 4\pi k_{max}^2 L^2 = 4\pi N^2 \tag{5.18}$$

where N is the number of radial sampling points per projection. Eq. 5.18 provides the number of half-echo acquisitions needed for a specific resolution, but does not constitute a recipe for calculating the angular distribution of projections.

There are several approaches to calculate this distribution. Two possibilities were tested to calculate the trajectories and achieve a homogeneous distribution of the data on the surface of the sphere:

- In the first approach [Chesler 1992] the surface of the k-space sphere of radius k_{max} is divided into an even number N_θ of rings (circles of latitude) separated by a distance $\Delta k_\theta = FOV^{-1}$. The azimuthal angle reads

$$\theta_m = \frac{m}{N_\theta}\pi \quad \Rightarrow \quad m \in [1, N_\theta] \tag{5.19}$$

  The projections $P(\theta_m, \phi_p)$ are distributed along the length of each ring separated by a distance Δk_ϕ. The polar angle reads

$$\phi_p = \frac{p}{N_\phi}2\pi \tag{5.20}$$

  with $p = [1, N_\phi(\theta_m)]$. The number of projections per ring $N_\phi(\theta_m)$ is calculated as follows:

$$N_\phi(\theta_m) = 2N_\theta \sin(\theta_m) \tag{5.21}$$

  The number of resolved pixels in the $FOV = L$ is

$$2k_{max} = 2N\Delta k \Rightarrow k_{max} = N\Delta k \tag{5.22}$$

  where N is the number of radial sampling points in a projection. The relationship between the required resolution and the number of rings can be obtained from

$$\Delta k \geq k_{max}\Delta\theta \quad \text{and} \quad \Delta\theta = \frac{\pi}{N_\theta} \tag{5.23}$$

which yields

$$N_\theta = \pi N \tag{5.24}$$

Considering that

$$2N\Delta x = FOV \tag{5.25}$$

the relationship between the desired spatial resolution and the number of rings is

$$N_\theta = \pi N = \frac{\pi FOV}{2\Delta x} \tag{5.26}$$

- The second approach calculates the spherical coordinates based on an algorithm by [Saff 1997] which distributes N points homogeneously on the surface of a sphere in a spiral manner. The azimuthal and the polar angle then become:

$$\theta_n = \arccos(h_n) \tag{5.27}$$

$$\phi_n = \left(\phi_{n-1} + \frac{3.6}{\sqrt{N(1-h_n^2)}}\right) \mod (2\pi) \tag{5.28}$$

where

$$h_n = -1 + \frac{2n}{N} \quad \text{with} \quad n \in [1, N] \tag{5.29}$$

Figure 5.8 shows the plot of both trajectories. While the first trajectory has small discontinuities between rings (figure 5.8.a and 5.8.c), the second trajectory forms a continuous spiral trajectory over the surface of the sphere (figure 5.8.b and 5.8.d). However, for a number of projections $N \geq 2500$, the rings are so close that the discontinuities are very small. Thus, it is not to be expected that the first trajectory is putting a stronger demand on the gradient system than the second one.

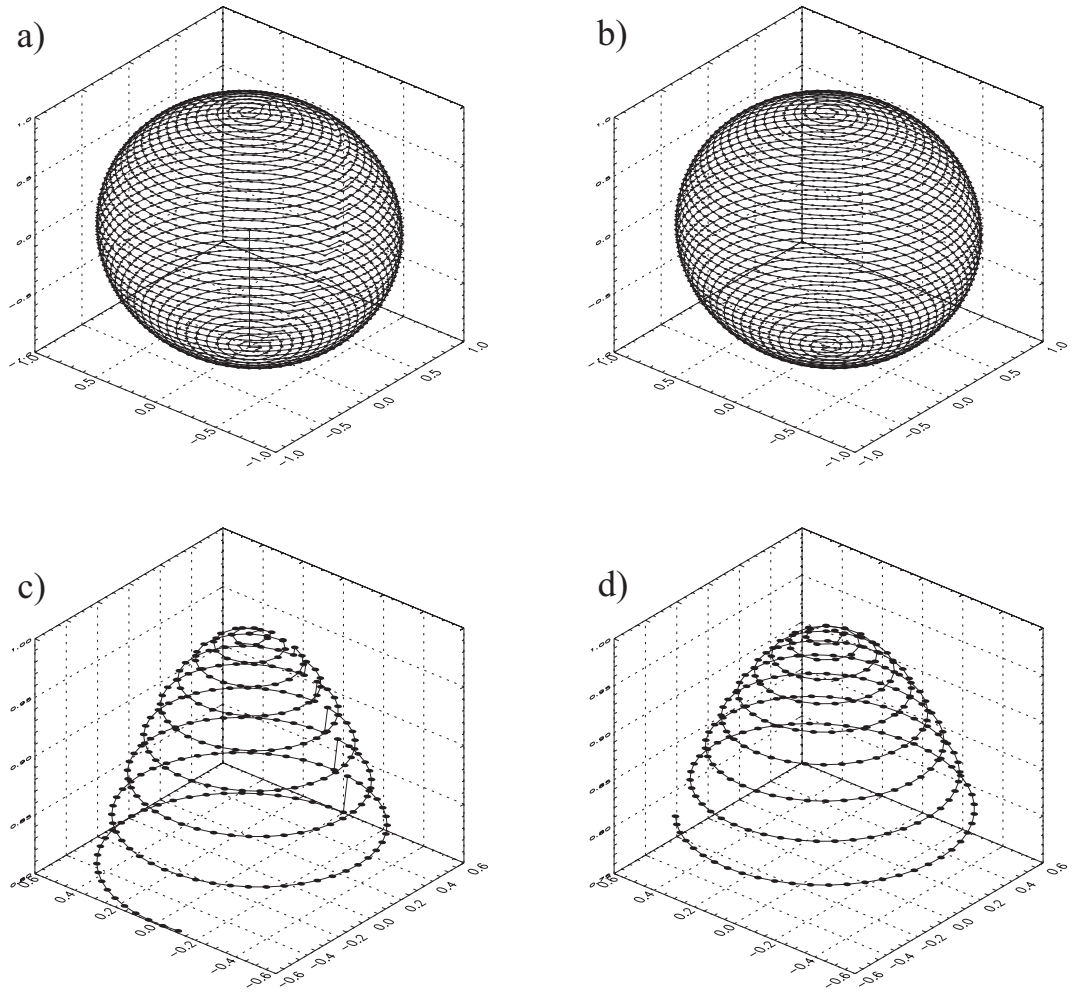

Figure 5.8: Radial paths as calculated with the algorithms that distribute rings (a) or a spiral over the surface of the sphere (b). The zooms (c) and (d) show that the first path creates small discontinuities.

Chapter 6

Reconstruction Algorithms

The standard MRI image reconstruction algorithm is the Fourier Transform (FT), which is ideally suited for conventional (Spin Warp) MRI raw data. However, the radial MRI data acquisition techniques in the previous chapter require an alternative image reconstruction algorithm. In general, the signal equation in MRI relates the MRI signal, $m(\vec{r})$, to the received signal, $M(\vec{k})$:

$$M(\vec{k}) = \int_{FOV} m(\vec{r})\, e^{-i\,2\pi\,\vec{k}\cdot\vec{r}}\, \mathrm{d}\vec{r} \tag{6.1}$$

where the integration occurs over the the whole space and

$$\vec{k}(t) = \gamma \int_0^t \vec{G}(\tau)\, \mathrm{d}\tau \tag{6.2}$$

$$\vec{G}(t) = (G_x(t), \quad G_y(t), \quad G_z(t)) \tag{6.3}$$

The reconstruction of $m(\vec{r})$ is done by an inverse Fourier Transform:

$$m(\vec{r}) = \int_{k-Space} M(\vec{k})\, e^{i\,2\pi\,\vec{k}\cdot\vec{r}}\, \mathrm{d}\vec{k} \tag{6.4}$$

This continuous domain formula assumes that the area of integration $\mathrm{d}\vec{k}$ is uniform. Upon sampling at locations $\vec{k}_j$ and discretising the above expression, one needs to account for the possibility that samples have been acquired non-uniformly in k-space. This leads to the following reconstruction expression:

$$m(\vec{r}) = \sum_j W(\vec{k}_j)\, M(\vec{k}_j)\, e^{i\,2\pi\,\vec{k}_j\cdot\vec{r}} \tag{6.5}$$

The discretised reconstruction formula (equation 6.5) is a Discrete Fourier Transform, where the weighting function $W(\vec{k}_j)$ accounts for non-uniform sampling. Eq. 6.5 has also been referred to as the conjugate phase reconstruction [Macovski99] or the weighted correlation method [Maeda85]. Although it provides an accurate reconstruction, it may become computationally very inefficient. However, if data are acquired on the Cartesian grid, then this weighting function is a constant and equation 6.5 can be evaluated using the Fast Fourier Transform (FFT) algorithm [Cooley 1965]. For matrix sizes $N = 2^n \quad (n \in \mathbb{N})$, it is readily implemented, and very efficient.

For non-cartesian sampling patterns such as radial k-space data, the FFT cannot be directly applied. There are different reconstruction methods for non-cartesian data-sets which are associated with characteristic image artefacts. Thus, the choice of reconstruction method will depend on the diagnostic application and how it is affected by these artefacts.

Several interpolation methods can be employed for resampling of the data onto a cartesian grid. They can be separated as taking place in image space or in k-space.

6.1 Interpolation in Image Space

Radially collected data can be reconstructed by means of the projection reconstruction algorithm. This method operates in image space and is based on the central slice theorem, which states that the one-dimensional FT of a projection is equivalent to a line through the two-dimensional FT of the object at the same angle as the projection [Brooks 1976].

By rewriting equation 6.4 in polar coordinates equation 6.6 is obtained:

$$m(\vec{r}) = \int_0^{2\pi} \left[\int_{-\infty}^{+\infty} M(k,\phi)\, e^{i\,2\pi\,\vec{k}\cdot\vec{r}}\, |k| \mathrm{d}k \right] \mathrm{d}\phi \tag{6.6}$$

This is the standard projection reconstruction relation. The inner integral is the filtered profile $m_\phi(r)$ given by:

$$m_\phi(r) = \int_{-\infty}^{+\infty} M(k,\phi)\, e^{i\,2\pi\,\vec{k}\cdot\vec{r}}\, |k| \mathrm{d}k \tag{6.7}$$

In practice, the filtered profile $m_\phi(r)$ is calculated for each r and its value is added to the nearest cartesian position which satisfies $r = (x\cos\phi + y\sin\phi)$. The process is repeated for all angles between $0 \leq \phi < 2\pi$.

It is interesting to note that in equation 6.6 the signal $M(k,\phi)$ is multiplied by a ramp function $|k|$ before the Fourier transformation. Therefore, the Projection Reconstruction (PR) method is also called Filtered Back-Projection. The disadvantage of this method for low SNR that is that the ramp or Ram-Lak filter [Kak 88] especially enhances the high spatial frequencies, therefore decreasing the SNR of the final image. ^{23}Na MRI is an

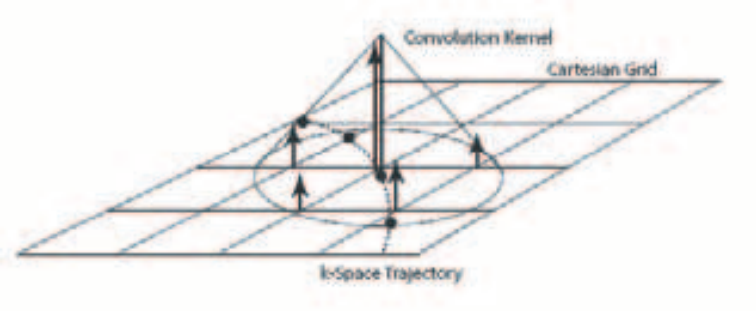

Figure 6.1: Gridding idea. Each data sample is convolved with the gridding kernel, and that convolution evaluated at the adjacent grid points.

intrinsically low SNR method, so PR is not the most appropriate reconstruction method. Besides, the Ram-Lak filter is only appropriate for radially distributed data with uniform sampling along the projections. As described in section 5.2, however, in this case the signal is sampled already during the readout gradient ramp-up time to achieve a short TE (section 5.2). Thus sampling near the centre of k-space is not uniform along the projection, and a conventional ramp filter is not suitable for such a k-space density compensation.

6.2 Interpolation in K-Space

Due to the problems associated with interpolation in image space, in this work interpolation of the non-cartesian samples into a cartesian grid was performed in k-space, followed by a conventional Fast-Fourier-Transform (FFT) Algorithm.

6.2.1 Nearest Neighbour

The most simple interpolation method is Nearest Neighbour interpolation [Oesterle 1999], where the signal from each radially measured data point is added to the nearest cartesian grid point. Correction for non-uniform sample density is applied prior to the FFT.

This method is fast and easily implemented, however, for k-space trajectories that are located centrally between the grid points the interpolation error is large.

6.2.2 Gridding

The basic concept of gridding interpolation is illustrated in figure 6.1. Data points are sampled along an arbitrary trajectory through k-space. To distribute the signal among the nearest grid points, each data point is first convolved with a gridding kernel. The

result resampled and accumulated on the cartesian grid. After all data samples have been processed, an FFT produces the reconstructed image [O'Sullivan 85], [Jackson 91].

Considering the two-dimensional case of equation 6.1, with $\vec{r} = (x,\, y)$ and $\vec{k} = (k_x,\, k_y)$ results in:

$$M(k_x, k_y) = \int m(x, y)\, e^{-i\,2\pi\,(k_x x + k_y y)}\, \mathrm{d}x\mathrm{d}y \tag{6.8}$$

To describe the non-cartesian sampling pattern, a sampling function S is introduced, consisting of N two-dimensional delta functions at positions $(k_{x,i}, k_{y,j}$:

$$S(k_x, k_y) = \sum_{i=1}^{N} \delta(k_x - k_{x,i}) \cdot \sum_{j=1}^{N} \delta(k_y - k_{y,j}) \tag{6.9}$$

The MR data sampled along the trajectory $M_S(k_x, k_y)$ is given by

$$M_S(k_x, k_y) = M(k_x, k_y) \cdot S(k_x, k_y) \tag{6.10}$$

In the gridding reconstruction, the sampled data is convolved with a window function $C(k_x, k_y)$ and sampled onto a cartesian grid with unit spacing:

$$M_{SCS}(k_x, k_y) = [M_S(k_x, k_y) \otimes C(k_x, k_y)] \cdot \mathrm{III}\left(\frac{k_x}{\Delta k_x}, \frac{k_y}{\Delta k_y}\right) \tag{6.11}$$

where $\otimes$ denotes a two-dimensional convolution (i.e. $f \otimes g = \int f(x) \cdot g(y - x)dx$), and the 2D comb function $\mathrm{III}\left(\frac{k_x}{\Delta k_x}, \frac{k_y}{\Delta k_y}\right)$ is defined by:

$$\mathrm{III}\left(\frac{k_x}{\Delta k_x}, \frac{k_y}{\Delta k_y}\right) = \sum_{i=1}^{N} \delta(k_x - i) \cdot \sum_{j=1}^{N} \delta(k_y - j) \tag{6.12}$$

The corresponding reconstructed image $m_{SCS}(x, y)$ is then given by the inverse Fourier Transform of $M_{SCS}(k_x, k_y)$ as

$$m_{SCS}(x, y) = \{[m(x, y) \otimes s(x, y)] \cdot c(x, y)\} \otimes \mathrm{III}\left(\frac{x}{FOV_x}, \frac{y}{FOV_y}\right) \tag{6.13}$$

The effects of the gridding process in image space are illustrated in figure 6.2. The ideal image $m(x, y)$ is first blurred by convolution with the transform of the sampling function $s(x, y)$. In addition, sidelobes are usually created due to the pattern of the samples in k-space. Next, the image is apodised by the transform of the gridding kernel $c(x, y)$. While

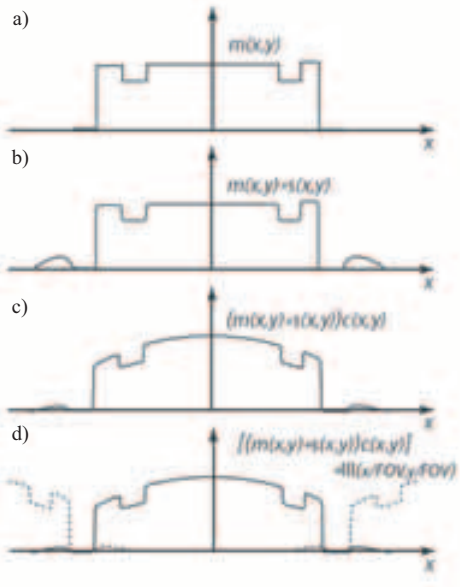

Figure 6.2: Effects of the Gridding Process on the object as observed in image space. The ideal image (a) $m(x, y)$ is first blurred by convolution with the transform of the sampling function $s(x, y)$ (b). Next, the image is apodised by the transform of the gridding kernel $c(x, y)$ (c). Finally, the rectilinear sampling in k-space III($\frac{x}{FOV_x}$, $\frac{y}{FOV_y}$) causes replication in image space (c). Courtesy of [Pauly 2004].

this has the undesirable side effect of introducing a shading in the image, it suppresses the sidelobes generated by the convolution with the sampling function. As will be explained in section 6.2.3, apodisation can be corrected for, and the image shading disappears, at the expense of re-introducing the aforesuppressed sidelobes. Finally, the rectilinear sampling in k-space III($\frac{x}{FOV_x}$, $\frac{y}{FOV_y}$) causes replication in image space. As a consequence, sidelobes from the first replicas interfere with the image. All of these reconstruction steps can impair image quality and, thus, need to be optimised.

6.2.3 Convolution Kernel

When choosing a convolution function, the behaviour of its Fourier transform both within and outside the FOV must be considered. Its Fourier transform should not vanish within the FOV, since division by zero would result in very pronounced artifacts. Secondly, according to Fourier theory, sampling in k-space results in replication of the object in the image domain (aliasing). By convolving the k-space samples with a convolution kernel (also called window function) $C(k_x, k_y)$, the resulting image replicates are multiplied by the Fourier transform (FT) of the convolution function $c(x, y)$. If $c(x, y)$ has significant energy contributions outside the FOV, then these contributions will be aliased back into the original image. If, on the other hand, the convolution function decays rapidly, it leads

to the fall-off in image intensity towards the edges of the image. This effect is known as apodisation and, in order to remove it, it is necessary to divide by the Fourier Transform of the convolution function $c(x, y)$. This process is known as deapodisation:

$$m(x,y) = \frac{1}{c(x,y)} \left[\{ [m(x,y) \otimes s(x,y)] \cdot c(x,y) \} \otimes \mathrm{III} \left(\frac{x}{L_x}, \frac{y}{L_y} \right) \right] \tag{6.14}$$

During the deapodisation process, the image is divided by the FT of the convolution function. Thus, optimisation of the convolution kernel must consider the amount of energy outside the FOV and the amount of amplification by deapodisation.

An optimal convolution function should posses there characteristics: its FT should be analytical, it should be separable $C(k_x, k_y) = C(k_x)C(k_y)$ and $c(x, y) = c(x)c(y)$, and the FT should decay sufficiently rapidly, without sidelobes, so as to avoid introducing image artefacts. Both the Gaussian function and the Kaiser-Bessel function fulfil these requisites.

6.2.3.1 Gaussian

The Gaussian is defined by

$$C(k) = \exp \left[-\frac{1}{2} \left(\frac{k}{\sigma} \right)^2 \right] \tag{6.15}$$

where σ is its width. The Fourier Transform of the Gauss reads

$$c(x) = \exp \left[-\frac{1}{2} \left(\frac{x}{\sigma} \right)^2 \right] \tag{6.16}$$

6.2.3.2 Kaiser-Bessel

The Kaiser-Bessel function is based on the zero-order modified Bessel function of the first kind I_0:

$$C(k) = \begin{cases} \frac{1}{W} I_0 \left[\beta \sqrt{1 - \left(\frac{2k}{W} \right)^2} \right] & \text{for } |k| \leq \frac{W}{2} \\ 0 & \text{otherwise} \end{cases} \tag{6.17}$$

where W is the width of the kernel and β is a shape parameter. The FT of the Kaiser-Bessel function is given by

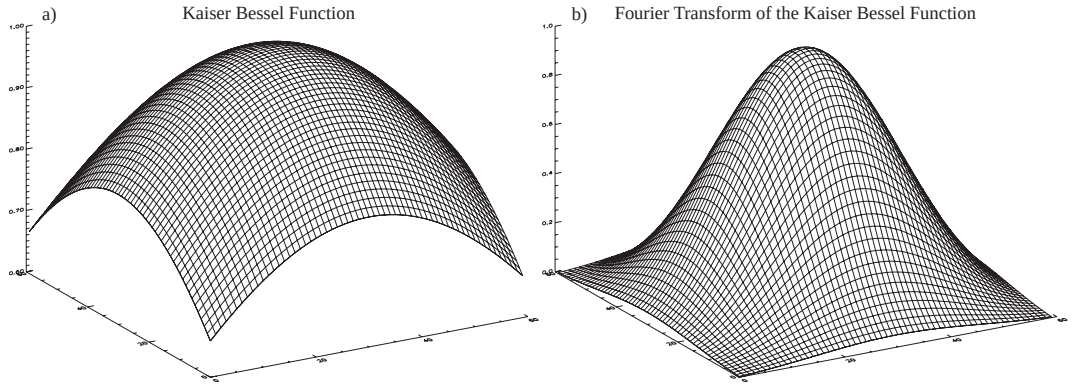

Figure 6.3: 2D Kaiser Bessel (KB) function and FT of the KB.

$$c(x) = \frac{\sin\sqrt{\pi^2 W^2 x^2 - \beta^2}}{\sqrt{\pi^2 W^2 x^2 - \beta^2}} \tag{6.18}$$

Figure 6.3 depicts the Kaiser-Bessel function and its FT in $2D$.

The optimal parameter values of the previous functions have been calculated by Jackson et al. [Jackson 91]. For a window width of 3.0, $\sigma = 0.5063$ for the Gaussian and $\beta = 4.2054$ for the Kaiser-Bessel function.

6.2.4 Density of the reconstruction grid

Since the cartesian grid is arbitrarily imposed, its density Δk_x and Δk_y can be freely chosen. The choice of k-space density has an effect on the amount of aliasing from the adjacent replicas, and, indirectly, on the apodisation of the kernel.

By choosing the grid to be denser than the sampling of the underlying k-space data, the spacing between replica sidelobes is increased, and aliasing is reduced (figure 6.4). In this way, narrower gridding kernels can be used and apodisation is reduced. For $\alpha > 1$, the cartesian grid is

$$\left(\frac{\Delta k_x}{\alpha}, \frac{\Delta k_y}{\alpha}\right) \tag{6.19}$$

and the reconstructed image may be written

$$m_{SCS}(x,y) = \frac{1}{c(x,y)}\left[\{[m(x,y) \otimes s(x,y)] \cdot c(x,y)\} \otimes \text{III}\left(\frac{x}{\alpha FOV_x}, \frac{y}{\alpha FOV_y}\right)\right] \tag{6.20}$$

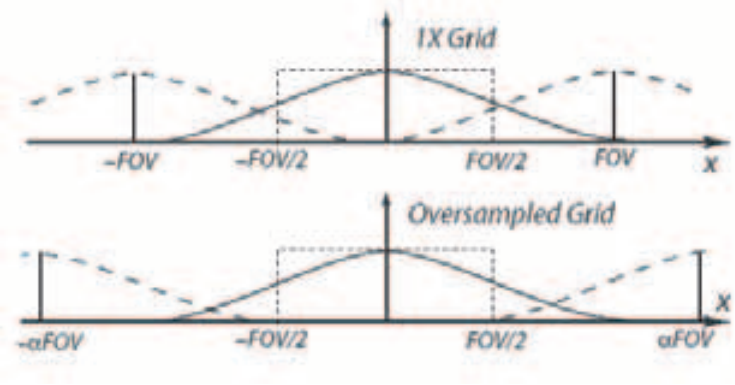

Figure 6.4: Reconstruction on a denser grid (oversampling) moves the replica sidelobes out, reducing aliasing and allowing less apodisation.

Often $\alpha = 2$ grid is used for the practical reason that the next power-of-two FFT can be applied. In this case, the aliased signal from the adjacent replica sidelobes is below the noise level for most MRI images. The disadvantage of oversampling is the increase in computation time and memory requirements. This can become a real limitation for $3D$ imaging, where a factor of $2^3 = 8$ more memory is required. Recently, very fast implementations of the FFT have become available for a whole range of FFT lengths [Pauly 2004]. This will allow for great flexibility in choosing the oversampling factor as a non-integer value between $1 < \alpha \leq 2$. For example, for a 2D data set with 128 points per projection, the $\alpha = 2$ grid would be 256^2, and its FT would last 15.63 ms, while the $\alpha = 1.75$ grid would be 224^2, and its FT would last 8.28 ms. The choice of α must be a tradeoff with the size and shape of the gridding kernel, the amount of aliasing that can be tolerated and reconstruction speed.

6.3 Density Compensation

In non-uniformly sampled imaging methods, the weighting function $W(\vec{k}_j)$ decreases the influence of redundant data. There are two options to compensate for non-uniform k-space densities: pre- and postcompensation.

- **Precompensation** is the density compensation for each measured data point before the gridding operation, and may be written:

$$M_{SWCS}(k_x, k_y) = \left[\left(M(k_x, k_y)\frac{S(k_x, k_y)}{\rho(k_x, k_y)}\right) \otimes C(k_x, k_y)\right] \times \text{III}\left(\frac{k_x}{\Delta k_x}, \frac{k_y}{\Delta k_y}\right) \tag{6.21}$$

For precompensation, the density $\rho(k_x\, k_y)$ must be precomputed since it is required prior to the gridding operation. The weighting applied during the gridding operation is the inverse of the sample density $\omega(k_x, k_y) = 1/\rho(k_x, k_y)$.

- **Postcompensation** is the density compensation after the gridding operation, and occurs is performed for each grid point individually:

$$M_{SWCS}(k_x,\, k_y) = \frac{1}{\rho(k_x,\, k_y)} \times [(M(k_x,\, k_y) S(k_x,\, k_y)) \otimes C(k_x,\, k_y)] \times \mathrm{III}\left(\frac{k_x}{\Delta k_x}, \frac{k_y}{\Delta k_y}\right) \tag{6.22}$$

The density matrix can itself be computed by gridding. Convolving delta functions at the k-space trajectory locations with the convolution function yields [Jackson 91]:

$$\rho(k_x,\, k_y) = [S(k_x,\, k_y) \otimes C(k_x,\, k_y)] \times \mathrm{III}\left(\frac{k_x}{\Delta k_x}, \frac{k_y}{\Delta k_y}\right) \tag{6.23}$$

Ideally, the density compensation should be done for each data point before the gridding operation. Precompensation is performed based on the assumption of an ideal acquisition, while postcompensation can be estimated at reconstruction time based on imperfections in the acquisition. Postcompensation works well only if the rate of change of the density pattern is not too rapid. At the origin of radially sampled data sets, the density changes happen in distances that are comparable to or smaller than the convolution kernel, so that they cannot be resolved with postcompensation density correction [Pauly 2004]. An alternative is to use both pre- and postcompensation in one reconstruction.

6.3.1 Choice of Weighting Function

In radial imaging, there is an excess of samples taken near the origin in k-space as shown in Figure 6.5. $W(\vec{k}_j)$ must be selected to compensate for this increased k-space density.

Many methods have been presented to address the determination of the sample density compensation functions (DCF) for arbitrary k-space trajectories [Pipe99], [Pipe 2000]. One possible expression for $W(\vec{k}_j)$ is the area in the cell surrounding each sample. For simple k-space trajectories such as radial sampling, the area associated with each sample can be computed geometrically. For a 2D radial data set, samples are located along radii (Fig. 6.5). For N projections the central sample is acquired N times and a weighting factor of $1/N$ needs to be multiplied by the area of the central disk closest to the k-space origin.

$$\omega_0 = \frac{1}{N}\, \pi \left(\frac{k_1}{2}\right)^2 \tag{6.24}$$

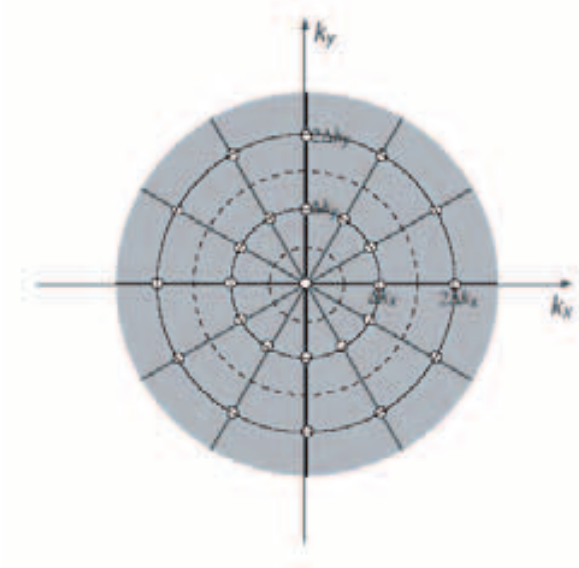

Figure 6.5: Calculation of the density matrix for a 2D radial data set. In this case, the sampling points lye equidistant along each projection.

The weighting for samples at radius k_n is given by the area in the next annular ring outside the central disk divided by the number of samples:

$$\omega_n = \frac{1}{N}\,\pi\left[\left(\frac{k_{n+1}}{2}\right)^2 - \left(\frac{k_n}{2}\right)^2\right] \tag{6.25}$$

For equidistant spacing Δk_r along the projection, the weighting function reads:

$$\omega_0 = \frac{2\pi}{N}(\Delta k_r)^2\frac{1}{8} \quad \text{and} \quad \omega_n = \frac{2\pi}{N}(\Delta k_r)^2 n \tag{6.26}$$

This function is called the rho filter.

Many other methods have been introduced to compute the density compensation function for arbitrary k-space trajectories. The ramp filter used by projection reconstruction (section 6.1), which is also known as Ram-Lak filter, or the Shepp-Logan filter, low-pass cosine filter and Hamming window, are all widely used in computed tomography (CT) [Kak 88]. These CT filters do not compensate for non-uniform sampling along the projections. The radial methods implemented in this work sample data already during gradient readout ramp-up time to minimise TE, leading to non-uniform sampling along the projections close to the centre of k-space, which cannot be properly corrected for with these CT filters. Rasche, et al. use areas of Voronoi cells around k-space sampling locations to determine the DCF for arbitrary k-space trajectories [Rasche99].

6.3.2 Density Compensation of Undersampled Data

Until now the density compensation has only been considered for data sampled more densely than the Nyquist limit, however, it is necessary to consider the effects of weighting undersampled data. Solid angle undersampling is often the case in radial techniques to compensate for the intrinsically longer acquisition times of radial MRI. According to equation 5.18, if N is the number of sampling points in a half-projection, the necessary number of half-projections is $N_{Proj} = 4\pi N^2$. Some examples for typical values of matrix size and number of half-projections for 2D and 3D radial techniques are written in table 6.1.

N	N_{Proj} 2D	N_{Proj} 3D
64	402	51471
128	804	205887
256	1609	823550

Table 6.1: Number of half-projections N_{Proj} corresponding to the number of sampling points N per half-projection for 2D and 3D radial data sets.

For an average value of $N = 128$ and $TR = 10\,\text{ms}$, the total scan time would be $T_{acq} \simeq 35\,\text{min}$. This is already unacceptably long for ^{1}H MRI, and impossible for ^{23}Na MRI where additional signal averaging is required. Undersampling is clearly necessary, and the reconstruction should correct for undersampling-corrected artefacts. Studies to overcome this problem have identified that higher resolution is obtained by weighting undersampled data according to the inverse sampling density, while better SNR and less aliasing artifacts are obtained by weighting undersampled data uniformly [Pipe 2000].

Pipe and Menon [Pipe99] studied the problem of undersampling in detail and created an iterative numerical solution to calculate a filter for undersampled data with only the trajectory as input. In this study it can be observed, that the filter tends to an asymptotic behaviour at some point, that is directly related to the percentage of undersampling. As a first approach, in this work, the rho filter was adapted for 2D and 3D techniques, and forced to an asymptotic value depending on the percentage of undersampling.

6.4 Implementation of the Reconstruction Methods

In this work the nearest neighbour (NN) method and the gridding technique have been implemented for offline as well as online reconstruction. The gridding technique was used with both Gauss and Kaiser-Bessel weighting functions. Pre- and postcompensation was tested, as well as different density compensation filters for ^{1}H and ^{23}Na taking into account different amounts of undersampling.

The gridding algorithm was implemented as follows:

- A measured data point $\vec{k}_j$ with the value $M(\vec{k}_j)$ is taken and multiplied by its density compensation value $\Omega(k)$ (precompensation) resulting in $M_\Omega(\vec{k}_j)$.
- The cartesian points $\vec{p}_i$ which are at a distance $d \leq \frac{W}{2}$ of $\vec{k}_j$, where W is the convolution window width, are identified.
- The convolution kernel $C(\Delta\vec{k})$ is calculated for each cartesian point $\vec{p}_i$ with respect to the radial point $\vec{k}_j$.
- The measured (and density compensated) value $M_\Omega(\vec{k}_j)$ is multiplied by the convolution kernel $C(\Delta\vec{k})$ and added to the interpolated signal at $\vec{p}_i$.
- The value of the convolution function $C(\Delta\vec{k})$ is saved in an additional density array $D(\vec{p})$ (postcompensation).
- The process is repeated for all the measured radial points.
- The resulting cartesian array $m(\vec{p})$ is divided by the density array $D(\vec{p})$ (postcompensation) resulting in $m_D(\vec{p})$.
- The cartesian data set $m_D(\vec{p})$ is Fourier transformed resulting in $m(\vec{x})$.
- The Fourier Transform of the convolution kernel $c(\vec{x})$ is calculated.
- Each cartesian data point is divided by the Fourier Transform of the convolution kernel $c(\vec{x})$ (deapodisation).

6.5 Trajectory measurement

In sequences which employ fast gradient switchings, the actual gradients produced by the gradient coils may be different from the ideal gradient envelope time courses for a number of reasons: imperfections due to eddy currents, cross-coupling between the gradient coils, preemphasis effect or gradient amplifier limitations. This can strongly degrade image quality, causing deformation or blurring. In radial imaging, where the signal is already sampled during readout gradient ramp-up time, small delays between the ADC and gradient timing can cause substantial, angle-dependent deviations from the expected trajectory.

Knowledge of the actual k-space trajectory allows for corrections during image reconstruction and avoids image artefacts. Several methods have been developed to measure the actual k-space trajectories ([Onodera 87], [Papadakis 97], [Mason 97], [Duyn 98]). In this work the method of Papadakis et al. [Papadakis 97] has been used. It uses a self-encoding gradient pulse that is assumed to produce an ideal M_0 preceding the acquisition interval. The self-encoding gradients are effectively phase encoding gradients switched in the direction of interest which act as dephasers, so that the echo takes place at a different point in k-space every time (figure 6.6).

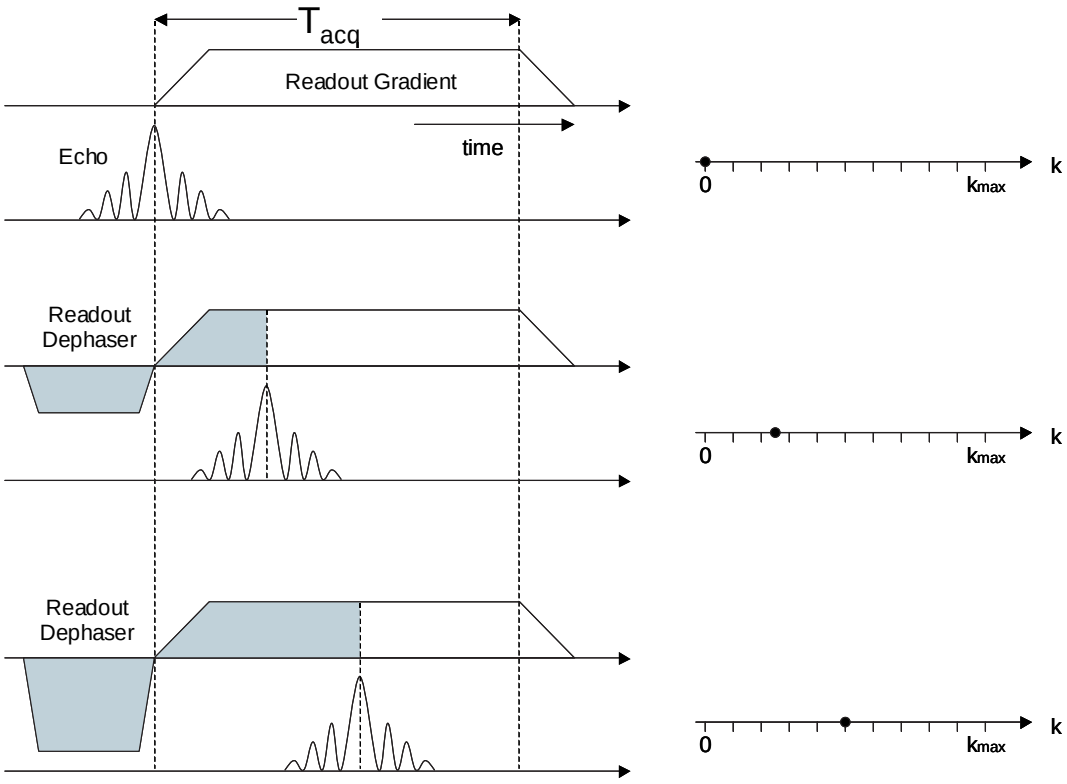

Figure 6.6: Depiction of the trajectory measurement sequence. Self-encoding gradients before the radial gradients help generate the desired k-space trajectory.

A sequence was developed, which had self-encoding gradients before the radial gradients to generate the desired k-space trajectory. A corresponding reconstruction program was developed for this application, which simply writes out the projection data in a file, as well as plotting its absolute value in the scanner as a sort of image. An IDL program was developed that would read every projection, calculate the absolute value of the complex signal and search its maximum. The position of the maximum signal was evaluated as a function of the self-encoding gradient strength. This measured curve was compared to the theoretical curve.

Being T_{acq} the acquisition time, and N the number of acquired samples, the dwelltime DT (i.e. the duration of the acquisition window for an individual data point) reads

$$DT = \frac{T_{acq}}{N} \tag{6.27}$$

and the number n_{ramp} of data points sampled during ramp-up time t_{ramp} corresponds to

$$n_{ramp} = \frac{t_{ramp}}{DT} \tag{6.28}$$

The expected theoretical curve is then given by

$$k = \begin{cases} \frac{n^2}{2n_{ramp}} & \text{for } n = 0, \ldots, n_{ramp} \\ n - \frac{n_{ramp}}{2} & \text{for } n = n_{ramp} + 1, \ldots, N \end{cases} \tag{6.29}$$

Part III

Results

Chapter 7

Hardware Results

7.1 Coils

In this section the results of the measurements with the different ^{23}Na coils described in sections 4.2.3 (page 52), 4.2.5 (page 53) and 4.2.4 (page 53) are presented.

7.1.1 Flip Angle Calibration

The plots of the signal intensities as a function of the transmitter voltage are depicted in figure 7.1. Due to their components characteristics, the self-developed coils (saddle coil and birdcage coil) can hold a maximum voltage of $V_{max} = 200\,\mathrm{V}$ at 50Ω. As can be observed, with the load used for these experiments, an inversion pulse $\alpha = 180°$ could not be achieved, while the Rapid birdcage coil managed to perform an inversion pulse. At $V \approx 120\,\mathrm{V}$, stripes of iso-field lines where the RF pulse angle was 180° became visible in the acquired with images the surface coil. For ^{23}Na NMR applications, inversion pulses are usually not required, so that the self-developed volume coils can be used for most of the studies. With smaller coil loading, these coils can also reach the inversion pulse. The reference voltages for a flip angle of $\alpha = 90°$ resulting from the fit of the curves to equation 4.3 are found in table 7.1.

Coils	V_{90}
Birdcage	179
Saddle	126
RAPID Birdcage	127
RAPID Surface coil	168

Table 7.1: Reference voltages V_{90} of the coils.

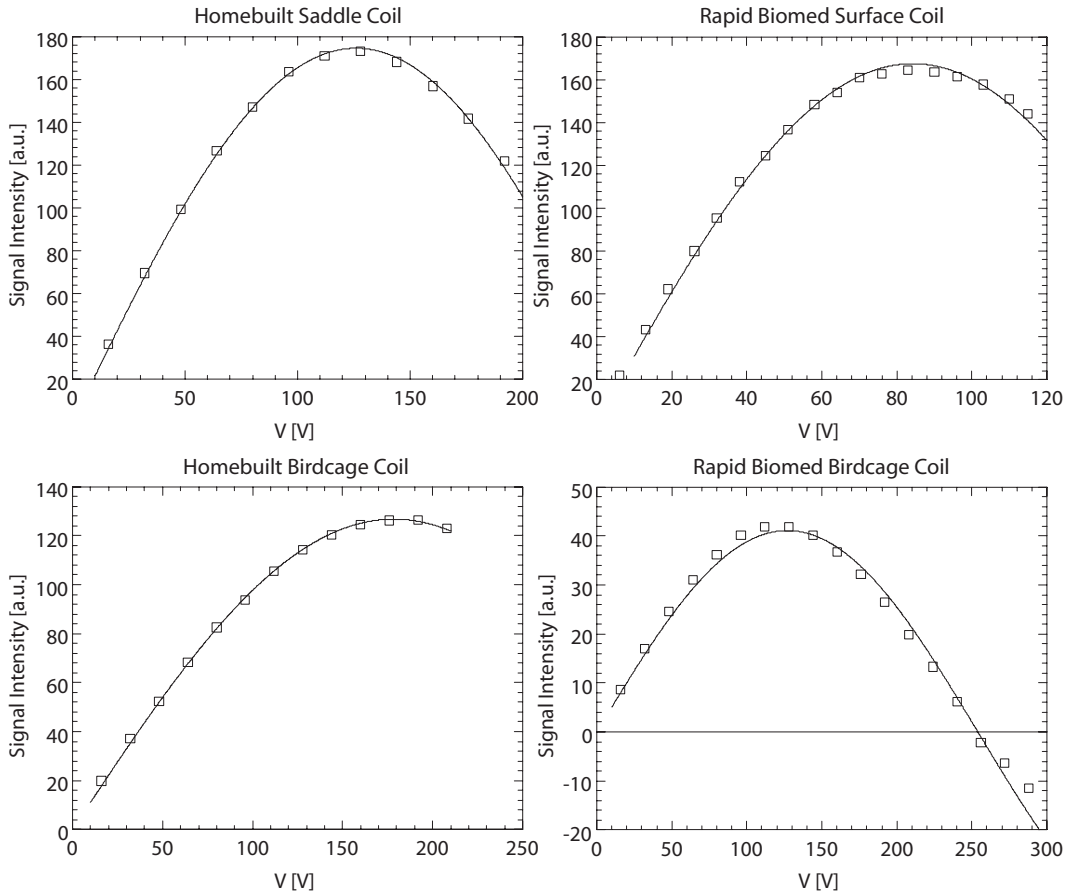

Figure 7.1: flip angle calibration plots for the saddle coil, the surface coil, the low-pass birdcage coil and the high-pass birdcage coil. For the same loading and sequence parameters, the high-pass birdcage coil is the only one that reaches $\alpha = 180°$.

7.1.2 B_1 Field Homogeneity

7.1.2.1 Saddle coil

Figure 7.2 shows transversal, coronal and sagittal views of the B_1 field distribution of the saddle coil. As can be observed in the coronal and sagittal images (figures 7.2.b and 7.2.c respectively), B_1 increases towards the edges. In the transversal view (figure 7.2.a), the higher sensitivity of the lower part compared to the upper part is remarkable. For a circular ROI of $\sim 300\,\mathrm{cm}^2$ placed in the centre of the transversal slice, the standard deviation of the intensity is 20.2%. This volume resonator has therefore poor B_1 homogeneity.

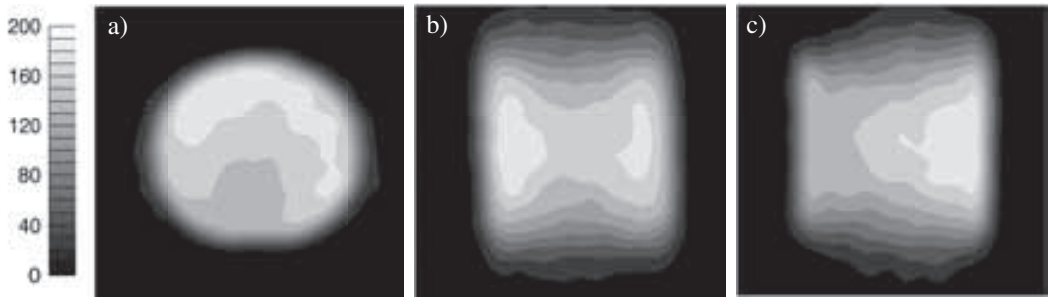

Figure 7.2: Saddle coil field maps. Transversal (a), coronal (b) and sagittal (b) views of the B_1 field distribution.

7.1.2.2 Birdcage coils

Low-pass birdcage

Figure 7.3 shows transversal, coronal and sagittal views of the B_1 field distribution of the low-pass birdcage coil. It can be seen that the distribution is rather homogeneous. For a circular ROI of $\sim 300\,\mathrm{cm}^2$ placed in the centre of the transversal slice, the standard deviation of the intensity is 13.8%.

High-pass birdcage

Figure 7.4 shows transversal, coronal and sagittal views of the B_1 field distribution of the high-pass birdcage coil. For a circular ROI of $\sim 300\,\mathrm{cm}^2$ placed in the centre of the transversal slice, the standard deviation of the intensity is 0.6%. This coil's homogeneity is therefore 24 times better than that of the low-pass birdcage coil, and 35 times better than that of the saddle coil.

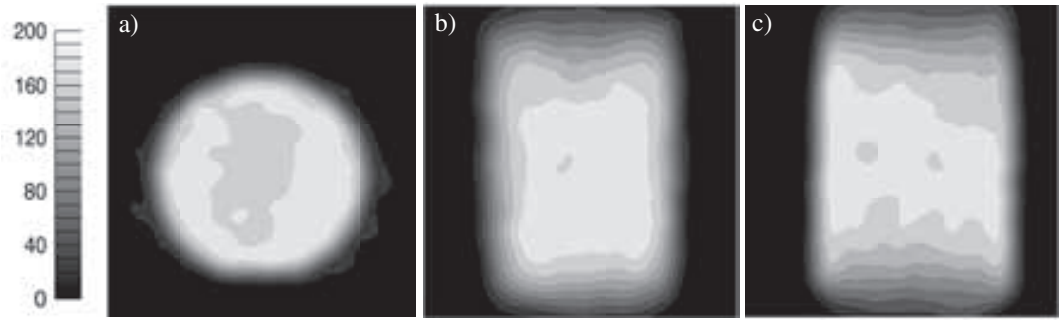

Figure 7.3: Low-pass birdcage coil field maps. Transversal (a), coronal (b) and sagittal (b) views of the B_1 field distribution.

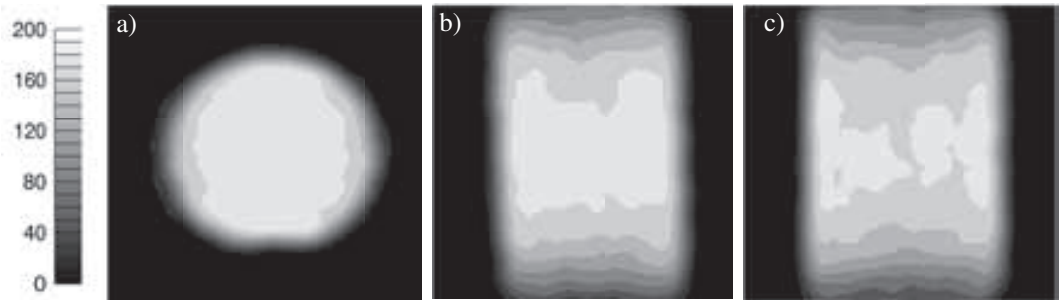

Figure 7.4: High-pass birdcage coil field maps. Transversal (a), coronal (b) and sagittal (b) views of the B_1 field distribution.

7.1.2.3 Surface coil

Figure 7.5 shows transversal, coronal and sagittal views of the B_1 field distribution of the surface coil. The sensitivity decrease with increasing distance from the coil is clearly to be observed. Moreover, the sagittal view (figure 7.5.c) depicts the roughly hemispherical region of sensitivity (radius $\sim$ 15 cm). The penetration depth is calculated as distance from the surface of the coil to the point where the signal intensity corresponds to the ratio $\frac{I_{max}}{e}$. In this case, a penetration depth of 7.8 cm was measured.

7.1.3 Quality Factor and Signal-to-Noise Ratio

Table 7.2 lists the calculated Q values of the self developed coils, as well as the Q values provided by the manufacturers for the acquired coils. Using equation A.6, the sensitivity of the coils has been calculated. So as to compare these sensitivities with some imaging results, gradient echo images ($TR = 200$ ms, $TE = 2.48$ ms, $FOV = 500$ mm, matrix size = 64×64, $N_{acq} = 10$, $BW = 200$ Hz/Pixel) of a homogeneous phantom were acquired for the four coils. Regions of interest were set and the SNR was calculated as the mean intensity

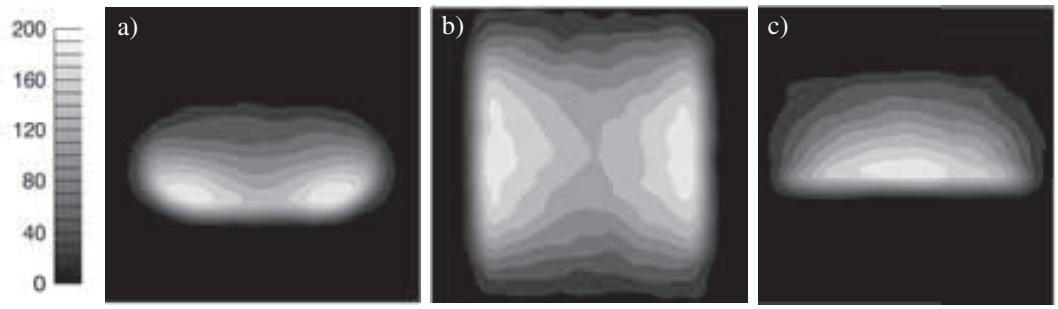

Figure 7.5: Surface coil field maps. Transversal (a), coronal (b) and sagital (b) views of the B_1 field distribution.

value in the phantom divided by the standard deviation of the background noise.

$$SNR = \frac{S_{phantom}}{\sigma_{background}} \tag{7.1}$$

Coils	$Q_{unloaded}$	Q_{loaded}	$Q_{loaded}/Q_{unloaded}$	$S/S_0(\%)$	SNR
Birdcage	170	61	0.41	77	31
Saddle	70	29	0.41	77	38
RAPID Birdcage	180	90	0.5	71	35
RAPID Surface coil	200	100	0.5	71	41

Table 7.2: Calculated Q values of the self developed coils, as well as the manufacturer's given Q values for the acquired coils. Comparison with the SNR of these coils. For the volume coils the same phantom was used. In the three cases the same sequence parameters were applied (2D FLASH, $TR = 200\,\text{ms}$, $TE = 2.48\,\text{ms}$, $FOV = 500\,\text{mm}$, matrix size $= 64 \times 64$, $N_{acq} = 10$, $BW = 200\,\text{Hz/Pixel}$)

The ratios $Q_{loaded}/Q_{unloaded}$ cannot be directly compared because thy have been measured in different conditions. They give, however, a rough idea of the quality of the coils and match fairly well with the SNR results.

Due to its better B_1 homogeneity and SNR, as well as the fact that it is a double-resonant coil, the high-pass birdcage coil was used for the phantom, volunteer, and clinical experiments that follow. Only the 1.5 T measurements for the comparison between 1.5 T and 4 T (section 9.2) were performed with the low-pass birdcage coil, because it was the only one available at the time.

The surface coil was used for *in-vivo* heart measurements in section 9.1.3 and for the measurements of the lower leg in section 10.2.1.

Chapter 8

Radial Reconstruction

8.1 Trajectory measurements

Figure 8.1 depicts two examples of the images created by the trajectory measurement sequence. A single projection trajectory is plotted. The white line represents the echoes and the initial curvature corresponds to the ramp-sampling period of equation 6.29, followed by a straight line corresponding to the plateau of the readout gradient.

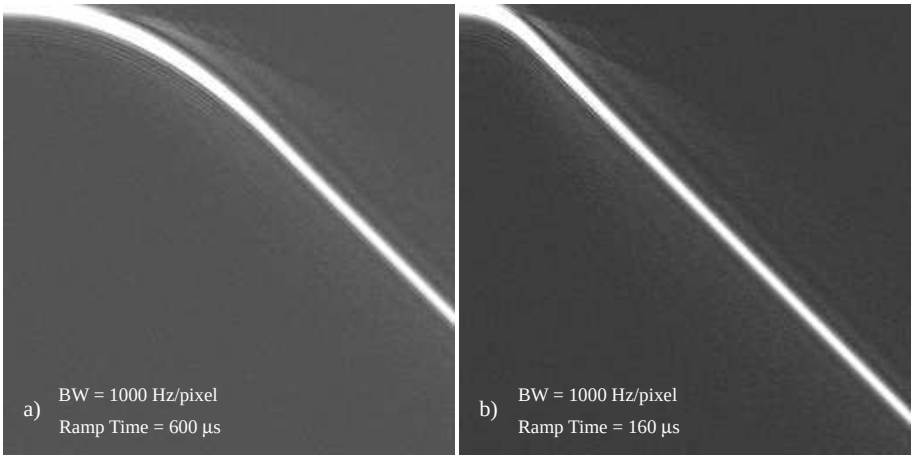

Figure 8.1: Trajectory Measurement Images as displayed on the scanner's screen.

The comparison of the theoretical and measured trajectories of figure 8.1 are shown in figure 8.2. The deviation from ideality can be estimated as follows:

$$|k_{theoretical} - k_{measured}| \leq \alpha \Delta k \tag{8.1}$$

For the plot in figure 8.2.a, $\alpha = 0.079$, while for the plot in figure 8.2.b, $\alpha = 0.487$. By introducing a gradient delay Δt in the theoretical trajectory calculation, these deviations can be minimised. For the data set in Fig. 8.2.a, $\Delta t = 0.6\,\mu s$ leads to $\alpha = 0.003$, while for the data set in Fig. 8.2.b, a $\Delta t = 3.7\,\mu s$ leads to $\alpha = 0.003$. The use of the theoretical trajectory during data reconstruction might therefore lead to image artefacts. As the gradient delay seems to vary, however, a priori trajectory correction is not possible.

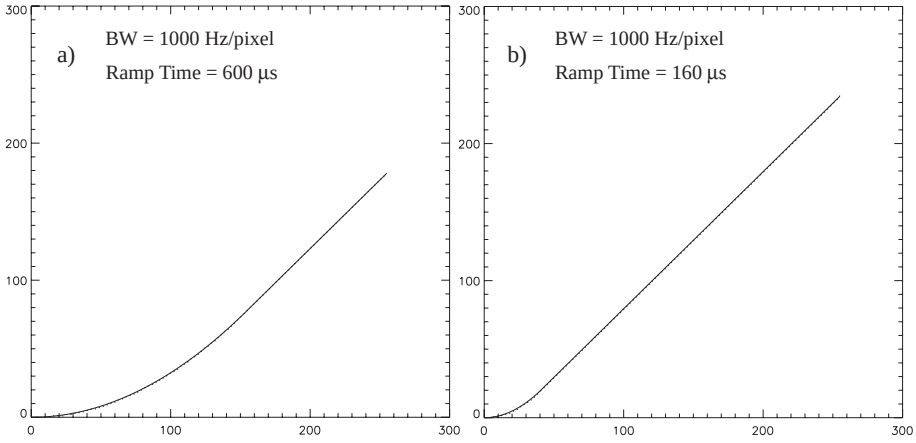

Figure 8.2: Comparison of the theoretical and measured trajectories in figure 8.1. Small deviations from ideality can be observed.

8.2 Optimisation of the Interpolation Methods

In this section, the results of the reconstruction methods described in section 6.4 are presented and analysed for both ^{1}H and ^{23}Na. For each case, a transversal, coronal and sagittal slice of a reconstructed $3D$ data set is displayed, together with the plot of the profile through the central image line, normalised to unity, in order to evaluate the achieved resolution and SNR of the images.

8.2.1 Comparison between Nearest Neighbour, Gauss and Kaiser-Bessel Windowing

A comparison between Nearest Neighbour interpolation (8.3.a and b) and Gauss (8.3.c and d) and Kaiser-Bessel (8.3.e and f) gridding for the same ^{1}H data set is shown in figure 8.3. All three reconstruction methods produce good quality images. The Kaiser-Bessel profile (fig. 8.3.f) has 50% and 60% higher SNR than the Nearest Neighbour (fig. 8.3.b) and the Gauss profile (fig. 8.3.d) respectively. However, the Kaiser-Bessel profile seems to suffer from apodisation, despite the use of a deapodisation filter. Comparing 8.3.f with 8.3.b, the intensity profile gradually decreases at the edges.

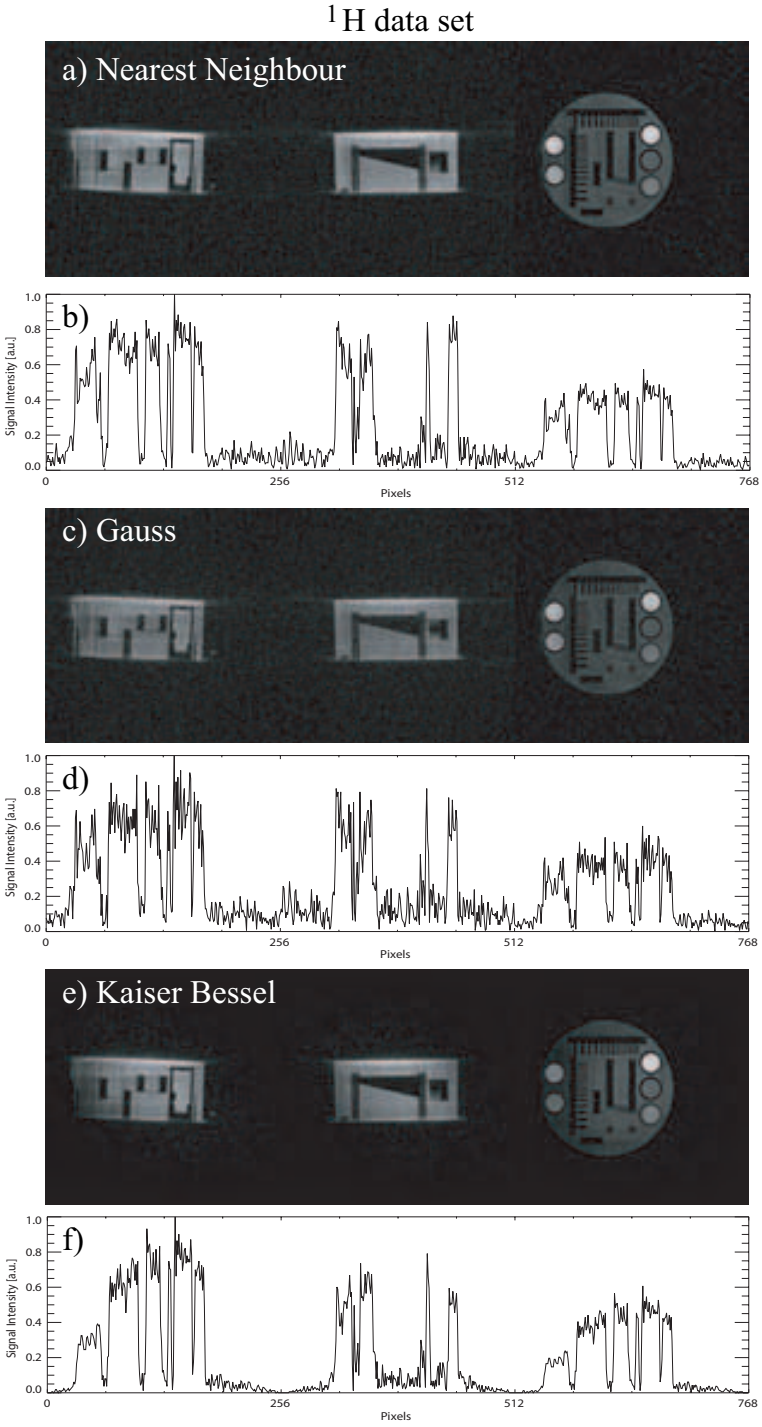

Figure 8.3: Comparison between images reconstructed with Nearest Neighbour interpolation (a), Gauss (c) and Kaiser-Bessel (e) gridding for a ^{1}H data set. Corresponding profiles of the central lines of the images are depicted in (b),(d)and (f).

Figure 8.4 shows a comparison between Nearest Neighbour interpolation (8.4.a and b) and Gauss (8.4.c and d) and Kaiser-Bessel (8.4.e and f) gridding for the same ^{23}Na data set. As in the previous case, all three reconstruction techniques provide similar image quality, with a noise level reduction of 25% and 50% in the reconstruction with Kaiser-Bessel windowing, compared to Nearest Neighbour and Gauss respectively.

For this reason, the remaining results of this chapter are all reconstructed with a Kaiser-Bessel function as convolution kernel.

8.2.2 Density Compensation

As mentioned in section 6.3, many filters have been proposed in the literature to compensate for non-uniform sampling of k-space. For a radial trajectory with both solid angle undersampling and inhomogeneous sampling along the projections, the most simple filter to implement is the rho filter, which analytically calculates the area (or volume) associated with each sample. Therefore, in this work, the rho filter was adapted for 2D and 3D radial techniques, and forced to an asymptotic value depending on the percentage of undersampling, as depicted in figure 8.5. The precompensation with these filters was compared to the postcompensation with the density matrix.

8.2.2.1 Comparison between Precompensation and Postcompensation

A comparison between two density compensated ^{1}H data sets; one that has been postcompensated with the density matrix and the another one that has been precompensated with the rho filter are shown in figures 8.6.a and 8.6.b respectively. The respective profiles in fig. 8.6.b and 8.6.d show that precompensation provides images with a better resolution and a more homogeneous intensity profile across the image.

8.2.2.2 Density Compensation of Undersampled Data

^{1}H data sets with solid angle undersampled data are shown in figures 8.7 and 8.8. The number of sampled points per projection is $N = 128$, so the Nyquist criterion requires a total number of projections of $N_{Proj} \sim 200000$. This data set is undersampled by a factor of 40 and contains only $N_{Proj} = 5000$. Figure 8.7.a displays a postcompensated data set. As can be seen from the profile in fig. 8.7.b, the image is blurred and its intensity profile is inhomogeneous. Figures 8.7.c, 8.7.e, 8.8.a and 8.8.c show precompensated data sets corresponding to the filters in Fig. 8.5, calculated from equations 6.24 and 6.25. However, after some point, they have been forced to an asymptotic value. The full rho filter is applied in figure 8.7.c. The images in figures 8.7.e, 8.8.a and 8.8.c were precompensated with filters that were tending to a constant value after 1/2, 1/4 and 1/8 of the total sampled points, as seen in figure 8.5.a. As can be observed, the SNR improved with less filtering, at the expose of a decreased resolution. That is to say that the point spread function (PSF) broadened.

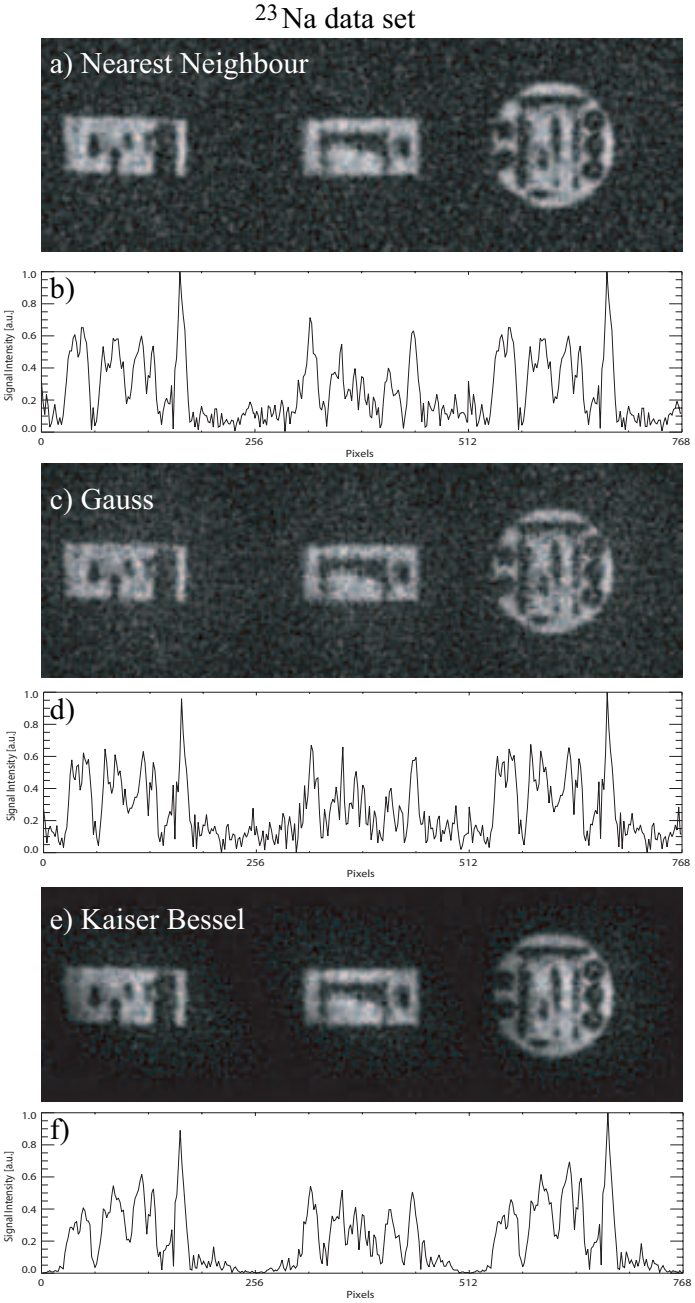

Figure 8.4: Comparison between images reconstructed with Nearest Neighbour interpolation (a), Gauss (c) and Kaiser-Bessel (e) gridding for a ^{23}Na data set. Corresponding profiles of the central lines of the images are depicted in (b),(d)and (f).

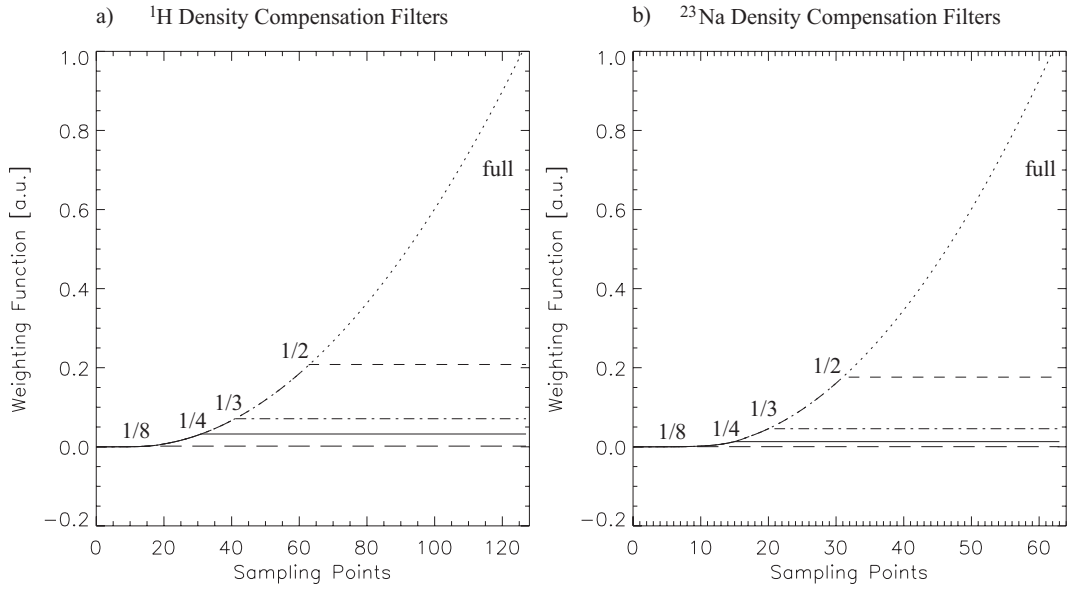

Figure 8.5: Density Compensation Filters. The dotted line corresponds to a full rho filter. The rest are forced to an asymptotic value after a certain percentage of the number of sampled points.

Figure 8.8.c shows an extreme case, where the outer k-space points are attenuated to such an extent over the k-space centre points, that only the coarse structures of the image are visualised, while the fine detail is completely lost. This image demonstrates that the choice of filter is a very important and sensitive parameter: enhancement of the higher frequencies reduces SNR, while outer k-space suppression produces blurring.

Figure 8.9 and 8.10 show ^{23}Na data sets of solid angle undersampled data. The number of sampled points per projection is $N = 64$, and the total number of projections should be $N_{Proj} \sim 50000$. This data set is undersampled by a factor of 4 and contains only $N_{Proj} = 5000$. Figure 8.9.a displays a postcompensated data set. Figures 8.9.c, 8.9.e, 8.10.a, 8.10.c and 8.10.e show images precompensated with filters that tend to a constant after 1/2, 1/3, 1/4 and 1/8 of the total number of sampled points. In figure 8.10.a an optimal compromise between SNR and resolution is found, with a rho filter that tends to a constant after 1/3 of the sampled data points.

For online image reconstruction at the standard image reconstruction environment of the MR scanner, a filter that tended to an asymptotic value after one half and one fourth of the sampled points was implemented for the reconstruction of ^{1}H and ^{23}Na data sets. These filters remain constant independent of the measurement protocol parameters. Consequently, the 3D radial data reconstructed online might suffer from blurring or from reduced SNR depending on the amount of angular undersampling.

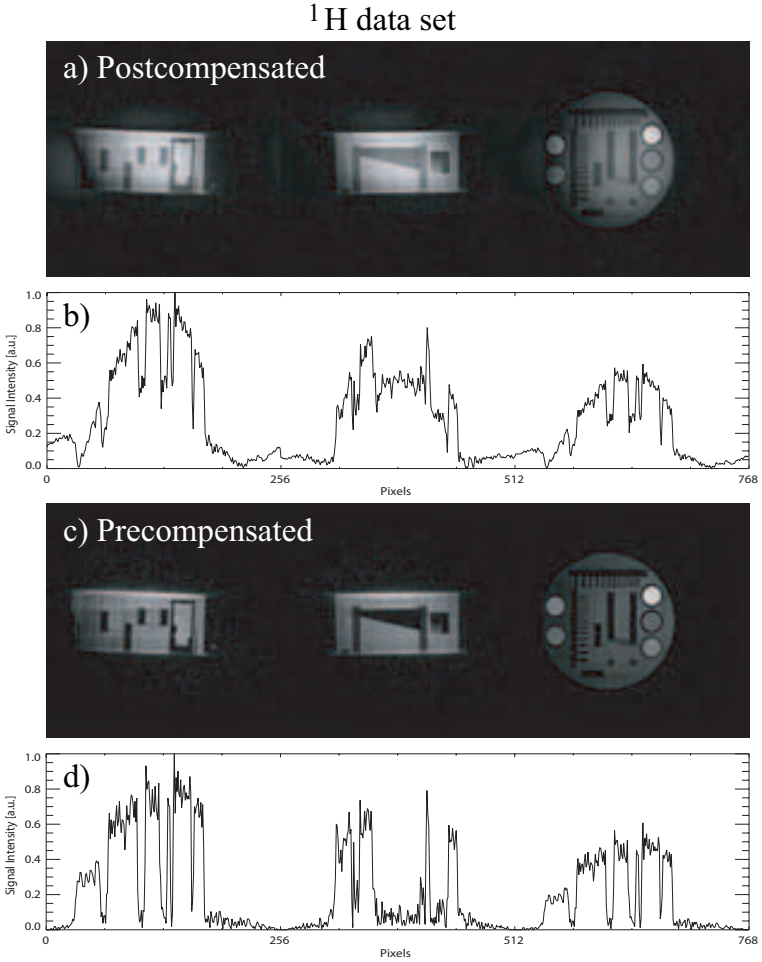

Figure 8.6: Density postcompensated (a,b) and precompensated (c,d) ^{1}H data set. Precompensation achieves better resolution and SNR.

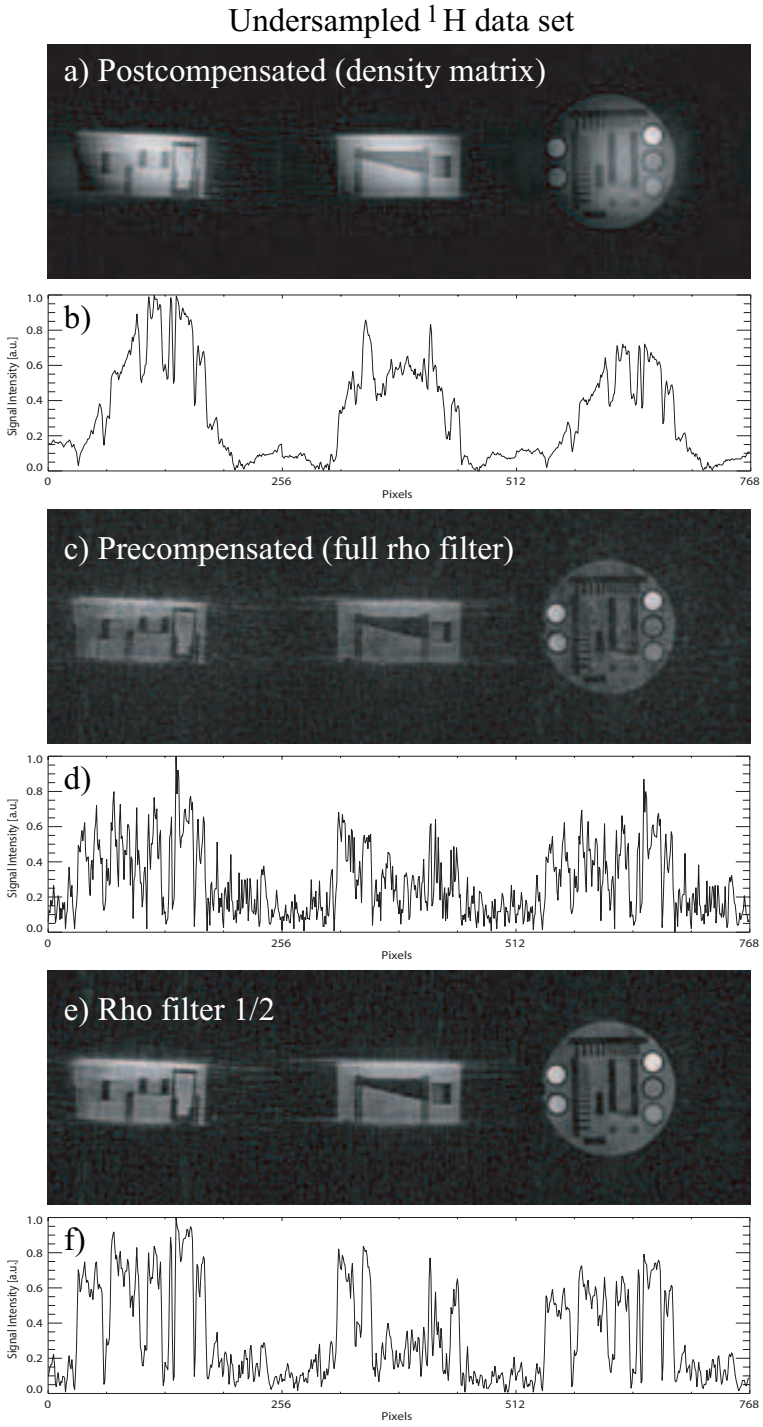

Figure 8.7: Density postcompensated (a) and precompensated [(c), (e)] undersampled ^{1}H data set. The data in image (c) have been filtered by a full rho filter, while the filter applied to image (e) tends to a constant value after a half of the sampled points.

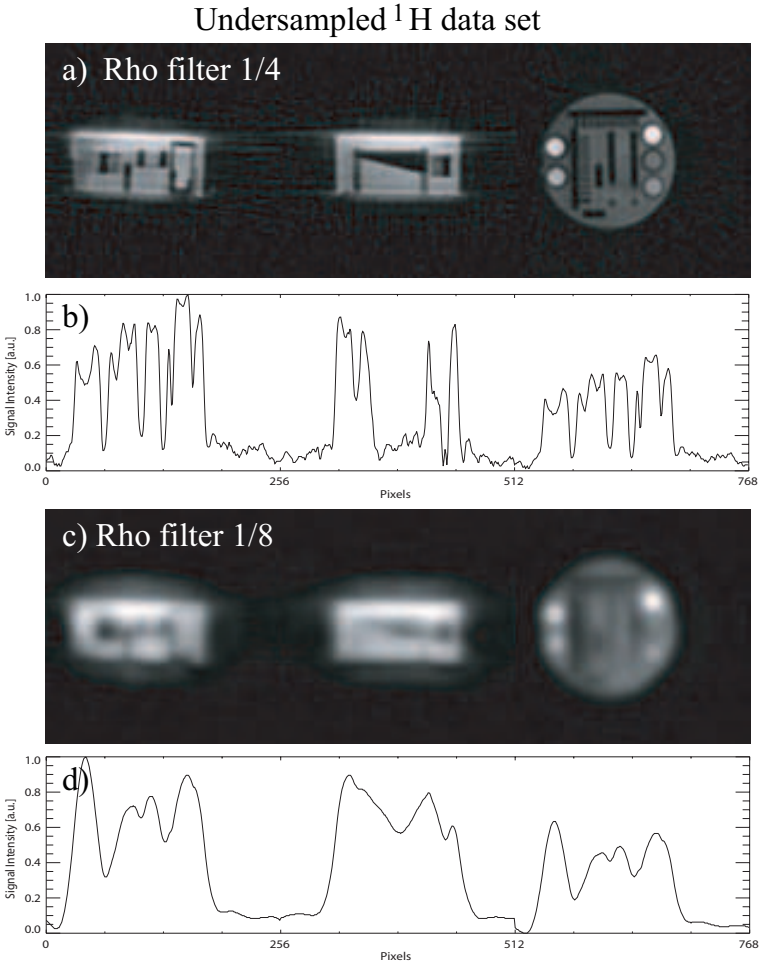

Figure 8.8: Density precompensated undersampled ^{1}H data set. The images have been filtered by a rho filter that tends to a constant value after one fourth (a) and one eighth (c) of the total sampled points. Figures (b) and (d) are the profiles of figures (a) and (c) respectively.

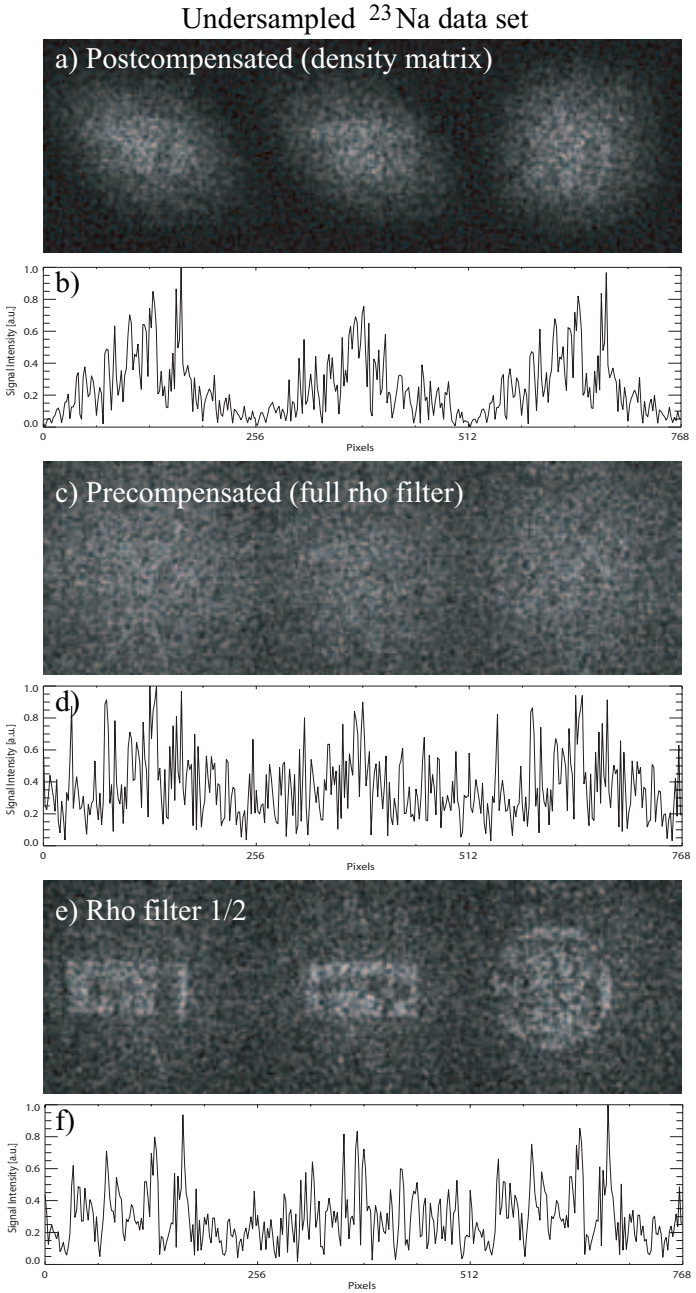

Figure 8.9: Density postcompensated (a) and precompensated [(c), (e)] undersampled ^{23}Na data set. The data in image (c) have been filtered by a full rho filter, while the filter applied to image (e) tends to a constant value after a half of the sampled points.

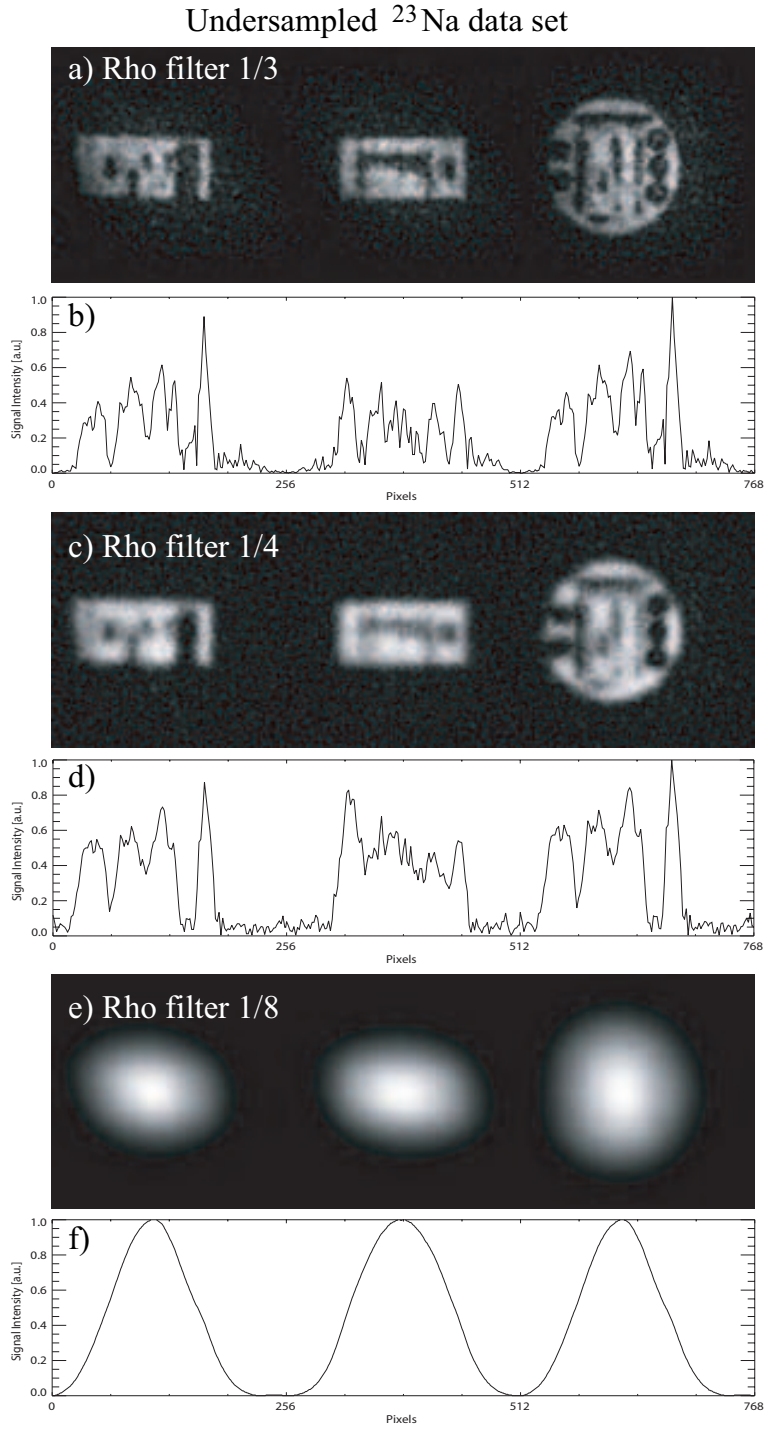

Figure 8.10: Density precompensated undersampled ^{23}Na data set. The images have been filtered by a rho filter that tends to a constant value after one third (a), one fourth (c) and one eighth (e) of the total sampled points. Figures (b),(d) and (f) are the profiles of figures (a), (c) and (e) respectively.

Chapter 9

3D Radial Measurements

9.1 Comparison of the cartesian and radial techniques

9.1.1 Phantom Experiments

The following experiments were performed with a resolution phantom containing 0.9% NaCl (physiological concentration). Figure 9.1 shows a comparison between ^{1}H and ^{23}Na images acquired with standard gradient echo sequences.

Figure 9.1.a shows a ^{1}H trueFISP image. In figure 9.1.b, an image acquired with a ^{23}Na 2D FLASH ($FOV = 320\,\text{mm}$, slice thickness $TH = 10\,\text{mm}$, $TR = 15\,\text{ms}$, $TE = 2.96\,\text{ms}$, $N_{acq} = 500$, $T_{acq} = 8\,\text{min}$, flip angle $\alpha = 55°$, matrix size $64 \times 64 +$ readout oversampling, $BW = 130\,\text{Hz/Px}$) can be observed. Figure 9.1.b shows one slice of a 3D data set acquired with a ^{23}Na 3D FLASH sequence ($FOV = 320\,\text{mm}$, 8 partitions, partition thickness 10 mm, 20% slice oversampling $TR = 15\,\text{ms}$, $TE = 2.89\,\text{ms}$, $N_{acq} = 80$, $T_{acq} = 10\,\text{min}\,14\,\text{s}$,

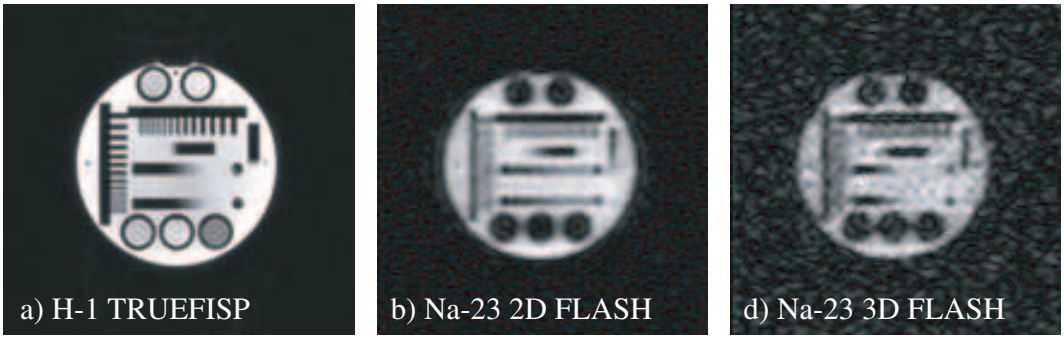

Figure 9.1: ^{1}H TrueFISP (a) ^{23}Na 2D FLASH (b,c) and ^{23}Na 3D FLASH images of a Resolution Phantom.

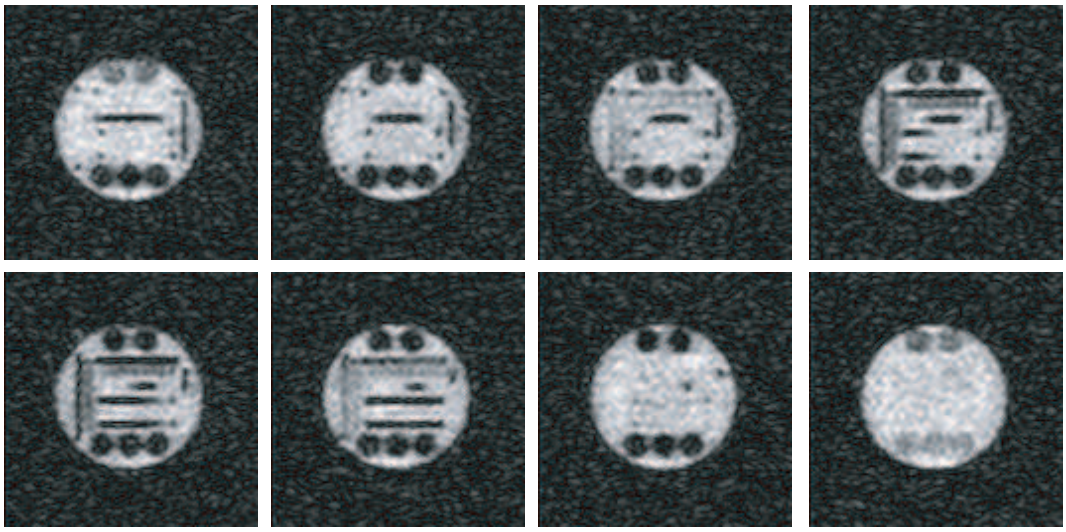

Figure 9.2: Eight slices of a 3D FLASH image of a Resolution Phantom.

flip angle $\alpha = 65°$, matrix size $64 \times 64 +$ readout oversampling, $BW = 130\,\mathrm{Hz/Px}$). The eight slices acquired with the 3D FLASH technique are shown in figure 9.2. The apparent better SNR of the 2D FLASH can be explained by the fact that the number of averages is much larger than that of the 3D FLASH ($\sqrt{N_{acq}(2DFL)/N_{acq}(3DFL)} = 2.5$ correction factor).

Figure 9.3 shows transversal, coronal and sagittal views of a 3D data set acquired with a ^{23}Na 3D radial sequence ($FOV = 320\,\mathrm{mm}$, $TR = 4\,\mathrm{ms}$, $TE = 0.2\,\mathrm{ms}$, $N_{acq} = 30$, $T_{acq} = 10\,\mathrm{min}$, 5000 projections, 64 sampling points/projection, $\alpha = 25$, $BW = 500\,\mathrm{Hz/Px}$). For comparison, transversal, coronal and sagittal views of a 3D data set acquired with a ^{1}H 3D radial sequence ($FOV = 320\,\mathrm{mm}$, $TR = 3.6\,\mathrm{ms}$, $TE = 0.07\,\mathrm{ms}$, 1 average, $T_{acq} = 2\,\mathrm{min}\,59\,\mathrm{s}$, 5000 projections, 128 sampling points/projection, $\alpha = 5°$, $BW = 530\,\mathrm{Hz/Px}$) are shown in figure 9.4. The ^{1}H data set has twice the resolution of the 2D ^{23}Na data set and ten times better SNR, at a threefold shorter acquisition time.

The SNR of the radial data set is 2.5 times better than that of the cartesian acquisition sequence. This is attributed to the shorter TE of the radial technique. Even though the nominal resolution of both sequences is identical, the FLASH sequence better resolved the structures in the phantom than the radial sequence, which suffers from blurring due to a suboptimal density compensation filter, as explained in section 8.2.2.2. Further improvement of the radial reconstruction method to minimise this effect will be necessary.

Figure 9.3: Transversal, coronal and sagittal views of a 3D data set acquired with a ^{23}Na 3D radial sequence ($FOV = 320$, $TR = 4ms$, $TE = 0.2ms$, $N_{acq} = 30$, $T_{acq} = 10min$, 5000 projections, 64 sampling points/projection, $\alpha = 25$, $BW = 500Hz/Px$).

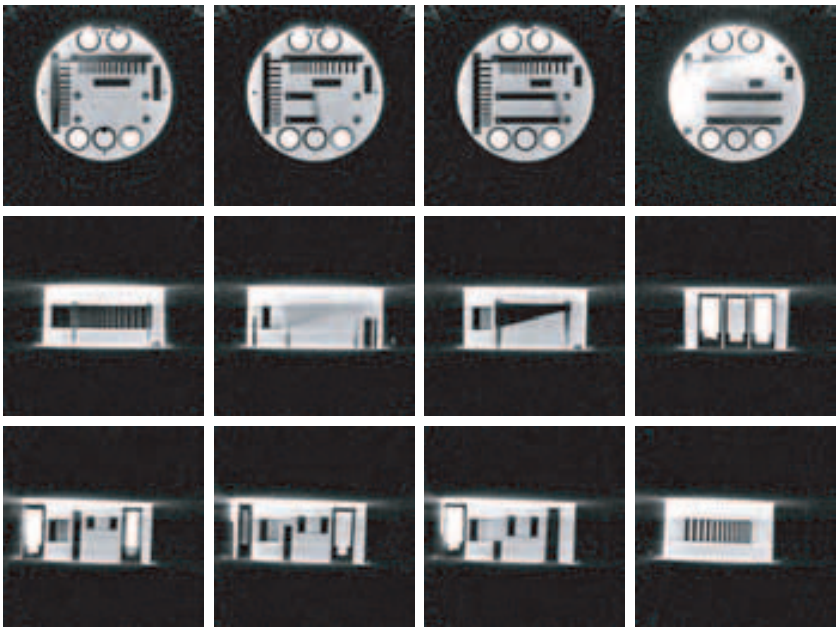

Figure 9.4: Transversal, coronal and sagittal views of a 3D data set acquired with a ^{1}H 3D radial sequence ($FOV = 320$, $TR = 3.6ms$, $TE = 0.07ms$, 1 average, $T_{acq} = 2min59s$, 5000 projections, 128 sampling points/projection, $\alpha = 5$, $BW = 530Hz/Px$).

9.1.2 *In vivo* Experiments - Head

A 3D radial and a 3D cartesian GRE sequence were used to image the head of a healthy volunteer. These experiments were carried out with the high-pass double resonant birdcage coil (Rapid Biomed GmbH).

Figure 9.5 shows the 3D FLASH images ($FOV = 500\,\text{mm}$, 20 partitions, partition thickness 10 mm, 10% slice oversampling $TR = 15\,\text{ms}$, $TE = 2.69\,\text{ms}$, $N_{acq} = 30$, $T_{acq} = 7\,\text{min}30\,\text{s}$, flip angle $\alpha = 45°$, matrix size 64×64+readout oversampling, $BW = 130\,\text{Hz/Px}$) of the head of a healthy volunteer. Even with a high readout bandwidth of $BW = 500\,\text{Hz/Px}$, the minimum echo time that could be achieved was $TE_{min} \sim 2\,\text{ms}$. Such a long TE would not allow for the detection of the fast T_2 component of the ^{23}Na signal. Thus, a low readout bandwidth was chosen to increase the final SNR of the image.

Figures 9.6 and 9.7 show respectively transversal, sagittal and coronal views of the ^{23}Na 3D data set acquired with the 3D radial technique ($FOV = 500\,\text{mm}$, $TR = 4\,\text{ms}$, $TE = 0.2\,\text{ms}$, $N_{acq} = 30$, $T_{acq} = 10\,\text{min}$, 5000 projections, 64 sampling points/projection, $\alpha = 25°$, $BW = 500\,\text{Hz/Px}$).

Regions of interest (ROI) were positioned in the vitreous humour of the eyes, cerebrospinal fluid (CSF) and brain tissue of the transversal images to compare their SNR. The results are summarised in table 9.1.

ROI	3D FLASH	3D RADIAL
Vitreous Humour	39.0	40.8
CSF	34.7	36.0
Brain Tissue	17.4	25.3

Table 9.1: SNR Comparison 3D FLASH and 3D radial images of the head of a healthy volunteer ($SNR = \frac{Signal_{ROI}}{Standard\,Deviation_{Bakground}}$).

The SNR of brain tissue is about 1.5 times larger in the radial images than in cartesian sampling. In CSF and the vitreous humour the difference is not so pronounced, which can be explained by the fact that thy are liquid media and ^{23}Na decays monoexponentially with a T_2 relaxation time larger than 1 ms.

Although the nominal resolution of the radial images is higher than the FLASH images, they are clearly more blurred, which prevents distinguishing some of the structures of the brain. There are two possible reasons for the obvious discrepancy between nominal and observed spatial resolution. First, the sampling density compensation filter is suboptimal, creating blurring in the image. Secondly, due to the short ^{23}Na T_2, signal decay occurs during data sampling. This leads to a broadening of the point spread function (PSF). This blurring effect affects only radial sampling. In cartesian sampling, the short component has died out before data acquisition, and the signal decay due to the long component during data sampling is neglectful. Thus, cartesian sampling does not suffer from blurring

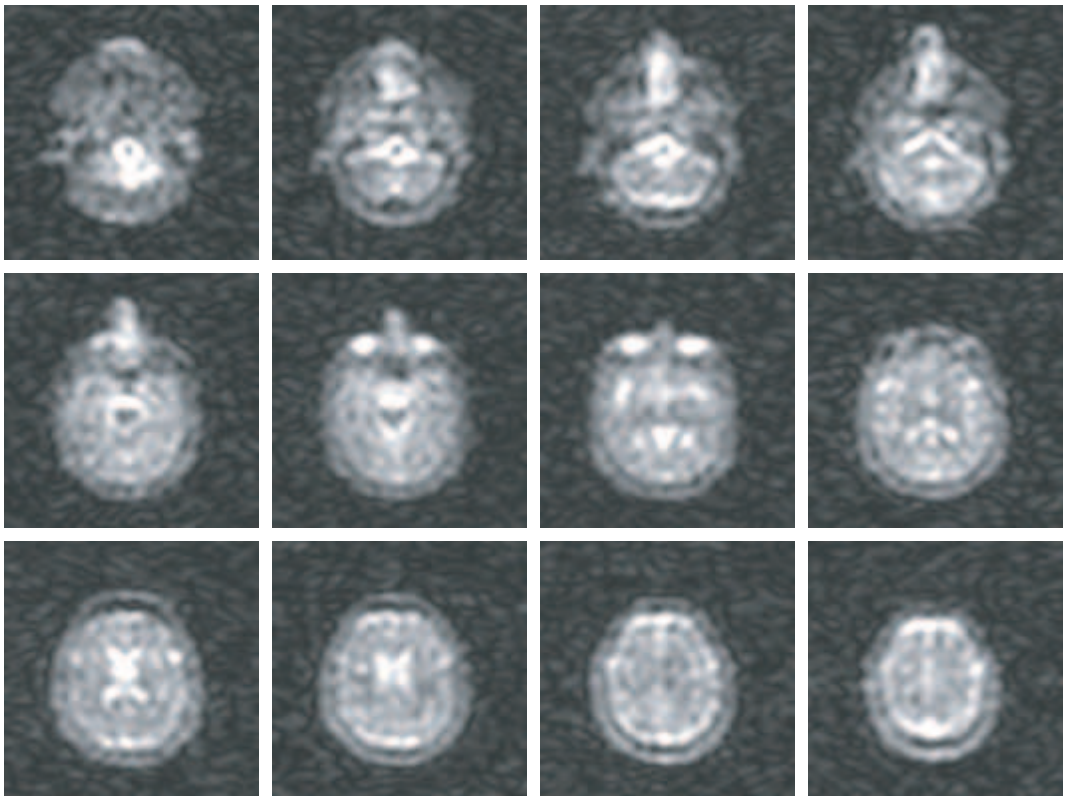

Figure 9.5: 75% zoomed 20 ^{23}Na transversal slices of the head of a healthy volunteer measured with a 3D FLASH ($TR = 15\,\text{ms}, TE = 2.69\,\text{ms}, FOV = 500\,\text{mm}, 64 \times 64$ + oversampling, partition thickness10 mm, $BW = 130\,\text{Hz/pixel}, N_{acq} = 30, T_{acq} = 10\text{min}$).

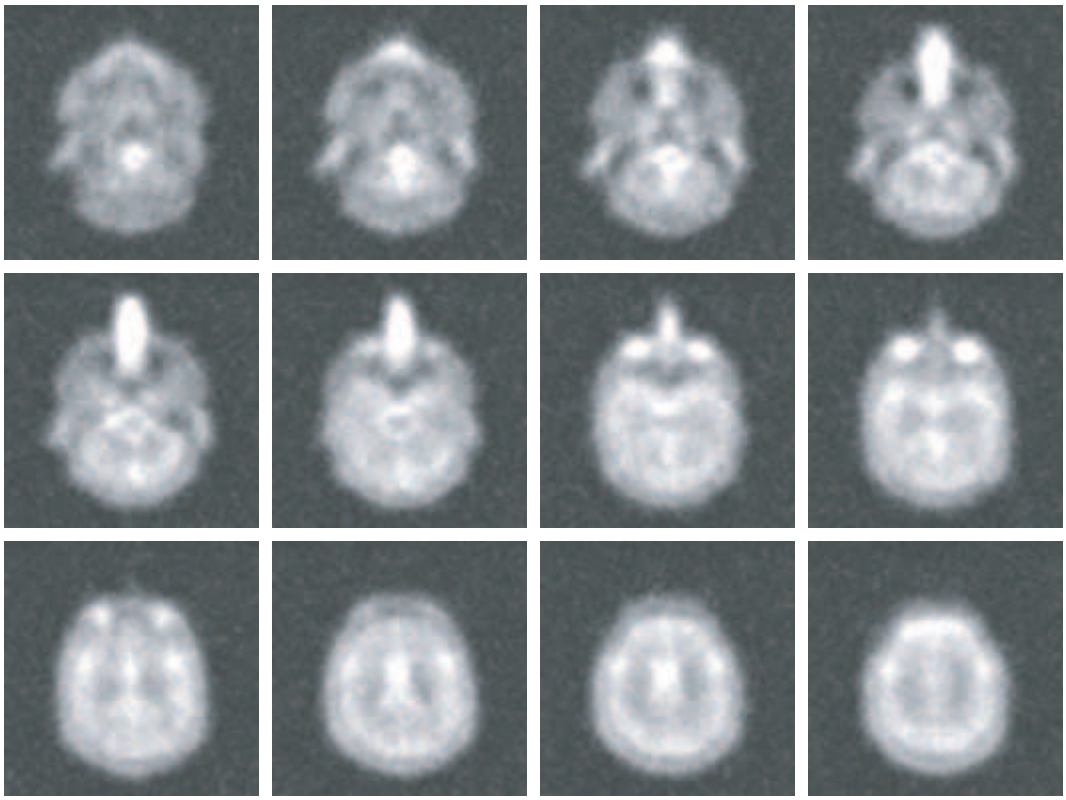

Figure 9.6: 75% zoomed 20 transversal views of the head of a healthy volunteer measured with a 3D radial technique ($FOV = 500\,\text{mm}$, $TR = 4\,\text{ms}$, $TE = 0.2\,\text{ms}$, $N_{acq} = 30$, $T_{acq} = 10\,\text{min}$, 5000 projections, 64 sampling points/projection, $\alpha = 25°$, $BW = 500\,\text{Hz/Px}$).

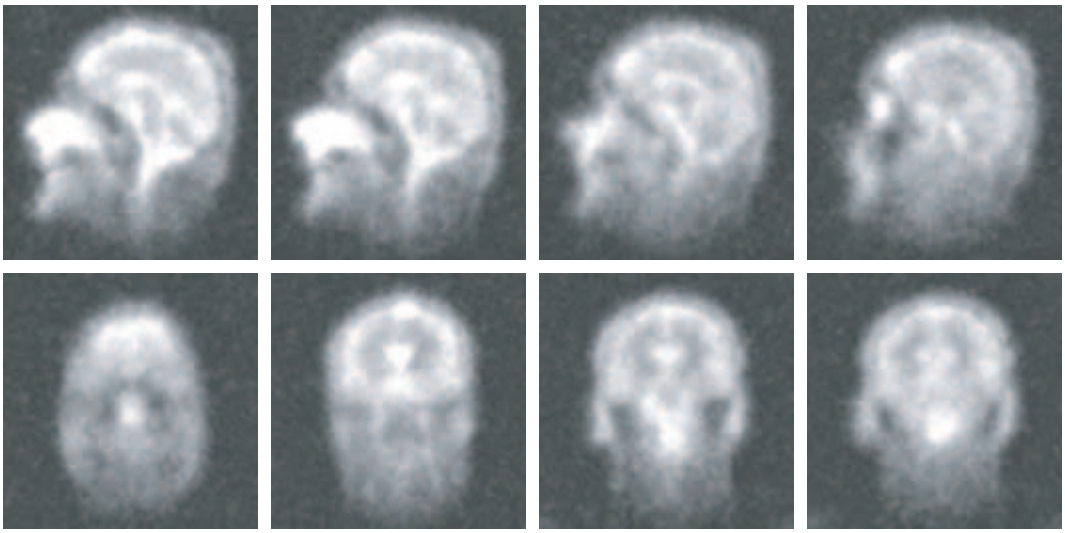

Figure 9.7: 75% zoomed coronal and sagittal views of the head of a healthy volunteer measured with a 3D radial technique ($FOV = 500\,\text{mm}$, $TR = 4\,\text{ms}$, $TE = 0.2\,\text{ms}$, $N_{acq} = 30$, $T_{acq} = 10\,\text{min}$, 5000 projections, 64 sampling points/projection, $\alpha = 25°$, $BW = 500\,\text{Hz/Px}$).

at the expense of not acquiring the total ^{23}Na signal.

A simulation was made, which is illustrated in figure 9.8, where the full width at half maximum (FWHM) of the 1D point spread function after image reconstruction is plotted as a function of the ratio between readout time T_S and a tissue $T_2 = 500\,\mu\text{s}$. With the experimental readout time of $T_S = 1/BW = 2000\,\mu\text{s}$, a twofold increase in the FWHM is expected.

This result matches with the theoretical approximation of the FWHM of the PSF for a gradient echo sequence, which gives an estimate of the spatial extent of the blur caused by the T_2 decay [Haacke 99]:

$$FWHM_{T_2^*} = \frac{\sqrt{3}}{\pi}\left(\frac{T_S}{T_2^*}\right)\Delta x \tag{9.1}$$

which, for $T_S = 2000\,\mu\text{s}$ and $T_2 = 500\,\mu\text{s}$ results in $FWHM_{T_2^*} = 2.2\,\Delta x$.

In order to minimise this blurring effect, two solutions are available. First, the readout bandwidth could be increased. Due to hardware problems, the readout bandwidth $BW = 500\,\text{Hz/Px}$ can, however, not be increased significantly. Secondly, it is possible to apply a correction filter on the radial data during image reconstruction which would compensate the T_2 decay. This, however, would imply that the biexponential T_2 decay times in vivo were accurately known, which is not the case. An about twofold decrease of spatial resolution is therefore to be expected in radial ^{23}Na data sets with short TE.

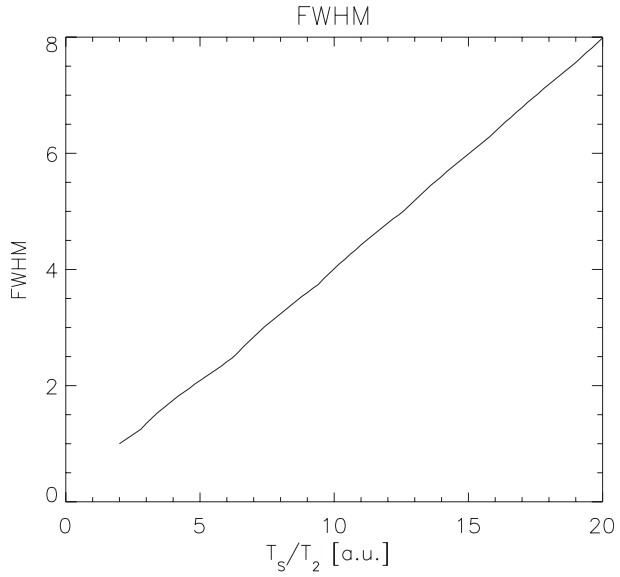

Figure 9.8: The full width at half maximum (FWHM) of the point spread function after image reconstruction is plotted as a function of the ratio between readout time T_S and a tissue $T_2 = 500\,\mu$s. With the experimental readout time $T_S = 1/BW = 2000\,\mu$s, a twofold increase in the FWHM is expected.

It is important to consider, however, which information can be assessed by ^{23}Na MRI. High resolution MRI ($\Delta x < 1\,$mm) is currently the domain of ^{1}H methods. From ^{23}Na methods sensitive information about tissue vitality is expected. As the radial method allows for the acquisition of the whole ^{23}Na signal, it is more sensitive to changes in ^{23}Na concentration and, therefore, of more interest from the diagnostic point of view. Its lower resolution compared to cartesian methods is a drawback that must be put up with in exchange for the higher sensitivity. and delivers functional information, which often can be of low spatial resolution without compromising its use in clinical environments.

9.1.3 *In vivo* Experiments - Heart

9.1.3.1 Comparison between ECG-gated 2D Radial Projection and Gradient Echo Techniques

The temporal resolution of the 3D radial techniques is limited by the amount of projections that need to be acquired. Conventional gradient echo (GRE) techniques, on the other hand, allow for time resolved imaging of the heart, but their longer TE prevents the accurate quantification of the total sodium content. In this work, a segmented ECG-gated 2D radial projection technique with a minimum $TE = 0.6\,$ms that allows for time resolved ^{23}Na imaging of the heart was implemented and compared to a standard segmented ECG-gated GRE technique with a minimum $TE = 3\,$ms.

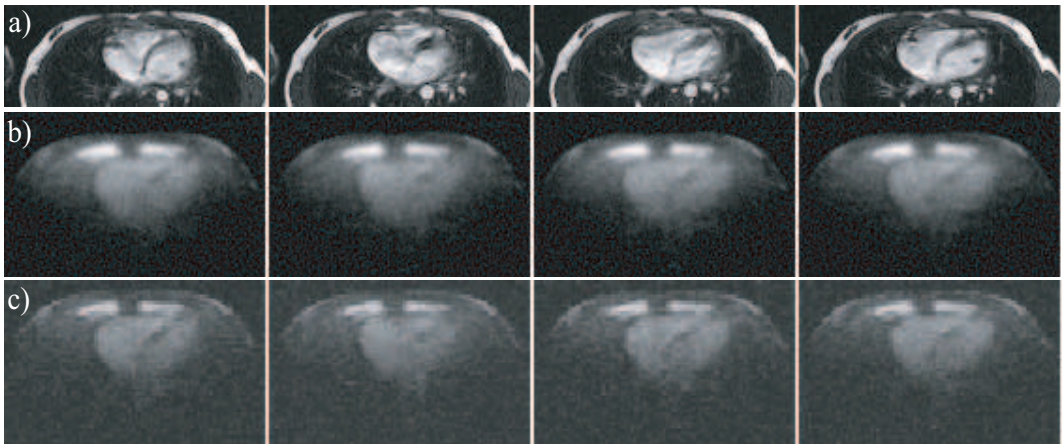

Figure 9.9: Transverse MRI images of the heart of a healthy volunteer. Time series of ^{23}Na radial (a) and cartesian (b) gradient echo images. The images show four heart phases. Right and left ventricle are visualised together with the myocardium. The SNR in the ventricle is 1.6 times larger in the radial technique compared to the cartesian technique.

Before acquisition of the ^{23}Na images, an ECG-triggered ^{1}H True-Fisp sequence was used for slice positioning and anatomical localisation of the ^{23}Na images (figure 9.9.a). For both ^{23}Na ECG-triggered techniques, an acquisition window of 1000s was used to obtain 4 different cardiac phases. The resolution of the cartesian data set was $30 \times 4 \times 4\,\mathrm{mm}^3$, while for the 2D radial data set the final nominal resolution after reconstruction was $30 \times 2 \times 2\,\mathrm{mm}^3$. With a $BW = 190\,\mathrm{Hz/Px}$, $TR = 8\,\mathrm{ms}$ and $N_{acq} = 200$, the total scan time was $T_{acq} = 15\,\mathrm{min}$.

Figure 9.9 shows a comparison between the cartesian and the radial ^{23}Na images corresponding to 4 different cardiac phases, together with the reference ^{1}H images. Right and left ventricles are visualised together with the myocardium. In both data sets it is possible to observe the contraction of the ventricles. The SNR in the ventricle is 10 for the cartesian sequence and 16 for the radial acquisition. The radial images suffer from blurring, as explained in section 9.1.2. Compared to the 3D radial technique, the 2D radial acquisition allows for time resolved ^{23}Na imaging of the heart in clinically acceptable measurement times ($T_{acq} = 15\,\mathrm{min}$). On the other hand, the TE of the 2D radial sequence is longer than that of the 3D radial, but sufficiently short to allow for the measurement of the total sodium signal and, potentially, the quantification of the total sodium content in tissue.

9.1.3.2 3D Radial

The 3D radial acquisition was performed without ECG-triggering because, although the sequence has been implemented to perform cardiac triggering, the total acquisition time of approximately a 15 min to acquire a 3D ^{23}Na data set of the heart, the breathing motion creates more blurring than the cardiac movement. Respiration triggering was not used in

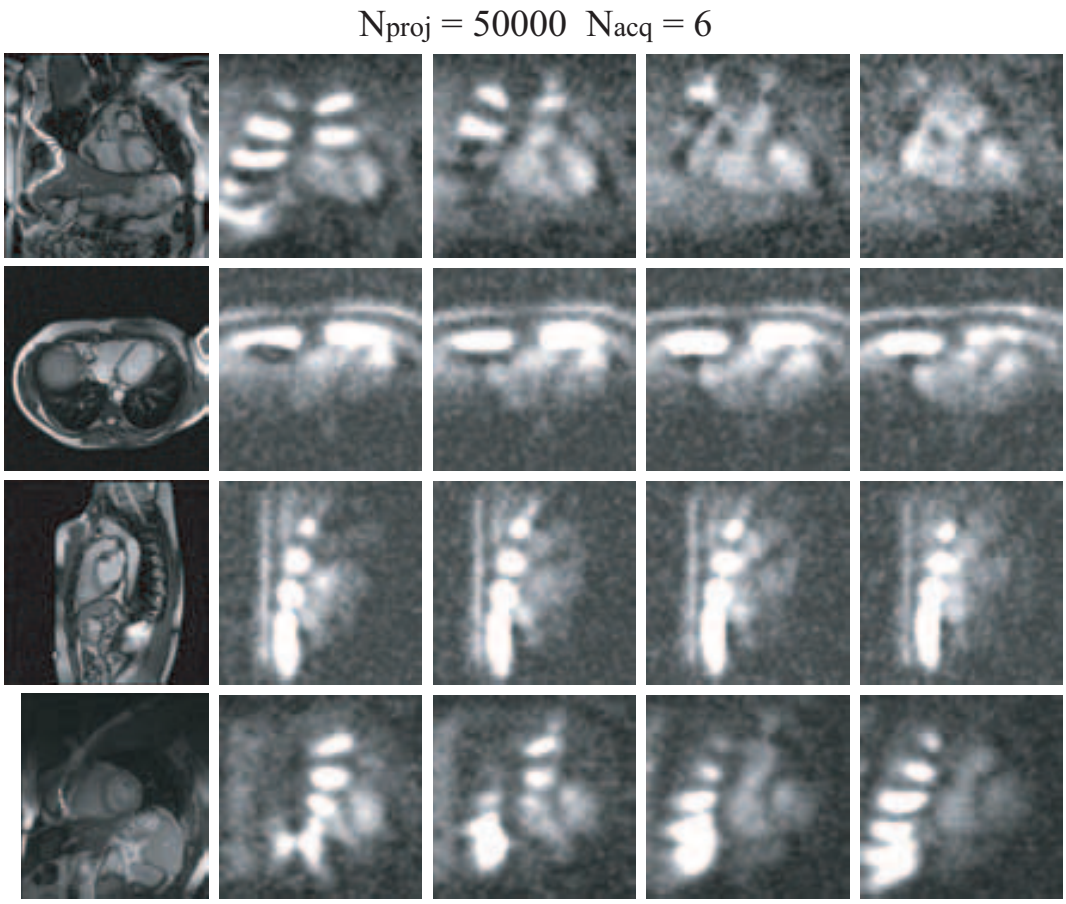

Figure 9.10: Coronal, transversal sagittal and two-chamber views of a fully sampled ^{23}Na 3D data set acquired with a 3D radial sequence ($FOV = 500\,\text{mm}$, $TR = 3.2\,\text{ms}$, $TE = 0.2\,\text{ms}$, $N_{acq} = 6$, $T_{acq} = 16\,\text{min}$, 50000 projections, 64 sampling points/projection, $\alpha = 51°$, $BW = 500\,\text{Hz/Px}$).

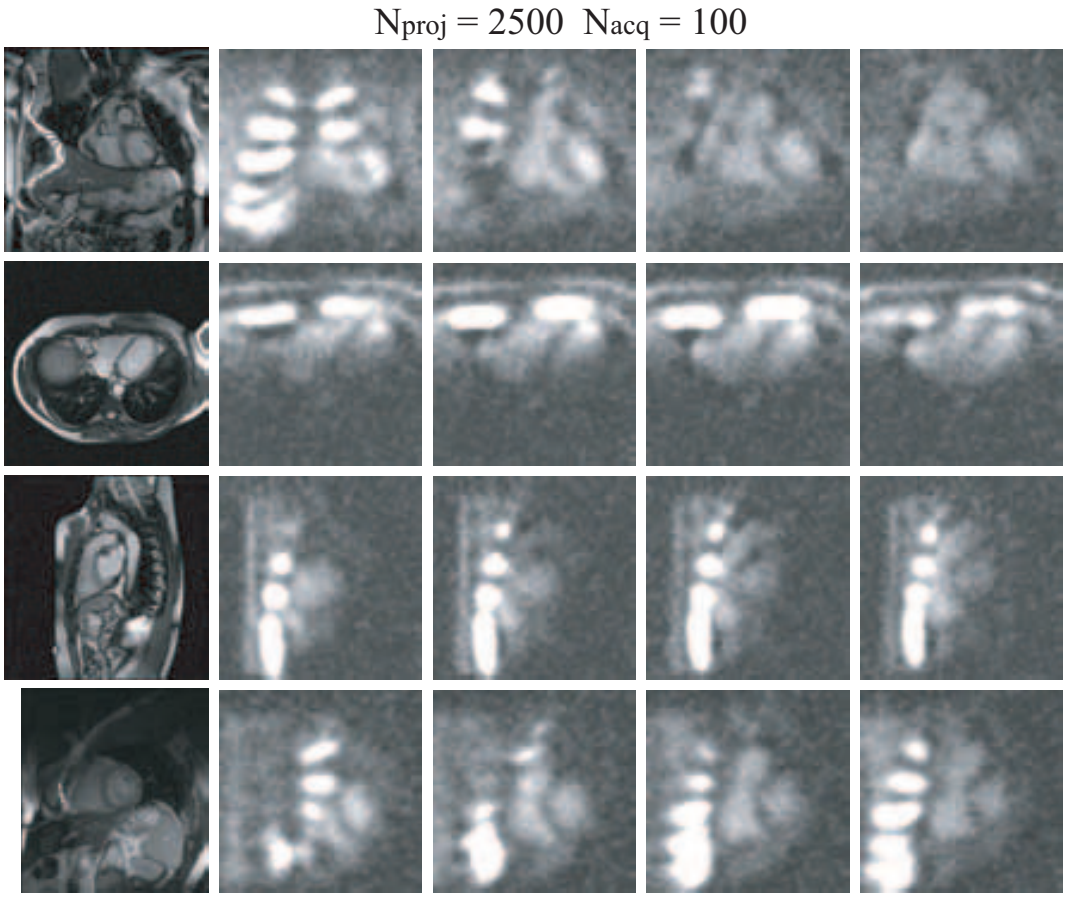

Figure 9.11: Coronal, transversal sagittal and two-chamber views of a ^{23}Na 3D data set acquired with a 3D radial sequence ($FOV = 500\,\text{mm}$, $TR = 3.6\,\text{ms}$, $TE = 0.2\,\text{ms}$, $N_{acq} = 100$, $T_{acq} = 15\,\text{min}$, 2500 projections, 64 sampling points/projection, $\alpha = 51°$, $BW = 500\,\text{Hz/Px}$).

order not to extend the total measurement time.

Figure 9.10 shows coronal, transversal, sagittal and two-chamber views of a fully sampled ^{23}Na 3D data set acquired with the 3D radial sequence ($FOV = 500\,\text{mm}$, $TR = 3.2\,\text{ms}$, $TE = 0.2\,\text{ms}$, $N_{acq} = 6$, $T_{acq} = 16\,\text{min}$, 50000 projections, 64 sampling points/projection, $\alpha = 51°$, $BW = 500\,\text{Hz/Px}$).On the other hand, figure 9.10 shows coronal, transversal, sagittal and two-chamber views of an undersampled but averaged ^{23}Na 3D data set acquired with a 3D radial sequence ($FOV = 500\,\text{mm}$, $TR = 3.6\,\text{ms}$, $TE = 0.2\text{ms}$, $N_{acq} = 100$, $T_{acq} = 15\,\text{min}$, 2500 projections, 64 sampling points/projection, $\alpha = 51°$, $BW = 500\,\text{Hz/Px}$).

The ^{23}Na images suffer from the small surface coil penetration depth and the posterior parts of the heart are almost not visible. The cartilage of the ribs gives a strong ^{23}Na signal, which partially obscures the visualisation of the heart. Comparison between the two data sets brings about the problem of resolution and SNR. The first data set was acquired with no solid angle undersampling and very small number of averages ($N_{acq} = 6$), while the second data set was acquired with twentyfold undersampling and $N_{acq} = 100$. As both data sets have been reconstructed online with the same density compensation filter, the second data set is clearly more blurred than the first, while it provides a better SNR. In order to achieve the best possible image quality, a compromise between resolution and SNR has to be made, and an optimisation of the filter is necessary for each imaging protocol.

9.2 Comparison of ^{23}Na MRI at 4 T and 1.5 T

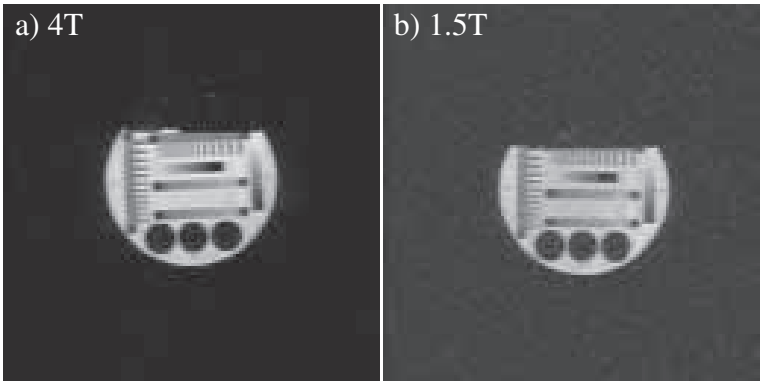

Figure 9.12: ^{23}Na 2D FLASH images at 4 T(a) and 1.5 T(g) of a resolution phantom ($TR = 30\,\text{ms}, TE = 2.31\,\text{ms}, FOV = 400\,\text{mm}, 128128$, slice thickness 20 mm, $BW = 190\,\text{Hz/pixel}, N_{acq} = 64, Tacq = 4\,\text{min}$).

As mentioned before, compared to ^{1}H, ^{23}Na NMR sensitivity is low due to the lower spin density, smaller gyromagnetic ratio and shorter T_2. This leads to reduced SNR and, thus, to low spatial resolution images and long acquisition times due to signal averaging. As the NMR sensitivity is directly proportional to the magnetic field strength B_0, higher B_0

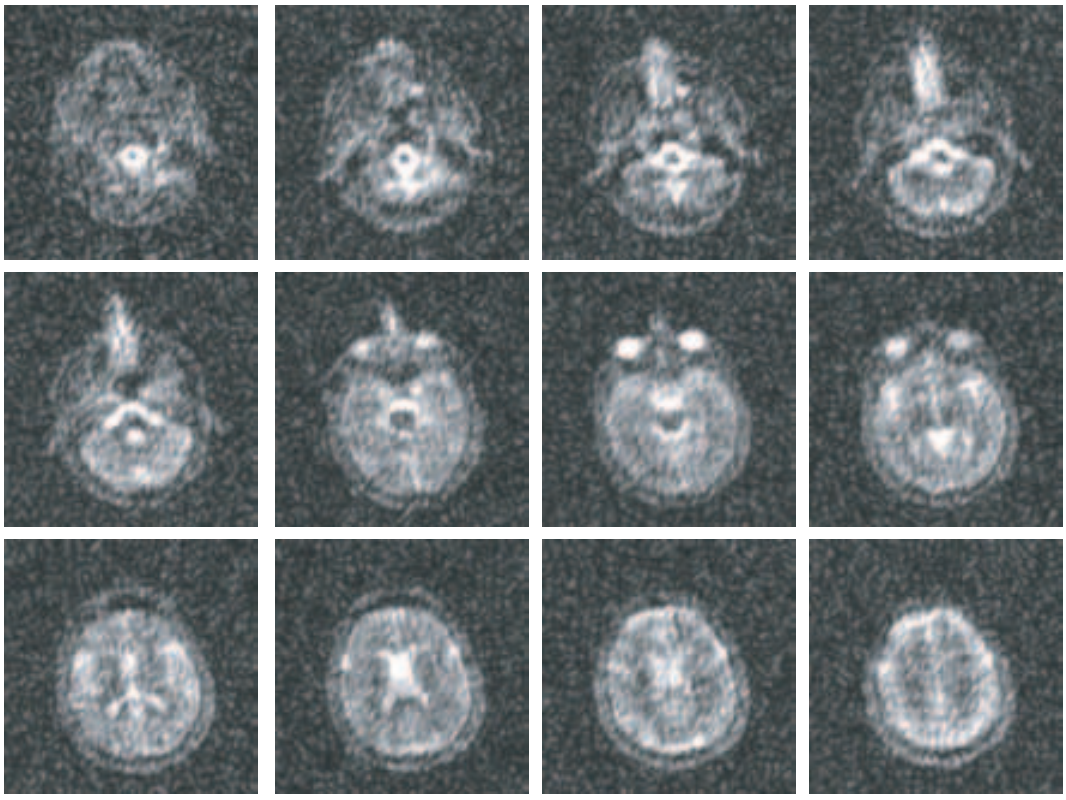

Figure 9.13: *In-vivo* Zoomed 3D cartesian GRE images ($TR = 30\,\text{ms}, TE = 2.25\,\text{ms}, FOV = 400\,\text{mm}, 128 \times 128$ interpolated to 256×256, partition thickness : 10 mm, $BW = 190\,\text{Hz/pixel}, N_{acq} = 48, Tacq = 33\,\text{min}$) at 1.5 T.

may allow ^{23}Na MRI to become a relevant clinical application. ^{23}Na NMR images were acquired at 1.5 T and 4 T using a gradient-echo and a radial technique to compare their performance in terms of SNR and resolution.

Phantom and volunteer experiments were carried out on a Bruker/Siemens MedSpec 4 T system (Bruker Biospin MRI GmbH, Germany) equipped with Siemens Sonata Gradients (40 mT/m, 200 T/(m · s) and a double-resonant (44.5/168.2 MHz) TEM volume head coil (MR Instruments Inc.) [Vaughan 94] as well as in the 1.5 T Symphony (Siemens AG Medical Solutions, Germany) equipped with Siemens Quantum Gradients (30 mT/m, 100 T/(m · s)) and the home-built single-resonant (16.84 MHz) birdcage coil. Both systems are based on the same clinical user interface (*syngo*) using identical software for image acquisition. Images were acquired with a standard 3D cartesian GRE sequence ($TR = 30\,\text{ms}$, $TE = 2.25\,\text{ms}$, $FOV = 400\,\text{mm}$, matrix 128×128, partition thickness 10 mm, $BW = 190\,\text{Hz/pixel}$, $N_{acq} = 48$, $T_{acq} = 33\,\text{min}$) and the 3D radial GRE sequence ($TR = 30\,\text{ms}$, $TE = 0.4\,\text{ms}$, $FOV = 400\,\text{mm}$, $BW = 190\,\text{Hz/pixel}$, 2500 projections × 128samples per projection, $N_{acq} = 10$, $T_{acq} = 12\,\text{min}$). An offline reconstruction regridded the data with Gauss interpolation onto a Cartesian grid followed by a conventional 3D

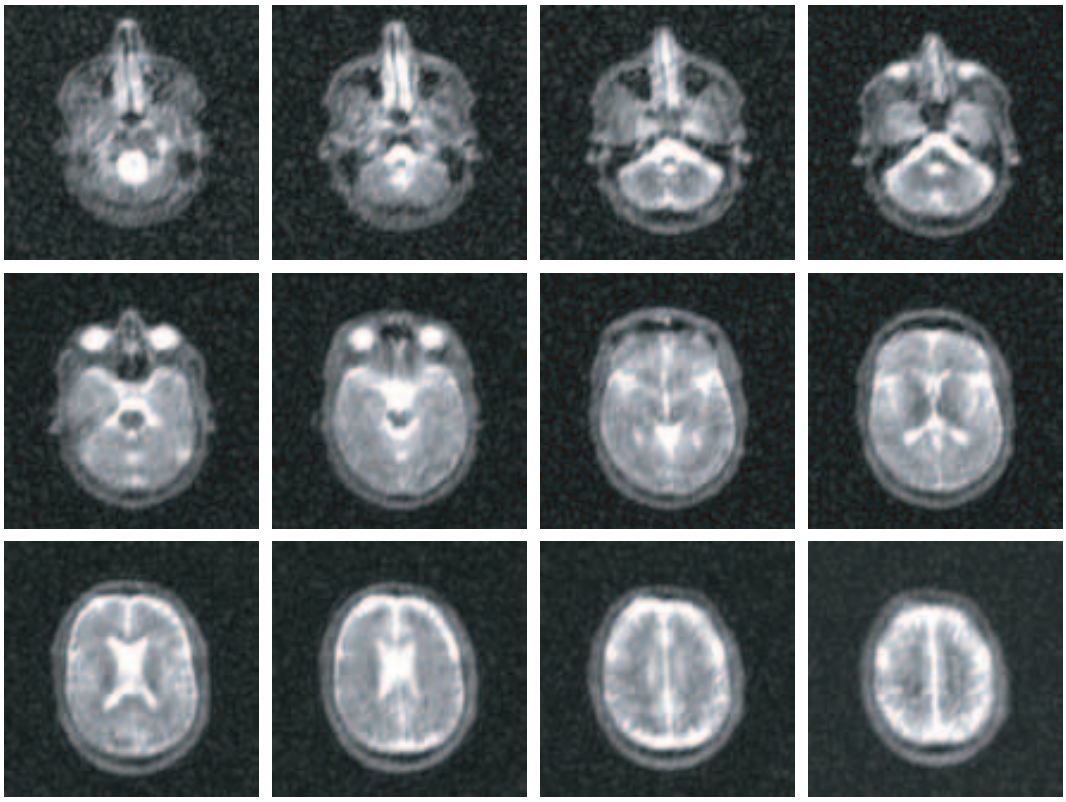

Figure 9.14: *In-vivo* Zoomed 3D cartesian GRE images ($TR = 30\,\text{ms}, TE = 2.25\,\text{ms}, FOV = 400\,\text{mm}, 128 \times 128\,\text{interpolatedto}\,256 \times 256, \text{partitionthickness} : 10\,\text{mm}, BW = 190\,\text{Hz/pixel}, N_{acq} = 48, Tacq = 33\,\text{min}$) at 4 T.

FFT.

ROI	4T	4T	1.5T	1.5T
Eyes	101	61.6	22	25
CSF	102	60	20	25
Brain Tissue	25	38	6.3	14

Table 9.2: $SNR = \frac{Signal_{ROI}}{Standard\,Deviation_{Bakground}}$.

^{23}Na 2D cartesian GRE images of a resolution phantom are shown in figure 9.12. The ratio $SNR_{4\text{T}}/SNR_{1.5\text{T}}$ is 2.7. Figures 9.13 and 9.14 show 20 slices of the 3D cartesian GRE *in-vivo* data set. Table 9.2 shows the SNR values calculated from the cartesian GRE and radial images. Comparing the *in-vivo* 3D cartesian GRE data, $SNR_{4\text{T}}/SNR_{1.5\text{T}}$ is around 4.0. In order to compare the SNR of both imaging techniques, the SNR of the radial data must be corrected by a factor 2.19 reflecting the different number of signal

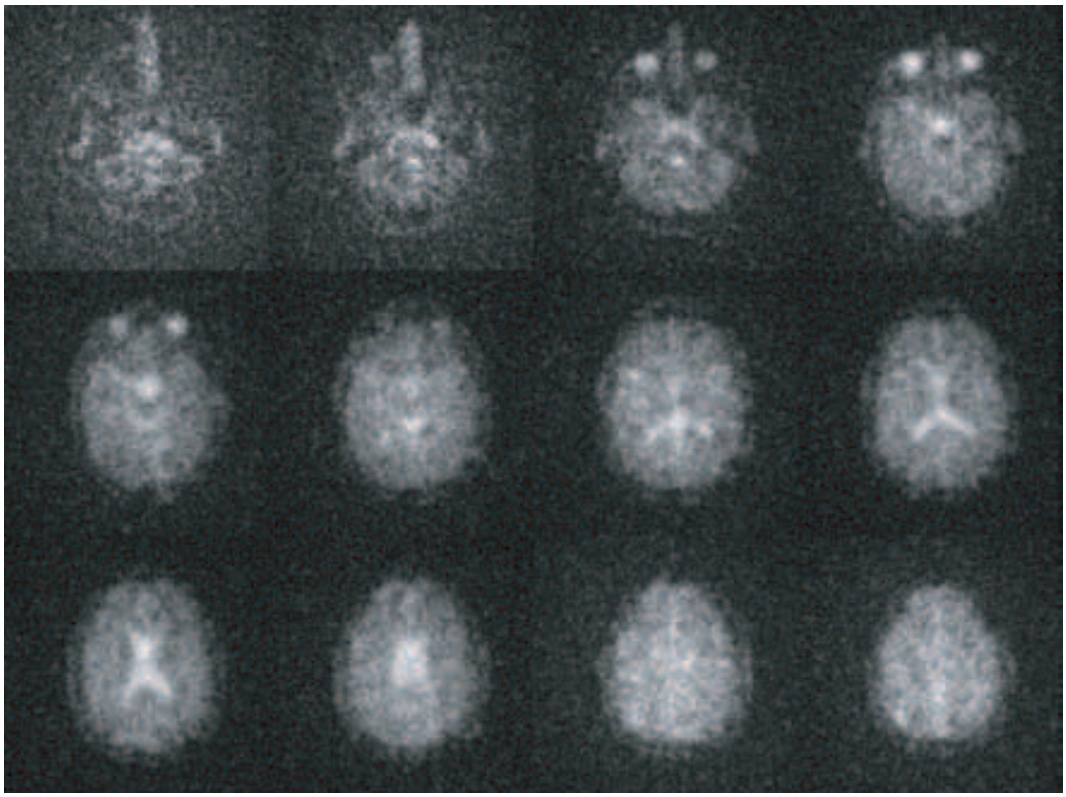

Figure 9.15: Transversal slice of ^{23}Na 3D data set of a healthy volunteer acquired with a 3D radial sequence ($TR = 30\,\text{ms}$, $TE = 0.4\,\text{ms}$, $FOV = 400\,\text{mm}$, $BW = 190\,\text{Hz/pixel}$, 2500 projections $\times$ 128samples per projection, $N_{acq} = 10$, $T_{acq} = 12\,\text{min}$) at 1.5 T.

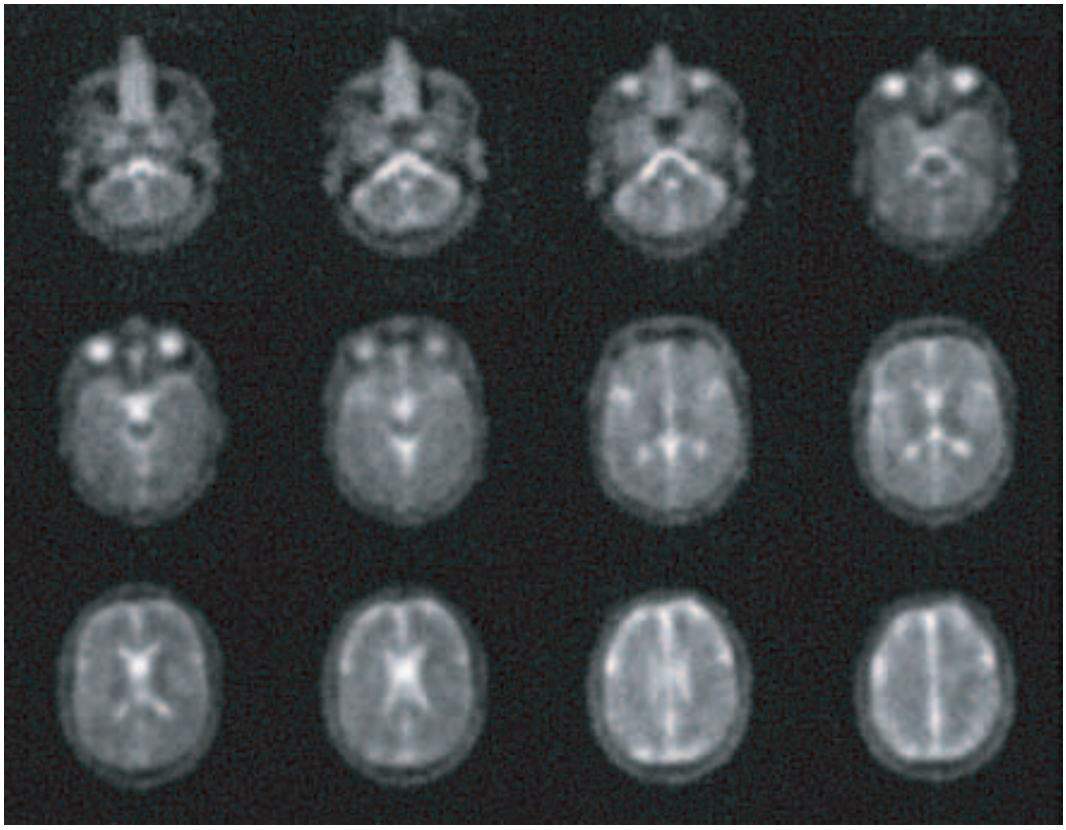

Figure 9.16: Transversal slice of ^{23}Na 3D data set of a healthy volunteer acquired with a 3D radial sequence ($TR = 30\,\text{ms}$, $TE = 0.4\,\text{ms}$, $FOV = 400\,\text{mm}$, $BW = 190\,\text{Hz/pixel}$, 2500 projections $\times$ 128samples per projection, $N_{acq} = 10$, $T_{acq} = 12\,\text{min}$) at 4 T.

averages. This correction results in a ratio SNR_{RADIAL}/SNR_{CAR} of 2.5 at 1.5 T and 1.3 at 4 T.

While SNR increased with increasing B_0 as seen in the phantom data consistent with the theoretical value of $4/1.5 = 2.7$, the improvement observed in the *in-vivo* data of a factor of 4 is superior to that. This indicates that the performance of the 16.84 MHz birdcage coil is very sensitive to loading. The higher SNR achieved by the 3D Radial technique can be explained by its shorter TE. As already mentioned, due to the ^{23}Na signal bi-exponential T_2 decay ($T_{2\,fast} \sim 1$ ms, $T_{2\,slow} \sim 15$ ms at 1.5 T) sequences with short TE are required. T_2 shortening with increasing B_0 might make it impossible at high B_0 to measure the short T_2 component. However, SNR evaluation shows that at 4 T the radial technique still performs better than the cartesian GRE, indicating that the T_2 decrease does not impair the diagnostic usefulness of the method at 4 T. Due to the very low SNR at 1.5 T, it is not possible to evaluate reliably the SNR improvement between both techniques.

Although radial images suffer inherently of blurring, these radial images are especially blurred mainly as a consequence of the non-optimised protocol parameters. The reason for this is that this measurements took place at an early stage of this thesis, when the completion of the optimisation of the radial protocol had not yet taken place. The readout bandwidth was very low and the TR quite long. The $BW = 190$ Hz/pixel, implies a readout time $T_S \sim 5000\,\mu$s, which leads to a FWHM of the PSF of $FWHM = 5.5\,\Delta x$ as calculated from equation 9.1. As can be seen in section 9, images taken on the Symphony scanner in later stages of this thesis have a higher quality due to optimised protocol parameters. To be consequent with the field strength comparison, however, the radial images for the 4 T and 1.5 T experiments have the same measurement parameters.

In conclusion, it has been shown that ^{23}Na MRI benefits from higher B_0, achieving images of high SNR at acceptable measurement times.

9.3 Relaxation Time Measurements

9.3.1 Phantom Experiments

To assess if the radial method can measure the ^{23}Na relaxation times an experiment with four phantoms containing 0.3% NaCl, 0.3% NaCl + 0.2% $CuSO_4$, 0.3% NaCl + 4% Agarose, 0.3% NaCl + 0.2% $CuSO_4$ + 4% Agarose, was carried out. A series of radial 3D data sets were acquired with increasing TE ($FOV = 500$ mm, $TR = 12.4$ ms, $TE = 0.2, 0.4, 0.8, 1.2, 2, 4, 6, 8$ and 10 ms, $N_{acq} = 6$, $T_{acq} = 3$ min, 2500 projections, 64 sampling points/projection, $\alpha = 15°$, $BW = 780$ Hz/Px). The experiments were performed with the high-pass birdcage coil. ROI's were selected and the data was fitted to mono- ($S = M_0 e^{-t/T_2}$) and bi-exponential ($S = M_{fast} e^{-t/T_{2\,fast}} + M_{slow} e^{-t/T_{2\,slow}}$) decays (figure 9.17). The resulting values are found in table 9.3.

The SNR of the images was around 10, which is extremely low to expect reliable results. In

Solution	M_{fast}	$T_{2\,fast}$ (ms)	M_{slow}	$T_{2\,slow}$ (ms)
NaCl	n.a.	n.a.	137	40
NaCl + $CuSO_4$	n.a.	n.a.	140	32
NaCl + Agarose	61	0.3	92	18
NaCl + $CuSO_4$ + Agarose	7	0.96	150	11

Table 9.3: Transversal relaxation time values for different solutions.

order to measure accurately the relaxation times, a better SNR would have been needed, as well as the acquisition of more data sets with longer TE, especially in the case of the phantoms without agarose, which have a monoexponential decay and much longer T_2. These preliminary experiments, however, demonstrate that, with the 3D radial method, it is possible to detect and evaluate mono- and biexponential decay (figure 9.17). The reduction of T_2 in the presence of $CuSO_4$ and the biexponential behaviour of the solutions with agarose can be observed.

A series of gradient echo sequences at $\alpha = 90°$ and with variable TR were applied to measure the T_1 of a 0.3% NaCl and a 0.3% NaCl + 4% Agarose solution. Figure 9.18 shows the plots of these data and their respective fits. For 0.3% NaCl, $T_1 = 50\,\text{ms}$, and for 0.3% NaCl + 4% Agarose, $T_1 = 23\,\text{ms}$.

9.3.2 *In-vivo* Experiments - Head

In order to test the capability of the radial method to measure the ^{23}Na relaxation times *in-vivo*, a volunteer experiment was carried out. The 3D radial sequence was applied ($FOV = 500\,\text{mm}$, $TR = 8\,\text{ms}$, $TE = 0.2, 0.4, 0.8, 1.2 \text{ and } 2$, $N_{acq} = 12$, $T_{acq} = 8\,\text{min}$, 2500 projections, 64 sampling points/projection, $\alpha = 15°$, $BW = 600\,\text{Hz/Px}$) to acquire four data sets of the brain of a volunteer with increasing TE. ROI's were selected in brain tissue and the data was fitted to a biexponential decay (figure 9.19). The result for a ROI located in brain tissue was $M_{fast} = 0.3$, $T_{2\,fast} = 0.5\,\text{ms}$, $M_{slow} = 0.7\,\text{ms}$, $T_{2\,slow} = 16\,\text{ms}$. While the values of the relaxation times match with those found in the literature [Constantinides 2000], the proportion of slow to fast component is an interesting parameter. From the physical point of view, a 60% of fast component and a 40% of slow component is expected. However, *in-vivo* we measure also the intra- and extracellular concentration, and the signal of the biexponential decay is mixed with the signal of the monoexponential decay from the free sodium. Consequently, it would be possible that the percentages vary from those expected from the ideal type c spectrum of figure 2.4 (page 26). The question would be then, why these percentages are not to be found for the saline solutions with agarose. Maybe the solutions are also a mixture of different spectra. The SNR and the number of acquired images were too low to evaluate reliably these results. Both better phantom and *in-vivo* experiments would be necessary to analyse the relaxation behaviour of ^{23}Na accurately. The purpose of these experiments was only

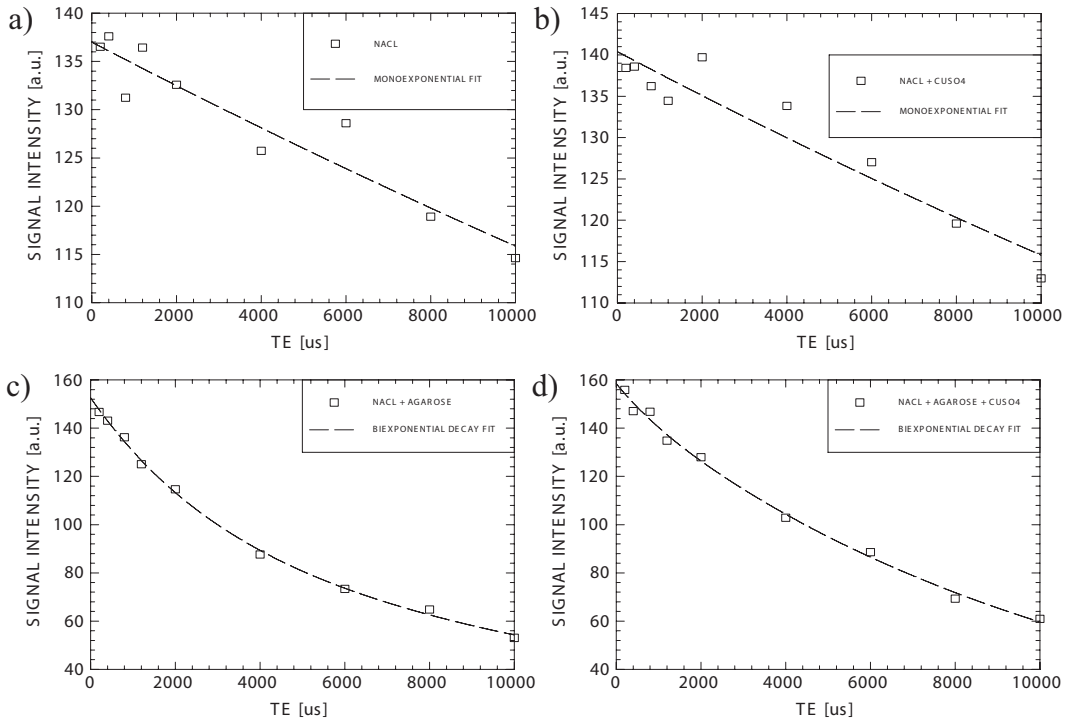

Figure 9.17: T_2 fits of 0.3% NaCl (a), 0.3% NaCl + 0.2% $CuSO_4$ (b), 0.3% NaCl + 4% Agarose (c), 0.3% NaCl + 0.2% $CuSO_4$ + 4% Agarose (d). (a) and (b) are monoexponential, while (c) and (d) are biexponential.

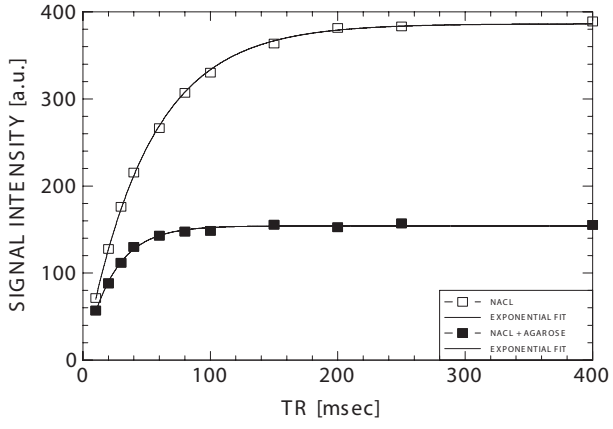

Figure 9.18: T_1 fit of a saline solutions and a 0.3% NaCl + 4% Agarose.

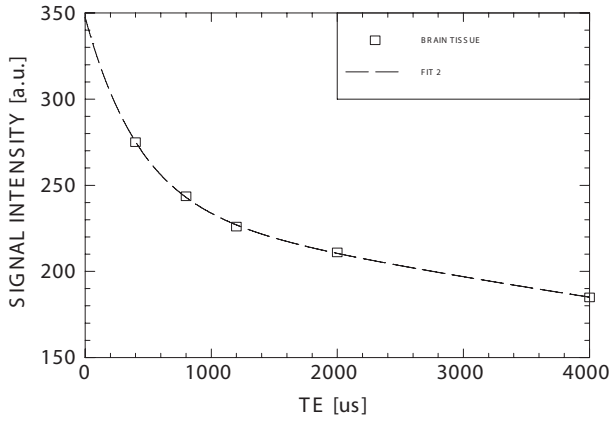

Figure 9.19: Fit of the biexponential T_2 decay in brain tissue.

to qualitatively demonstrate that the 3D radial method is an appropriate tool to perform ^{23}Na relaxometry.

9.3.3 Quadrupolar Splitting

While *in-vivo* quadrupolar splitting of the ^{23}Na signal has already been demonstrated using spectroscopy, to date it has not been detected using MRI (references). The flip angle as a function of *RF* pulse amplitude was analysed using MRI, to investigate the presence of ^{23}Na quadrupolar splitting in-vivo. As mentioned before, ^{23}Na is a spin 3/2 nucleus with three possible transitions corresponding to four energy levels. The ^{23}Na nucleus, however, has an electric quadrupole moment, which affects the energy levels of the nucleus in the presence of an electric field gradient. If the sodium ions are bound to macroscopically ordered structures, quadrupolar splitting of the energy levels can also occur. Joseph and Summers [Joseph 87] proposed a method based on the prediction that the nutation rate of the unshifted inner spectral line is twice that of a system without quadrupolar splitting. A voxel containing both sodium with and without quadrupolar splitting could be characterised by a partial volume approach:

$$S = S_1 \sin(\omega u) + S_2 \sin(2\omega u) \tag{9.2}$$

where S_1 and S_2 are the signals from the unsplit and split components respectively, u is the *RF* amplitude and ω is the frequency of the sinusoidal function. This flip-angle effect (FAE) has been demonstrated in the liquid crystal sodium linoleate in water, however, in-vitro experiments of skeletal muscle and brain tissue samples indicated the absence of quadrupolar splitting [Joseph 87].

Sodium linoleate in water was prepared by mixing equimolar quantities of 99% linoleic acid (Sigma Aldrich, Germany) and 1.0 N sodium hydroxide. An isotonic (0.9%) and a

0.3% NaCl solution were used as references for the phantom experiment with the liquid crystal and volunteer experiments performed in the calf. Images were acquired both in the 1.5 T Vision system and the 1.5 T Symphony system with a home-built ^{23}Na saddle coil, and later on, with the high-pass birdcage coil. A GRE sequence with $TR = 100$ms, $TE = 3.3$ ms, 20 mm slice thickness and $N_{acq} = 754$ was used. The RF amplitude was varied between $0 - 160$ V to observe the signal response as a function of RF amplitude. Regions of interest were selected and the data were fit to equation 9.2. The resulting frequency ω was used to fit a simple sinusoidal function to the saline data. The percentage of signal associated with the flip-angle effect is:

$$\%FAE = \frac{S_2}{S_1 + S_2} \times 100 \tag{9.3}$$

To confirm that the flip angle behaviour was not influenced by different TR/T_1 ratios in the samples, data was acquired at various TR.

Figure 9.20.a and b show the plots of the signal intensity as a function of RF amplitude and the fits to this data. The variation of the TR values in the phantom experiments did not affect the signal behaviour with respect to RF amplitude, and considering that the published T_1 values *in-vivo* and in saline solution are similar $(30 - 50$ ms$)$[4], we would not expect the TR/T_1 ratios to influence the volunteer experiments.

The flip angle effect can be clearly observed in the liquid crystal data. The $\%FAE$ calculated from the fit is 93% in sodium linoleate, quite in agreement with the result of 77% from [Joseph 87]. It can be observed, on the other hand, that the muscle data does not show to be affected by the $\%FAE$, also in agreement with the results of Joseph and Summers [Joseph 87]. There seems to be a tendency to have a larger α than the saline, but a two-compartmental model cannot be reliably fitted. As can be seen in figure 9.20.c, different regions of the calf give different signal response to the applied voltage. Although this might mean that some regions do show quadrupolar splitting behaviour, it might as well be B_1 field inhomogeneity. In fact, experiments were performed both with the saddle and the head coil. With the saddle coil quadrupolar splitting in the muscle seemed to be clearly detectable. However, further examinations showed that what was to be seen in the saddle coil, was difficult to repeat with the birdcage coil.

Nevertheless, the results achieved did not completely discard the possibility that ^{23}Na quadrupolar splitting takes place in the human calf muscle. Various parameters might have been inaccurate. First of all, if the RF pulse bandwidths were not narrow enough, the satellite lines would be excited together with the central line, and consequently the flip angle effect would vanish. Secondly, if the percentage of signal associated with the flip angle effect were very small, considering the low SNR of these experiments, it might be possible that the effect could not be detected.

Further analysis must be performed to determine more precisely the sources of inaccuracy in this experiment, as well as to optimise the RF pulse (duration, BW, etc.). The method currently requires long measurement times at low spatial resolution, but it still provides

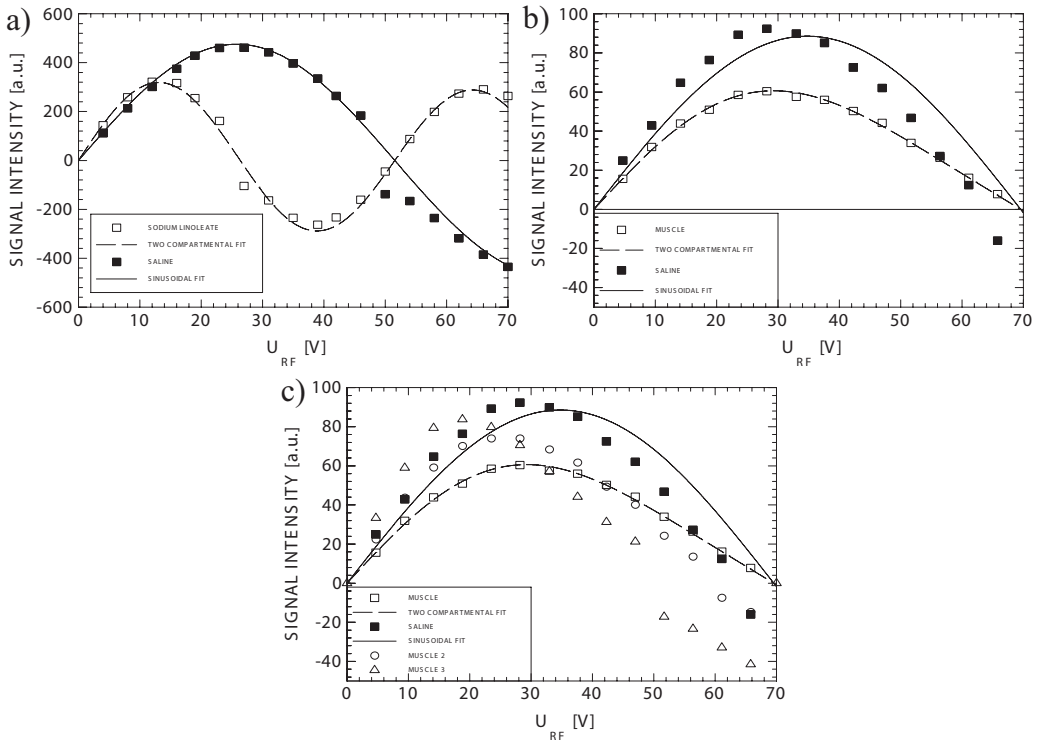

Figure 9.20: .Signal versus RF-amplitude: (a) sodium-linoleate and saline, (b) calf muscle of a volunteer and saline. (c) shows the response to voltage from different regions in the muscle.

a unique opportunity to measure with MRI whether ^{23}Na quadrupolar splitting *in-vivo* occurs.

9.4 Ultra-Short Echo Time Imaging

The 3D radial method developed in this work for short TE ^{23}Na MRI imaging can also be used for ^{1}H ultra-short echo time (UTE) imaging. By shortening the hard RF pulse duration to $60\mu s$ and bringing down the delay time between RF and readout to the scanner's specified $40\mu s$, it is possible to achieve a $TE = 70\mu s$. Figures 9.21, 9.22 and 9.23 are some examples of images acquired with this technique.

The most widely used clinical magnetic resonance imaging techniques for the diagnosis of parenchymal disease employ heavily T_2-weighted sequences to detect an increase or decrease in the signal from long T_2 components in tissue. Tissues also contain short T_2 components that are not detected or only poorly detected with conventional sequences. These components are the majority species in tendons, ligaments, menisci, periosteum, cortical bone and other related tissues, and the minority in many other tissues that have predominantly long T_2 components. The development and clinical application of techniques to detect short T_2 components are still in preliminary stages. Such techniques include magic angle imaging, as well as short echo time (TE), and ultrashort TE (UTE) pulse sequences. Magic angle imaging increases the T_2 of highly ordered, collagen-rich tissues such as tendons and ligaments so that signal can be detected from them with conventional pulse sequences (reference). UTE sequences detect short T_2 components before they have decayed, both in tissues with a majority of short T_2 components and those with a minority. In the latter case steps usually need to be taken to suppress the signal from the majority of long T_2 components. Fat suppression of different types may also be helpful. Once signal from short T_2 components has been detected, different pulse sequences can be used to determine increases or decreases in T_1 and T_2 and study contrast enhancement. Using these approaches, signals have been detected from normal tissues with a majority of short T_2 components such as tendons, ligaments, menisci, periosteum, cortical bone, dentine and enamel (the latter four tissues for the first time) as well as from the other tissues in which short T_2 components are a minority. Some diseases such as chronic fibrosis, gliosis, haemorrhage and calcification may increase the signal from short T_2 components while others such as loss of tissue, loss of order in tissue and an increase in water content may decrease them. Changes of these types have been demonstrated in tendonopathy, intervertebral disc disease, ligament injury, haemachromatosis, pituitary perivascular fibrosis, gliomas, multiple sclerosis and angiomas. Use of these techniques has reduced the limit of clinical detectability of short T_2 components by about two orders of magnitude from about $10ms$ to about $100\mu s$. As a consequence it is now possible to study tissues that have a majority of short T_2 components with both "bright" and "dark" approaches, with the bright (high signal) approach offering options for developing tissue contrast of different types, as well as the potential for tissue characterization. In addition, tissues with a minority of short T_2 components may demonstrate changes in disease that are not

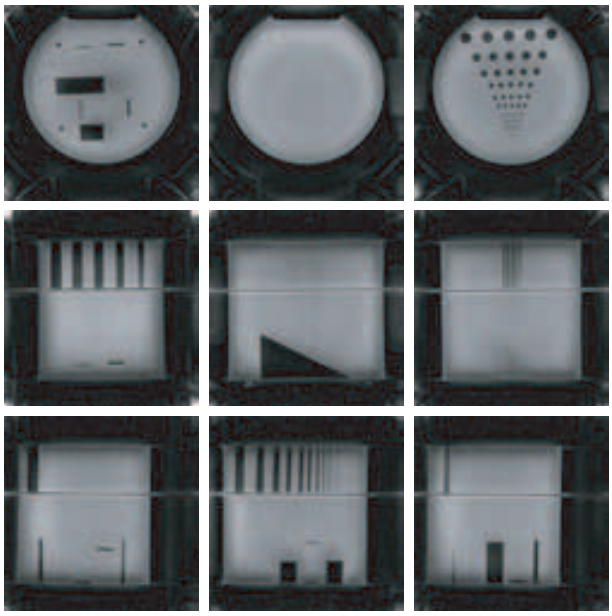

Figure 9.21: 3D radial ^{1}H UTE images of a resolution phantom ($FOV = 320\,\text{mm}$, $TR = 2.4\,\text{ms}$, $TE = 0.07\,\text{ms}$, 1 average, $T_{acq} = 2\,\text{min}$, 50000 projections, 128 sampling points/projection, $\alpha = 5°$, $BW = 780\,\text{Hz/Px}$).

apparent with conventional heavily T_2-weighted sequences [Gatehouse 2003].

Figure 9.21 shows ^{1}H images of a resolution phantom acquired with a 3D radial UTE sequence ($FOV = 320\,\text{mm}$, $TR = 2.4\,\text{ms}$, $TE = 0.07\,\text{ms}$, $N_{acq} = 1$, $T_{acq} = 2\,\text{min}$, 50000 projections, 128 sampling points/projection, $\alpha = 5°$, $BW = 780\,\text{Hz/Px}$). Coronal, transversal and sagittal slice of a ^{1}H data set of the feet of a healthy volunteer acquired with a 3D radial UTE sequence ($FOV = 220\,\text{mm}$, $TR = 2.4\,\text{ms}$, $TE = 0.07\,\text{ms}$, $N_{acq} = 1$, $T_{acq} = 2\,\text{min}$, 50000 projections, 128 sampling points/projection, $\alpha = 5°$, $BW = 780\,\text{Hz/Px}$) are shown in figure 9.22.

Figure 9.23 shows ^{1}H images of the head of a healthy volunteer acquired with a 3D radial UTE sequence ($FOV = 320\,\text{mm}$, $TR = 2.8\,\text{ms}$, $TE = 0.07\,\text{ms}$, $N_{acq} = 1$, $T_{acq} = 2\,\text{min}\,20\,\text{s}$, 50000 projections, 128 sampling points/projection, $\alpha = 5°$, $BW = 530\,\text{Hz/Px}$). The coil and earplugs can also be seen, as they are made of short T_2 material, which demonstrates the capability of the sequence to acquire signals with short T_2.

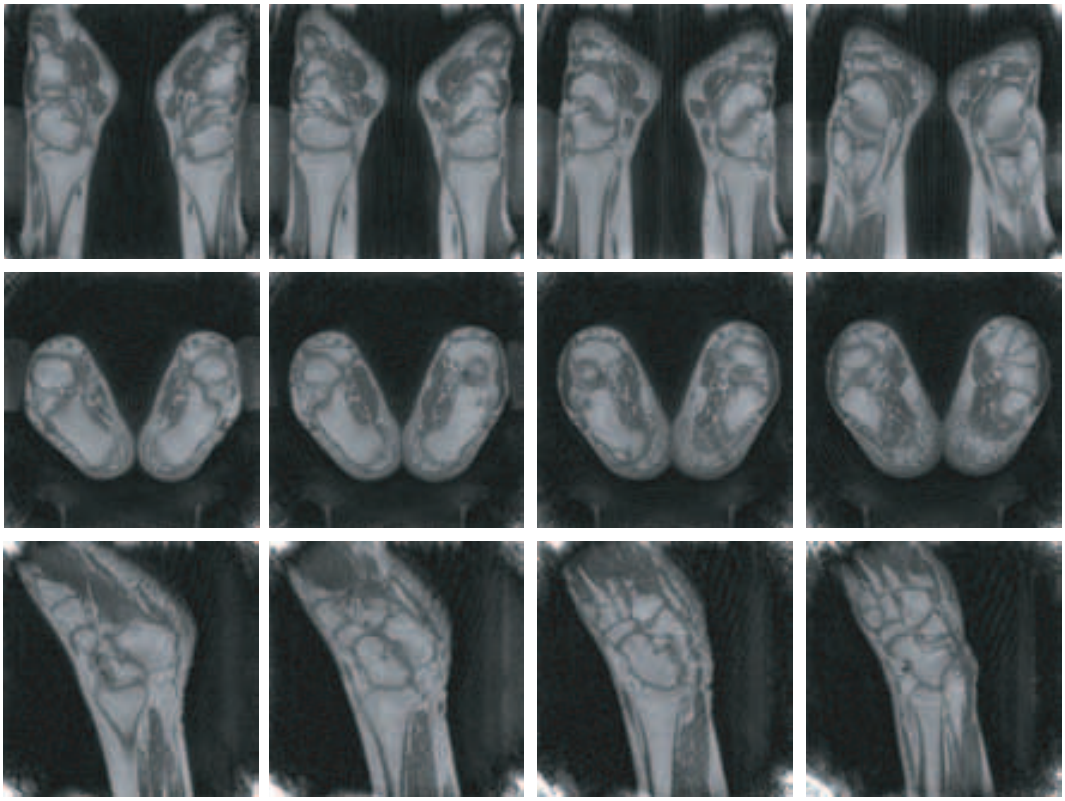

Figure 9.22: 3D radial ^{1}H UTE images of the feet of a healthy volunteer ($FOV = 220\,\text{mm}$, $TR = 2.4\,\text{ms}$, $TE = 0.07\,\text{ms}$, $N_{acq} = 1$, $T_{acq} = 2\,\text{min}$, 50000 projections, 128 sampling points/projection, $\alpha = 5°$, $BW = 780\,\text{Hz/Px}$).

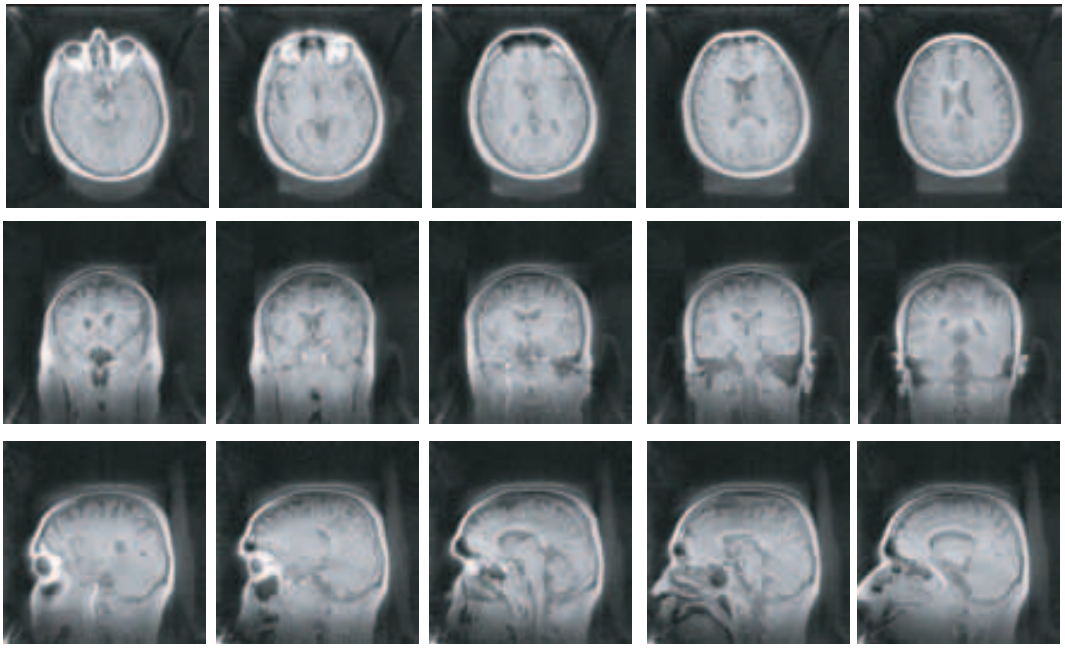

Figure 9.23: 3D radial ^{1}H UTE images of the head of a healthy volunteer (3D Radial FOV = 320 mm, TR = 2.8 ms, TE = 0.07 ms, N_{acq} = 1, T_{acq} = 2 min 20 s, 50000 projections, 128 sampling points/projection, $\alpha = 5°$, BW = 530 Hz/Px).

Chapter 10

Clinical cases

10.1 ^{23}Na MRI in Brain Tumour Patients

Sodium concentration is sensitive to disease as an indicator of cellular and metabolic integrity and ion homeostasis. Angiogenesis and cellular proliferation are important indicators of tumour malignancy. Changes in sodium/hydrogen (Na^+/H^+) exchange kinetics are part of the signaling mechanism that initiates cell division. Cell division and the acidic extracellular microenvironment of tumour cells are both associated with an increase in intracellular Na concentration ($[Na^+]_{in}$). Increased $[Na^+]_{in}$, increased Na/H transporter activity, and altered (Na^+/K^+)-adenosine triphosphatase activity have all been linked to tumour malignancy. In a recent study, investigators subcutaneously implanted a 9L glioma model in rats and indicated that successful chemotherapy can lead to normalisation of the initially elevated sodium concentration as seen with conventional (single-quantum) and multiple-quantum ^{23}Na magnetic resonance (MR) spectroscopy.

The observed tissue sodium concentration is composed of the weighted average of extracellular sodium content $[Na^+]_{ex}$ and the intracellular sodium content $[Na^+]_{in}$ in the tissue being examined. $[Na^+]_{ex}$ at 140 mmol/L is typically much higher than is $[Na^+]_{in}$, which is about $10 - 15$ mmol/L. Arguably, the more physiologically relevant information is in the intracellular component, reflecting the ability of the cell to pump out sodium ions, whereas $[Na^+]_{ex}$ will remain virtually constant as long as there is adequate perfusion to the tissue. When the relative contribution of the $[Na^+]_{in}$ to the tissue sodium concentration is large, as it is in brain tumours, the sodium concentration provides a measure of metabolic changes affecting $[Na^+]_{in}$. Estimates for the extracellular volume fraction in the brain vary from 6% to 20%. When one considers that tissue perfusion fixes the extracellular concentration at about 140 mmol/L, assuming a normal intracellular concentration of 12 mmol/L, it can be calculated that the contribution of $[Na^+]_{in}$ in normal tissue is between 26% and 57%. More than half of the combined ^{23}Na signal is due to intracellular ^{23}Na when the partial volume of the extracellular compartment is less than 7%. Thus, despite the inability to resolve intra- and extracellular components of the ^{23}Na signal, the

measurement of sodium concentration is a sensitivity measure of $[Na^+]_{in}$.

In order to test the diagnostic capability of the 3D radial method developed in comparison to the 3D cartesian method, a patient with a glioma was examined with the Rapid high-pass birdcage coil. Thanks to the fact that it is double-resonant, the whole MRI examination could be performed without moving the patient. The ^{23}Na part of the examination lasted twenty minutes.

Figure 10.1.a and d show FLAIR images of the brain. Figure 10.1.b and e shows transversal and coronal views of the ^{23}Na 3D data set acquired ($FOV = 500$mm, $TR = 4$ ms, $TE = 0.2$ ms, $N_{acq} = 30$, $T_{acq} = 10$ min, 5000 projections, 64 sampling points/projection, $\alpha = 25°$, $BW = 500$ Hz/Px). In the area where the tumour is located, there is a strong signal enhancement. Figure 10.1.c shows a ^{23}Na cartesian data set of the same patient. SNR values of the cartesian and radial methods are found in table 10.1. It can be observed that the SNR of the radial method is about 1.5 times better than that of the cartesian. The contrast to noise ratio (CNR) between tumour and healthy brain tissue, tumour and vitreous humour and tumour and CSF was evaluated as follows:

$$CNR = SNR_{Tumour\,Tissue} - SNR_{Healthy\,Tissue} \tag{10.1}$$

ROI	3D FLASH	3D RADIAL
Vitreous Humour	35.0	54.4
CSF	33.7	43.3
Brain Tissue	18.5	32.4
Tumour Tissue	36.7	55.3

Table 10.1: SNR Comparison 3D FLASH and 3D radial images of the head of a patient with brain tumour ($SNR = Signal_{ROI}/Standard\quad deviation_{Bakground}$).

The resulting CNR values were 21% for the healthy tissue, 1% for the vitreous humour and 12% for the CSF. The CNR between tumour and brain tissue of the radial and the cartesian technique were calculated, and resulted in $CNR_{Cartesian} = 18.2\%$ and $CNR_{Radial} = 22.9\%$. The ratio between the two is 20.5%, so the radial sequence provides a better contrast to visualise the tumour.

This results prove that ^{23}Na MR imaging can help identify malignant tumours with regard to the intrinsic changes that occur in tumour Na^+/K^+ pump function. Therapies that alter tumour ion homeostasis or affect or destroy tumour cell membrane integrity are likely to generate changes that are observable with ^{23}Na MR imaging and sodium concentration measurements. With these measurements, changes can be observed much earlier than the effects of anatomic remodeling. Therefore, these techniques may prove useful in providing early noninvasive metabolic markers of tumour response to therapy without requiring exogenous contrast-enhanced or radionuclide imaging agents. When used in conjunction with ^{1}H MR imaging protocols such as the FLAIR sequence, MR imaging contrast agents,

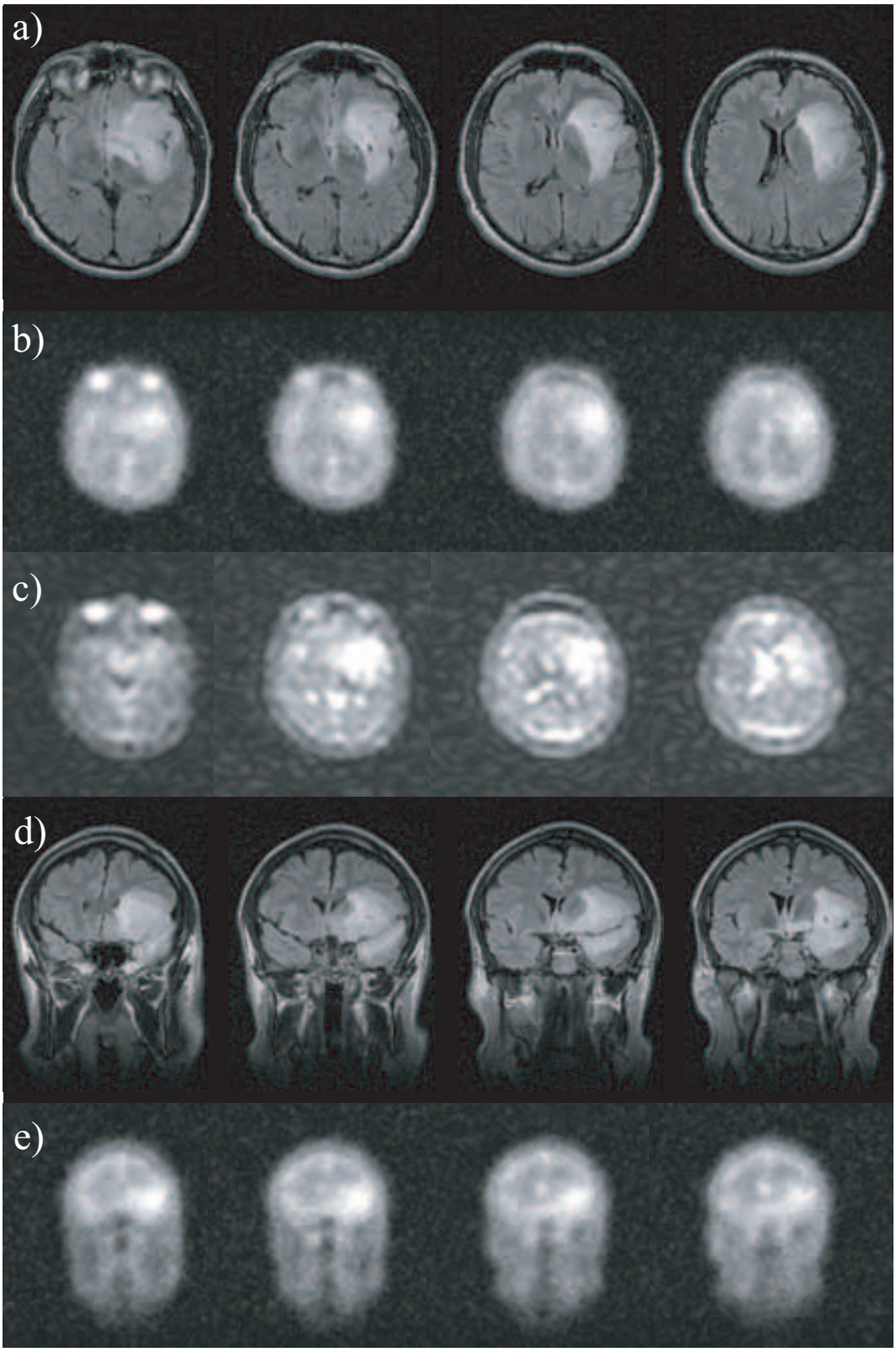

Figure 10.1: FLAIR images (a,d) and ^{23}Na radial (b,e) and FLASH (c) images of a brain tumour. The outline of the area with signal enhancement in the ^{23}Na images agrees with the shape of the tumour in the standard ^{1}H MR images.

and T2-weighted imaging methods, ^{23}Na MR imaging may provide additional functional information on the morphology of tumours that may enhance visualisation of a necrotic core or proliferating periphery or improve diagnostic specificity with multiparametric analysis methods. Other groups have managed to quantify the sodium concentration by the use of reference phantoms [Ouwerkerk 03].

10.2 Muscle

10.2.1 ^{23}Na MRI in Patients with Muscular ^{23}Na Channelopathy

To visualise the intracellular sodium accumulation and the effects of specific therapy in patients with the inherited sodium channelopathy, paramyotonia congenita (PC), five patients with confirmed PC and 10 healthy volunteers were examined on the 1.5 T MR system using the 16.8 MHz surface coil. ^{23}Na MRI was performed before and after local cooling and exercising of the left lower leg. The ^{23}Na MRI examination was repeated the next day and, in patients with PC, after 4 days of oral medication with mexiletin that blocks sodium channels. The ^{23}Na MRI protocol comprised a 2D-FLASH ($TR = 13$ ms, $TE = 3.53$ ms), a 2D-radial ($TR = 13$ ms, $TE = 0.6$ ms) and a free induction decay (FID, $TR = 1000$ ms, $TE = 0.2$ ms) sequence. After cooling, a 3D radial ^{23}Na data set ($FOV = 500$ mm, $TR = 4$ ms, $TE = 0.2$ ms, $N_{acq} = 30$, $T_{acq} = 10$ min, 5000 projections, 64 sampling points/projection, $\alpha = 25°$, $BW = 500$ Hz/Px) was acquired using the high-pass double-resonant birdcage coil (Rapid Biomed GmbH). The FID data was fitted to a biexponential decay to evaluate the fast and slow component of the T_2 relaxation time. The fast component was related to the intracellular and the long component to the extracellular sodium concentration. Regions of interest were selected in the 2D radial images using a physiological saline solution as reference. Additionally, standard T_1 weighted and T_2 weighted NMR images were acquired to exclude other muscular pathologies (figure 10.2). The experimentally induced paresis was scored by a neurologist.

All 5 patients with PC developed considerable weakness of the left foot after local cooling and exercise, while no weakness was observed in volunteers. In patients with PC, ^{23}Na FID showed a decrease in the ratio of the extra-/intracellular sodium concentration (median decrease 17%, p¡0.05, Mann-Whitney U test) that most likely reflects the intracellular sodium accumulation. Volunteers, in contrast, showed no significant alteration (median decrease 0%, p=0.23, Mann-Whitney U test). After sodium channel blockage in patients with PC, cooling and exercise induced almost no weakness, and ^{23}Na MRI remained unchanged. The results of 2D-radial MRI correlated well with the FID results (r=0.6, Pearson's correlation coefficient).

In the 2D radial images before and after cooling, a signal intensity increase in the cooled zone could be observed (figure 10.3). The 3D radial data sets acquired after cooling show a clear difference between the cooled leg and the reference leg (figure 10.4). The high signal regions on the upper part of the legs do not relate in this case to pathological

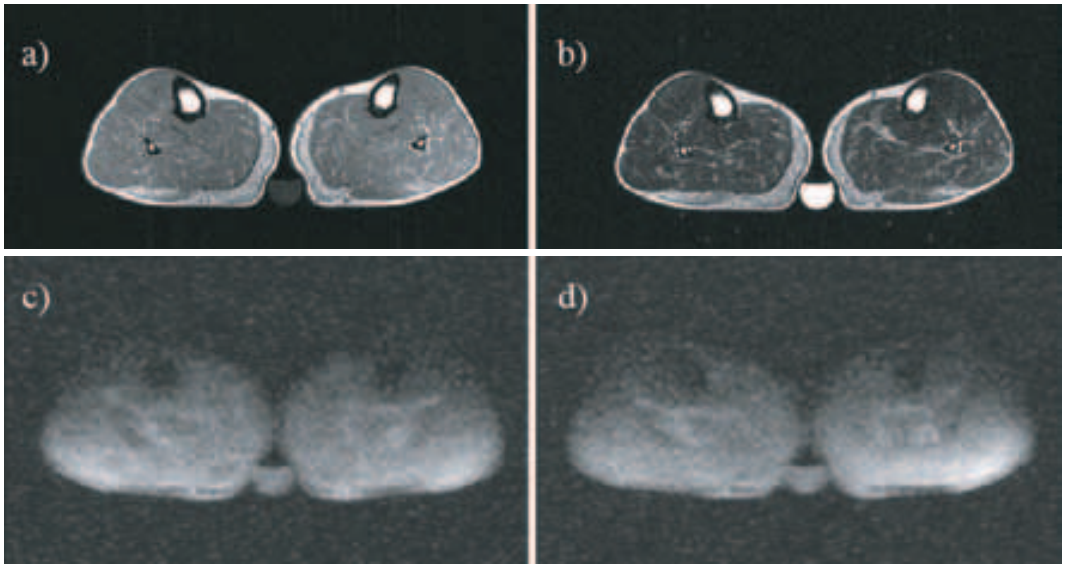

Figure 10.2: ^{1}H T_1 (a) and T_2 (b) weighted images of the calf of a patient with Paramyotonia Congenita. ^{23}Na FLASH of this patient before (c) and after cooling the left leg (d). A reference phantom with a 0.3% NaCl solution is placed between both legs.

changes, but to the fact that both legs fit very tight inside the birdcage coil and some B_1 field inhomogeneity effects influence the results. The CNR between the cooled leg and the reference leg is about 8% for the FLASH, 11% for the 2D radial and 10% for the 3D radial.

This study proves that ^{23}Na MRI visualises intracellular sodium accumulation that is associated with muscle weakness in patients with PC. Furthermore, effects of a specific therapy can be monitored.

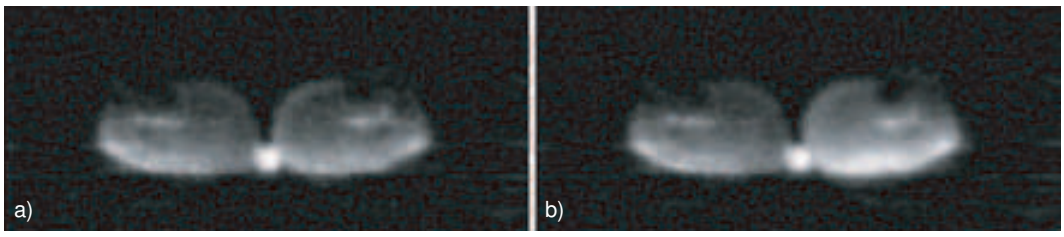

Figure 10.3: ^{23}Na 2D radial images of a patient with Paramyotonia Congenita before (a) and after (b) cooling the left leg.

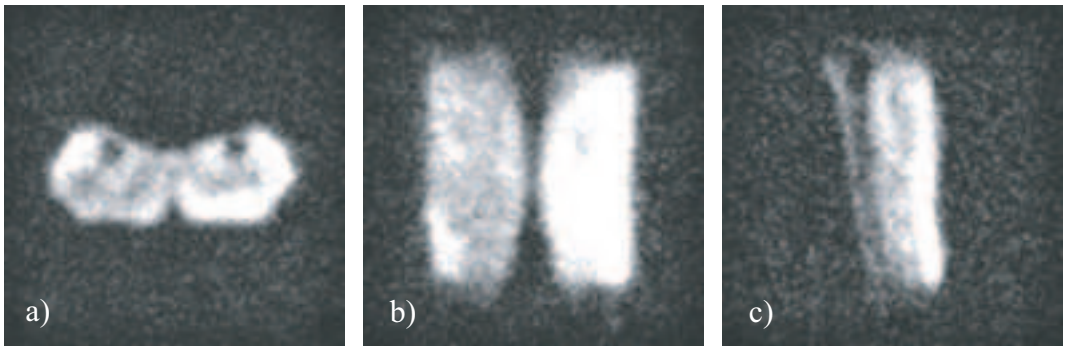

Figure 10.4: Transversal (a), coronal (b) and sagittal (c) views of a ^{23}Na 3D radial data set of the legs of a patient with Paramyotonia Congenita after cooling the left leg.

Part IV

Discussion

Chapter 11

Discussion

In this work, measurement techniques and hardware were developed for ^{23}Na MRI of the human brain, heart and muscle in a clinical scanner at 1.5 T. A 3D radial gradient echo (GRE) sequence was implemented, with a minimum echo time $TE_{min} = 70\,\mu$s for ^{1}H and 200 μs for ^{23}Na. Several reconstruction algorithms were implemented and optimised for both ^{23}Na and ^{1}H MRI. The resulting method was compared with a standard cartesian GRE sequence and a twofold improvement in SNR was measured. Measurements were carried out at 4 T and the results showed 2.7 times better SNR compared to the experiments at 1.5 T. Both in patients with brain tumours and with ^{23}Na channelopathy, a ^{23}Na MRI signal increase related to the increase in intracellular ^{23}Na concentration was measured.

11.1 Hardware Results

Among the few ^{23}Na coils used in this work, the high-pass birdcage coil (Rapid Biomed GmbH) achieved the best performance of the three volume *RF* coils. Loaded with the same phantom and using identical MRI sequence parameters, the high-pass birdcage coil requires a voltage of $V = 127\,$V for a 90° pulse and is capable of reaching $\alpha = 180°$ (at $V = 250\,$V). Its field homogeneity and SNR are better compared to the other two volume coils. The saddle coil, on the other hand, has a good filling factor at similar reference voltage, however, it suffers from B_1 field inhomogeneity. The low-pass birdcage coil needs $V = 179\,$V for a 90° pulse, which can become a limiting factor in high SAR experiments. The surface coil (Rapid Biomed GmbH) showed a penetration depth of only $\sim 7\,$cm, and *in-vivo* coverage of the whole heart was not possible.

The fact that the high-pass birdcage coil is double-resonant allows for simultaneous ^{1}H and ^{23}Na MR imaging, as well as for proper shimming before the ^{23}Na MRI measurements, which increases image quality. In clinical routine double-resonant ^{23}Na coils are much more efficient than single-resonant coils. As a low-SNR and low-resolution technique, ^{23}Na MRI

only complements ^{1}H MRI. The use of a single-resonant ^{23}Na coil implies repositioning of the patient, which is time inefficient and causes repositioning errors. However, for phantom experiments and volunteer experiments, the self-developed volume coils have been very useful and have allowed for the development and optimisation of the ^{23}Na measurement techniques.

In clinical routine, the surface coil has three basic limitations: First, the patient is positioned prone on the coil in order to minimise image blurring due to breathing. The long measurement times of ^{23}Na MRI due to signal averaging require free breathing examinations. By lying prone on the coil, the position of the heart with respect to the coil does not vary as strong as in supine position. Patients with cardiac pathologies, however, do not tolerate long measurement times in prone position. Secondly, the surface coil was made of a rigid material. A flexible coil could be better adapted to each patient's anatomy. Moreover, it would allow for examinations of other body parts (such as the legs in chapter 10) achieving a better filling factor. Thirdly, it is only single-resonant. ^{23}Na examinations are only useful when they are accompanied by ^{1}H images. A double-resonant Helmholtz coil might solve the previously mentioned problems. Firstly, a Helmholtz coil has a better B_1 field distribution, so that it would manage to cover the whole heart. Secondly, it would be possible to lye both in prone and supine position, with an adjustable distance between the two loops. The blurring due to breathing for patients in supine position could be minimised by using a special type of corset that minimises the movement of the chest, or by respiratory triggering.

Future work will concentrate on the construction of a double-resonant Helmholtz coil for cardiac and peripheral ^{23}Na MRI studies. Lee et al. [Lee00] designed and built a broadband phased-array system to convert the ^{1}H transmitter signal to the non-^{1}H frequency for excitation and, conversely, the non-^{1}H phased-array MRI signals to the ^{1}H frequency for presentation to the narrowband ^{1}H receivers of a clinical whole-body 1.5 T MRI system. With this system, the scanner was operating at the ^{1}H frequency, whereas phased-array MRI occurred at the frequency of the other nucleus. The array produced an SNR improvement of 20% relative to the best-positioned single coil, but gains of $300-400\%$ were realised in many voxels located outside the effective field-of-view of the single coil. Even though this approach is very complicated to implement, phased-array techniques in general are very promising for ^{23}Na MR signal enhancement.

11.2 3D Radial Reconstruction

The radial reconstruction results in chapter 8 demonstrate that Nearest Neighbour, as well as gridding (with a Gaussian or a Kaiser-Bessel function) interpolations achieve good results, as long as the proper precompensation filters are used. Due to the higher SNR, the reconstruction of ^{1}H data sets is less sensitive to artefacts than the reconstruction of ^{23}Na data sets. This implies that the choice of reconstruction method and the optimisation of the reconstruction parameters needs to be much more carefully made for ^{23}Na than for

^{1}H: First, the SNR of ^{1}H images is about tenfold higher than that of ^{23}Na images. All the reconstruction methods work well when the SNR is high ($\sim$ 400), but they do not take into account noise, which needs special corrections such as filtering. ^{1}H data sets do not require signal averaging, and the scan time can be invested in the acquisition of more projections, minimising data undersampling and, consequently, simplifying the choice of density compensation method. ^{23}Na acquisitions are, on the other hand, long compared to ^{1}H ones and solid angle undersampling is necessary and undersampling factors of $10-100$ are common. To correct for undersampling, a compromise between SNR and blurring has to be made. The ^{23}Na signal decays much faster than the ^{1}H signal, leading again to a reduced point-spread-function PSF (i.e. blurring). Although higher readout bandwidths help to minimise this effect, the about fourfold lower gyromagnetic ratio of ^{23}Na requires four times stronger gradients, and harware limits are reached very fast. The filters to compensate for undersampling implemented and tested in this work provide images with acceptable SNR and resolution. Nevertheless, to further improve image quality, filters must be implemented that take into account T_2 decay, low SNR and undersampling.

11.3 3D Radial Measurements

Both phantom and volunteer experiments have shown the superiority of ^{23}Na 3D radial MRI over 3D FLASH MRI with regard to SNR. This is attributed to the one order of magnitude shorter TE of the radial technique, which, consequently, manages to acquire the total ^{23}Na MR signal (short and long T_2 components). On the other hand, the 3D FLASH has a better resolution than the 3D radial technique, which suffers from blurring. The interpolation of the radial data onto a cartesian grid induces blurring in the images. Adequate sampling density correction filters must be used to compensate for undersampling of the data, as well as for the low SNR of the ^{23}Na images. Furthermore, the fast decay of the short component of the ^{23}Na signal ($T_{2,short} \sim 0.5\,\text{ms}$) leads to a broadened point-spread-function (PSF) in all directions. The cartesian method is not affected by blurring because $T_{2,short}$ has already decayed before data acquisition, and $T_{2,long}$ is much larger than the acquisition window T_{acq}. The use of high readout bandwidths (BW) could reduce the blurring effect, however, the $BW = 500\,\text{Hz/Px}$, is already at the hardware limits for ^{23}Na MRI. During image reconstruction, the radially acquired data could be filtered by a function that compensates for the biexponential T_2 decay. Since T_2 values are not known a priori and vary for each tissue, this compensation strategy is not feasible for *in-vivo* data.

The sampling density correction filters used to reconstruct the radial images need further improvement. More elaborate algorithms that optimise the filters based on the particular non-uniform trajectories will be implemented [Pipe99], [Pipe99]. The inherent blurring of the 3D radial images due to T_2 decay will, however, remain. This disadvantage is acceptable because of the capability of these images to acquire the total ^{23}Na signal.

Twisted projection imaging (TPI) is a further development of the 3D radial MRI or projec-

tion imaging (PI) [Boada 1997b], [Boada 1997c]. This technique is based on the premise that improvements in the sampling efficiency of 3D radial scanning can be achieved by removing the nonuniform sampling density that results from uniform sampling in time along radial lines in k-space. The result are helix-shaped trajectories on the surface of cones which start at the centre of k-space and finish in a circle on the surface of the sampling sphere. These trajectories improve the k-space coverage per RF excitation, at the expense of longer readout times. In order to compensate for the corresponding T_2 signal attenuation during readout, spectrally weighted TPI has been developed [Boada 1997c], in which the sample density at higher frequencies decreases in an SNR efficient fashion according to a prescribed sample weighting function. This reduces blurring due to T_2 decay without penalty in the SNR. TPI is however hindered by the lengthy repetition time TR, which prevents the exploitation of the short T_1 (approximately 5060 msec) of sodium in vivo. The complicated trajectories place high demands on gradient performance, and deviations from the ideal trajectories might create imaging artefacts.

The SPRITE technique, developed over the past few years for non-biological imaging, is a method that allows the formation of images from fast-relaxing species [Balcom 98]. By sampling only one point, following RF excitation, convolution of the signal with T_2^* decay is avoided and high resolution images of a population of fast-relaxing spins can thus be achieved. However, the single point sampling scheme is inefficient and hence SPRITE suffers from long acquisition times [Romanzetti 04].

11.3.1 Comparison of ^{23}Na MRI at 4 T and 1.5 T

The results presented in the comparison between ^{23}Na MRI at 1.5 T and 4 T demonstrate that ^{23}Na MRI benefits from higher B_0, achieving images of high SNR at acceptable measurement times. Until recently, clinical scanners had a maximum field strength of $B_0 = 1.5\,\mathrm{T}$. Nowadays, however, scanners with a field strength $B_0 = 3\,\mathrm{T}$, are being introduced for routine whole body MRI. This evolution might help ^{23}Na MRI get into the clinical routine, where the examination time per patient is an important parameter. There are, however, some issues to be considered when using higher field strengths.

The RF power deposited in the patient produces heating. The energy deposited is expressed as the specific absorption rate (SAR) or power absorption per unit body mass. At higher field strengths, more power is required to produce the same flip angles, and SAR limitations become a greater concern. The relatively short T_1 of sodium allows for shorter TR with minimal signal loss. At first, this might seem advantageous because, for the same total imaging time, the N_{acq} and SNR could be increased relative to acquisitions with longer TR. Unfortunately, decreasing the TR increases the RF duty cycle and, hence, increases SAR. This becomes a limiting factor for most conventional imaging sequences. The cartesian and the radial FLASH sequences make use of low flip angles, allowing for the use of short TR. To reduce the RF duty cycle, Twisted Projection Imaging (TPI) could be used, since this method uses longer TR.

At higher field strengths, T_1 increases and T_2 and T_2^* get shorter. As a consequence, TR needs to increase accordingly together with the readout bandwidth, which is already limited by the gradient hardware. For ^{23}Na MRI, it will be necessary to make proper measurements of the relaxation times to evaluate the amount of T_2-shortening. Particularly, the fast component of the transverse relaxation $T_{2\,fast}$ must be measured to assure that proper TE values are chosen for acquisition of the total ^{23}Na signal.

It has been demonstrated that ^{23}Na MRI at 4 T produces very good quality results at acceptable measurement times: For the same measurement protocol, an SNR improvement $SNR_{4\mathrm{T}}/SNR_{1.5\mathrm{T}} = 2.7$ is achieved. Conversely, the same SNR can be achieved with $T_{acq\,4\mathrm{T}} \approx T_{acq\,1.5\mathrm{T}}/7$. The prospect of using high field scanners for ^{23}Na MRI raises the potential of the technique to become a clinical application.

11.3.2 Relaxation time measurements

The preliminary results from the relaxation time measurements suggest that the 3D radial technique is an appropriate tool for ^{23}Na relaxometry. A possible optimisation of this method is the implementation of a multi-echo sequence, which acquires two or more data sets with different TE simultaneously. If the shortest possible $TE = 0.2$ ms, and the readout bandwidth is $BW = 500$ Hz/Px, it would be possible to create a sequence with an echo spacing of about $\Delta TE = 2$ ms. Such a multi-echo sequence would reduce the necessary time to acquire a collection of 3D data sets with different TE while at the same time the SNR would increase with the longer TR.

The hypothesis that the fast relaxation component $T_{2\,fast}$ relates to the intracellular ^{23}Na and the slow component $T_{2\,slow}$ relates to the extracellular ^{23}Na has motivated the effort to separate fast and slow T_2 components to quantify intra- and extracellular ^{23}Na concentrations. The hypothesis is based on the different molecular environment, however, animal studies with shift reagents have shown that biexponential relaxation of ^{23}Na takes place both in intra- and extracellular space [Van Emous 2001]. ^{23}Na T_2 times inside the cell might be shorter than those outside the cell due to the lower mobility of the ^{23}Na nuclei inside the cell. Consequently, instead of biexponential decay of the ^{23}Na signal, two biexponential decays related to four time constants might be required to describe the phenomenon adequately. With the present SNR at 1.5 T, such measurements *in-vivo* would require unrealistically long measurement times ($\sim$ 4 hours), if they were at all possible. Although it would be interesting to characterise the relaxation process more accurately, it remains questionable if any relevant diagnostic information could be extracted. If both systems show biexponential decays, the separation of the components would not relate to intra- and extracellular compartments. Under pathological conditions, however, the increase in ^{23}Na signal relates to the increase in intracellular ^{23}Na, because the extracellular ^{23}Na concentration remains constant due to perfusion in tissue. This validates the diagnostic usefulness of ^{23}Na MRI, because the parameter that relates to tissue viability and the ability of the cell to remove sodium ions is the intracellular ^{23}Na concentration. The measurement of the total ^{23}Na signal with the 3D radial technique thus might provide

a sensitive tool to evaluate tissue viability.

11.3.3 3D Radial ^{1}H MRI

The 3D radial technique implemented in this work can produce an isotropic ^{1}H 3D data set of good resolution ($\Delta x = 1.25\,\text{mm}$) and $SNR = 100$ with a total acquisitions time of less than 3 min. Images of a resolution phantom, as well as *in-vivo* the head and the feet have been acquired. 3D radial sequences have already found applications in angiography [Du 04], [Stehning 2004] because of their ability to image the entire heart with high spatial resolution and their insensitivity to motion, which enables extended acquisitions per cardiac cycle.

Hyperpolarised ^{3}He gas MRI is used to visualise breath-hold images of ventilation in humans. This method can benefit from 3D radial techniques [Wild 03] due to their short TE, which makes them inherently robust in the presence of field inhomogeneities that are prevalent in the lung. Since the centre of k-space can be sampled immediately after the start of the readout gradient, diffusion attenuation is kept to a minimum. Radial sequences are also robust to motion artifacts, since the centre of k-space is oversampled with every view.

Tendons, ligaments, menisci, periosteum, cortical bone and other related tissues contain short T_2 components that are not or only poorly detected with conventional sequences. To detect the MRI signal originating from these tissues, 2D ultra-short echo time (UTE) techniques have been developed, which achieve $TE \leq 100\,\mu\text{s}$ by using half excitation pulses and radial imaging from the centre of k-space [Robson 03]. With its short $TE = 0.07\,\text{ms}$, the 3D radial technique is suitable for UTE MRI. 2D UTE techniques can suppress fat and/or long T_2 components [Gatehouse 2003]. This is more difficult to implement for a 3D UTE technique. The 3D technique covers k-space more efficiently. In order to compare their performance, both techniques will be implemented and optimised for several diagnostic applications.

11.4 Applications and Clinical cases

11.4.1 ^{23}Na MRI in Brain Tumour Patients

The measurements performed in patients with a malignant brain tumour clearly show signal enhancements in regions affected by a tumour. The results match well with the T_2-weighted proton images. The CNR of the radial technique is 20% higher than that of the FLASH technique. In order to determine the usefulness of ^{23}Na MRI in patients, it would be necessary to determine whether the signal increase relates to an increase in the intracellular ^{23}Na concentration in the area of the tumour due to, for example, necrosis, or if it relates to an accumulation of liquid in this region. It has been observed that regions

like the vitreous humour and CSF also provide a high ^{23}Na signal. This distinction could be made by accurately measuring the T_2 relaxation times in this regions. If the higher signal would relate to liquid the expected T_2 should be quite long, while if the higher signal would relate to intracellular ^{23}Na increase, the expected T_2 should be much shorter. This method would require long measurement times that are impracticable in clinical cases. It is also possible to compare the ^{23}Na results with the ^{1}H T_2 weighted results in order to determine if the signal increase relates to liquid accumulation or intracellular ^{23}Na increase.

11.4.2 ^{23}Na MRI in Patients with Muscular ^{23}Na Channelopathy

In patients with inherited muscular ^{23}Na channelopathy (Paramyotonia Congenita) the ^{23}Na imaging techniques demonstrate a signal increase related to the increase in intracellular ^{23}Na concentration, but also the FID's provided information. The fact that the proportion of fast to slow component tends to increase when the $[Na^+]_{in}$ increases seems to strengthen the hypothesis that the fast component is associated more with $[Na^+]_{in}$ and the slow with $[Na^+]_{ex}$. These FID measurements, however, were non-selective, so that signal from the whole leg was acquired. The use of the surface coil minimised this problem due to its small region of sensitivity. Nevertheless, the variability of these measurements was high. The increase in the fast-to-slow component ratio, however, was detected in all pathological cases.

The two clinical studies demonstrate the sensitivity of ^{23}Na MRI to detect changes in the intracellular ^{23}Na concentration related to different pathologies. This method may therefore provide a new tool to study many different diseases related to malfunctioning of the ^{23}Na cellular pumps such as neurodegenerative diseases, epilepsy, migraine or to distinguish between ischemia and necrosis.

Part V

Summary

Chapter 12

Summary

Sodium ions (^{23}Na) play a vital role in cellular homeostasis and electrochemical activity throughout the human body. The *in-vivo* detection of ^{23}Na with magnetic resonance imaging (MRI), however, is hindered by the fast transverse relaxation ($T_2 \simeq 0.5\,\mathrm{ms}$), low tissue equivalent concentration, and small gyromagnetic ratio of sodium ions compared to protons (^{1}H). The goal of this work was to provide techniques and hardware for ^{23}Na MRI of the human brain, heart and muscle in a clinical whole-body scanner at $B_0 = 1.5\,\mathrm{T}$.

For this purpose, two radiofrequency (RF) volume coils (a saddle coil and a low-pass birdcage coil) were developed and a transmit/receive switch was adapted for ^{23}Na MRI at $\omega_0(1.5\,\mathrm{T}) = 16.84\,\mathrm{MHz}$. Furthermore, for volunteer and patient studies, a certified double-resonant high-pass birdcage and a surface coil (Rapid Biomed GmbH) were used. The performance of the RF coils was evaluated in terms of SNR, B_1 field homogeneity and RF efficiency. The double-resonant high-pass birdcage coil achieved about 10% higher SNR and significantly better B_1 homogeneity compared to the saddle coil and the low-pass birdcage coil.

A 2D and a 3D radial MR technique were developed, which acquired the data in a star-like fashion. The 3D radial sequence achieved a minimum echo time $TE_{min} = 70\,\mu\mathrm{s}$ for ^{1}H and $200\,\mu\mathrm{s}$ for ^{23}Na, allowing to detect both the short ($T_2^* = 0.5\,\mathrm{ms}$) and the long ($T_2^* = 12 - 25\,\mathrm{ms}$) components of the ^{23}Na NMR signal for total ^{23}Na content evaluation.

To reconstruct the radial data sets, Nearest Neighbour, Gauss and Kaiser-Bessel interpolation algorithms were implemented and tested. Similarly, sampling density pre- and postcompensation approaches were introduced. The optimal algorithm consisted of a Kaiser-Bessel gridding (window width 3.0, $\beta = 4.2054$) with a rho filter modified to correct for undersampling. This algorithm was implemented in the standard image reconstruction environment of the scanner, to achieve instantaneous image reconstruction of the acquired data. To evaluate the gradient performance of the radial MR pulse sequence, a pulse sequence was developed to measure the radial trajectory. It was found that the measured trajectory matched accurately with the theoretically expected one.

Phantom measurements were carried out to compare the 3D radial method to a standard cartesian gradient echo (GRE) sequence. Although radial images showed a 2.5 times higher SNR, they suffer from blurring due to suboptimal sampling density compensation. For an acquisition time of 10 min and a nominal resolution Δx of 4 mm, the $SNR = 35$ of the *in-vivo* ^{23}Na 3D radial images was twofold higher than that of the standard cartesian GRE results ($TE_{min} = 2$ ms). In the radial images *in-vivo* blurring due to T_2 signal decay during data acquisition was observed, reducing the resolution by approximately a factor of two.

Relaxation time measurements were carried out in both phantoms and volunteers. 3D radial data sets with increasing TE were acquired, ROI's were set in the resulting images and the data were fit to mono- and biexponential decays. For a a saline solution (NaCl), the expected monoexponential decay could be verified ($T_2 = 30$ ms, $T_1 = 50$ ms), while for a solution with NaCl and agarose, a biexponential relaxation with $T_{2\text{short}} = 0.96$ ms and $T_{2\text{long}} = 11$ ms was measured ($T_1 = 23$ ms). The *in-vivo* experiments showed a $T_{2\text{short}} = 0.5$ ms and $T_{2\text{long}} = 16$ ms for brain tissue.

Experiments were carried out in order to compare image quality (SNR and resolution) of the 3D radial and the cartesian GRE techniques at 1.5 T and 4 T. An SNR increase with increasing field strength B_0 of $SNR_{4\text{T}}/SNR_{1.5\text{T}} \sim 4$ was measured *in-vivo*. In phantoms, $SNR_{4\text{T}}/SNR_{1.5\text{T}} = 2.7$, as expected from the theory. Both cartesian and radial techniques produced good quality images, the cartesian method providing better spatial resolution and the radial technique better SNR. These results demonstrate that ^{23}Na MRI will significally benefit from higher field strengths.

The ^{23}Na 3D radial and cartesian techniques were applied to image brain tumours. A 20% ^{23}Na MRI signal increase in the tumour region was detected. The outline of the area with signal enhancement in the ^{23}Na images agreed with the shape of the tumour in the standard ^{1}H MR images. The contrast-to-noise ratio $CNR = 23\%$ between healthy tissue and tumour achieved with the 3D radial technique was 20% higher than the CNR of the cartesian sequence. It should be noted that the TE of the cartesian sequence is approximately one order of magnitude larger than that of the radial technique and consequently, the cartesian images do not represent the total ^{23}Na signal.

In order to visualise the intracellular sodium accumulation and the effects of specific therapy in patients with inherited sodium channelopathy (paramyotonia congenita) free induction decays (FID's), cartesian GRE, 2D and 3D radial images were acquired before and after local cooling and exercising of the patient left lower leg. A signal enhancement of $\sim 10\%$ was observed in the affected areas directly related with the pathologic inflow of ^{23}Na into the cell. The FID's yielded an increase in the fast to slow T_2 component ratio of 17%. The CNR between the cooled leg and the reference leg was 8% for the GRE technique, 11% for the 2D radial method and 10% for the 3D radial acquisition.

In conclusion, methods have been developed in this work to integrate ^{23}Na MRI into clinical routine. The clinical results and the results at higher field strengths are proofs that ^{23}Na MRI has the potential to evolve from research topic to clinical diagnostic tool.

Part VI

Appendix

Appendix A

MRI System

Figure A.1 shows a schematic diagram of the essential components of an MRI System. The main items of hardware are:

- the magnet
- three sets of magnetic field gradients and their drivers
- the *RF* transmit and receive coils and their electronics
- a transmitter chain
- a receiver chain
- a data acquisition system, a processing system and an image display

A.1 Magnets

Magnets used in MRI should ideally produce a strong magnetic field of high temporal stability and spatial uniformity over the entire imaging region. Additionally, the magnetic field should decrease rapidly with distance from the magnet exterior. High spatial uniformity of the field is needed to ensure that the NMR resonance frequency does not vary too significantly in the imaging region. In imaging experiments, B_0 inhomogeneity causes image distortion and enhanced T_2^* signal decay, which corresponds to broadening of the spectral lines in spectroscopy. A strong field is required to produce a large net nuclear magnetisation ($M_0 \propto B_0$) and, thus a large NMR signal. Temporal variations of the field lead to resonance frequency variations, which can cause image artefacts.

At present, three different magnet types are used for MRI: permanent magnets, resistive magnets and superconducting magnets.

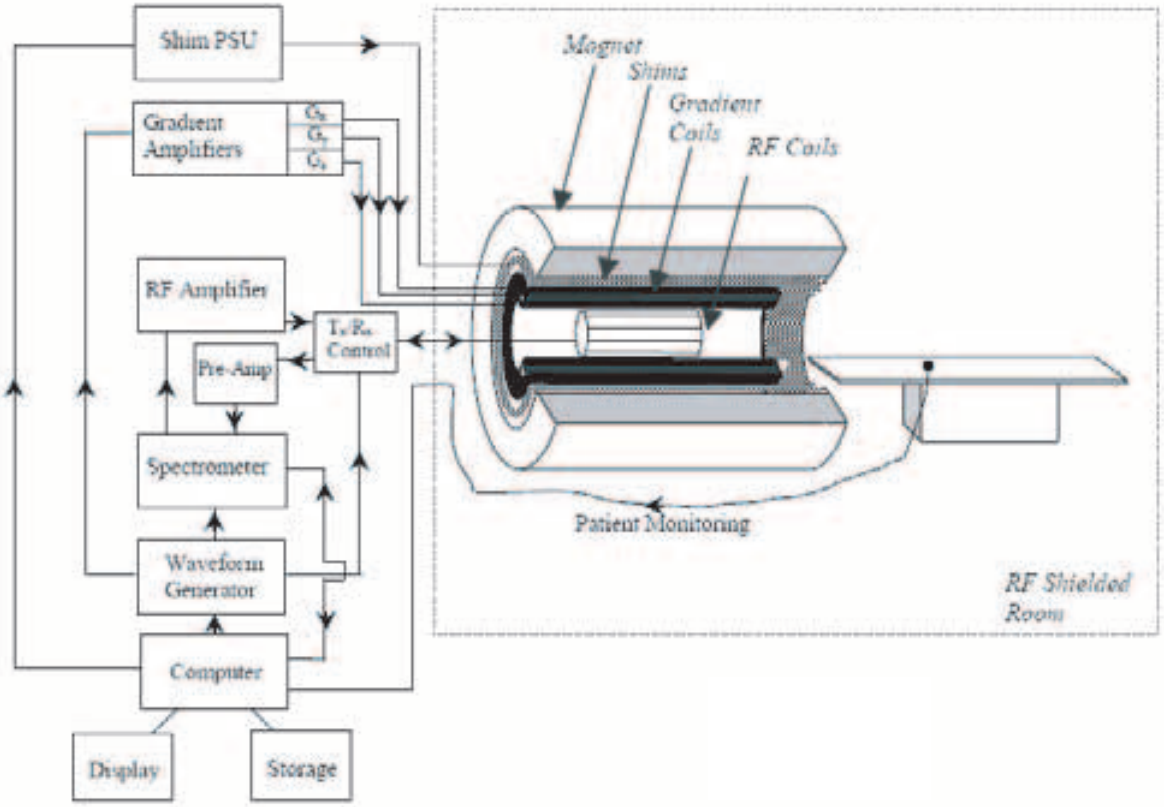

Figure A.1: Schematic diagram of an MRI System. Courtesy of [Bowtell 2004]

Permanent magnets are simple and affordable. They have very weak fringe fields, which makes MRI scanner site planning easier since the apparatus does not need to be magnetically shielded. In experiments using permanent magnets, the subject is placed between the two poles of the magnet. Alignment of the pole faces is difficult, since a very uniform magnetic field over the volume of interest is required. Another problem is the temperature drift of permanent magnets, since the RF frequency is usually not controlled by any feedback mechanism and would not remain at the Larmor frequency if the temperature were to change after the calibration.

Resistive magnets consist of coils of either copper or aluminium conductors, usually in the form of rectangular wire or flat strip, each coil being water-cooled. Resistive magnets are inexpensive and easy to maintain and fabricate. However, they have a high power consumption and a certain amount of field instability, as well as changes of field homogeneity as the magnet heats up. The maximum field strength that can economically be achieved is about $0,28\,\mathrm{T}$. Above this, power consumption becomes excessive and thermal stresses are a major problem.

The main magnet sketched in figure A.1 and shown in figure A.2.a is a superconducting magnet with a cylindrical bore. In this magnet, a strong, uniform magnetic field of strength B_0 is produced by a current flowing within the magnet windings of zero electrical resistance. The most commonly used material for the wires of superconducting magnets is an alloy of niobium and titanium, which becomes superconducting at temperatures below $10\,K$. In this state, no electrical power is dissipated in the wires and it is possible to pass very large, persistent currents through them to generate high magnetic fields. To keep the wires in superconducting state, they are encaged in a cryostat, which is a cooling system with liquid helium at $4\,K$. It consists of a liquid helium bath for the wires, encased by a vacuum space for thermal insulation, a radiation shield that is cooled by the helium gas as it boils off, and a liquid nitrogen store at $77\,K$ insulated from the room temperature by a vacuum space. Within the bore of the magnet there are three additional sets of coils: the shim coils, the gradient coils and the RF coils.

A.2 Shim Coils

The shim coils are placed closest to the wall of the magnet bore and are used to improve the homogeneity of the main magnetic field. The magnetic field produced by a bare magnet alone may vary as much as $100ppm$ in the imaging region. Magnetic susceptibility variation in the human body leads to field perturbations which can be as large as $9ppm$. Field shimming is the process of reducing the spatial variations in the main magnetic field by applying correcting fields.

The shim coils are made up of copper wires wound on a cylindrical former. There are typically several coaxial shim coils to correct linear and higher order field variations in x, y and z direction.

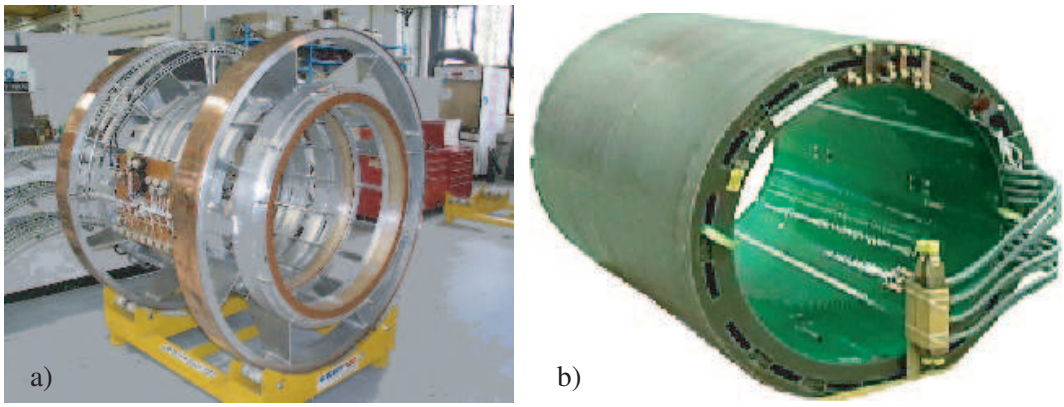

Figure A.2: Superconducting magnet (a) and Gradient Coil Set (b).

A.3 Gradient Coil Set

The gradient coil set lies within the shim coil cylinder and is made up of three separate coil arrangements which are used to generate linear variations of the magnetic field along the three cartesian axes x, y and z. In the cylindrical magnet geometry shown in Figure A.1, the windings used to generate each gradient are positioned on two coaxial cylinders, forming an inner primary coil and an outer screen. The screen cancels the field from the inner coil at locations outside the gradient coil. Generally the coils are held together with epoxy resin forming a single cylindrical annulus, which is suspended from the ends of the magnet structure. The currents in the gradient coils are produced by three amplifiers (one for each axis), which must be able to produce both high currents ($I \leq 500\,\mathrm{A}$) and high voltages ($V \leq 2000\,\mathrm{V}$) allowing these gradients to be rapidly switched on and off.

A.4 Transmit chain

RF pulses are produced by a transmitter and an *RF* coil. The transmitter defines the *RF* pulse shape, duration and power, as well as the sequence timing. The *RF* coil couples the energy generated by the transmitter to the nuclei of the sample.

In the transmitter, an oscillator generates the carrier frequency of the amplitude-modulated pulses. The carrier frequency is not necessarily identical to the Larmor-frequency of the system because, due to the application of a selection gradient during the *RF* pulse, the frequency may have to be shifted for off-center slice excitation. The frequency shift is performed by the synthesizer, which delivers an *RF* signal with a carefully computer controlled frequency. Subsequently, the carrier is amplitude modulated with the *RF* pulse envelope. The shape of the envelope is generated in the waveform generator, which drives the modulator, the output of which is an amplitude modulated *RF* pulse. The power

amplifier amplifies the small RF signalk to several kilowatts.

In case a quadrature coil is used, the quad hybrid splits the power into an I and a Q channel, which have a 90° phase difference. These signals are fed into the quadrature transmit coil, which will convert the power into a circularly polarized RF magnetic field. The quad hybrid also has an integrated transmit-receive (T/R) switch, which protects the preamplifier in the receive chain during the transmit pulse. Finally, the power monitor measures the forward power going into the patient, and compares it to federally regulated limits [Boskamp 2004].

The waveform generator produces the gradient waveforms required for each imaging sequence and generates the gating pulses and control logic required to direct other hardware elements, such as the T/R switch and the analogue-to-digital converters (ADC's) used to sample the signal.

A.5 Receive chain

The receiver chain starts with the RF coil (not necessarily identical to the transmit coil), which is close to the image sample. Once the signal has been detected by the RF coils, it is amplified by low noise amplifiers, to prevent the weak signal from being dominated by noise as it travels down the transmission line to the main receiver. The receiver circuit demodulates the signal from the RF band (e.g. 64 MHz) into a low frequency band (100 kHz) can then be digitised by the ADC. The demodulation is usually done with respect to a reference frequency ω_r equal to that of the transmitted RF. In quadrature demodulation, the signal is split and mixed with 2 reference signals that are 90 degrees out of phase, in order to maintain the information about the frequency spectrum of the signal. After mixing the signal at ω_0 with the reference frequency ω_r, the result is a mixture of signals at different frequencies. The term we are interested in is the one at $\omega_0 - \omega_r$. A single mixer with a single reference signal does not distinguish between $\omega_0 - \omega_r$ and $\omega_r - \omega_0$. By doing the quadrature detection, $\omega_r - \omega_0$ can be distinguished from $\omega_0 - \omega_r$, and the SNR and spectral information are maintained. The rejection of the unwanted signal may occur before going into a single ADC by using phase shifters, or in the computer after the digitization of the ADC's.

After demodulation, the signal passes through a low pass filter and is fed into the ADC, which then connects to the computer for reconstruction.

A.6 RF Coils

The RF coils are located inside the gradient coil set in proximity to the sample. The so-called body coil, which is often used as transmitter coil, is a large cylinder at the inner surface of the gradient coil. This surface is lined with a conducting layer, which acts as an

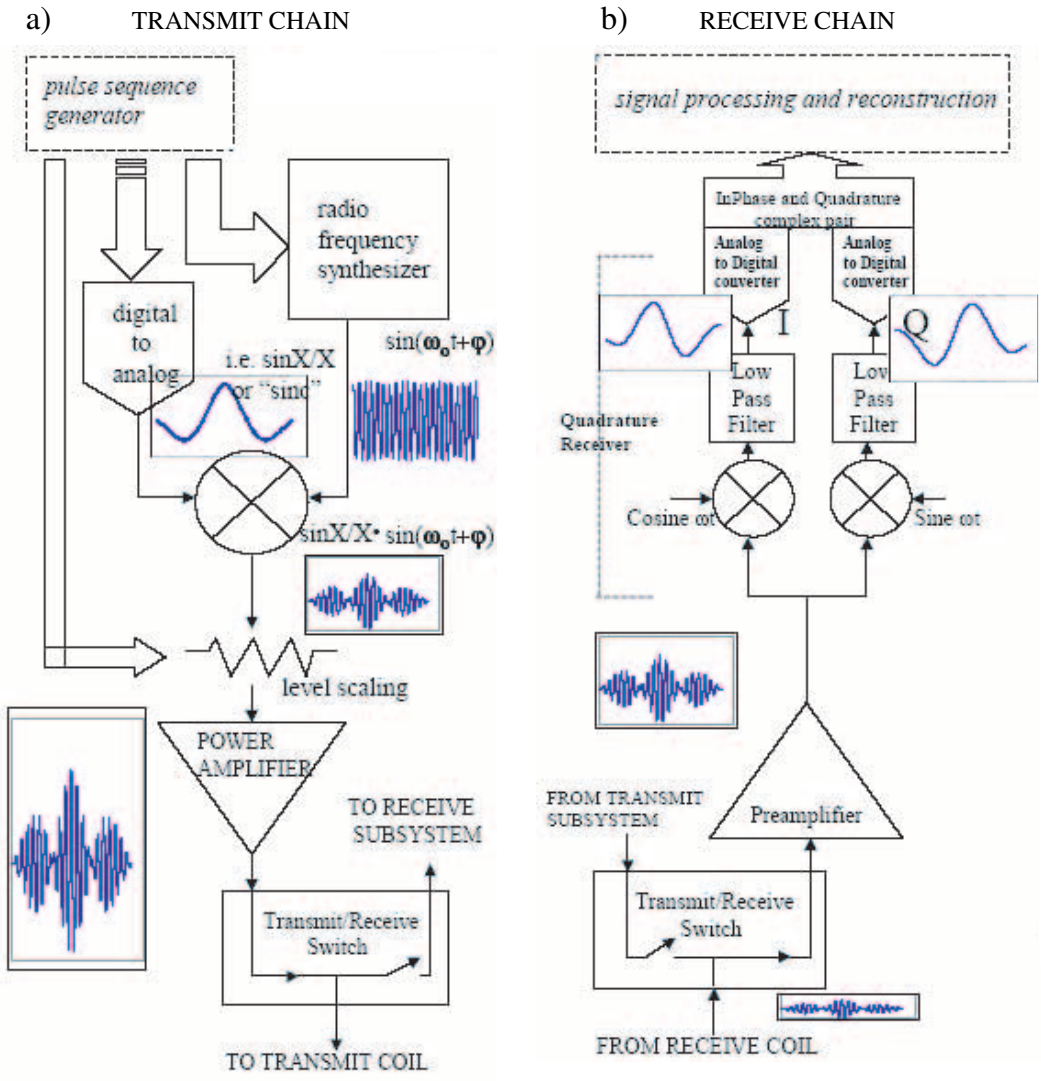

Figure A.3: Transmit Chain (a) and Receive Chain (b) of an MR scanner.

RF screen preventing interactions of the *RF* coil with the surrounding conductors of the gradient coil. The thickness of the screen is greater than the skin depth of the material from which it is formed at the operational radio frequency to achieve adequate *RF* screening. Slotting the screen helps to prevent the formation of unwanted eddy currents from gradient switching. The transmitter coil is designed to generate a strong, spatially uniform magnetic field B_1 that rotates in the plane orthogonal to the static B_0 magnetic field at the Larmor frequency. A uniform B_1 field is required for homogeneous *RF* excitation over the whole imaging region. A high-power *RF* amplifier is used to generate the large coil currents needed to yield acceptable *RF* pulse lengths. The required *RF* power increases as the size of the *RF* coil is increased, and is greater in high field systems, because of the higher Larmor frequency.

The receiver coils used to detect the NMR signal are placed close to the sample to maximize the strength of the detected signal relative to the noise produced in the coil by effects of the sample (or at lower B_0 fields by Johnson noise due to the coil resistance). In modern MRI systems there are typically multiple *RF* receiver coils positioned to optimally detect signals from different portions of the imaging region.

The receive and transmit coils are resonant at the same frequency, and when brought into proximity to one another, will electrically couple. This potentially degrades the uniformity of *RF* excitation, and the signal-to-noise ratio of the detected signal. To avoid this effect, the receiver coils are detuned while *RF* pulses are applied, so that they are no longer resonant at the same frequency as the transmitter coil, and the transmitter coil is detuned during signal reception. This active detuning can be accomplished by placing PIN diodes in parallel with tuning elements of the coil, and using a DC gating pulse to switch the diodes (Tx/Rx Control, Fig. A.1).

When an *RF* coil generates a linearly polarised B_1 field, the coil is called a linear coil. This field can be decomposed in two counter-rotating circularly polarised components, of which only one rotates with the precessing spins, while the other cannot be used for MR excitation or reception. A quadrature *RF* coil directly produces a circularly polarised B_1 field. In doing so, the *RF* power requirement can be reduced by a factor of two, avoiding *RF* strain and reducing the power deposited in the sample (specific absorption rate, SAR). Similarly, the *RF* signal emitted by spins is a circularly polarised field. When a linear coil is used for reception, only one component can be detected. By using a quadrature coil, both components are detected and the SNR of the received signal can be increased by a factor of $\sqrt{2}$. Moreover, the use of quadrature excitation and detection can reduce the intensity of artefacts caused by dielectric standing wave effects and conduction currents [Jin 98].

A.6.1 Tuning and matching network

During *RF* transmission ideally all of the *RF* power should be transferred to the coil and no power should be reflected. This is the power match situation, where the transmitter,

the coil and the cable should have the same impedance Z_0. The characteristic impedance Z_0 of the coaxial cable is given by the inductance L_0 and the capacitance C_0 per unit length of the cable as $Z_0 = \sqrt{L_0/C_0}$. In NMR, generally coaxial cables with $L_0 = 50\Omega$ are used. In order to transfer all the RF power to the coil, an input impedance of the coil of 50Ω is required, and the output impedance of the power amplifier has to be 50Ω. A tuning and matching network is used to match the impedance of the coil with the impedance of the coaxial cable. This matching network typically consists of capacitors, potentially in combination with an inductance. In general the components of the matching network should have low losses. Its design depends on the application and the Larmor frequency of the nucleus observed.

A.6.2 Sensitivity criteria and Signal-to-Noise Ratio

The principle of reciprocity establishes that the B_1 field strength of a coil at any point in space at a fixed power during transmission is equivalent to the sensitivity during detection (Hoult and Richards 1976). Therefore, to maximise the received signal, the B_1 field in the sample needs to be maximised. There are two parameters of the RF coil that can be modified for optimisation. First, the coil dimensions should match the sample dimensions as closely as possible. This is quantified by the filling factor [Haase 2000]. Second, all loss mechanisms should be reduced in order to achieve a high sensitivity. This is described quantitatively by the quality factor Q [Haase 2000]. The Q of the coil components, such as capacitors and inductors, is defined as the ratio of its ability to store energy to the total sum of all energy loss within the component.

$$Q = 2\pi \frac{\text{maximum energy stored}}{\text{total energy dissipated per period}} \tag{A.1}$$

In practical terms, this ratio reduces to the following formula:

$$Q = \frac{X}{R} \tag{A.2}$$

where X is the reactance of the device (given by the imaginary part of its impedance $Z = R + jX$) and R is the total Ohmic resistance. A resistance R at a temperature T, generates a random white noise across its terminals with a root mean square (rms) value V_N, given by the Johnson noise formula:

$$V_N = \sqrt{4kTR\Delta\nu} \tag{A.3}$$

where k is Boltzmann's constant ($k = 1,38 \cdot 10^{-23} J/K$), $\Delta\nu$ is the acquisition bandwidth and R is the sum of all resistances r_i that can be attributed to the different loss mechanisms found in NMR coils.

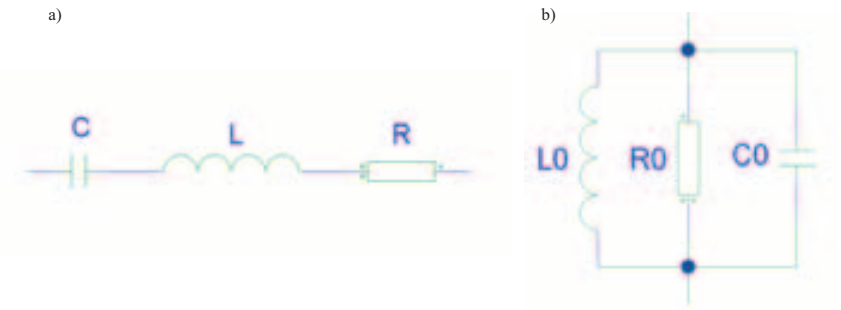

Figure A.4: Series (a) and Parallel (b) Equivalent circuit of an NMR coil.

In the design of the RF probe, only the temperature T (cooled copper coils and superconducting coils (references)) and the resistance R can be controlled. The four main contributions to this resistance are losses within the wires (ohmic resistance of the wire), losses due to magnetic interactions in the near field of the coil, losses due to electric interactions in the near field of the coil and losses due to electromagnetic radiation [Haase 2000].

The intrinsic signal-to-noise ratio SNR is the ratio between the NMR signal which originates from the region-of-interest (ROI) and the noise originating from the same region of the sample. The sensitivity of a RF probe is characterised by the B_1 field strength that is generated within the sample when a given power P is applied to the probe's input port. Therefore, the sensitivity of a RF probe at a certain location can be characterised by the ratio $B_1/\sqrt{P}$.

The key parameters to describe an RF coil are the B_1 field strength and homogeneity, the losses in the probehead and the losses induced by the sample. The latter two can be characterised by the quality factor. The quality factor Q is a measure of how sharply the coil is tuned, and is inversely proportional to its resistive losses. Any NMR resonator can be modelled by an inductance L, a capacitance C and a resistance connected either in series r_S or in parallel r_P (equivalent circuit analysis)([Jin 98], [Haase 2000]). Considering the series configuration in figure A.4.a, the quality factor can be defined as [Chen 1989]

$$Q = \frac{\omega L}{R} \tag{A.4}$$

for the parallel configuration in figure A.4.b, the quality factor is defined as

$$Q = \frac{R}{\omega L} \tag{A.5}$$

A high Q is equivalent to a coil with low losses. If the coil interacts with its surroundings (which will happen in an NMR experiment) Q can be decreased by the additional losses in the environment. Loading the coil with a subject or a phantom of similar conductivity should significantly lower Q, indicating that the losses in the sample dominate.

The sensitivity S of the RF probe relative to the sensitivity S_0 of an ideal coil as a function of the quality factors of an empty and loaded coil, $Q_{unloaded}$ and Q_{loaded} respectively, is given by:

$$\frac{S}{S_0} = \sqrt{1 - \frac{Q_{loaded}}{Q_{empty}}} \tag{A.6}$$

Taking only coil parameters into account, the SNR is proportional to the square root of the loaded Q_{loaded}. To optimize SNR, patient noise should be the dominant noise source, and coil losses should not play an important role for the SNR. Therefore, it is desirable that $Q_{loaded}/Q_{unloaded} < 5$. The effective volume of the coil, V_{eff}, is the volume integral of the magnetic energy in the entire volume normalized on that of the region of interest, and is not the same as the geometric volume. However, in general this means that the coil has to fit the anatomy of interest, and should not be made any bigger than necessary [Boskamp 2004].

A.7 Radiofrequency Shielding

The RF receiver coil constitutes an extremely sensitive antenna, and will respond to any environmental electromagnetic radiation at or near the Larmor frequency. To prevent spurious radio frequency signals from being picked up by the RF coil and thus producing artefacts in images and spectra, as well as to protect other sensitive equipment in the vicinity from radiation due to the various excitation pulses, the scanner is sited within an RF shielded room. The shielded room forms a six-sided enclosure made of electrically conducting material. Typically this attenuates externally generated RF within the room by at least $90dB$, thus reducing interfering signals to much weaker levels than that of the NMR signal. Transparent windows to the room can be formed using fine conducting mesh embedded within glass. It is important to ensure that any conducting wire that enters the room (e.g. mains power leads) do not breach the shielding by forming a path for transmission of external radio interference into the screened room. This can be accomplished by connecting such wires to electrical filtering circuitry at their point of entry into the screened room. The presence of a hole in the screening material as small as $1/30^{th}$ of a wavelength in size can compromise the screening, but by attachment of a waveguide, consisting of a long conducting cylinder, RF can be prevented from entering the room via the hole. Such waveguides can provide a port for optical projection into the scanner room using an external video projector and also for piping in medical gases. The waveguide has a cut-off frequency of approximately $230/D\,MHz$ where D is the waveguide diameter in meters, and only provides good shielding at frequencies well below this value. The achievable attenuation at low frequency increases with the square root of the ratio of length to diameter of the tube.

A.8 Data acquisition and processing system

The data collection and processing computer controls the carrying out of the experiments and takes care of the image reconstruction, postprocessing, display and storage.

A.9 MRI Systems used

For the ^{23}Na and ^{1}H MRI measurements inthis work, two different clinical shole body MR systems were used: a MAGNETOM Vision and a MAGNETOM Symphony (Siemens AG Medical Solutions, Erlangen, Germany). Due to technical limitation of the Vision system described in section 4.3 (page 55), predominantly the hardware and the software of the Symphony scanner were used to perform ^{23}Na MRI.

A.9.1 Technical description of the MAGNETOM Vision

Manufacturer

SIEMENS AG, Medical Solutions, Erlangen, Germany

Magnet

- Superconductive Magnet (wire material: Niobium Titanium - NbTi)
- Nominal field strength: 1.5 T
- Homogeneity: < 0.1 ppm for a diameter spherical volume of $10cm$ diameter
- Cooling system: liquid Helium ($T = 4.2°$K) in a closed circuit
- Weight: 7000 kg
- Bore: 160 cm length, 90 cm diameter
- Shim System: passive (metal plates) and active (12 separately controllable shim channels)

Gradient System

- Gradient coils in x-, y- and z-direction
- Maximum gradient strength: 25 mT/m
- Minimum rise time: $24\,\mu$s/$(\frac{\mathrm{mT}}{\mathrm{m}})$
- Maximum Slew Rate: $42\,\mathrm{T}/(\mathrm{m}\cdot\mathrm{s})$

- EPI booster

High frequency System

- Frequency range: $10 - 85$ MHz
- Transmit amplifier bandwidth: 500 kHz
- Gain stability (5 min): < 0.1 dB (low signal path)
- Noise figure < 0.5dB

Receiver System

- 4 analog/digital receiver channels
- Receiver bandwidth: 1 MHz (for each channel)
- Sampling rate: 10 MHz (Sampling resolution: $100ns$)
- Dynamic range of each channel up to 128 dB (automatic control)

Digital Signal Processing System

- Analog quadrature demodulation
- Analog/digital filtering

A.9.2 Technical description of the MAGNETOM Symphony

Manufacturer

SIEMENS AG, Medical Solutions, Erlangen, Germany

Magnet

- Superconductive Magnet (Niobium Titanium)
- Nominal field strength: 1.5 T
- Homogeneity: $< 0.1ppm$ for a diameter spherical volume of 10 cm diameter
- Cooling system: liquid Helium ($T = 4.2°$K) in a closed circuit
- Weight: 5500 kg
- Bore: 160 cm length, 90 cm diameter

- Shim System: passive (metal plates) and active (12 separately controllable shim channels)

Gradient System

- Gradient coils in x-, y- and z-direction
- Maximal gradient strength: $30\,\mathrm{mT/m}$
- Minimum rise time: $10\,\mu\mathrm{s}/(\frac{\mathrm{mT}}{\mathrm{m}})$
- Maximum Slew Rate: $100\,\mathrm{T}/(\mathrm{m}\cdot\mathrm{s})$

High frequency System

- Frequency range: $10-85\,\mathrm{MHz}$
- Transmit amplifier bandwidth $500\,\mathrm{kHz}$
- Gain stability (5 min): $< 0.1\,\mathrm{dB}$ (low signal path)
- Noise figure $< 0.5\,\mathrm{dB}$

Receiver System

- 8 digital receiver channels (quadrature)
- Receiver bandwidth: 1MHz
- Sampling rate: $10\,\mathrm{MHz}$ (Sampling resolution: $100\,\mathrm{ns}$)
- Dynamic range of each channel up to $128\,\mathrm{dB}$ (automatic control)

Digital Signal Processing System

- Analog quadrature demodulation
- Analog/digital filtering

Appendix B

Circuitry

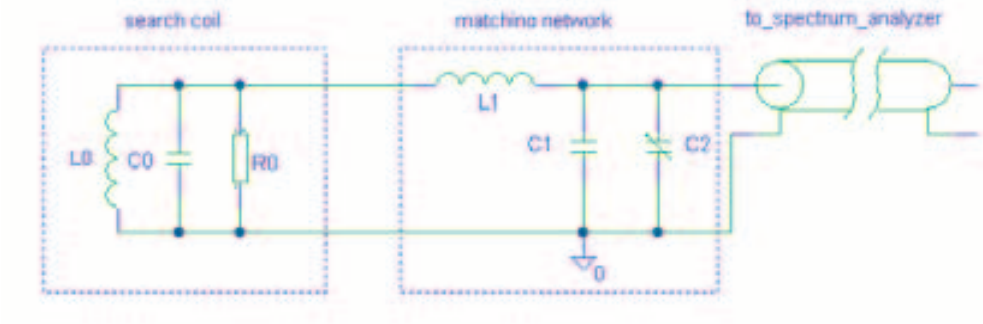

Figure B.1: Search Loop tuning and matching circuit.

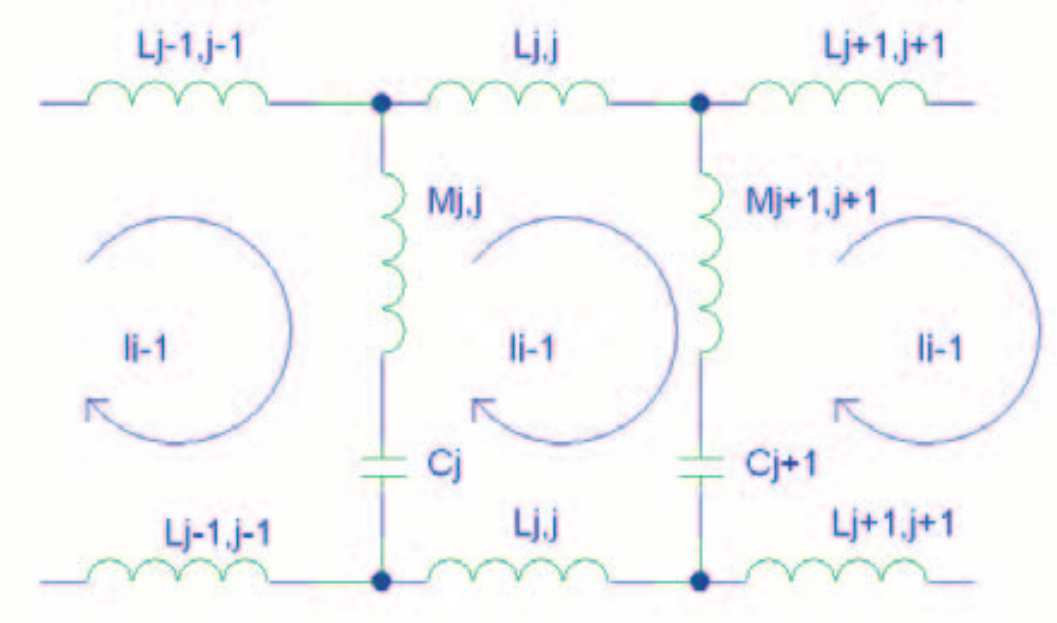

Figure B.2: Low-pass birdcage equivalent circuit.

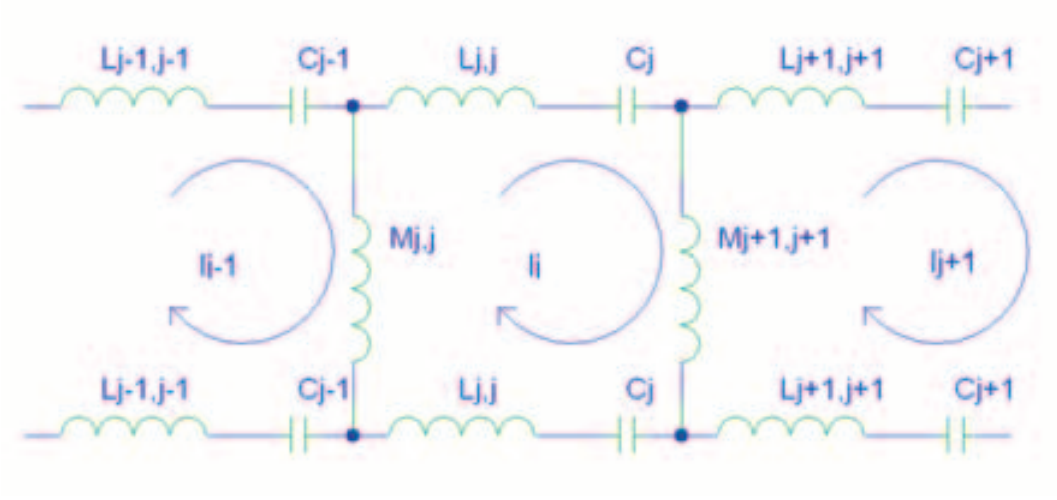

Figure B.3: High-pass birdcage equivalent circuit.

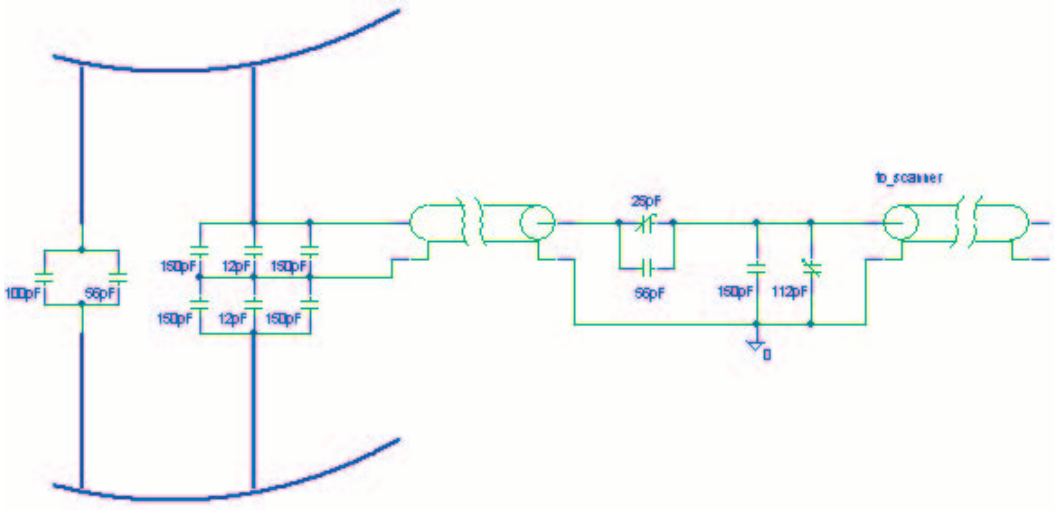

Figure B.4: Birdcage coil tuning and matching system.

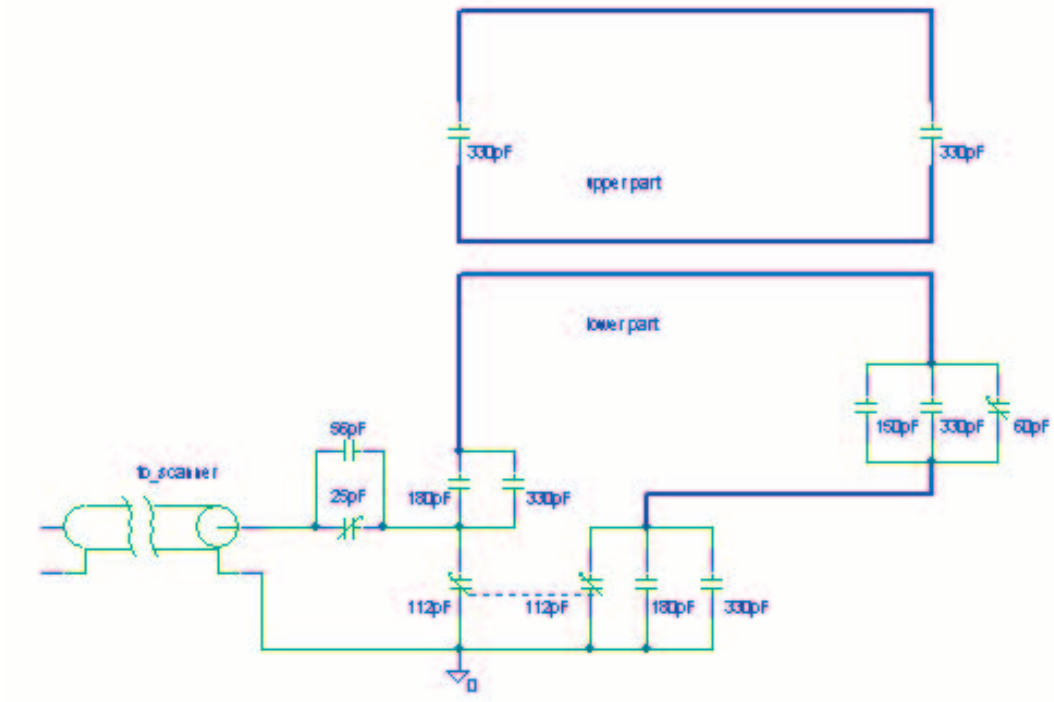

Figure B.5: Saddle coil tuning and matching circuit.

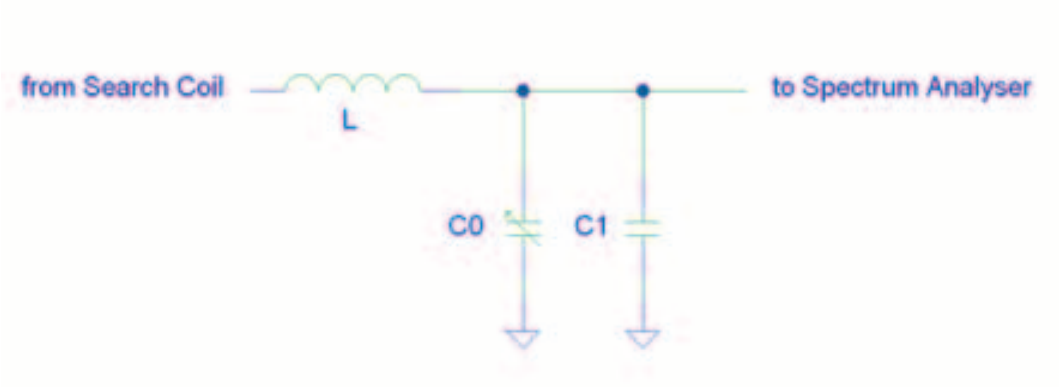

Figure B.6: L-section tuning and matching circuit.

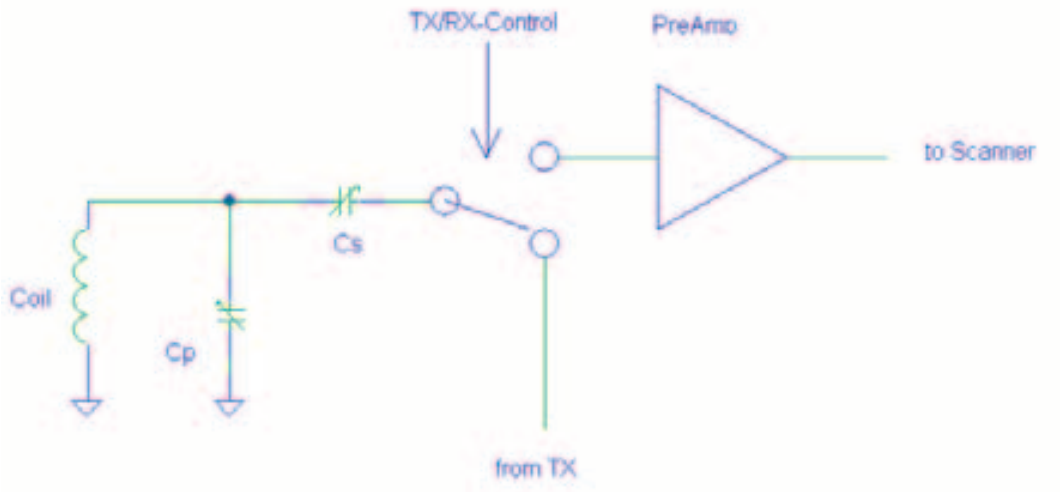

Figure B.7: Schematic diagram of the preamplifier.

Bibliography

[Abra61] Abragam A
Principles of Nuclear Magnetism
Oxford University Press, New York (1961)

[Balcom 98] Balcom BJ
SPRITE Imaging of Short Relaxation Time Nuclei
in: Spatially Resolved Magnetic Resonance
pp. 75-86, Wiley-VCH, Toronto (1998)

[Bedall 1988] Bendall MR
Calibrated uncoupling of tightly coupled concentric surface coils for in vivo NMR
Magn Reson Med. 1988 Dec;8(4):380-93.

[Bernstein 1998] Bernstein MA,
Concomitant Gradient Terms in Phase Contrast MR:
Analysis and Correction.
Magnetic Resonance in Medicine 1998; 39:300-308.

[Boada 1997a] Boada FE, Christensen JD, Gillen JS, Thulborn KR
Three-Dimensional Projection Imaging with Half the Number of Projections
Magnetic Resonance in Medicine 37:470-477 (1997)

[Boada 1997b] Boada FE, Gillen JS, Shen GX, Chang SY, Thulborn KR
Fast Three Dimensional Sodium Imaging
Magnetic Resonance in Medicine 37:706-715 (1997)

[Boada 1997c] Boada FE, Shen GX, Chang SY, Thulborn KR
Spectrally Weighted Twisted Projection Imaging: Reducing T2 Signal Attenuation Effects in Fast Three Dimensional Sodium Imaging
Magnetic Resonance in Medicine 38:1022-1028 (1997)

[Borthakur 99] Borthakur A, Hancu I, Boada FE, Shen GX, Shapiro EM, Reddy R
In vivo triple quantum filtered twisted projection sodium MRI of human articular cartilage
Journal of Magnetic Resonance (1999) 141, 286-290.

[Brooks 1976] Brooks RA, DiChiro G
Principles of computer assisted tomography (CAT) in radiographic and radioisotopic imaging
Physics in Medicine and Biology 1976; 21(5):689-732.

[Boskamp 2004] Boskamp EB
RF Subsystem. MR Physics for Physicists
ISMRM Kyoto (2004)

[Bowtell 2004] Bowtell R
Overview of an MRI system. MR Physics for Physicists
ISMRM Kyoto (2004)

[Bull 72] Bull TE
Journal of Magnetic Resonanace (1972) vol. 8,p. 344.

[Bull 79] Bull TE, Forsen S, Turner DL
Journal of Chemical Physics (1979) vol. 70,p. 3106.

[Cannnon 86] Cannon PJ, Maudsley AA, Hilal SK, Simon HE, Cassidy F
Sodium nuclear magnetic resonance imaging of myocardial tissue of dogs after coronary artery occlusion and reperfusion
Journal of the American College of Cardiology (1986) 7:573-579.

[Callaghan 1991] Callaghan PT
Principles of Nuclear Magnetic Resonance Microscopy
Oxford Science Publ. (1991)

[Chen 1989] Chen C-N and Hoult DI
Biomedical Magnetic Resonance Technology
Adam Hilger, Bristol and New York (1989)

[Chesler 1992] Chesler J, Vevea F, Boada F, Reese T, Change C, Barrere B, Liu A, Thulborn K
Rapid 3D reconstruction from 1D projections for metabolic MR imaging of short T2 species.
Proc. SMRM, 11th Annual Meeting, Berlin, p.665 (1992)

[Constantinides 2000] Constantinides CD, Gillen JS, Boada FE, Pomper MG, Bottomley PA
Human Skeletal Muscle: Sodium MR Imaging and Quantification - Potential Applications in Exercise and Disease
Radiology (2000) 216:559-568.

[Cooley 1965] Cooley JW, Tukey JW
An Algorithm for Machine Calculation of Complex Fourier Series
Math Computation vol.19 pp.297-301 (1965)

[Du 04] Du J, Korosec FR, Thornton FJ, Grist TM, Mistretta CA
High-resolution mujltistation peripheral MR angiography using undersampled projection reconstruction imaging
Magn. Res. Med. 2004 Jul, 52(1):204-8.

[Duvvuri 99] Duvvuri U, Leigh JS, Reddy R
Detection of residual quadrupolar interaction in the human breast in vivo using sodium-23 multiple quantum spectroscopy J Magn Reson Imaging. 1999 Mar;9(3):391-4.

[Duyn 98] Duyn JH, Yang Y, Frank JA, van der Veen JW
Simple correction method for k-space trajectory deviations in MRI
Journal of Magnetic Resonance (1998) vol 132, pp. 150-153.

[Ernst66] Ernst RR, Anderson WA
Application of Fourier transform spectroscopy to magnetic resonance
Review of Scinetific Intrum., 37:93-102 (1966)

[Gatehouse 2003] PD and Bydder GM
Magnetic resonance imaging of short T2 components in tissue
Clinical Radiology (2003) 58:1-19.

[Goldsmith 75] Goldsmith M, Damadian R
NMR in cancer. VII. Sodium-23 magnetic resonance of normal and cancerous tissues
Physiol Chem Phys (1975) 7:263269.

[Haacke 99] Haacke EM Brown RW, Thompson MR, Venkatesan R
Magnetic Resonance Imaging: Physical Principles and Sequence Design
John Wiley & Sons, New York (1999)

[Haase 86] Haase A, Frahm J, Matthaei D, Haenicke W, Merboldt KD
Rapid NMR imaging using low flip-angle pulses
J. Magn. Reson. (1986) 67:258-266.

[Haase 2000] Haase A, Odoj F, von Kienlin M, Warnking J, fidler F, Weisser A, Nittka M, Rommel E, Lanz T, Kalusche B, Griswold M
NMR Probeheads for In Vivo Applications
Concepts in Magnetic Resonance (2000) 12(6):361-388.

[Harpen 87] Harpen MD
Sample noise with circular surface coils
Medical Physics (1987) 14:616-618.

[Hayes 1985] Hayes CE, Edelstein WA, Schenck JF, Mueller OM and Eash M
An efficient highly homogeneous radiofrequency coil for whole-body NMR imaging at $1.5T$
Journal of Magnetic Resonance (1985) vol. 63, pp. 622-628.

[Hayes 1986] Hayes CE, Edelstein WA and Schenk JF
Radio frequency coils in NMR in Medicine
Thomas SR and Dixon RL Eds.
New York, 1986 American Association Physicists Med., pp. 142-165.

[Hilal 83] Hilal SK, Maudsley AA, Simon HE, et al
In vivo NMR imaging of tissue sodium in the intact cat before and after acute cerebral stroke
AJNR Am J Neuroradiol (1983) 4:245249.

[Hilal 85] Hilal SK, Maudsley AA, Ra JB, et al.
In vivo NMR imaging of sodium- 23 in the human head
J. Comput. Assist. Tomogr. (1985) 9:17.

[Hilal 88] Hilal SK et al
Sodium Imaging
In: Stark and Bradley eds. Magn. Res. Imaging (1988) pp. 715-29.

[Hoult 96] Hoult et al.
Sensitivity of the NMR Experiment
Grant DM, Harris RK ed.
Encyclopedia of Nuclear Magnetic Resonance. Volume 7, pp. 4256-4266
John Wiley and Sons, New York (1996).

[Jaccard 86] Jaccard G, Wimperis S, Bodenhausen G
Multi-quantum NMR spectroscopy of $S = 3/2$ spins in isotropic phase: A new probe for multiexponential relaxation
Journal of Chemical Physics (1986) 85(11):6282-6293.

[Jackson 91] Jackson J, Meyer C, Nishimura D, Macovski A
Selection of a convolution function for Fourier inversion using gridding
IEEE Trans Med Imaging (1991) MI-10(3):473-478.

[Jerecic 2001] Jerecic R
Development and Optimisation of Techniques for the Measurement of Spin-Spin Relaxation times in Sodium Magnetic Resonance Imaging at 1.5T
Physics PhD Thesis, University of Heidelberg (2001).

[Jin 98] Jin J
Electromagnetic Analysis and Design in Magnetic Resonance Imaging
CRC Press.

[Joseph 96] Joseph PM
Sodium-23 Magnetic Resonance of Human Subjects
Encyclopedia of Nuclear Magnetic Resonance
Grant DM and Harris RK Editors
John Wiley and Sons 1996.

[Joseph 87] Joseph and Summers
The flip-angle effect: a method for the detection of sodium-23 quadrupole splitting in tissue
MRM (1987) 4:67-77.

[Kak 88] Kak AC and Slaney M
Principles of Computerized Tomographic Imaging
IEEE Press, New York 1988.

[Kim 97] Kim RJ, Lima JA, Chen EL, Reeder SB, Klocke FJ, Zerhouni EA, Judd RM
Fast 23Na magnetic resonance imaging of acute reperfused myocardial infarction. Potential to assess myocardial viability
Circulation. 1997 Apr 1;95(7):1877-85.

[Kim 97b] Kim RJ, Judd RM, Chen EL, Fieno DS, Parrish TB, Lima JA
Relationship of Elevated ^{23}Na Magnetic Resonance Image Intensity to Infarct Size After Acute Reperfused Myocardial Infarction
Circulation. 1999 Jul 13;100(2):185-92.

[Lee00] Lee RF, Giaquinto R, Constantinides C, Souza S, Weiss RG, Bottomley PA.
A broadband phased-array system for direct phosphorus and sodium metabolic MRI on a clinical scanner.
Magn Reson Med. (2000) 43(2):269-77.

[Lethmate 03] Lethmate R, Ratiney H, Wajer FT, Cremillieux Y, van Ormondt D, Graveron-Demilly D
Dynamic magnetic resonance imaging paragraph sign with radial scanning: a post-acquisition paragraph sign keyhole approach
MAGMA. (2003) 16(1):21-8.

[Macovski 99] Macovski A
Volumetric NMR imaging with time-varying gradients
Magn Reson Med (1983) 2:29-40.

[Maeda 85] Maeda A, Sano K, Yokoyama T
Reconstruction by weighted correlation for MRI with time-varying gradients
IEEE Trans of Med Imaging (1985) 7:26-32.

[Man 96] Man PP
Quadrupolar Interactions
Grant DM, Harris RK ed.
Encyclopedia of Nuclear Magnetic Resonance
John Wiley and Sons, New York (1996).

[Mason 97] Mason GF, Harshbarger T, Hetherington HP, Zhang Y, Pohost GM, Twieg DB
A method to measure arbitrary k-space trajectories for rapid MR imaging
Magnetic Resonance in Medicine (1997) vol. 38, pp.492-496.

[Narayana 88] Narayana PA, Kulkarni MV, Mehta SD
NMR of ^{23}Na in Biological Systems
in: Magnetic Resonance Imaging (Second Edition) vol. 2 pp. 1553-1563
editors: Partain CL, Price RR, Patton JA, Kulkarni MV, Everette James A Jr. 1988

[Onodera 87] Onodera T, Matsui S, Sekihara K, Kohnop H
A method for measuring field-gradient modulation shapes. Application to high-speed NMR
Journal of Physics E: Scientific Instrument. (1987) vol. 20, pp. 416-419.

[Oesterle 1999] Oesterle C, Markl M, Strecker R, Kraemer FM, Hennig J
Spiral Reconstruction by Regridding to a Large Recrtilinear Matrix: A Practical Solution for Routine Systems
Journal of Magnetic Resonance Imaging (1999) 10:84-92.

[O'Sullivan 85] O'Sullivan J
A fast sinc function gridding algorithm for Fourier inversion in computer tomography
IEEE Trans Med Imaging (1985) 4(4):200-207.

[Ouwerkerk 03] Ouwerkerk R, Bleich KB, Gillen JS, Pomper MG nad Bottomley PA
Tissue Sodium Concentration in Human Brain Tumors as Measured with ^{23}Na MR Imaging
Radiology (2003) 227:529537.

[Papadakis 97] Papadakis NG, Wilkinson AA, Carpenter TA, Hall LD
A general method for measurement of the time integral of variant magnetic field gradients: application to $2D$ spiral imaging
Magnetic Resonance Imaging (1997) vol. 15, num. 5, pp. 567-578.

[Parrish 97] Parrish TB, Fieno DS, Fitzerald SW, Judd RM
Theoretical Basis for Sodium and Porassium MRI of the Human Heart at 1.5T
MRM 38:653-661 (1997).

[Pauly 2004] Pauly J
Reconstruction of Non-Cartesian Data
Standford (2004).

[Pipe 2000] Pipe JG
Reconstructing MR Images From Undersampled Data: Data-Weighting Considerations
Magnetic Resonance in Medicine 2000; 43:867-875.

[Pipe99] Pipe JG, Menon P
Sampling density compensation in MRI: Rationale and an iterative numerical solution
Magnetic Resonance in Medicine 1999; 41:179-186.

[Rasche99] Rasche V, Proksa R, Sinkus R, Bornert P, Eggers H
Resampling of data between arbitrary grids using convolution interpolation
IEEE Trans Med Imaging 1999; 18(5):385-392.

[Robson 03] Robson MD, Gatehouse PD, Bydder M, Bydder GM Magnetic resonance: an introduction to ultrashort TE (UTE) imaging
J Comput Assist Tomogr. 2003 Nov-Dec;27(6):825-46.

[Romanzetti 04] Romanzetti AS, Halse M, Kaffanke J, Rioux J, Balcom BJ,N. J. Shah
A Comparison of Three SPRITE-Based Techniques for the Quantitative 3D Imaging of the ^{23}Na Spin Density on a 4 T Whole-Body Machine
Abstract 1698. Proceedings of the ISMRM 2004, Kyoto.

[Rooney 96] Rooney WD, Springer CS Jr
A Comprehensive Approach to the Analysis and Interpretation of the Resonances of Spins 3/2 from Living Systems
NMR in Biomedicine, vol.4, pp.209-226 1991.

[Rotin 89] Rotin D, Steele-Norwood D, Grinstein S, Tannock I
Requirement of the Na/H exchanger for tumor growth
Cancer Res 1989; 49:205211.

[Saff 1997] Saff EB and Kuijaars ABJ
Distributing many points on a sphere
Mathematical Intelligencer 19.1 (1997) 5-11.

[Schlichter 89] Schlichter CP
Principles of Magnetic Resonance
Electric Quadrupole Effects, pp. 485-502.
Springer Verlag 1989.

[Springer 96] Springer CS Jr
Biological Systems: Spin-3/2 Nuclei Encyclopedia of Nuclear Magnetic Resonance
Grant DM and Harris RK Editors
John Wiley and Sons 1996.

[Stehning 2004] Stehning C, Bornert P, Nehrke K, Eggers H, Dossel O
Fast isotropic volumetric coronary MR angiography using free-breathing 3D radial balanced FFE acquisition
Magn Reson Med. (2004) 52(1):197-203.

[Thulborn 99] Thulborn KR, Davis D, Adams H, Gindin T, Zhou J
Quantitative tissue sodium concentration mapping of the growth of focal cerebral tumors with sodium magnetic resonance imaging
Magn Reson Med (1999) 41:351359.

[Thulborn 99b] Thulborn KR, Gindin TS, Davis D, Erb P
Comprehensive MR imaging protocol for stroke management: tissue sodium concentration as a measure of tissue viability in nonhuman primate studies and in clinical studies
Radiology (1999) 213:156166.

[Van Emous 2001] Van Emous JG, Vleggeert-Lankamp CL, Nederhoff MG, Ruigrok TJ, Van Echteld CJ
Postischemic Na(+)-K(+)-ATPase reactivation is delayed in the absence of glycolytic ATP in isolated rat hearts
Am J Physiol Heart Circ Physiol. (2001) 280(5):H2189-95.

[Vaughan 94] Vaughan JT, Hetherington HP, Otu JO, Pan JW, Pohost GM
High frequency volume coils for clinical NMR imaging and spectroscopy
Magn Reson Med. 1994 Aug;32(2):206-18.

[Vega 96] Vega AJ
Quadrupolar Nuclei in Solids
Encyclopedia of Nuclear Magnetic Resonance
Grant DM and Harris RK Editors
John Wiley and Sons 1996.

[Watkins and Fukushima 1987] Watkins JC and Fukushima E
A Pickup Loop which is sensitive only to RF magnetic field
TMAU Newsletter 346, pp. 56-57, 1987.

[Werbelow 96] Werbelow LG
Relaxation Theory for Quadrupolar Nuclei
Encyclopedia of Nuclear Magnetic Resonance
Grant DM and Harris RK Editors
John Wiley and Sons 1996.

[Wild 03] Wild JM, Paley MN, Kasuboski L, Swift A, Fichele S, Woodhouse N, Griffiths PD, van Beek EJ
Dynamic radial projection MRI of inhaled hyperpolarized 3He gas
Magn Reson Med. (2003) 49(6):991-7.

[Winter 01] Winter PM, Poptani H, Bansal N
Effects of chemotherapy by 1,3-bis(2-chloroethyl)-1- nitrosourea on single-quantum- and triplequantum- filtered Na-23 and P-31 nuclear magnetic resonance of the subcutaneously implanted 9L glioma
Cancer Res (2001) 61: 20022007.

List of Figures

List of Tables

Acknowledgements

I would like to thank Prof. Dr. Lothar Schad an Prof. Dr. Dr. Wolfhard Semmler, as well as Prof. Dr. Christian Wacker and Prof. Dr. Dr. Wolfgang Bauer, for the opportunity to work in the German Cancer Research Centre and the supervision of my PhD thesis. Thanks for their interest and support. I would also like to thank Prof. Dr. Josef Bille for accepting the supervision of my thesis in the Physics University of Heidelberg.

I wish to express my sincere thanks to Dr. Michael Bock for his interest, help and guidance during this work, as well as for proofreading of this thesis. Special thanks to Dr. Renate Jerecic for introducing me in the world of ^{23}Na MRI, for her help and encouragement. For his interest and help, I would like to thank Prof. Dr. Peter Bachert.

For their help during the implementation of the radial sequences, I would like to thank my colleagues Dr. Michael Bock, Dr. Achim Bankamp, Dr. Andre Bongers, Dr. Sven Zuehlsdorff and Dr. Michael Amann, as well as Dr. Peter Speier and Dr. Stefan Thesen from Siemens Medical Solutions. Thanks to Dr. Rainer Umathum for his support with the hardware part of this thesis. For proofreading the thesis and helping me with the layout thanks to Dr. Peter Siegler, Dr. Michael Amann and Falko Lohberger.

For his collaboration in the ^{23}Na MRI clinical studies and optimism I would like to thank Dr. Marc-Andre Weber.

Thanks to all my colleagues for providing help and advice in different aspects of this project as well as for providing a pleasant and friendly atmosphere in which to work.

Special thanks to Dr. Ioannis Panagiotelis for uncountable hours in the scanner, moral support and useful advise during the project, as well as for proofreading the thesis.

Finally, I wish to express my gratitude to my family for their unconditional love, patience, encouragement, as well as moral and material support.